

Development of Functionalized Fibrous Structures

Vývoj funkcionalizovaných vláknitých struktur

Habilitation Thesis

Mohanapriya Venkataraman, M.Tech., M.F.Tech., Ph.D.

2024

Annotation

This habilitation thesis is a set of selected published scientific papers or engineering papers supplemented with a commentary according to §72 paragraph 3-point Act No. 111/1998 Coll. on universities. In total, the full set of scientific paper contains 24 research works published in impact factor journals and 2 published books. The chosen scientific papers are mainly focused on the study of fibrous structures for functional properties. The fibrous structures' peculiarities are explained where the important structural properties, such as porosity, are described. The possibilities of using different materials to boost selected functional properties are discussed. The development of nanoporous membranes by using electrospinning and electrospraying techniques are described. The efficacy of middle layers in multi-layered fibrous structures are detailed and embedding polyethylene glycol in silica aerogel, polytetrafluoroethylene fibrous layer filled with Aerogels and Phase Change Materials, aerogel-coated Kevlar Woven Fabrics, and PEG/Metal particle-coated viscose fabric is also described. The application of advanced structures for enhanced functionality is also provided. The conclusion summarizes this research topic's findings, benefits, and future direction.

Keywords: Fibrous Structures, Aerogels, Thermal properties, Phase change materials, Functional properties, Measurement Techniques

Anotace

Tato habilitační práce je souborem vybraných publikovaných vědeckých prací nebo technických prací doplněných komentářem podle §72 odst. 3 písm. zákona č. 111/1998 Sb. o vysokých školách. Celkem soubor vědeckých prací obsahuje 24 vědeckých prací publikovaných v časopisech s impakt faktorem a 2 vydané knihy. Vybrané vědecké práce jsou zaměřeny především na studium vlákných struktur z hlediska funkčních vlastností. Jsou vysvětleny zvláštnosti vlákných struktur, kde jsou popsány důležité strukturní vlastnosti, jako je např. poróznost. Jsou diskutovány možnosti využití různých materiálů pro zvýšení vybraných funkčních vlastností. Je popsán vývoj nanoporézních membrán pomocí technik elektrospinningu a elektrosprejování. Podrobně je popsána účinnost středních vrstev ve vícevrstvých vláknitých strukturách a zapouštění polyethylenglykolu do křemičitého aerogelu, polytetrafluorethylenová vlákná vrstva plněná aerogely a materiály s fázovou změnou, kevlarové tkaniny potažené aerogely a viskózní tkanina potažená částicemi PEG/kovu. Je rovněž uvedena aplikace pokročilých struktur pro zvýšení funkčnosti vlákných struktur. V závěru jsou shrnuty poznatky, přínosy a budoucí směřování tohoto výzkumného tématu.

Klíčová slova: Vlákenné struktury, aerogely, tepelné vlastnosti, materiály s fázovou změnou, funkční vlastnosti, měřicí techniky

Contents

1	Introduction	4
2	Fibrous Materials	5
3	Development of Fibrous Structures	10
3.1	Influence of Fiber Geometry on Thermal Insulation	11
3.2	Fabric Structure and Thermal Insulation	12
3.3	Chemical Coating and Embedded Particles	12
3.4	Nonwoven Structures with Enhanced Thermal Properties	13
3.5	Porous and Multi-layered Fibrous Materials	14
3.6	Embedding Polyethylene glycol in Silica Aerogel	16
3.7	Electrospun Nanofibrous Membranes	19
3.8	Electrosprayed Microporous Membranes with Aerogel	19
3.9	Electrosprayed Microporous Membranes with Aerogels/Phase Change Materials	22
3.9.1	Effect of Aerogels and PCMs on Thermal Comfort Properties	23
3.10	Thermal Performance of a Multi-layer Composite	25
3.11	Effect of Laser Irradiation on Kevlar Fabric Treated with Nanoporous Aerogel	26
3.12	Performance improvement using PCM	26
4	Measurement of Thermal Insulation	27
4.1	Effect of Laser Irradiation	28
5	Simple Determination of Key Structural Parameters for Fibrous Materials	30
6	Applications	31
7	Conclusion	32
8	Published Outputs	33
9	Declaration	35
10	References	35
11	Appendix: Full Texts of Selected Publications	46
11.1	Author contributions	46
11.2	Publication 1: Electrospun nanofibrous membranes embedded with aerogel for advanced thermal and transport properties	49
11.3	Publication 2: Preparation of Electrospun, Microporous Particle Filled Layers	60
11.4	Publication 3: Modelling and simulation of heat transfer by convection in aerogel treated nonwovens	73
11.5	Publication 4: Structural analysis of embedding polyethylene glycol in silica aerogel	87
11.6	Publication 5: Transport Properties of Electro-Sprayed Polytetrafluoroethylene Fibrous Layer Filled with Aerogels/Phase Change Materials	97
11.7	Publication 6: Mass transfer and the thermal buffering effect of hydrophobic fabrics with a single-side coating of MPCMs	112
11.8	Publication 7: Hydrophobicity, water moisture transfer and breathability of PTFE-coated viscose fabrics prepared by electrospinning technology and sintering process.	129

1 Introduction

The use of new fibrous-based materials in new applications is influenced by emerging industries such as biotechnology, which are looking for efficient, environmentally friendly technological alternatives. The solutions focus on renewable local resources and eliminating dependence on petrochemical-based raw materials and imported resources, including fibers, which become the subject of speculative manipulations on the markets. Similarly, progressive nanotechnologies, nanomaterials, and new, energetically, and ecologically efficient processes of physical (pre)activation and surface modification (hybridization) of fibrous substrates are applied in multidisciplinary, innovative concepts of the textile industry. The prevailing long-term development trend is the construction of new textile structures for clothing textiles capable of adapting to changes in environmental conditions and special technical textiles with unique properties required for their applications [1].

The future textiles will cover several functions related to their use for both clothing and technical purposes. These highly functional textiles will represent a wide class of products, providing several properties needed to improve their practical applicability or for utilization in special conditions. The highly functional textiles also have common general requirements for:

- Ecological production and disposal.
- Slow aging processes (e.g., by improving abrasion resistance).
- Easy maintenance.
- Aesthetic and sensory functions (appearance, hand, formability).
- Protection against dangerous environmental influences (UV radiation, electromagnetic radiation, microorganisms, extreme temperatures, chemicals, etc.).

Several special functions can be partially achieved by modifying standard textile production procedures and selecting suitable fibers or finishing procedures. The main goal is to use materials and structures with an adaptive response, i.e., they only react in the positive direction when conditions change. Future clothes will also serve as an information system. The use of clothing textiles as an interface for the transmission of information is natural because clothing is an integral part of a person and accompanies him in most activities. Basic information about a person's condition will be obtained from textile sensors of temperature, heart rate, and breathing.

The final use of products based on special materials can be divided into two groups in terms of the complexity of the environment for which they are intended. One group consists of products with specific required properties, the design of which is standard, and no special requirements are placed on them in terms of their physical and mechanical properties. Such products include sheets with antibacterial effects, non-flammable fabrics for curtains, and antistatic socks. The second group includes products with specific new properties intended for more demanding conditions. The physical and mechanical properties of the materials used will reach high parameters. This category mainly includes special work and protective clothing for sports and leisure. The quality and properties of such products are determined by the fiber material used, the strength of the yarn, and the construction of the fabric. Fibers with high-performance properties will be used primarily for special protective functions.

Textiles often serve as a barrier protecting people from nature's extremes, continuously impacting humans. There are several uses for textile materials for thermo-physiological comfort in the application area [2]. The fibrous constructions and structural parameters change functional capabilities, and the efficacy can be improved further by varying the combinations

of textile construction, coatings, and treatments[3] as the composite structure's fiber, moisture and air drive its thermal behaviors [3–6]. Thickness, weight per unit area, and packing density (p.d.) or porosity are the crucial construction parameters [4–6].

In multilayer clothing, the middle layer often prevents the temperature extremes from seeping through to affect the body. The middle thermal insulating layer comprises several fiber materials, including conventional nonwovens. Contemporary research is focused on alternate, high-performing, cost-effective systems. Before improvements in materials and garment design can be achieved, a comprehensive analysis of functional mechanisms is necessary [7].

Treatment of nonwoven fibrous structures with aerogel is limited to high-performance applications due to the high cost of aerogels. Also, phase change materials (PCMs), a class of substances that absorb and release thermal energy during a phase transition, may enhance textiles' thermal performance.

This habilitation thesis represents development in the field of selected functional properties of fibrous structures accompanied by a set of author research findings published mainly in scientific papers in impact factor journals, books, and reputable conference papers indexed in the Scopus database. The full texts of the 8 selected articles are in the appendix of this thesis.

This thesis is organized to articulate the novelties of the research work conducted. The Introduction provides the background for the study of fibrous structures for functional properties. The fibrous structures' peculiarities are explained in the second chapter, where the important structural properties, such as porosity, are described. The third chapter explores the possibilities of using different materials (Aerogels, Phase Change Materials (PCM), etc.) to boost some functional properties. The fourth chapter elaborates on the development of structures with improved functionality. The development of nanoporous membranes by using electrospinning and electrospraying techniques are described. Experiments to demonstrate the efficacy of middle layers in multi-layered fibrous structures are detailed. Embedding polyethylene glycol in silica aerogel, polytetrafluoroethylene fibrous Layer Filled with Aerogels and Phase Change Materials, aerogel-coated Kevlar Woven Fabrics, and PEG/Metal particle-coated viscose fabric is described. The fifth chapter deals with the application of advanced structures for enhanced functionality. The following chapter showcases selected research work done on the topic of this thesis with its Impact factor. The conclusion summarizes this research topic's findings, benefits, and future direction.

It is to be noted this research had partial support from various agencies, including the Grantová agentura České republiky/Czech Science Foundation (GACR) and Technologická agentura České republiky („TA ČR”).

2 Fibrous Materials

The fibrous structures are used today not only for clothing purposes (the consumption of clothing textiles is directly related to the size of the human population) but also for technical applications (the consumption of technical fibrous structures is related to the maturity of human society). Structures produced from fibrous materials by textile technologies play a decisive role in the development of new products, e.g., composites. These materials significantly influence not only traditional industries such as construction and the automotive or aviation industry but also the fields of medicine, ecology, and environmental protection. Sufficient comfort is also a requirement for protective clothing and barrier textiles, which often require special solutions. The textile structures of the present and the future have a dual role. They are typical consumer

products and special construction materials with specific manifestations. In textiles for clothing purposes, the traditional aspect of fashion, style, and comfort prevailed. In the future, it can be expected that clothing textiles will need to ensure:

- Suitable air permeability.
- Improved thermal insulation properties.
- Water vapor permeability (0.4 nm), but liquid water impermeability (100 μm).
- Protection against dangerous environmental influences (microorganisms, UV radiation).
- Ecological production and disposal (biodegradability).
- Self-cleaning effects and dust repellency.
- Improved resistance to wear (abrasion).
- Health care support (vital functions, healing processes).
- Support for cosmetic manifestations (regeneration processes on the skin).
- Easy maintenance, including cleaning and ironing.
- Improved hand, aesthetic sensations and appearance even after several cycles of use and maintenance.
- Controlled active identification of textiles in conditions of limited visibility.

There exist partial solutions enabling the implementation of some of these requirements. In the future, multifunctional effects and solutions to problems associated with a limited lifetime can be expected.

Fibrous structures are based on fibers as very specific materials with extraordinary properties compared to polymers of the same chemical composition.

Basic fiber features are:

Fibrous structure due to the irreversible orientation of macromolecules along the length of fibers and partial crystallization (i.e., three-dimensional arrangement).

The cooperative nature of viscoelastic deformation is due to the interconnection of the segments of polymeric chains by secondary bonds.

The organoleptic characteristics of the fibers are hand, drape, and gloss.

Fibers are a very specific group of materials whose behavior depends on both time and temperature. The specific structural peculiarity of fibrous materials is their huge porosity P [–]. The IUPAC defined three pore groups: micropores (less than 2 nm), mesopores (from 2 to 50 nm), and macropores (more than 50 nm). Micro- and mesopores are typical for fibers (typical fiber diameter is over 10 μm), and macropores are typical for fibrous assemblies (structural unit dimension in mm). Volume porosity is generally defined as the ratio between fibrous structures ρ_S and corresponding fiber ρ_F densities. Alternatively, it is possible to use fabric volume V_S and fiber volume V_F or volume portion of fibrous phase $v_F = V_S/V_T$; see eqn (1)

$$P = 1 - \rho_S / \rho_F = 1 - V_S / V_F = 1 - v_F \quad (1)$$

One problem is how to specify fiber density because there are some pores in fibers, and the density of the corresponding polymer (fiber mass density) is influenced by the fibers' supermolecular structure. It is shown in [7] that polymer density is related to crystallinity and

orientation and can be predicted by the molar contributions method. E.g., amorphous polyethylene terephthalate has a density of 1330 kg m^{-3} , and fully crystalline PET has a density of 1500 kg m^{-3} , and their ratio is $\rho_c / \rho_a = 1.13$ [8]. For semicrystalline polymer with crystallinity x_c and density, ρ_{sc} is valid.

$$\rho_{sc} = \rho_a / (1 - 0.103 x_c) \quad (2)$$

Based on experimentally evaluated fiber density [kg m^{-3}] (by weighting of fibers of known diameter and length) and density of corresponding polymer ρ (fiber mass density), it is possible to evaluate fiber porosity P_f from equation (3) [7].

$$P_f = 1 - \rho_f / \rho \quad (3)$$

Fiber porosity of natural fibers is around 5-20% and 1-2% for synthetic fibers but most are closed micropores [6,9]. For the linear textile structures as staple yarns, the porosity P_Y [-] is closely related to packing density μ as the ratio between fiber volume V_f and whole yarn volume V_y is given by the equation (4);

$$P_y = 1 - \mu = 1 - V_f / V_y = 1 - 4T / \pi D^2 \rho \quad (4)$$

The product of the effective cross-section area of yarn S (sum of fiber areas in yarn cross-section) and fiber mass density ρ [kg m^{-3}] is, in fact, the yarn fineness T [tex]. Real yarn diameter is $D = \sqrt{4T / \pi \mu \rho}$. The porosity of yarns is interrelated with their real density ρ_Y which depends on the twist and production technology of the yarn. For the middle level of twist, it was found that $\rho_Y / \rho F = \mu_Y \approx 0.525$ approximately. This correction can be used to calculate yarn diameter [6].

The porosity of planar textiles can be evaluated from their structural parameters. The basic structural parameters of woven fabrics (a) DC weft sett [1/m] and the DM warp sett [1/m]; (b) planar mass W [kg m^{-2}], and; (c) fabric thickness h [m]. For an ideal layout, the thickness of the yarns in the fabric is equal to $t_1 = d_C + d_M$, where d_C is the diameter of the weft yarns, and d_M is the diameter of the warp yarns. If $W \approx t_1$, the yarns in the fabric have an approximately circular cross-section [9,10]. Fabric porosity can be divided into three categories:

1. Macro - porosity related to the spaces between warp and weft yarns.
2. Meso-porosity related to the arrangement of fibers in yarns (packing density).
3. Micro porosity related to voids and pores in fibers.

For planar textile structures, it is possible to calculate the total „volume“ porosity P [-] based on planar mass and thickness only by relation (5);

$$P = 1 - \frac{W}{h r_F} \quad (5)$$

where h [m] is fabric thickness, and W [kg m^{-2}] (usually [g m^{-2}]) is the planar mass – gsm. For heavy fabrics and lower-thickness fabrics, the porosity is 85%. Low planar mass and high thickness lead to a porosity of over 95 %.

This is typical for textile structures in that the thickness h [m] is not arbitrarily selected but functionally dependent on planar mass W [kg m⁻²] and total porosity P by relation (6);

$$h = \frac{W}{r_F (1 - P)} \quad (6)$$

The porosity influences the thermal properties of fibrous structures. Thermal comfort and thermal resistance of the fabric R [m² K W⁻¹] are correlated as the reciprocal value of the amount of heat that has passed through the unit of time over the unit area of the textile at unit temperature difference [11].

$$R = \frac{\Delta T}{Q} = \frac{h}{\lambda} \quad (7)$$

where specific heat flux is Q [W m⁻²];

Thermal conductivity is λ [W m⁻¹ K⁻¹],

and the thickness of the textile structure is h [m].

Thermal resistance is dependent on the thickness of the textile structure and directly related to thermal comfort. “Clo” is used to quantify thermal comfort [12]. It defines insulation as a clothing system that ensures comfort of a seated person in a standard ventilated room with a flow speed of air is 0.1 m/s, at a temperature T_a of 21 °C and relative air humidity RH less than 50%. Under these circumstances, approximately 24% of metabolic heat is estimated to be lost by evaporation from the surface of the skin. The total metabolic heat under these conditions is 1 Met, which is equivalent to a value of 50 kcal m⁻² h⁻¹, i.e. 58.153 W m⁻². The remaining 76% of metabolic heat, i.e., $Q_e = 44.1963$ Wm⁻² (38 kcal m⁻² h⁻¹), must be dissipated through clothing via radiation, convection, and conduction modes.

The temperature of the skin is in a comfortable state, estimated as $T_s = 33$ °C. The total thermal resistance R_T (insulation) of system clothing and surrounding insulating layer is then given by the relation (8);

$$R_T = \frac{T_s - T_a}{Q_e} = \frac{33 - 21}{44.1963} = 0.2715 \text{ [m}^2 \text{ K W}^{-1}] \quad (8)$$

The insulation of the air layer under the above conditions is chosen to be $R_a = 0.12$ m² K W⁻¹ [13].

Air conductivity $\lambda_a = 0.024$ W m⁻¹ K⁻¹ is an intensive quantity, and the thickness of the surrounding insulation air layer h_l is under these conditions equal to

$$h_l = \lambda_a R_a = 0.12 \times 0.024 = 0.0028 \text{ [m]} \quad (9)$$

Therefore, the insulation of only the clothing system is $R_O = R_T - R_a = 0.1515$, i.e., approximately 0.155 m² K W⁻¹ i.e. 1 Clo. One of the major factors that influence thermal properties of textiles is their thickness, which in turn influences particular porosity of structures [14]. Fig 1 shows the minimum material thickness (with thermal conductivity of air) securing the given clo [14].

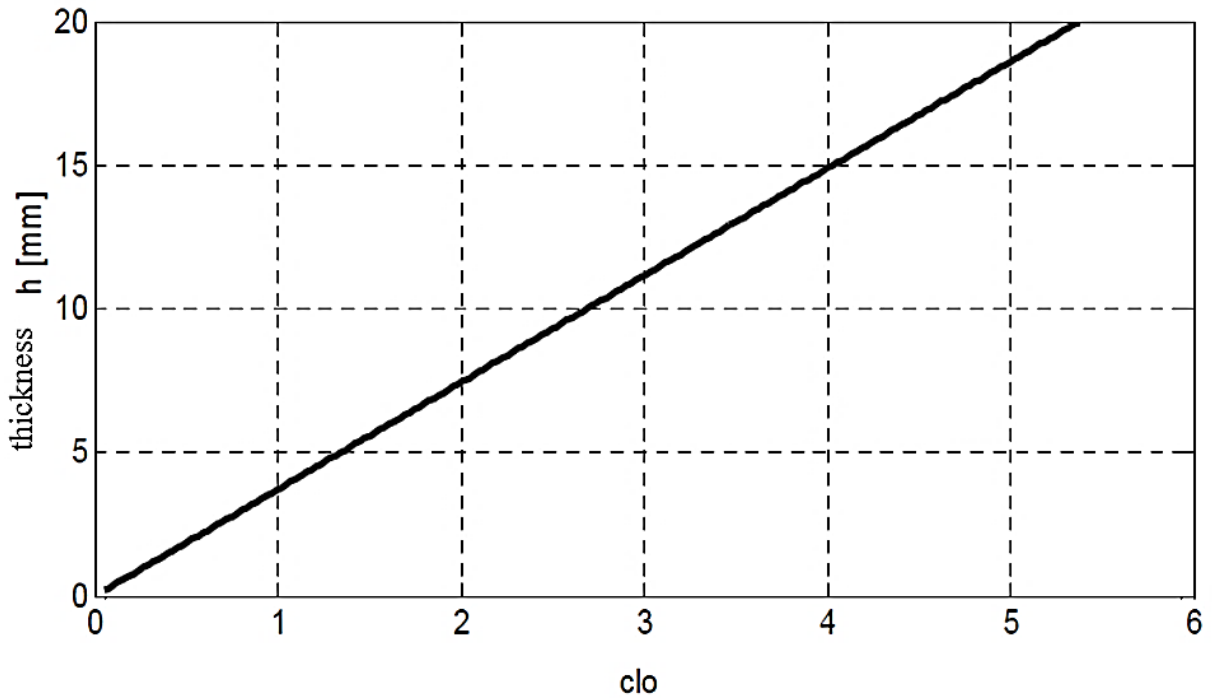


Figure 1 The minimum thickness h of the fabric having the thermal conductivity of the air for the given thermal comfort clo .

The heat balance defined by the ISO standard (ISO/TR 11079) is used for complex evaluation of thermal comfort [14,15],

$$M - W = K + C + S + E + C + E + H \quad (10)$$

Where:

M [$W m^{-2}$] is the metabolic rate,

W [$W m^{-2}$] is the mechanical power,

K [$W m^{-2}$] is heat loss by conduction from the skin,

C [$W m^{-2}$] is heat loss by flow (convection) from the skin,

S [$W m^{-2}$] is heat loss by radiation from the skin,

E [$W m^{-2}$] is the evaporative heat loss from the skin,

C_{res} [$W m^{-2}$] is the heat loss through respiration,

E_{res} [$W m^{-2}$] is the evaporative heat loss during respiration,

H [$W m^{-2}$] is the rate of accumulation of body heat.

Details about the evaluation of these quantities are given in [15].

One of the very important characteristics for calculating thermal comfort is the thermal conductivity of components. The general theory for predicting the thermal conductivity of polymers has not yet been fully developed. A simple model based on the so-called phonon model of the thermal conductivity of polymers is described by Krevelen and Hoftyzer [16]. Heat transport is realized in quanta of energy from one layer to another with the speed of sound. The heat transfer is directly proportional to the density and heat capacity. For thermal expression, the Debye equation is then commonly used for conductivity [17]

$$\lambda = \rho u L C_p \quad (11)$$

where C_p [J/(kg K)] is the specific heat capacity at constant pressure,

L [m] is the distance between molecules in adjacent isothermal layers, and

u [m s⁻¹] is the speed of elastic waves (speed of air propagation).

Assuming L is approximately constant and independent of temperature, it turns out that there is a direct dependence between the thermal diffusivity DT and the propagation speed of air u .

For amorphous polyethylene terephthalate (PET), a thermal conductivity of 0.218 [Wm⁻¹ K⁻¹] was found. The thermal conductivity of crystalline polymers can then be determined if the density ratio ρ_c/ρ_a is known. For less regular crystalline polymers, it is possible to use the relation (12) [18].

$$\frac{\lambda_c}{\lambda_{am}} = 1 + 5.8 \left(\frac{\rho_c}{\rho_{am}} - 1 \right) \quad (12)$$

Calculated thermal conductivity of semi-crystalline polyethylene terephthalate (PET) with crystallinity of 0.40 correlates well with the experimental value of 0.272 [W m⁻¹ K⁻¹] [19].

The thermal conductivity of flat textiles can be predicted using two-phase models composed of yarns with thermal conductivity λ_Y (or often fibers with thermal conductivity λ_f) and air with thermal conductivity λ_a . The proportion of the air phase corresponds to the porosity P , and the proportion of the yarn/ fibrous phase is $1 - P$. Lower thermal limit conductivity then corresponds to the serial arrangement of the phases, and the upper limit of the thermal conductivity corresponds to the parallel arrangement. In real textiles, it is advantageous to calculate the effective thermal conductivity as a linear combination of upper and lower limits [9,10,20].

Lower and upper limits are special cases of the general mixing rule where the thermal conductivity of system λ_p (see eqn. 13) is equal to the power-weighted mean for suitable power n .

$$\lambda_p = \sqrt[n]{P\lambda_a^n + (1-P)\lambda_Y^n} \quad (13)$$

For $n = 1$, the upper limit results (arithmetic mean); for $n = -1$, the lower limit (harmonic mean) results; and for $n = 0$, the geometric mean results. It holds that the limit of x^n for n approaching zero is approximately $\log(x)$.

Thermal conductivity is generally different for dry and wet fibers, where absorption of water vapor may potentially cause an exothermic shift that alters the thermal conductivity. Also, latent heat is diffused through the pores of materials. Loss of heat is accelerated when physical activity leading to sweating is stopped, resulting in faster cooling. Such challenges need to be addressed to develop effective cold-weather clothes [21].

3 Development of Fibrous Structures

The research on design and investigation the thermal behavior of high-performance fabrics was focussed on researching different combinations of insulation materials, battings, and coatings, investigating innovative means for thermal measurements, and comprehend conductive, convective, and radiative modes of heat transfer [22].

3.1 Influence of Fiber Geometry on Thermal Insulation

Fabrics' primary constituent is fiber. In most cases, fibers are converted into yarns, which are then interlaced (woven), interloped (knitted), or otherwise made into a porous fabric structure. Without creating yarns, nonwoven fabrics are made directly from fibers or filaments [23]. The still air trapped within the fabric structure is crucial for materials to resist heat flow or fabric thermal insulation. The simple upper limit of the thermal conductivity is the weighted arithmetic mean of the two-phase system composed of fibers and air.

The fineness and form of the fibers in the fabric structure create air gaps, interrupt the flow of air, and reduce heat loss through radiation. The boundary air layer that exists between the inner surface of the fabric and the human body surface makes an important contribution to the fabric's thermal insulation. The boundary-layer hypothesis explains this. The air is at rest in relation to the surface area of the fiber or fabric in the immediate vicinity. As a result, the boundary air layer and still air already present boost thermal insulation and offer significant resistance to heat transfer through the fabric [24].

The fineness, crimp, and length of fiber all contribute to its physical composition. Because there is less conduction and convection through motionless air, there is more thermal insulation. The use of fine microfibrils to provide excellent thermal insulation is demonstrated well by Fibrefill®. In recent years, microfibers have been added to clothing to improve functionality, especially in athletics, sleeping bags, and tents. Microfiber yarns have a higher number of fibers and a greater surface area [24].

Moreover, the diameter of the fibers in a fabric affects how much heat is transferred by radiation. Lee [25] reported that high-density microfibers are most effective in minimizing radiation loss; low-density microfibers and fine fibers are second, and regular fibers are third. He also reported that there is no significant difference in radiation conductivity (λ_r) between solid and hollow regular fibers and between polyester and polypropylene microfibers. For all the battings, λ_r increases slightly as diameter increases, a phenomenon commonly referred to as the "thickness effect" in literature. Certain fibers have geometrical forms like "Crimp" that improve the air insulation by trapping the air within the yarn structure. Naturally, wool has a natural crimp that increases insulation, and similar results may be achieved by artificially introducing crimp or surface irregularity.

The investigations [26] show a considerable correlation between fabric thickness and thermal insulation. Heat and moisture transport is influenced by the porosity and arrangement of the fibers. The hollowness of the fibers with parallel and perpendicular arrangements helps with thermal insulation [27].

The planar mass and fabric thickness, which are in charge of the fabric's overall porosity, are determined to be the key contributors to the thermal conductivities of textile constructions with particular cross sections. The numerical simulation method emerges as a very practical and efficient way to assess the fiber's thermal conductivity due to the measurement limitations of thermal conductivity. This experiment examines a variety of fiber types with various circular hollow sizes. It quantified how planar mass and fabric thickness affect the fabric's thermal conductivity [28].

The overall thickness of the garment increases with the number of fabric layers, which contributes to the overall insulation offered by the clothing system. The inner, middle, and outer layers are typically the three layers that make up the multilayer principle. Along with the skin, the inner layer creates the microclimate. Direct heat and moisture conduction begin at this

stratum. The majority of the thermal insulation typically comes from the middle layer. This layer typically consists of materials with a lot of trapped air. The major purpose of the outer layer is to protect and preserve the integrity of the garment. Excellent mechanically performing materials must be used to build the outer layer. A chemical finish is typically applied to the outer layer to obtain certain desirable features, such as water repellency [11,29].

3.2 Fabric Structure and Thermal Insulation

The ability of fabrics to insulate against heat is influenced by their construction and variations in the yarn structure. The yarn structure may influence radiation, moisture transport, and conduction in fabrics in conjunction with the fiber geometry and fabric construction. Compared to flat filament yarn, spun yarn or textured filament yarn can trap more air, resulting in greater thermal insulation. The degree of yarn twist also has an impact on heat and moisture transmission since tighter-knit yarns require less air volume and may enhance the capillary effect in the transport of moisture [24].

Many studies show that fabric thickness is the most crucial factor in determining thermal insulation [30]. More air is trapped in the fabric because thicker fabrics have more air space. Fabric thermal insulation occasionally shows a linear relationship with fabric thickness (in accordance with the known relation between thermal conductivity and thermal insulation). Much better insulation is offered by multilayer fabrics than by a single thick fabric. However, for multilayer fabrics, the relationship between heat resistance and thickness is nonlinear [31]. Because different fabric structures have different porosity levels, the amount of trapped air in the fabric also varies. Generally, knitted materials trap more air than woven fabrics, though the tightness of the weave or knit is also important. As a result of the numerous dead air gaps created by the yarns or fibers that run perpendicular to the surface, fabrics with pile or napped constructions can improve their heat insulation. Fabric thermal insulation performance is significantly influenced by fabric weight. Cold-weather apparel must balance good thermal insulation and low weight to increase comfort. Fabrics with higher density have a lower propensity to loss heat through radiation. The heat conductivity of textiles depends on the material (kind of fiber) and manufacturing factors (porosity or packing density) [32]. How to anticipate the thermal conductivity of multiphase systems with particular geometrical layouts continues to be discussed.

3.3 Chemical Coating and Embedded Particles

Chemical treatment of a fabric can change not only its fiber, yarn, and fabric features but also its thermal properties. Chemical coatings and embedded particles that can store heat have been developed, and as the environment changes, they might release heat.

Phase change materials (PCMs) have been the subject of numerous studies regarding the treatment of fabrics [33–35]. When phase change materials are included in textiles, they absorb heat energy as they move from a solid to a liquid form and release heat as they change back to a solid state. Several hypotheses suggest that clothes composed of PCM-treated fabric can tune body temperature temporarily as the environment changes. For instance, they have used PCM-enhanced clothing to show a small, fleeting heating/cooling impact [36]. The application of PCMs can be included in the spinning dope of manufactured fibers or into the structure of fabrics by coating, printing, or laminating PCMs on a foam, which is necessary to avoid leakage or by capsules.

Phase change materials (PCMs) are physically a class of substances that absorb or release thermal energy due to phase transition. The PCMs could be used in various industries, such as

smart textiles, solar energy storage, construction materials, food storage, thermal management of electronic systems, and so forth[35]. PCM textiles could be used for thermal regulation or energy harvesting. There are various commercial PCM textile products over the globe. Due to their flexibility and effective production using cutting-edge technology, ultrafine fibers are highly compatible with various materials.

The fabric has a sturdy, porous structure as well. Many uses for the fabric were suggested by changing its properties, including those for antibacterial protection, oil/water separation, particle filtration, thermal control, Joule heating, optical properties, EMI shielding, etc [35].

Aerogels have extremely low solid material densities (between 0.08 and 0.4 g/cm³) and high interior surface areas (between 900 and 1000 m²/g) [11,37] and are known for their exceptional insulation properties. The complex nanoporous structure of silica aerogel is linked to its heat transfer phenomenon through its tortuous structure and closed pores [38]. They are created using sol-gel technique and solvent extraction in a supercritical condition[39]. Studies show aerogels in fibrous structures can potentially enhance the thermal performance of the fibrous materials.

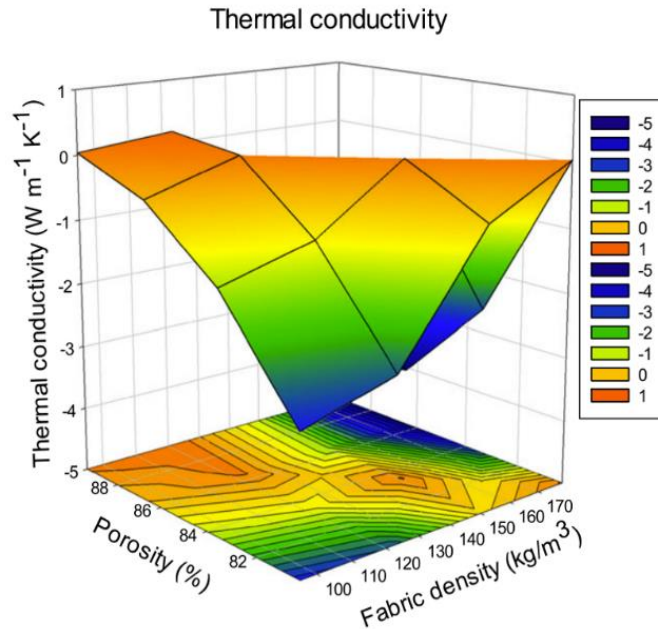
Silica aerogel has low-density and high-porous structures, very low thermal conductivity, low bulk density, and high specific surface area. It is prepared from different precursors containing silica. However, it has poor mechanical stability (low strength and high brittleness). The application of aerogel is limited to coating, padding, and impregnation due to its poor mechanical stability, brittleness, lack of compression, and cost. Using additional binders with aerogel reduces the pore size.

3.4 Nonwoven Structures with Enhanced Thermal Properties

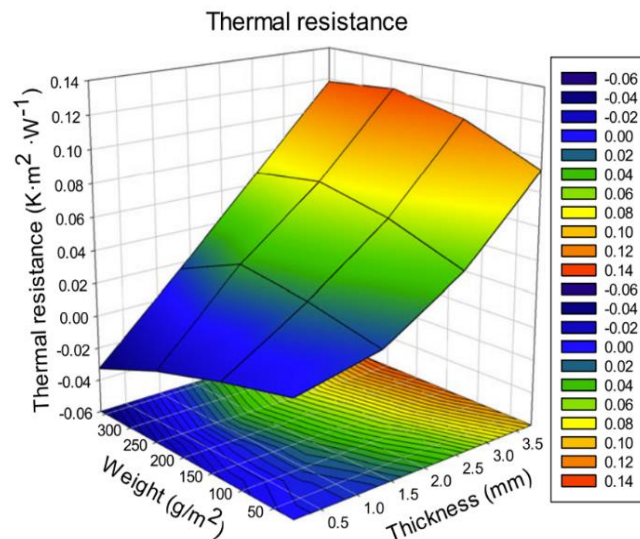
A nonwoven is a network of fibers joined together randomly or in a specific direction. Nonwoven fabrics are frequently utilized in several technical applications [40,41]. Many nonwoven manufacturing techniques and products have been developed [42–44]. In the creation of nonwoven fabrics, various fiber kinds are used. Polypropylene (PP) has played a significant role in the manufacture of melt-blown and spun-bonded nonwovens in recent years [45,46]. Textile applications like clothing, blankets, sleeping bags, interlinings, building insulation, cars, airplanes, and industrial process equipment depend on resistance, conductivity, and insulation. [47]. Ageing process may lead to irreversible shrinkage, which would affect thermal insulation. Hence, it is important to find alternative nonwoven, woven, and knitted materials [47,48] with the necessary physical and structural parameters for their thermal insulation performance [49][50]. The potential of aerogel-based Nonwoven structures required further exploration as current research is restricted to simulations of heat transfer coefficients.

Increased density of perpendicular-and cross-laid nonwoven fabrics has demonstrated increase thermal conductivity, which, however, decreases beyond a critical value[51] [42]. With the fabric thickness, thermal resistance was found to be inversely proportional to packing fraction [43]. In Polypropylene nonwoven fabrics, the calendaring process led to a decrease in thermal resistance and an increase in thermal conductivity [52]. In needle-punched nonwoven fabrics, increasing the needle barbs decreased thermal conductivity, which reversed when the barbs increased. [40]. A detailed study of heat and moisture transport through nonwoven fabrics confirmed the influence of thermal insulation by parameters like volume fraction, orientation against heat flow direction, and density significantly influence thermal insulation [53] The content of polyester hollow fibers and low-melting-temperature PET fibers (low-T_m fibers) decreases thermal conductivity [54]. Cellulosic-based nonwoven composites highlighted the

differences based on vegetable fibers used, the ratio of cellulose to the synthetic, binder, and bulk density[55]. In the case of PP melt blown and multi-layered nonwoven textiles, weight, thickness, porosity, and density impacted on thermal conductivity, thermal diffusivity, and thermal resistance, air permeability, water vapor permeability (WVP) of the fabrics were established. [50]



(a)



(b)

Figure 2 (a) Thermal conductivity (b) Thermal resistance [50].

3.5 Porous and Multi-layered Fibrous Materials

Porosity determines the thermal performance of fibrous materials [56–58] and is described as the fraction of void space in the total material volume, and its increase impacts thermal conductivity decreases at a near-linear rate [6,59,60]. Pore dimensions and proximity weaken heat convection, resulting in a decrease in thermal conductivity and thereby improving thermal insulation [6,60,61].

Considering the potential of aerogels, researchers have characterized the thermal performance of highly porous fibrous materials in combination with aerogel particles [62]. Aerogels are embedded into the thermal barrier layer of firefighters' protective clothing [62–64], coated on wool-Aramid blended fabrics [65], and incorporated with polyester/polyethylene nonwovens [29,39]. Multi-layer fibrous materials consisting of middle layers with high-loft nonwoven and alternates filled by aerogel particles were developed [66]. These multilayered fabrics may have applications in building and industrial facilities for energy efficiency. It could be used in building structures and hot water plumbing to reduce heat loss. [67]. Studies generally conclude that aerogels present in fibrous structures improve thermal insulation ability [68].

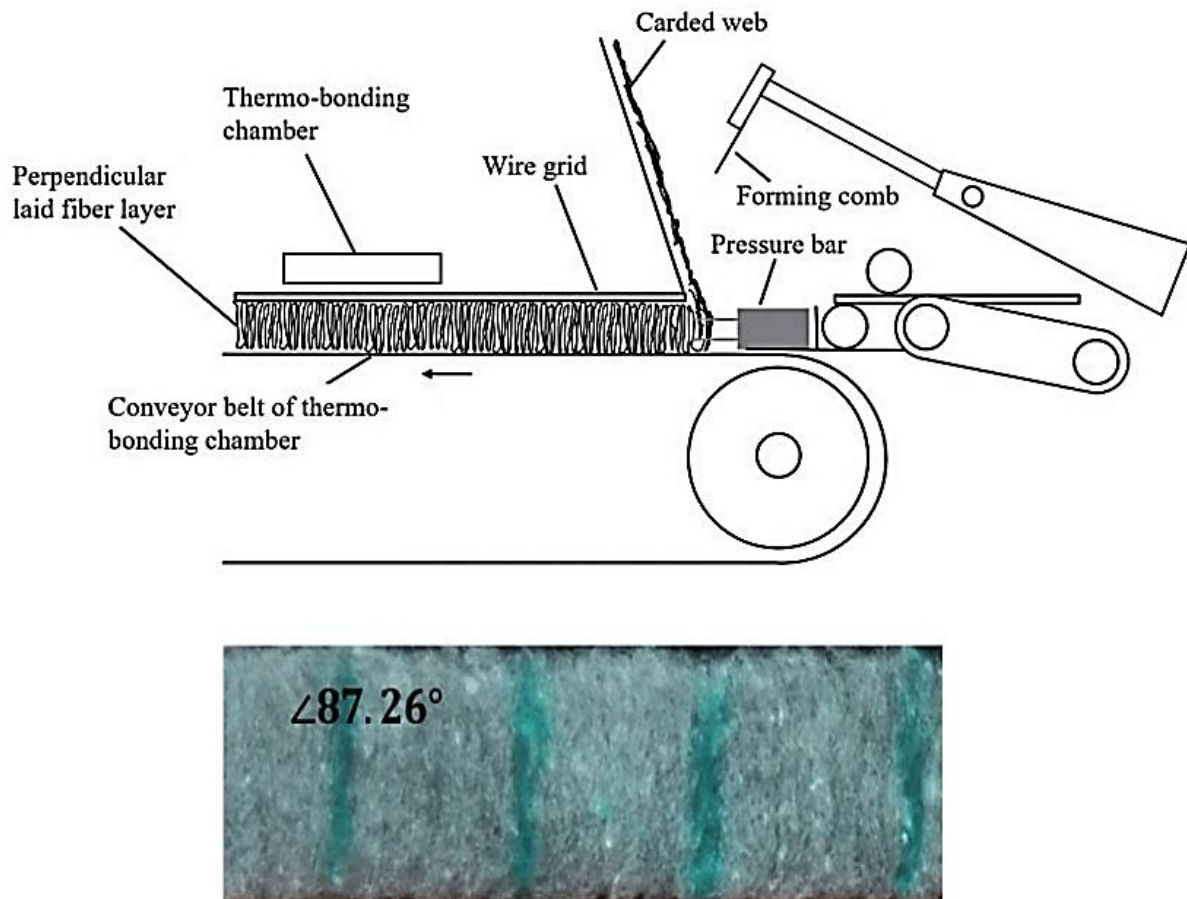


Figure 3 Vibrating perpendicular lapper fabricates Struto nonwoven and Fiber orientation in Struto nonwoven structure [69].

New developments in aerogel-based fibrous material by laser engraving technique and evaluation of convective thermal behavior using an unconventional methods [6,69]. The findings improve the understanding of influence of air pockets and aerogels on convective thermal behavior in cross-flow [11]. Analysis of the results from continuous heating showed that a remarkable increase in the heat transfer rate of the multi-layered fibrous material occurs at airflow velocity over 10 m/s [6].

Among the three structures, the materials with air pockets and encapsulated aerogels have higher heat transfer rates in cross-flow and less variations of this value at different airflow velocities. It was concluded that the different structures play an important role in determining the thermal behavior at airflow velocity less than 5 m/s but give less effect to thermal performance at higher airflow velocity.

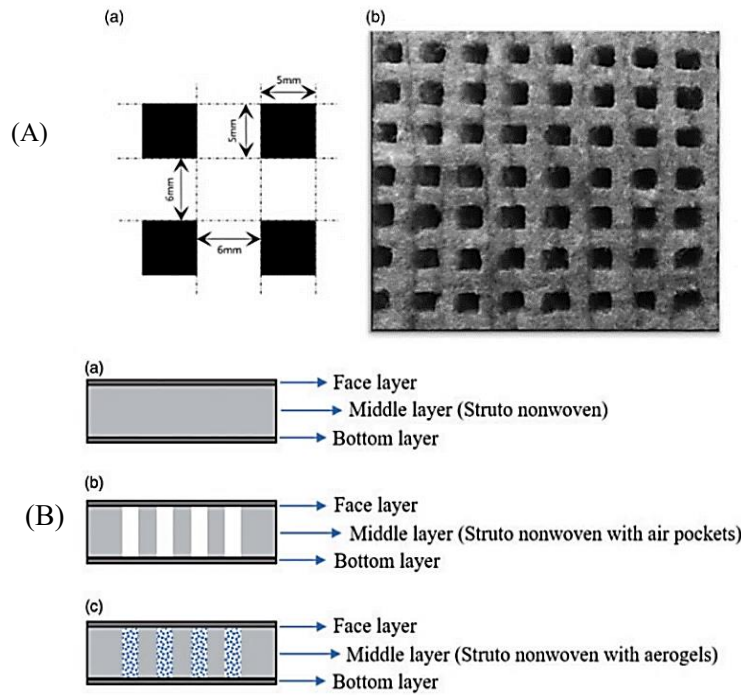


Figure 4 (A) Dot pattern for laser treatment: (a) Designed dot pattern and (b) Image of Struto nonwoven after laser treatment. (B) Cross-sectional structures of the three-layered fibrous materials: (a) regular structure, (b) air pockets structure, (c) aerogel encapsulated structure [69].

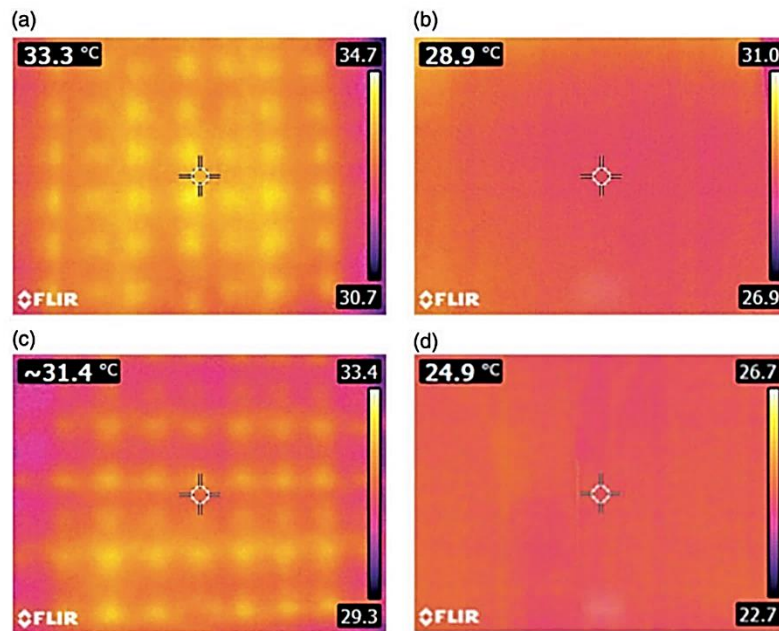


Figure 5 Infrared thermography images of the multilayered fabrics: (a) sample Q2 at wind speed 0 m/s; (b) sample Q2 at wind speed 1 m/s; (c) sample Q3 at wind speed 0 m/s; (d) sample Q3 at wind speed 1 m/s [69].

3.6 Embedding Polyethylene glycol in Silica Aerogel

Recently, incorporating PEG with porous materials [70] has attracted more attention and provided an alternative way to solve the aforementioned problems [71]. The encapsulation of the PEG by the porous materials was affected by internal and external factors. The internal factors were determined by the pores, including the pore topology (pore type and pore connection) and pore morphology (pore shape and pore size) [72]. The external factors were

the pH, temperature, and pressure during encapsulation [73]. By controlling the factors, various methods to incorporate the PEG into porous materials have been reported, including physical blending [74], sol-gel method [73], soaking [75], encapsulation [74], in-situ synthesis [76], and the necessity to avoid leakage.

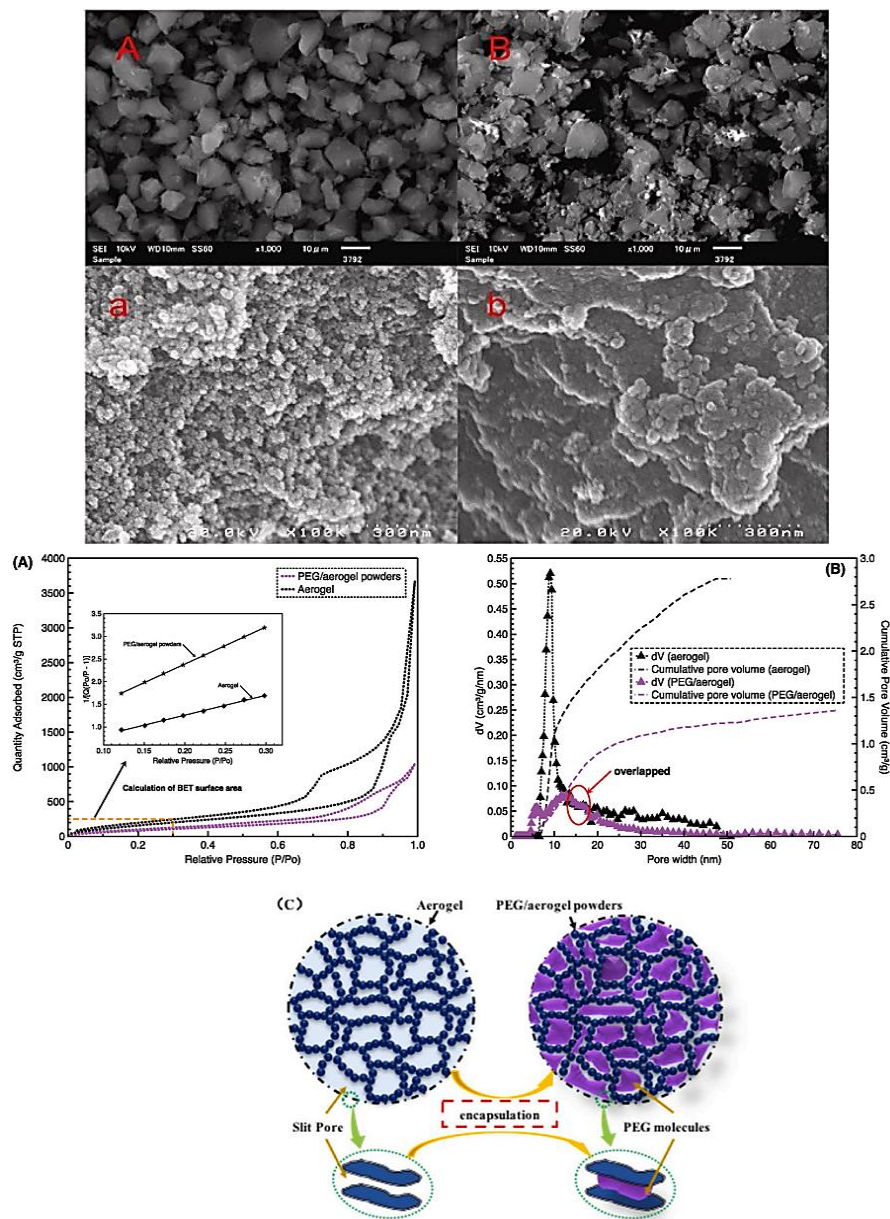


Figure 6 N_2 adsorption/desorption measurement of the aerogel powders and PEG/aerogel powders (A: Isothermal N_2 adsorption/desorption curves with a calculation of the BET surface area of the aerogel and the prepared PEG/aerogel powders, B: DFT curve of aerogel and the prepared PEG/aerogel powders, C: Scheme of encapsulation of PEG in aerogel) [85].

By comparing with the aforementioned various porous materials, the aerogel had different pores ranging from 2 to 200 nm [77]. The use of silica aerogel in conjunction with materials via the filtration method has been explored. Various organic PCMs, including eicosane [78], erythritol [79], and paraffin [80] have been embedded in silica aerogel powders. The encapsulation amount of the polymer in the aerogel (50%–90%) was considered large according to the high specific area and pore volume [81,82]. However, limited information is available for the structural analysis of the embedded PEG in the aerogel. It was noticeable that the longer PEG molecular chains and intrinsic entanglement were in the melting PEG [83]. The aerogel powder with micro- and mesopores affected the encapsulation of PEG on the surface

or trapped inside silica aerogel by using the filtration method [79]. By comparing with melted PEG, the PEG molecular chains in the solvent were extended and soft [84] which provided an alternative way to investigate the encapsulation of the PEG in the aerogel.

In special research [85], PEG/aerogel powders were successfully prepared via the physical blending and filtration method. However, the good compatibility between the water and PEG reduced the encapsulation efficiency. It was found that the different slit-shaped mesopores in the aerogel had further adsorption for the PEG molecules. A suitable pore size range for the adsorption of the PEG molecules was considered.

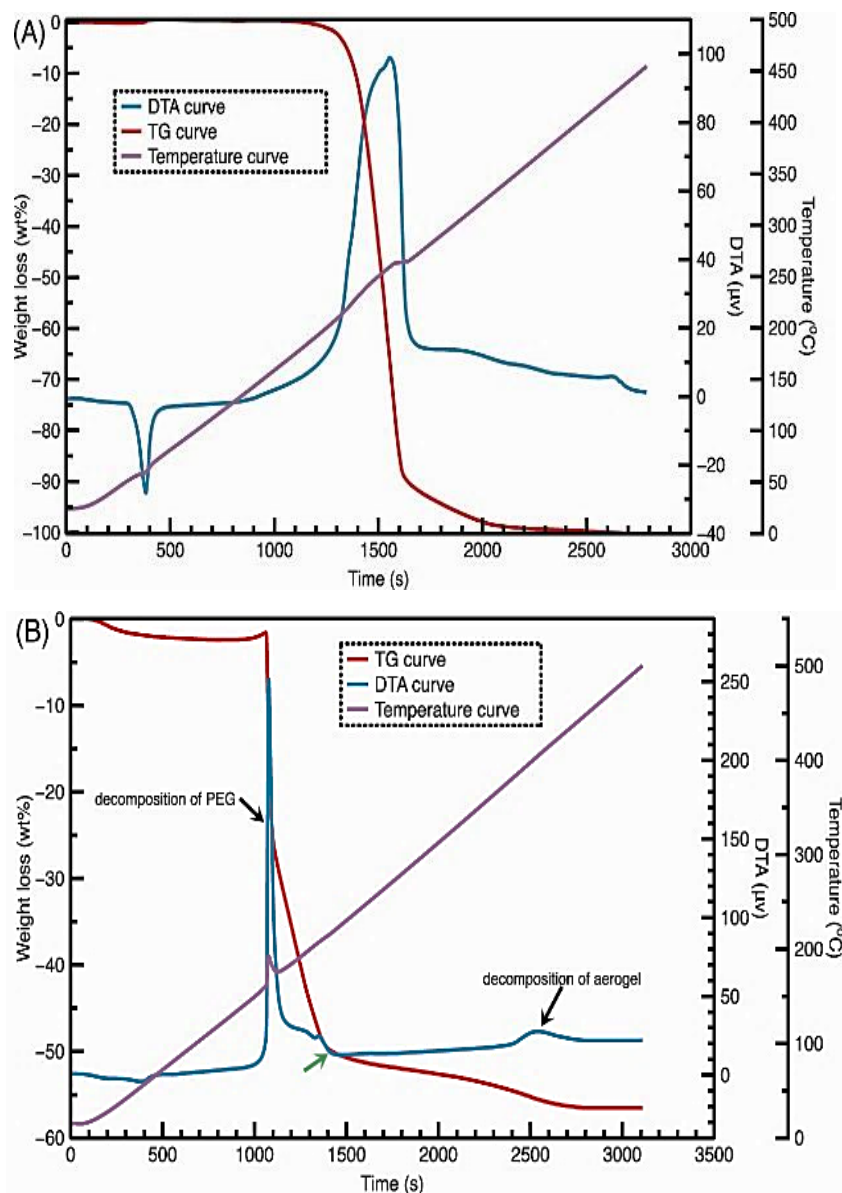


Figure 7 TG-DTA curves of the PEG (A) and the prepared PEG/aerogel (B) [85].

Both (120) and (112) crystal plane systems in the PEG were limited in the aerogel, accounting for decreasing crystallinity. The PEG crystals in the aerogel were limited as uncompleted compared to pure PEG and tended to be 2-D. No leakage and stable thermal capacity of the PEG/aerogel powders suggested the good encapsulation of the PEG molecules in the aerogel. The melted PEG molecules in the PEG/aerogel powders could be assumed as such a nanofluid to behold well in various mesopores of the aerogel powders due to the capillary force. The results of this work may initiate similar research relative to the reasonable choice for porous

materials with various pores to store the macromolecules [75] that are necessary to avoid leakage.

3.7 Electrospun Nanofibrous Membranes

Electrospinning is used to make polymer and ceramic nanofibers with superfine diameters [86–88]. The SiO₂ aerogel was strengthened using the electrospun polyurethane (PUR) and PVDF nanofibrous microstructures. It demonstrated improved mechanical strength and flexibility of the SiO₂ aerogels while maintaining a lower thermal conductivity [6,22,39,89,90]. Minute adjustments of fluid and spinning parameters were necessary to create flexible electrospun nanofibrous membranes embedded with silica aerogel [6,14,22,90,91]. The effects of the thermal and transport properties of the electrospun nanofibrous membranes embedded with SiO₂ aerogel have been investigated [38]. The methods of heat transfer through fibrous insulation with fiber diameters less than 1 μm were examined [6,14,22,38,90]. Further study is necessary on the usage of submicron fibers and their impact on thermal insulation [39].

3.8 Electrospayed Microporous Membranes with Aerogel

Many studies have been published that describe attempts to incorporate aerogels with PTFE materials. Mixing hydrophobic silica aerogel powders and PTFE powders in absolute alcohol, pressing the mixture to harden the composites, and sintering resulted in silica aerogel reinforced PTFE composites with 10-30 wt% silica aerogel [92]. The thermal conductivity of the composite decreases obviously with increasing aerogel content when the value is less than 18 wt%, but the decrease rate is relatively low above 18 wt%. The same approach was used in one study, where the starting materials were phenyltrimethoxy silane-coated SiO₂ powder and aqueous PTFE dispersion [93].

In a unique PTFE/silica nanoporous composite, the PTFE particles were fibrillated to create a PTFE matrix [94]. This composite, which has demonstrated chemical stability and strong electrochemical performance, was made by shear-blending aqueous PTFE dispersion with amorphous precipitated silica nanoparticles at high temperatures. The flexible and light material was created using a straightforward blade coating process, and it displayed good electrical insulation and dielectric properties [95]. Even though this research has successfully combined aerogels with PTFE, the involved fabrication techniques have high energy requirements and cause environmental contamination [96]. This is because casting PTFE materials is often done using a molding process. Furthermore, it is difficult to produce the desired continuous aerogel/PTFE layer for applications where minimalism and low weight are crucial.

Needleless electrospaying was used to combine PTFE and silica aerogels using an aqueous polytetrafluoroethylene dispersion as the primary spinning liquid [97]. From a colloidal suspension of solid nanoparticles or a solution of a substance, electrospay creates small monodisperse particles in the form of a thin film of fine particles. When a highly charged droplet is kept on a surface or a capillary tip in a strong electric field, surface tension causes the droplet to deform into a Taylor cone jet [98]. A continuous fluid will be released to produce a spray if the electric repulsive forces are potent enough to overcome the surface tension. The jet disintegrates downstream and then breaks into charged droplets because the spinning fluid has a sufficiently low viscosity [99]. Due to their huge surface-to-volume ratio and sub- or micrometer-sized size, these droplets quickly evaporate, resulting in electro-sprayed particles on the substrate material. The use of different fillers for performance modification or functionalization using electrospay increases the potential for the creation of porous materials or composites based on PTFE was optimized [97].

Embedding aerogel particles in PUR and PVDF nanofibrous layers has been achieved by electrospinning [38], thermal bonding in polyester nonwovens [69], and encapsulation in multilayered fibrous materials[100] to achieve lower thermal conductivity.

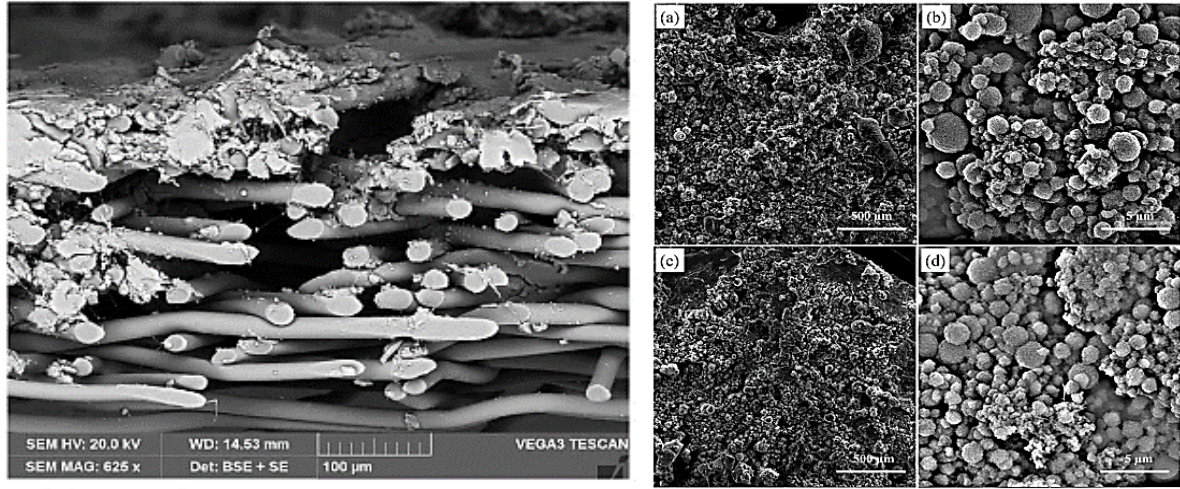


Figure 8 Cross-section image of the prepared mat and SEMs of the electrospayed materials (a)—sample S0 with low magnification; (b)—sample S0 with high magnification; (c)—sample S6 with low magnification; and (d)—sample S6 with high magnification nonwovens [101].

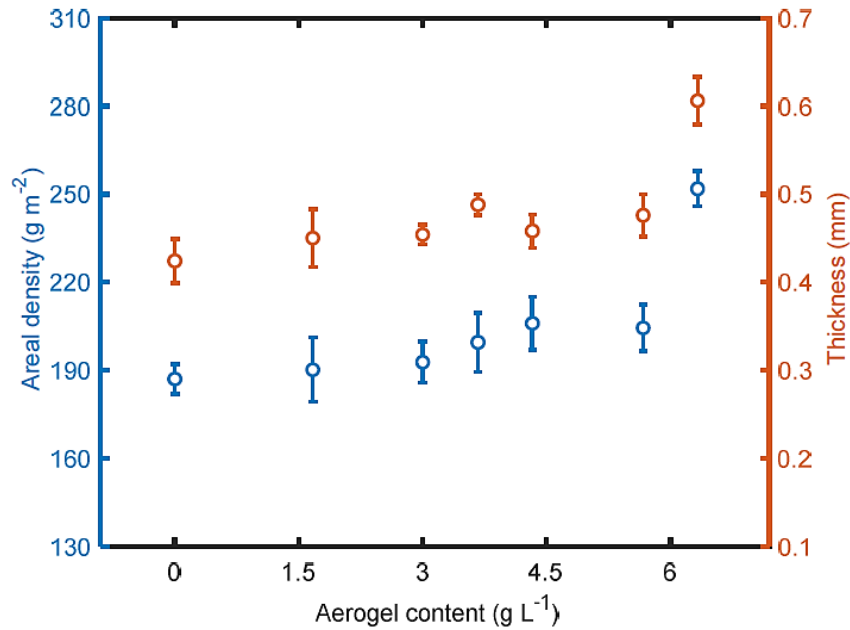


Figure 9 Areal density and thickness of the electrospayed materials nonwovens [101].

For the calculation of total volume porosity P [-] of arbitrary layers assembly based on aerogels, it is necessary to estimate its solid phase density ρ_f [kg m^{-3}]. This density for aerogel particles embedded in nanofibrous layers is calculated from the expression

$$\rho_f = \left(\frac{w_A}{\rho_A} + \frac{w_{PTFE}}{\rho_{PTFE}} + \frac{w_{PP}}{\rho_{PP}} \right)^{-1} \quad (14)$$

where w_A , w_{PTFE} , and w_{PP} are mass fractions of aerogel, PTFE, and PP, and $\rho_A = 120 \text{ kg m}^{-3}$, $\rho_{PTFE} = 2200 \text{ kg m}^{-3}$, and $\rho_{PP} = 920 \text{ kg m}^{-3}$ are the corresponding densities of components.

In Figure 9, the calculated values of P are displayed. The calculated overall porosity decreased as the aerogel content rose. Thus, the kinetics of particle arrival at the deposit dictate its morphology. A ballistic motion with a specific mean particle velocity v and a stochastic motion defined by a diffusion coefficient D_p combine to create the movement of particles as they approach the collector. The Péclet number, a dimensionless parameter, can be created by combining these two factors with the particle diameter D .

$$Pe = \frac{vD}{D_{p,diff}} \quad (15)$$

Common is $Pe = \frac{v D c_p \rho}{\lambda}$ where λ is the thermal conductivity, ρ the density, and c_p the specific heat capacity.

The porosity contributed by the agglomerates reaching the substrate diminishes because the Pe increases along with the increase in aerogel content since the mean particle size increases [102]. Consequently, by employing aerogel as filler and managing aerogel filler content, the porosity of the electrospayed PTFE materials could be adaptably modified, which may be useful in some situations when desired porosity is required for a particular application.

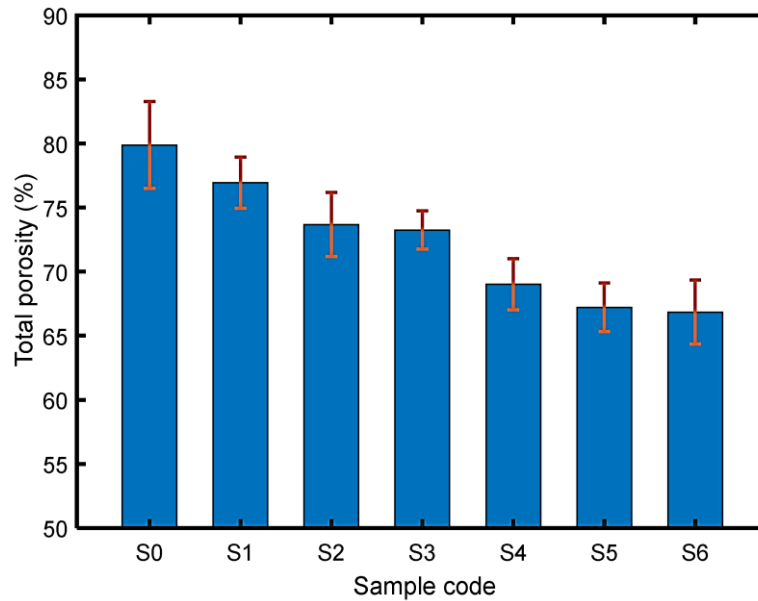


Figure 10 Calculated overall porosity of the nonwoven materials [101].

Using the needleless electrospay method, polytetrafluoroethylene microporous materials composited with aerogels were created [97,101]. The morphology of the surface, the distribution of particle sizes, the roughness of the surface, the hydrophobicity, and the thermal conductivity of the entire material were all determined for the developed materials. It was discovered that the electrospayed layers were composed of spherical particles with a rough surface and had a rather compact and chaotic stacking structure. The mean particle size of the electrospayed particles, areal density, and thickness of the multilayered materials increased along with the amount of aerogel added to the spinning liquid. Surface roughness tended to increase as aerogel content rose, and surface hydrophobicity was enhanced by the addition of aerogels with up to 147.88° of water contact angle.

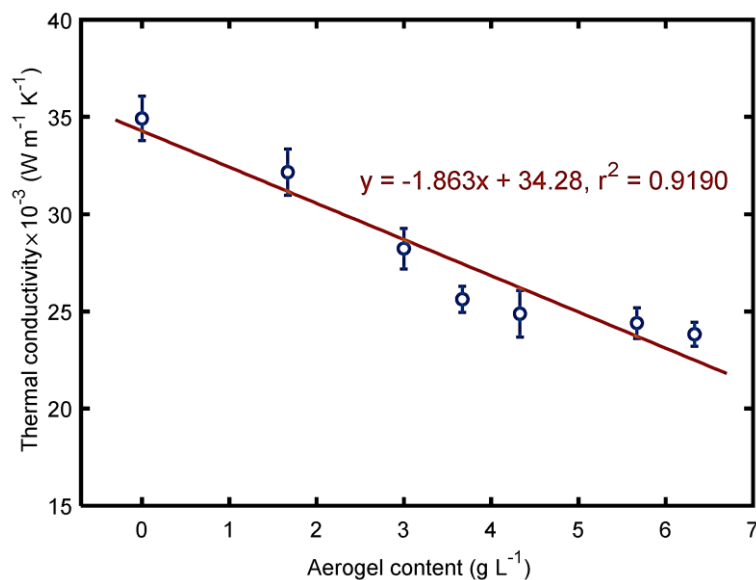


Figure 11 Thermal conductivity of electrospayed material nonwovens [101].

Furthermore, the PTFE/aerogel material that was electrospayed had a very low thermal conductivity (near $0.024 \text{ W m}^{-1} \text{ K}^{-1}$), suggesting a superior ability to block heat transmission. Materials with required qualities were flexibly generated by adjusting the spinning liquid and spinning conditions, offering a fairly increased variety of PTFE/aerogel materials for various purposes. It is important to note that the improved surface roughness opens the door for the application of additional useful nano- or microscale particles to increase a particular attribute, which may be relevant for further research in this field [97].

3.9 Electrospayed Microporous Membranes with Aerogels/Phase Change Materials

Phase change material (PCM) and silica aerogel are two particularly intriguing materials frequently employed as fillers in composites or fibrous materials to enhance their thermal properties. Because it has a lower thermal conductivity, silica aerogel has the potential to be used in low-weight composites with exceptional thermal and multifunctional properties [92]. This is because silica aerogel is a porous solid with air dispersed phase [103].

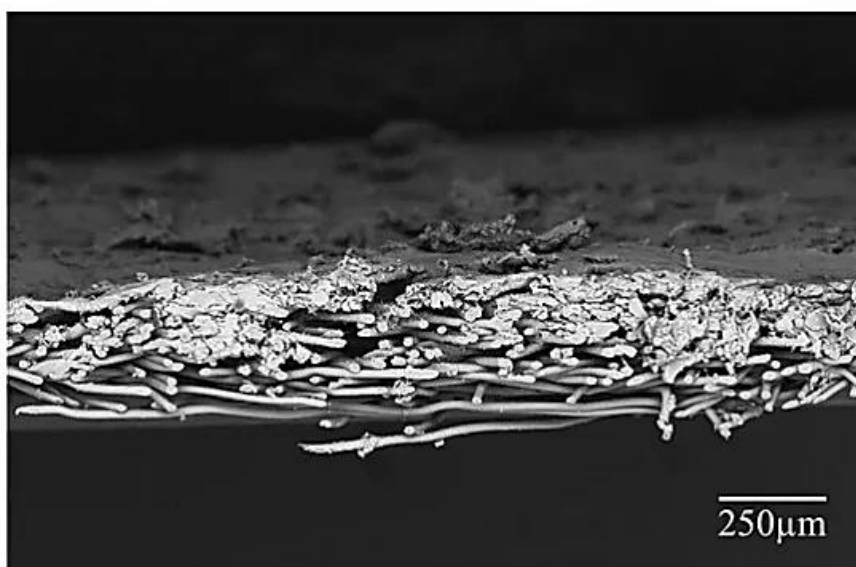


Figure 12 Typical cross-section image of the electro-sprayed material [105].

Thermal bonding has been used to combine the thin silica aerogel particles with polyester nonwovens on cotton woven fabric [104] and wool-Aramid blended fabric [65]. Encased in multi-layered composites [105], incorporated in a nanofibrous structure by electrospinning [38], and successfully lowered the overall structures' thermal conductivity. PCMs were employed for several years primarily for thermal regulation applications since they collect external incoming heat flux owing to phase change and act as thermal buffering of rapid heat changes. Several researchers have thoroughly demonstrated the temporary improvement in thermal protection provided by PCMs in firefighter clothing [63,106]. While the final performance of the proposed combination depends on the amount of PCM and its melting enthalpy, the simultaneous use of aerogels and PCMs coated on a multilayer fabric structure in a firefighter's protective garment provides superior thermal protection and comfort [78,107].

A significant amount of research has been done on PTFE porous materials, with a particular focus on the study of surface properties. Examples include the ultrafine fibrous PTFE porous material and the PTFE hollow fiber membrane [108,109]. Engineering publications that focus on PTFE/aerogel composites more typically use wet mixing utilizing aqueous PTFE dispersion or PTFE powder [92,110] or dry mixing of PTFE particles with aerogels [111]. The superhydrophobic behavior of the materials by fabricating PTFE porous materials using the electro-spray process was investigated [112,113]. The surface attributes, including roughness, electrical property, and hydrophobicity, were highlighted in prior research on electro-sprayed PTFE films loaded with carbon microparticles. However, the electro-spray process hasn't yet been used to create aerogel or PCM capsules embedded in PTFE microporous materials. It was unknown how well electro-sprayed PTFE porous materials transport various substances, including heat, air, and water vapor. In a detailed study, PTFE porous materials embedded with aerogels or PCMs were created using a needle-free electro-spray technique, and the microstructure characteristics and various transport parameters were examined. This research may significantly contribute to PTFE porous material development and performance modification. It might aid in better understanding the structural properties of electro-sprayed PTFE materials and the impact of PCMs, linked PCMs, and aerogels on the overall structure's transport properties. By optimizing the spinning liquid composition and the spinning parameters, the resulting materials may be employed for a variety of applications, such as barrier sheets and protective gear [105,114].

3.9.1 Effect of Aerogels and PCMs on Thermal Comfort Properties

Phase Change Materials capsules (PCM) present in the electro-sprayed PTFE materials have lower thermal conductivity, possibly due to the PCM shell's lower thermal conductivity ($0.19 \text{ W m}^{-1} \text{ K}^{-1}$ vs. $0.25 \text{ W m}^{-1} \text{ K}^{-1}$) than Teflon (Fig. 12). The results of samples T/AG and T/AP demonstrate this phenomenon. Particularly, sample T/AP performed better than the currently available porous insulation materials with a thermal conductivity as low as $0.029 \text{ W m}^{-1} \text{ K}^{-1}$. As stagnant air has a much lower thermal conductivity value ($0.024 \text{ W m}^{-1} \text{ K}^{-1}$) than most solid and liquid substances, traditional porous or fibrous insulation materials, such as polyurethane foam, fiber assemblies, or fabrics made from different natural or synthetic fibers, typically rely on this component to resist heat transfer through the structure [29,90,115]. Conventional porous materials could attain a thermal conductivity comparable to $0.030 \text{ W m}^{-1} \text{ K}^{-1}$ by modifying the structure features, especially total porosity. Since this value is below $0.033 \text{ W m}^{-1} \text{ K}^{-1}$, they might be categorized as good insulators.

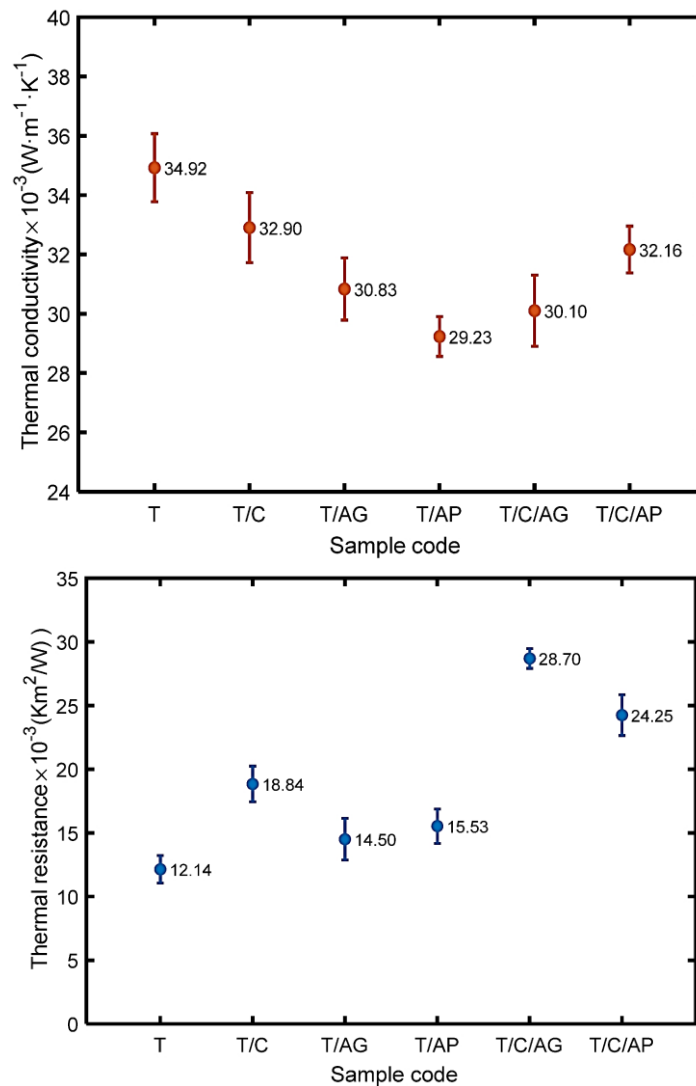


Figure 13 Thermal conductivity and resistance of the electro-sprayed materials [105].

These materials are suitable for technical usage since they are many millimeters or centimeters thick. Due to their low thermal conductivity and extremely small thickness, electro-sprayed materials have the potential to be used in barrier sheets and protective garments where there are severe limitations on material thickness. Also, it should be highlighted that in this work, aerogel powder outperforms aerogel granules in reducing the heat transfer rate. This is probably due to the smaller particle size, which allows for the development of a more uniform material with a higher aerogel content and a slower heat transfer rate. Aerogels and PCMs are used simultaneously, which results in somewhat lower thermal conductivity than sample T/C but no discernible advantage over samples T/AP and T/AG.

Thermal conductivity and material thickness determine thermal resistance, which expresses a material's capacity to stop heat flow through thickness over the unit surface area [105]. The samples' thermal resistance is shown in Fig. 12. When compared to sample T, aerogels in the forms of powder and granules were both able to produce significantly thicker materials with higher heat resistance. It is possible to produce much thicker materials with much improved thermal insulation properties by combining PTFE with PCMs and aerogels (powder or granules). Yet, due to the electro-sprayed materials' thinness, they might be employed as a liner in a garment or glove to improve insulating performance [105].

3.10 Thermal Performance of a Multi-layer Composite

A multi-layer structure with a PCM-loaded layer to make the PCM layer even, barrier nanolayers to prevent leakage, and protective layers from shielding the structure of the nanolayers were examined in the creation of a smart heat storage composite [33]. As the PCM loaded layer and proactive layers, Milife fabric, a non-woven polyester fabric with regulated density and thickness, was used. The nano barrier layer was made of PA 6 nanofibrous membranes.

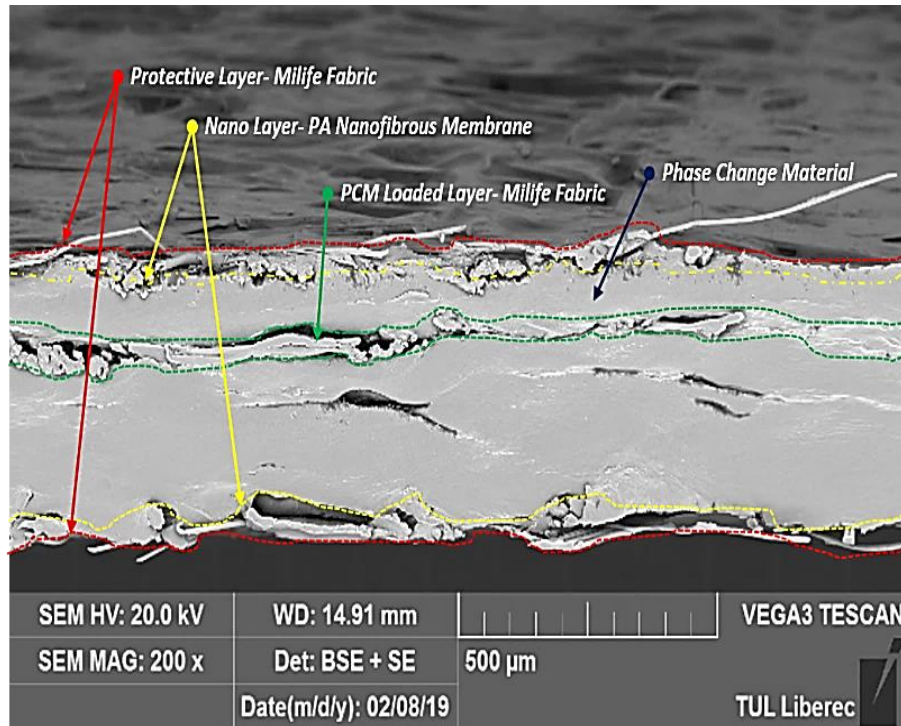


Figure 14 Cross-section Schematic of Multi-layer Composites Containing PCM composite [33].

From Table 1, it was obvious that the thermal insulation I value increased when PCM was deposited inside the multi-layer composites because C0 without any PCM had the lowest value, which revealed that the PCM supports better thermal insulation [33]. By comparing C1, C2, C3, C4, C5, and C6, the I increased, and C6 with L5 PCM obtained the highest I value. The upward trend may be caused by the decreased thermal conductivity of PEG/Laponite with more Laponite.

Table 1 Thermal insulation of multi-layer composite containing PCM composite [33].

Sample code	PCM content (wt%)	Laponite (wt%)	I_{value}
C0	0	0	0.130
C1	100	0	0.147
C2	97	3	0.147
C3	94	6	0.158
C4	91	9	0.196
C5	88	12	0.223
C6	85	15	0.253

3.11 Effect of Laser Irradiation on Kevlar Fabric Treated with Nanoporous Aerogel

In the composites of silica aerogel reinforced by aramid fibers, the aramid fibers serve as reinforcements. The composites were created by using ambient pressure drying and sol-gel technique [116,117]. The aramid fibers and the aerogel matrix contribute to the overall thermal conductivity, according to the heat transfer properties of the composites under a transient plane heat source and hot plate experiment [116–118]. Meanwhile, the composites' temperature differences grew with the amount of fiber present and showed some linearity. Via a rigorous procedure, silica aerogel's mesoporous structure has been successfully grafted onto aramid fibers to reduce the fiber heat conductivity [118]. The manufactured aramid fiber blanket's thermal conductivity is 25% less than the original ones, yet the thermal stability remains rather stable (fig. 14).

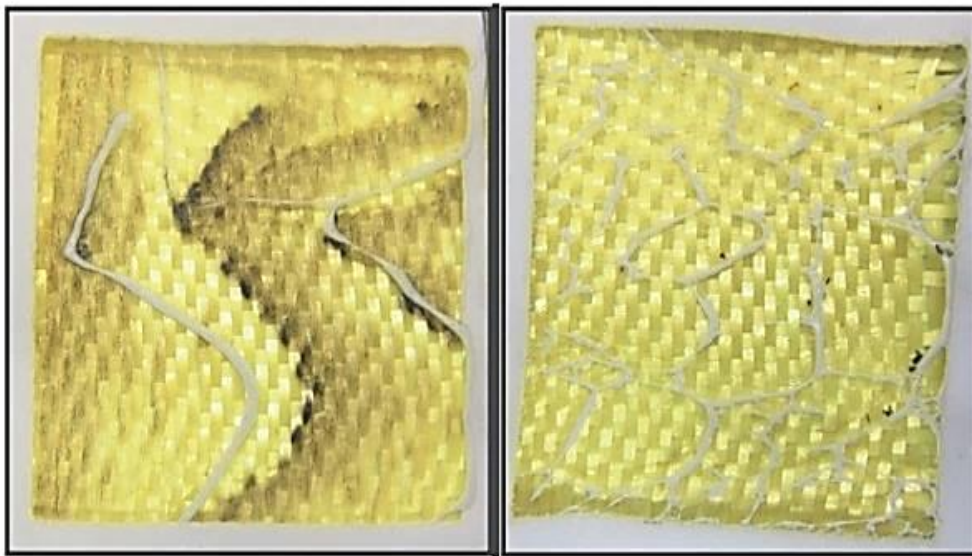


Figure 15 Images of laser experiment. [68,119].

According to a study on Kevlar fiber aerogel films made using spin-coating, sol-gel processing, and subsequent freeze-drying, the characteristic aerogel structure gave the films strong thermal insulation capabilities to minimize IR radiation and thwart effective heat transfer [120]. While the thermal comfort features of composites made of aramid fibers and aerogels were the focus of all these investigations, the thermal protection properties of Kevlar fabric made of aerogel were not sufficiently explored. The topic of the comprehensive study [119] was thermal protection using Kevlar fabrics covered with aerogel. RTV silicone was used as the binding substance to create a Kevlar woven fabric coated with aerogel particles. Investigations and discussions were conducted about the impact of aerogel and fly ash nanoparticles on thermal protection [68,119].

3.12 Performance improvement using PCM

The PEG was selected as PCM for the coating on the nonwoven viscose fabric. For enhancing the thermal conductivity of the system, the five micrometal particles (MP), including copper (Cu), aluminum (Al), silver (Ag), iron (Fe), and zinc (Zn) particles, were first blended with PEG, respectively. Then, the PEG/MP composites were coated on the viscose fabric, and the thermal behavior of the PEG/MP-coated viscose fabric was investigated. The melting and solidification process of the PEG/MP composites and the PEG/MP-coated viscose fabric was compared. Newton's cooling law was used for the characterization of the T-history of the PEG/MP-coated viscose fabric [34].

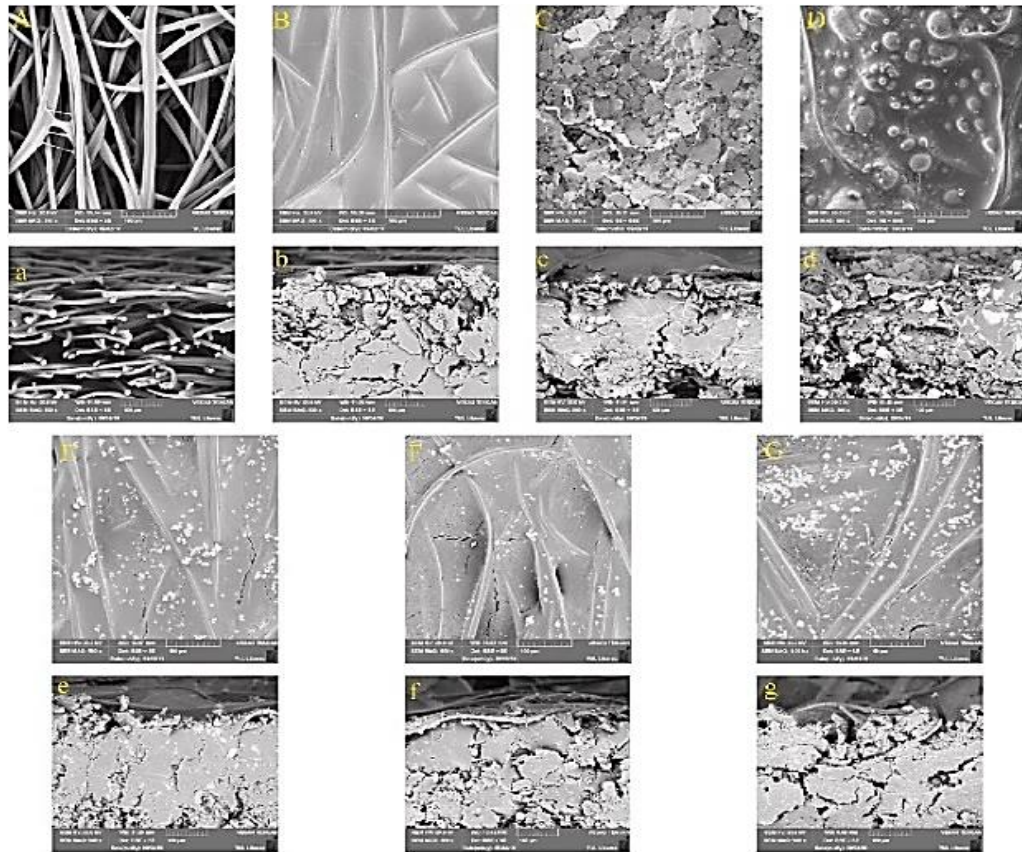


Figure 16 Morphology of PEG/MP-coated viscose fabrics [34].

Good adsorption of the molten PEG was assisted by the viscose fiber's capillary force and high porosity, as seen in Figure 15, where the PEG could cover the viscose fiber. The MPs were observed for the PEG/MP-coated viscose fabric, and most of them were filled in the PEG matrix by merging the morphology of MPs. The PEG/Cu composites, in contrast to other samples, completely coated the viscose fiber. The primary factor was the substantial alteration of the molten PEG/Cu composites' viscosity, distinct from other PEG/MP composites.

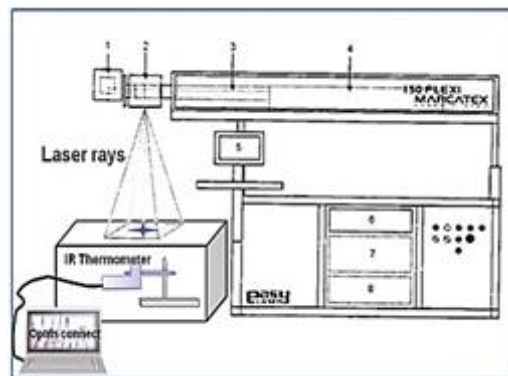
4 Measurement of Thermal Insulation

Different methodologies and procedures are used for the thermal characteristics of materials. Two such procedures are steady-state and transient-state [62]. In a steady state, the specimen is brought to a stable test temperature, while transient-state methods are used when an object is heating up or cooling down. More research has been done to comprehend textiles' transient features than their steady-state characteristics [22,62]. In place of a standard hot plate or cylindrical device, sweating plates and copper manikins are being used. Research is ongoing to better understand the principles of heat transmission through fabrics [121]. Numerous papers devoted to thermal insulation, the comfort properties of clothing, and the associated experimental techniques and measurement methods were reviewed [62,122–125]. The specification of fabric IR properties has also resulted in the development of numerous existing standard practices and testing methodologies [122,126]. Some ideas are based on creating a steady-state thermal conductivity regime when a sample is heated by an electric heater [123]. The "hot disk" [124] and the FRMT [125] are two experimental tools used to investigate the thermal comfort of fabrics, including finishing chemicals [127]. The Thermolabo KES-FB7

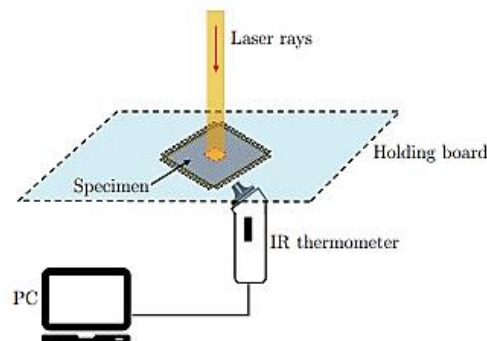
system [128] and Alambeta [129] are commercially available devices to assess the thermal contact characteristics considered when defining the so-called "warm/cool feeling [130]." The European Standard UNI EN 31092 [131] codes the measurement protocol of thermal and transpiration properties. This code is based on the application of a steady-state device, the so-called "Skin Model," simulating the quantities of heat and humidity transferred between the human body and the surrounding environment through clothing [130,132]. New instruments were found to correlate with the results from other standard equipment was described. Fresh insights into using unconventional techniques like PIV were gained [133]. A detailed exercise to correlate results from conventional and unconventional methods has generated a large amount of baseline data that could be useful for future research [29,68,119,133–135]. The standard measuring procedures should be carefully examined to determine their advantages and disadvantages. New equipment should also supplement or replace the existing measurement techniques and apparatus.

4.1 Effect of Laser Irradiation

A laser system and thermometer were used to assess the manufactured materials' thermal protection under high temperatures of up to several hundred degrees. A thermal camera tested the produced fabrics' thermal characteristics at room temperature (see fig. 19) [68,119]. The thermal barrier layer of kevlar and glass fabric was embedded with the aerogel to assess its thermal performance [68,119,136]. Several masses of aerogel implanted between kevlar and glass fabrics have been studied to give protection from laser devices to avoid unintentional laser irradiation of the skin. Several experimental setups were used for CO₂ laser treatment [68].

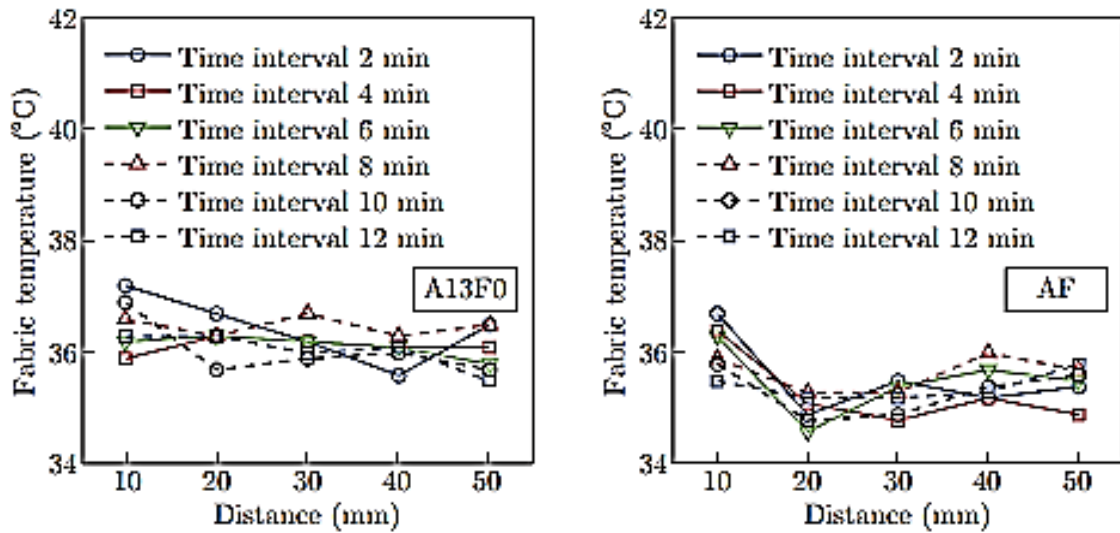


(a)

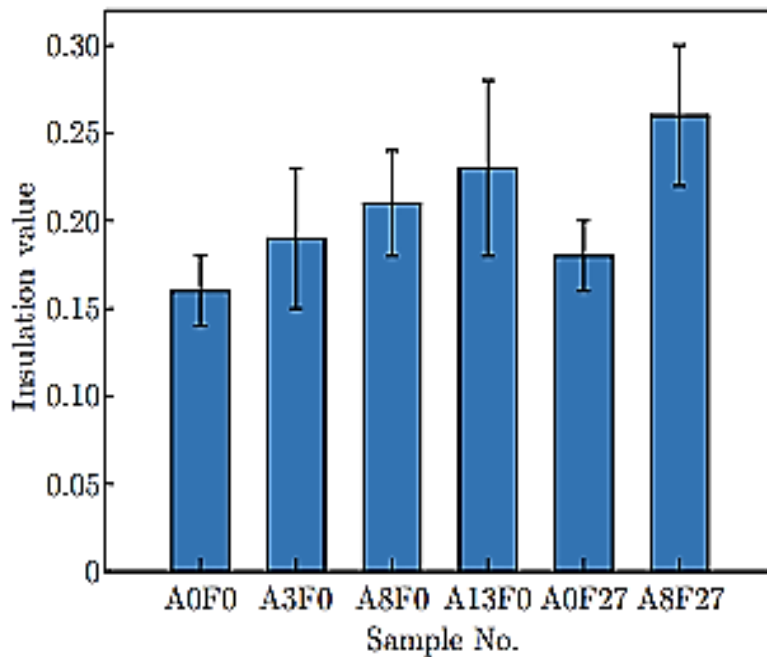


(b)

Figure 17 (a) Schematic diagram of Laser system (b) Set-up of the measurement of thermal protection properties [68,119].



(a)



(b)

Figure 18 (a) Effect of fabric to thermal camera distance on the measured fabric temperature. (b) Comparison of thermal insulation value for different materials [68,119].

The multilayer systems used in the construction of passive solution (Kevlar-aerogel-glass) have high passive protection levels for laser radiation. The capacity to deactivate the laser source upon irradiation above the threshold is provided by the insertion of silica aerogel into the multilayer structure, which can increase the protection level in personal protection equipments (PPE) [68,97].

5 Simple Determination of Key Structural Parameters for Fibrous Materials

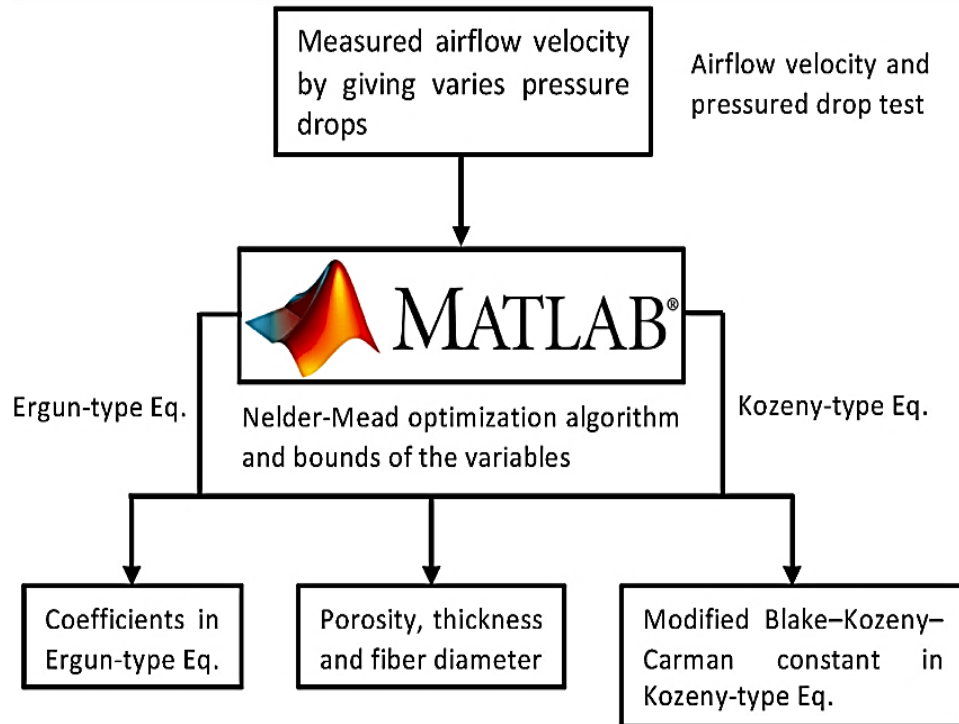


Figure 19 Inverse characterization procedure for structural parameters of fibrous materials [137].

In new research, an airflow-based method to determine fibrous materials' structural parameters (i.e., porosity, thickness, and average fiber diameter) was presented [36]. The FX 3300 Air Permeability Tester III was used to measure the velocity of airflow penetrating the fibrous samples under the pressured drop in a certain range (i.e., 20–120 Pa for regular nonwovens and 100–500 Pa for nanofibers membranes). The Ergun-type and the Kozeny-type equations were applied to compare the experimental airflow velocity-pressure drop relationship. The optimization method was conducted in the Matlab software to inversely determine the structural parameters, the coefficients of the Ergun-type equation, and the modified Blake–Kozeny–Carman constant of the Kozeny-type equation. The fiber diameter and its distribution were obtained by a semi-automatic Matlab-based tool (called SIMPoly) and ImageJ software. The inversely determined structural parameters were compared with the measured values[137].

It was found that the airflow velocity-pressure drop relationship from the Ergun-type equation has a good agreement with the results based on the directly measured values. The Kozeny-type equation is accurate for pressure drop prediction of the samples with less permeability, such as nanomembranes. It indicated that the Ergun-type equation is more suitable for normal nonwoven materials. Moreover, it was concluded that the coefficients of the Ergun-type equation are different for the samples made with the same material and technology but having different porosity. For the Kozeny-type equation, the modified Blake–Kozeny–Carman constant differed from the original value. Thus, it was recommended to determine the Ergun-type equation's coefficients and constant in the Kozeny-type equation for each fibrous material. By comparing and analyzing the results from SIMPoly and ImageJ, it was recommended that the average fiber diameter and diameter distribution obtained from SIMPoly be more representative of the fiber diameter in a geometrical sense. The Ergun-type equation showed good results for the samples with good permeability.

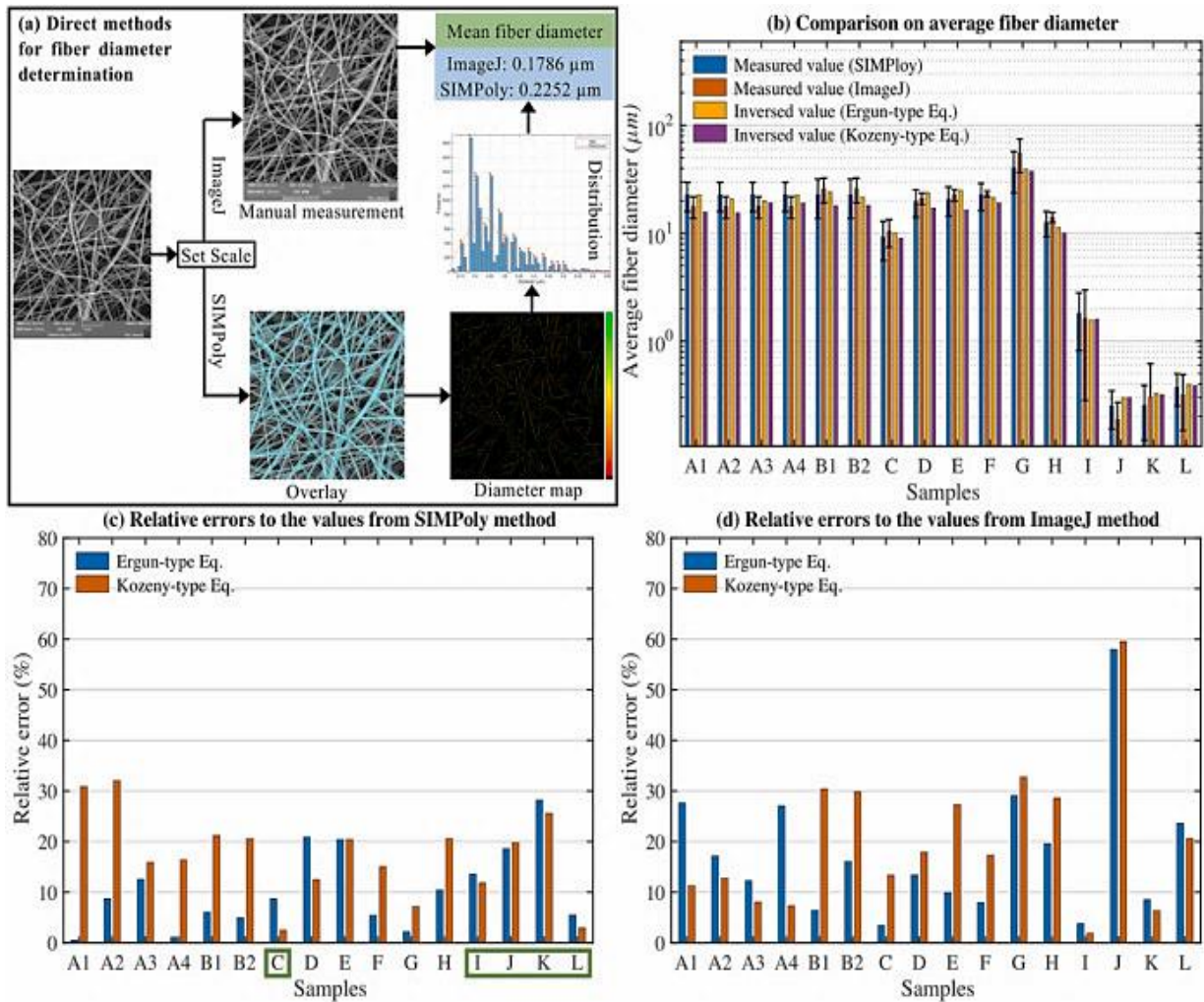


Figure 20 Direct methods used to determine the fiber diameter, comparison between measured and inversely determined average fiber diameter, and their relative error [137].

Considering the uncertainties during the direct measurements, it can be stated that the inverse characterization method on fibrous materials based on their air penetration behavior is applicable. This work may assist the characterizations of fibrous materials, especially for the complicated-determination parameters of nanomaterials, such as porosity and thickness. However, this work was limited by the material's homogeneity. Due to the inhomogeneity, the airflow-based characterization method may not be appropriate for the woven and knitted fibrous materials. A further study could build more accurate models for those inhomogeneous materials and assess the accuracy of the airflow-based characterization method. Last, the application of Ergun-type and Kozeny-type equations by means of the inverse characterization to derive the airflow-related properties can be further investigated [137].

6 Applications

A thorough investigation of the potential for nanofibrous membranes to serve as barrier layers in multi-layer PCM fabrics was conducted [36,138]. The interfacial adhesion between melting PCMs and nanofibrous membranes, which was controlled, had a substantial impact on the findings of leakage. Figure 21 shows the thermal buffering effect of nanofibrous membrane incorporated multi-layer fabric with or without PW (A: T-history curve, B: Characterization of heating process according to Newton's cooling law and C: incorporation of UPWV into

commercial fabrics)(Error bars in 'A': standard errors, red line and blue line in 'B': the fitting model corresponded to the solid phase and SL phase transition, respectively) [36].

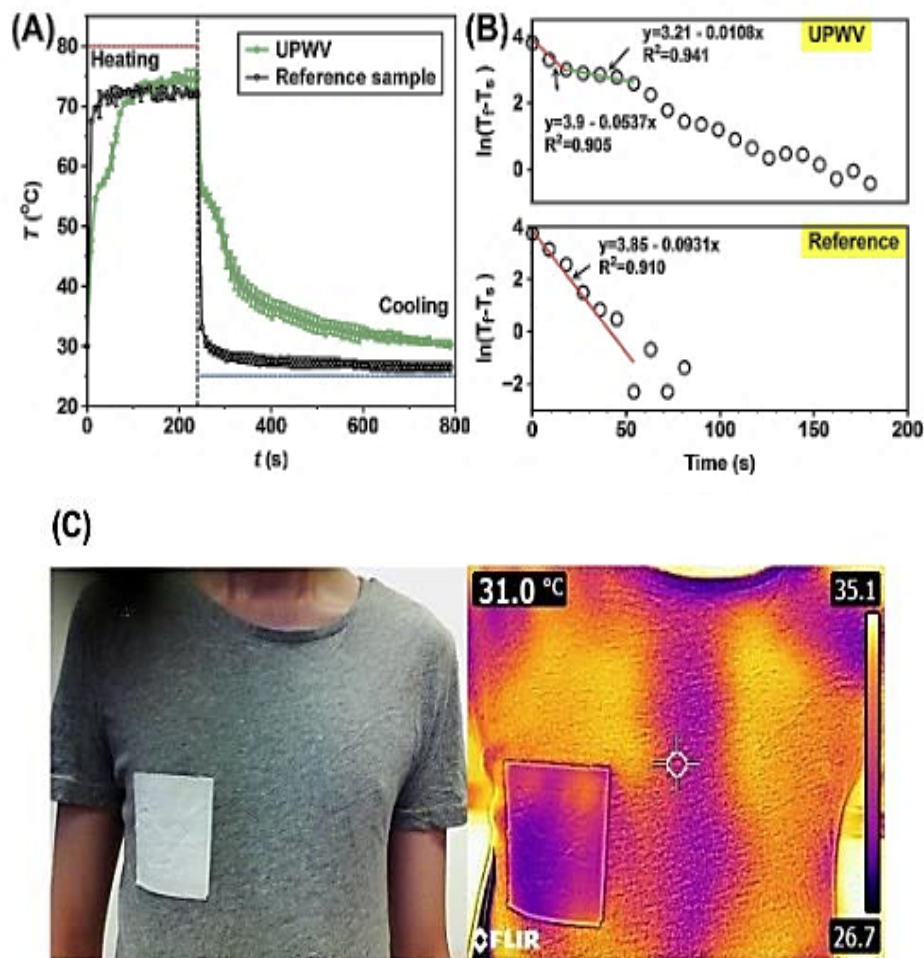


Figure 21 Thermal buffering effect with or without PW [36].

The PU nanofibrous membranes resisted melting PW and the associated multi-layer PCM fabric without leaking. Also, the multi-layer PCM fabric's ultimate features included a stable phase transition, high thermal energy storage, and thermal buffering. The work supports not just the textile industry but also other areas that need PCMs [36].

7 Conclusion

This thesis is conceived as a summary of published scientific and professional works authored by the writer of this thesis. The body of work represents and demonstrates the author's contribution to the field of textile technology and materials science and the novelty and motivation of the author's research activities. The original work of the author has been supplemented with citations from other research work to provide context and present the totality of the work performed.

The bulk of this thesis is based on the research published in journals with impact factors indexed in SCOPUS, books, and international conferences. The complete list has been provided as a chapter, and selected works have been provided as an appendix. The content of the thesis includes a summary of different methods for the development of fibrous structures for thermal insulation with enhanced thermal properties, stability, and comfort.

The selected areas of focus are the characterization of materials to enhance thermal insulation, development of custom instruments for thermal measurements for effective comparison with traditional techniques, evaluation of unconventional methods like Particle Image Velocimetry (PIV), usage of electrospinning technique to manufacture innovative nanofibrous layers embedded with silica aerogel (PUR and PVDF), heat transfer through convection and radiation, synthesis of aerogel and PCM for textiles and modeling of convective heat transfer phenomena in fabrics treated with different materials.

The future direction of this research would be synthesis of cellulose-based aerogels, novel techniques for production and incorporation of aerogels and aerogel-PCM in fibrous structures, evaluation of sustainable bio-based materials, and development of advanced multi-layered structures for enhanced thermal performance of textiles. There is immense potential to use the knowledge derived from this research in multiple application areas.

8 Published Outputs

The table summarizes the author's publications (24 journal papers and 2 books) related to the specific research. The impact factor of the journal, the JIF quartile category, and the number of citations of the papers are displayed. This research has been presented at various international conferences. The supplementary documentation of this habilitation provides a comprehensive list of all the research.

Table 2 Detailed information related to the chapters about the author's publication outputs (journal IF, JIF category quartile, and citations given as of 13/4/23).

S. No.	Journal paper	Journal IF	Quartile	Times Cited
1.	Venkataraman, M. , Mishra, R., Militky, J, et al. Electrospun nanofibrous membranes embedded with aerogel for advanced thermal and transport properties. <i>Polymer Advance Technologies</i> . 29, (2018). 2583– 2592. DOI:10.1002/pat.4369	3.665	Q1	30
2.	Venkataraman, M. , Yang, K., Xiong, X., Militky, J., Kremenakova, D., Zhu, G., Yao, J., Wang, Y., Zhang, G. Preparation of Electrospayed, Microporous Particle Filled Layers. <i>Polymers</i> . 12, (2020). 1352. DOI:10.3390/polym12061352	5.063	Q1	6
3.	Venkataraman, M. , Xiong, X., Novotná, J., Kašparová, M., Mishra, R., Militký, J. Thermal Protective Properties of Aerogel-coated Kevlar Woven Fabrics. <i>Journal of Fiber Bioengineering and Informatic</i> . 12, (2019). 93-101. DOI:10.3993/jfbim0032	0.743	Q4	6
4.	Venkataraman, M. , et al. Aerogel-Based High-Performance Thermal Insulation Materials. <i>IOP Conference Series: Material Science Engineering</i> . 553, (2019). DOI: 10.1088/1757-899X/553/1/012043	0.48	Q4	1
5.	Zhang, G., Cai, C., Wang, Y., Guojin, L., Zhou, L., Yao, J., Militky, J., Marek, J., Venkataraman, M. , Zhu, G. Preparation and evaluation of thermo-regulating bamboo fabric treated by microencapsulated phase change materials. <i>Textile Research Journal</i> . 89(16), (2019). 3387-3393. DOI:10.1177/0040517518813681	2.455	Q2	5
6.	Coetzee, D., Venkataraman, M. , Militky, J., Petru, M. Influence of Nanoparticles on Thermal and Electrical Conductivity of Composites. <i>Polymers (Basel)</i> . 12, (2020).742. DOI: 10.3390/polym12040742.	5.063	Q1	65
7.	Yang, K., Venkataraman, M. , Wang, Y.F., Xiong, X., Yang, T., Wiener, J., Militky, J., Mishra, R., Marek, J., Zhu, G., Yao, J. Thermal Performance of A Multi-layer Composite Containing PEG/Iaponite as PCMs. <i>Journal of Fiber Bioengineering and Informatics</i> . (2020) 61-68. DOI:10.3993/jfbim00330	0.743	Q4	3

S. No.	Journal paper	Journal IF	Quartile	Times Cited
8.	Wiener, J., Militký, J., Marek, J., Venkataraman, M. , Zhu, G., Yao, J. Nanocomposite Sandwiches Containing Phase Change Materials. <i>Vlakna a Textil.</i> 27(5), (2020). 37 – 40.	-	Q4	0
9.	Xiong, X., Venkataraman, M. , Yang, T., Kucerova, K., Militký, J., Yang, K., Zhu, G., Yao, J. Transport Properties of Electro-Sprayed Polytetrafluoroethylene Fibrous Layer Filled with Aerogels/Phase Change materials. <i>Nanomaterials.</i> 10, (2020). DOI: 10.3390/nano10102042	5.719	Q1	7
10.	Wang, Y., Yao, J., Zhu, G., et al. A novel method for producing bi-component thermo-regulating alginate fiber from phase change material microemulsion. <i>Textile Research Journal.</i> 90(9-10), (2020). 1038-1044. DOI:10.1177/0040517519886075	2.455	Q2	4
11.	Yang, K., Venkataraman, M. , Karpiskova, J., Suzuki, Y., Ullah, S., Kim, I., Militky, J., Wang, Y.F., Yang, T., Wiener, J., Zhu, G., Yao, J. Structural analysis of embedding polyethylene glycol in silica aerogel, Microporous, and Mesoporous Materials. 310, (2021). DOI: 10.1016/j.micromeso.2020.110636.	5.876	Q1	18
12.	Xiong, X., Venkataraman, M. , Jašíková, D., et al. An experimental evaluation of convective heat transfer in multi-layered fibrous materials composed of different middle layer structures. <i>Journal of Industrial Textiles.</i> 51, (2021). DOI:10.1177/1528083719878845	3.050	Q1	9
13.	Xiong, X., Venkataraman, M. , Jašíková, D., Yang, T., Mishra, R., Militký, J., Petrů, M. Thermal Behavior of Aerogel-Embedded Nonwovens in Cross Airflow. <i>Autex Research Journal.</i> 21(1), (2021). 115-124. DOI:10.2478/aut-2019-0082	1.944	Q2	3
14.	Gericke, A., Militky, J., Venkataraman, M. , Steyn J.H., Vermaas, J. Investigation of thermal comfort properties of fabrics containing mohair, <i>The Journal of The Textile Institute.</i> 113:4, (2021) 616-627, DOI: 10.1080/00405000.2021.1896158	1.77	Q1	2
15.	Qin, Z., Yi, L., Wang, S., Wang, L., Yao, J., Zhu, G., Militky, J., Venkataraman, M. , Zhang, M. Supercooling suppression and mechanical property improvement of phase change nanofibers by optimizing core distribution, <i>Polymer.</i> 233, (2021). DOI: 10.1016/j.polymer.2021.124176.	3.08	Q1	3
16.	Militký, J.; Křemenáková, D.; Venkataraman, M. ; Večerník, J.; Martínková, L.; Marek, J. Sandwich Structures Reflecting Thermal Radiation Produced by the Human Body. <i>Polymers.</i> 13, (2021). 3309. https://doi.org/10.3390/polym13193309	4.39	Q1	5
17.	Yang, K., Wiener, J., Venkataraman, M. , Wang, Y.F., Yang, T., Zhang, G., Zhu, G., Yao, J., Militky, J., Thermal analysis of PEG/Metal particle-coated viscose fabric, <i>Polymer Testing.</i> 100, (2021). DOI: 10.1016/j.polymertesting.2021.107231.	4.931	Q1	16
18.	Yang, K., Venkataraman, M. , Zhang, X. <i>et al.</i> Review: incorporation of organic PCMs into textiles. <i>Journal of Material Science.</i> 57, 798–847 (2022). DOI:10.1007/s10853-021-06641-3	4.682	Q1	9
19.	Yang, K., Zhang, X., Wiener, J., Venkataraman, M. , Wang, Y.F., Zhu, G., Yao, J., Militky, J. Nanofibrous Membranes in Multilayer Fabrics to Avoid PCM Leakages. <i>ChemNanoMat.</i> 8, (2022). DOI: 10.1002/cnma.202200352	3.82	Q1	-
20.	Yang, K., Martinkova, L., Ctibor, O., Zhang, X., Venkataraman, M. , Wiener, J., Zhu, G., Zhang, G., Yao, J., Militky, J., Mass transfer and the thermal buffering effect of hydrophobic fabrics with a single-side coating of MPCMs, <i>Progress in Organic Coatings.</i> 172, (2022). DOI: 10.1016/j.porgcoat.2022.107151.	6.206	Q1	2
21.	Yang, T., Hu, L., Yu, D., Xiong, X., Chvojka, J., Venkataraman, M. , Petrů, M., Tomková, B., Morikawa, H., Militký, J. Simple determination of key structural parameters for fibrous materials enabled by Ergun-Type and Kozeny-type equations, <i>Polymer Testing.</i> 108, (2022). DOI: 0.1016/j.polymertesting.2022.107514.	4.931	Q1	3

S. No.	Journal paper	Journal IF	Quartile	Times Cited
22.	Yang, K., Peng, Q., Venkataraman, M. , Novotna, Karpiskova, J., Mullerova, J., Wiener, J., Vikova, M., Zhu, G., Yao, J., Militky, J. Hydrophobicity, water moisture transfer and breathability of PTFE-coated viscose fabrics prepared by electrospraying technology and sintering process, <i>Progress in Organic Coatings</i> . 165, (2022). DOI: 10.1016/j.porgcoat.2022.106775.	6.206	Q1	5
23.	Yang, K., Venkataraman, M. , Wiener, J., Zhang, X., Stuchlik, M., Zhu, G., Yao, J., Militky, J. Crystallization mechanism of micro flake Cu particle-filled poly(ethylene glycol) composites. <i>Thermochimica Acta</i> . 710, (2022). DOI:10.1016/j.tca.2022.179172.	3.378	Q1	5
24.	Militký, J., Křemenáková, Dana., Venkataraman, M. , Večerník, J., Martínková, L., Marek, J., Procházka, J. A review of textiles reflecting FIR produced by the human body. <i>Autex Research Journal</i> , (2022). DOI: 10.2478/aut-2022-0035	1.944	Q3	1

S. No.	Books	Publisher	Month	Times Cited
25.	Militky, J., Venkataraman, M. , Periyasamy, A.P. (2022). <i>Fibrous Structures and Their Impact on Textile Design</i> . DOI: 10.1007/978-981-19-4827-5.	Springer Nature	September, 2022	4
26.	Militky, J., Venkataraman, M. (2023). <i>Advanced Multifunctional Materials from Fibrous Structures</i> . DOI: 10.1007/978-981-99-6002-6	Springer Nature	October, 2023	-

9 Declaration

I would like to express my gratitude to all the co-authors of the papers I submitted as a part of the habilitation thesis. I express gratitude to my mentors, research scholars, and subject matter experts who have provided invaluable inputs to this research. I sincerely affirm that I contributed more or equal to the planning, carrying out, and interpreting of the results in every instance than any other co-author.

10 References

- [1] Militký J, Venkataraman M, Periyasamy AP, editors. *Fibrous Structures and Their Impact on Textile Design*. vol. 1. 1st ed. Singapore: Springer Nature Singapore; 2022. <https://doi.org/10.1007/978-981-19-4827-5>.
- [2] Varkiyani S, Rahimzadeh H, Bafekrpoor H. Influence of punch density and fibre blends on thermal conductivity on nonwoven. *Open Textile Journal* 2011;4:1–6.
- [3] Xie T, He YL, Hu ZJ. Theoretical study on thermal conductivities of silica aerogel composite insulating material. *Int J Heat Mass Transf* 2013;58:540–52.
- [4] Cohen E. *Thermal properties of advanced aerogel insulation*. Massachusetts: 2011.
- [5] Gun AD. Dimensional, physical and thermal comfort properties of plain knitted fabrics made from modal viscose yarns having microfibers and conventional fibers. *Fibers and Polymers* 2011;12:258–67. <https://doi.org/10.1007/s12221-011-0258-2>.
- [6] Xiong X. *Vysoce funkční materiály s obsahem aerogelu*. Disertační práce. Technical University of Liberec, 2018.

- [7] Frydrych I, Dziworska G, Biliska J. Comparative analysis of the thermal insulation properties of fabrics made of natural and man-made cellulose fibres. *Fibres Text East Eur* 2002;39:40–4.
- [8] D.W. VAN KREVELEN. *Properties of Polymers*. 3rd ed. Elsevier; 1997. <https://doi.org/10.1016/C2009-0-05459-2>.
- [9] Sestak J. *Science of Heat and Thermophysical Studies*. Elsevier; 2005. <https://doi.org/10.1016/B978-0-444-51954-2.X5000-0>.
- [10] Jamshaid H. *Hybridní tkané struktury*. Doctoral theses. Technical University of Liberec, 2016.
- [11] Venkataraman M, Mishra R, Militky J, Hes L. Aerogel based nanoporous fibrous materials for thermal insulation. *Fibers and Polymers* 2014;15:1444–9. <https://doi.org/10.1007/s12221-014-1444-9>.
- [12] Gagge AP, Burton AC, Bazett HC. A Practical System of Units for the Description of the Heat Exchange of Man with His Environment. *Science* (1979) 1941;94:428–30. <https://doi.org/10.1126/science.94.2445.428>.
- [13] Huang J, Xu W. A new practical unit for the assessment of the heat exchange of human body with the environment. *J Therm Biol* 2006;31:318–22. <https://doi.org/10.1016/j.jtherbio.2005.12.008>.
- [14] Venkataraman M, Mishra R, Jasikova D, Kotresh TM, Militky J. Thermodynamics of aerogel-treated nonwoven fabrics at subzero temperatures. *Journal of Industrial Textiles* 2015;45. <https://doi.org/10.1177/1528083714534711>.
- [15] *Ashrae Handbook - 1997 Fundamentals*. Georgia: ASHRAE; 1997.
- [16] van Krevelen DWF, Hoftyzer PJ. *Properties of polymers : correlations with chemical structure*, 1972.
- [17] Sakiadis BC, Coates J. Prediction of specific heat of organic liquids. *AIChE Journal* 1956;2:88–93. <https://doi.org/10.1002/aic.690020119>.
- [18] Haghi A. Factors effecting water-vapor transport through fibers. *Journal of Theoretical and Applied Mechanics* 2003;30:277.
- [19] Eiermann K. Thermal conductivity of high polymers. *Journal of Polymer Science Part C: Polymer Symposia* 2007;6:157–65. <https://doi.org/10.1002/polc.5070060118>.
- [20] Militky J. Prediction of textile fabrics thermal conductivity. 6th International Thermal Manikin and Modelling Meeting Proceedings, 2006, p. 131–8.
- [21] Jussila K, Valkama A, Remes J, Anttonen H, Peitso A. The Effect of Cold Protective Clothing on Comfort and Perception of Performance. *Int J Occup Saf Ergon* 2010;16:185–97.
- [22] Venkataraman M. *Thermal Insulation of High Performance Fibrous Materials*. Doctoral theses. Technical University of Liberec, 2015.
- [23] Collier BJ, Bide MJ, Tortora PG. *Understanding Textiles*. 7th ed. Hoboken: Pearson Prentice Hall; 2009.

- [24] Song G. Thermal insulation properties of textiles and clothing. In: Williams JT, Steen WM, editors. *Laser material processing*, New York: Springer; 1991.
- [25] Lee CK. *Heat Transfer of Fibrous Insulation Battings*. Natick, Massachusetts: 1984.
- [26] Bogaty H, Hollies NRS, Harris M. Some Thermal Properties of Fabrics: Part I: The Effect of Fiber Arrangement. *Textile Research Journal* 1957;27. <https://doi.org/10.1177/004051755702700605>.
- [27] Kong LX, Li Y, She FH, Gao WM, Wong B. Effect of fiber geometry and porosity on heat and moisture transfer in textiles. *Proceedings of the Textile Institute 81st World Conference - An Odyssey in Fibers and Spaces*, Melbourne: The Textile Institute; 2011.
- [28] Křemenáková D, Militký J, Venkataraman M, Mishra R. Thermal Insulation and Porosity—From Macro- to Nanoscale, 2017. https://doi.org/10.1007/978-3-319-45899-1_20.
- [29] Venkataraman M, Mishra R, Wiener J, Militky J, Kotresh TM, Vaclavik M. Novel techniques to analyse thermal performance of aerogel-treated blankets under extreme temperatures. *Journal of the Textile Institute* 2015;106. <https://doi.org/10.1080/00405000.2014.939808>.
- [30] Holcombe BV, Hoschke BN. Dry Heat Transfer Characteristics of Underwear Fabrics. *Textile Research Journal* 1983;53:368–74. <https://doi.org/10.1177/004051758305300608>.
- [31] Wilson CA, Niven BE, Laing RM. Estimating thermal resistance of the bedding assembly from thickness of materials. *International Journal of Clothing Science and Technology* 1999;11:262–76. <https://doi.org/10.1108/09556229910297536>.
- [32] Militký J, Křemenáková D. A simple method for prediction of textile fabrics thermal conductivity. *5th International Conference on Heat Transfer, Fluid Mechanics and Thermodynamics*, Sun City, South Africa: HEFAT; 2007.
- [33] Yang K, Venkataraman M, Wang YF, Xiong XM, Yang T, Wiener J, et al. Thermal performance of a multi-layer composite containing peg/laponite as pcms. *Journal of Fiber Bioengineering and Informatics* 2020;13. <https://doi.org/10.3993/jfbim00330>.
- [34] Yang K, Wiener J, Venkataraman M, Wang Y, Yang T, Zhang G, et al. Thermal analysis of PEG/Metal particle-coated viscose fabric. *Polym Test* 2021;100. <https://doi.org/10.1016/j.polymertesting.2021.107231>.
- [35] Yang K, Venkataraman M, Zhang X, Wiener J, Zhu G, Yao J, et al. Review: incorporation of organic PCMs into textiles. *J Mater Sci* 2022;57. <https://doi.org/10.1007/s10853-021-06641-3>.
- [36] Yang K, Zhang X, Wiener J, Venkataraman M, Wang Y, Zhu G, et al. Nanofibrous Membranes in Multilayer Fabrics to Avoid PCM Leakages. *ChemNanoMat* 2022;8. <https://doi.org/10.1002/cnma.202200352>.
- [37] Venkataraman M, Wiener J, Mishra R, Militky J, Exnar P. A study on penetration of polymers in Aerogel granular particles. *NANOCON 2013 - Conference Proceedings, 5th International Conference*, 2013.

- [38] Venkataraman M, Mishra R, Militky J, Xiong X, Marek J, Yao J, et al. Electrospun nanofibrous membranes embedded with aerogel for advanced thermal and transport properties. *Polym Adv Technol* 2018;29. <https://doi.org/10.1002/pat.4369>.
- [39] Venkataraman M, Mishra R, Kotresh TM, Sakoi T, Militky J. Effect of compressibility on heat transport phenomena in aerogel-treated nonwoven fabrics. *Journal of the Textile Institute* 2016;107. <https://doi.org/10.1080/00405000.2015.1097084>.
- [40] Maity S, Singha K. Structure-Property Relationships of Needle-Punched Nonwoven Fabric. *Frontiers in Science* 2013;2:226–34. <https://doi.org/10.5923/j.fs.20120206.16>.
- [41] Chapman RA. *Applications of Nonwovens in Technical Textiles*. 2010. <https://doi.org/10.1533/9781845699741>.
- [42] Lin JH, xu ZH, Lei CH, Lou CW. Effect of Fiber Arrangement on the Mechanical Properties of Thermally Bonded Nonwoven Fabrics. *Textile Research Journal* 2003;73. <https://doi.org/10.1177/004051750307301012>.
- [43] Lin JH, Lei CH, Chang CH, Sun KM. Electrical conductive composites produced by laminated nonwovens via thermal compression. *Journal of Advanced Materials* 2005;37.
- [44] Lei CH, Lin JH, Chang CH, Lou CW. The Residual Electrostatic Voltage of Laminated Nonwovens with Different Surface Patterns. *Textile Research Journal* 2004;74. <https://doi.org/10.1177/004051750407400502>.
- [45] Russell SJ. *Handbook of Nonwovens*. 2006. <https://doi.org/10.1533/9781845691998>.
- [46] Lou C-W, Lin J-H, Su K-H. Recycling Polyester and Polypropylene Nonwoven Selvages to Produce Functional Sound Absorption Composites. *Textile Research Journal* 2005;75:390–4. <https://doi.org/10.1177/0040517505054178>.
- [47] Kumar Ghosh S, Bairagi S, Dutta S, Bhattacharyya R. A Comparative Study of the Thermal Insulation Properties of Jute and Jute -Polyester fibre Blended Nonwoven Fabrics. *American Journal of Engineering Research* 2016.
- [48] Ghosh SK, Bairagi S, Bhattacharyya R, Mondal MM. Study on potential application of natural fibre made fabrics as thermal insulation. *American International Journal of Research in Science, Technology, Engineering & Mathematics* 2016.
- [49] Abdel-Rehim ZS, Saad MM, El-Shakankery M, Hanafy I. Textile fabrics as thermal insulators. *Autex Research Journal* 2006;6.
- [50] Kucukali Ozturk M, Venkataraman M, Mishra R. Influence of structural parameters on thermal performance of polypropylene nonwovens. *Polym Adv Technol* 2018;29. <https://doi.org/10.1002/pat.4423>.
- [51] Morris GJ. Thermal properties of textile materials. *Journal of the Textile Institute Transactions* 1953;44. <https://doi.org/10.1080/19447025308662608>.
- [52] Kopitar D, Skenderi Z, Mijovic B. Study on the influence of calendaring process on thermal resistance of polypropylene nonwoven fabric structure. *Journal of Fiber Bioengineering and Informatics* 2014;7. <https://doi.org/10.3993/jfbi03201401>.

- [53] Woo SS, Shalev I, Barker RL. Heat and Moisture Transfer Through Nonwoven Fabrics. *Textile Research Journal* 1994;64:149–62. <https://doi.org/10.1177/004051759406400305>.
- [54] Lin CM, Lou CW, Lin JH. Manufacturing and Properties of Fire-Retardant and Thermal Insulation Nonwoven Fabrics with FR-Polyester Hollow Fibers. *Textile Research Journal* 2009;79. <https://doi.org/10.1177/0040517508090492>.
- [55] Yachmenev VG, Parikh D V., Calamari JA. Thermal insulation properties of biodegradable, cellulosic-based nonwoven composites for automotive application. *Journal of Industrial Textiles* 2001;31. <https://doi.org/10.1106/152808302029087>.
- [56] Farnworth B. Mechanisms of heat flow through clothing insulation. *Textile Research Journal* 1983;53:717–25.
- [57] Wu H, Fan J, Du N. Thermal energy transport within porous polymer materials: Effects of fiber characteristics. *J Appl Polym Sci* 2007;106. <https://doi.org/10.1002/app.26603>.
- [58] Cheng X, Fan J. Simulation of heat and moisture transfer with phase change and mobile condensates in fibrous insulation. *International Journal of Thermal Sciences* 2004;43. <https://doi.org/10.1016/j.ijthermalsci.2003.11.006>.
- [59] Wang M, He J, Yu J, Pan N. Lattice Boltzmann modeling of the effective thermal conductivity for fibrous materials. *International Journal of Thermal Sciences* 2007;46. <https://doi.org/10.1016/j.ijthermalsci.2006.11.006>.
- [60] Sun J, Hu Z, Li J, Zhang H, Sun C. Thermal and mechanical properties of fibrous zirconia ceramics with ultra-high porosity. *Ceram Int* 2014;40. <https://doi.org/10.1016/j.ceramint.2014.04.008>.
- [61] Li Y, Ren S. *Building Decorative Materials*. 2011. <https://doi.org/10.1533/9780857092588>.
- [62] Venkataraman M, Mishra R, Militky J. Comparative Analysis of High Performance Thermal Insulation Materials. *Journal of Textile Engineering & Fashion Technology* 2017;2. <https://doi.org/10.15406/jteft.2017.02.00062>.
- [63] Hu Y, Huang D, Qi Z, He S, Yang H, Zhang H. Modeling thermal insulation of firefighting protective clothing embedded with phase change material. *Heat and Mass Transfer/Waerme- Und Stoffuebertragung* 2013;49. <https://doi.org/10.1007/s00231-012-1103-x>.
- [64] Venkataraman M, Mishra R, Wiener J, Štěpánková M, Arumugam V, Militky J. Effect of laser irradiation on kevlar fabric treated with nanoporous aerogel. *NANOCON 2015 - 7th International Conference on Nanomaterials - Research and Application, Conference Proceedings, 2015*.
- [65] Shaid A, Furgusson M, Wang L. Thermophysiological Comfort Analysis of Aerogel Nanoparticle Incorporated Fabric for Fire Fighter's Protective Clothing. *Chemical and Materials Engineering* 2014;2:37–43. <https://doi.org/10.13189/cme.2014.020203>.
- [66] Xiong X, Venkataraman M, Jašíková D, Yang T, Mishra R, Militký J, et al. An experimental evaluation of convective heat transfer in multi-layered fibrous materials

- composed by different middle layer structures. *Journal of Industrial Textiles* 2021;51:362–79. <https://doi.org/10.1177/1528083719878845>.
- [67] Al-Homoud MS. Performance characteristics and practical applications of common building thermal insulation materials. *Build Environ* 2005;40. <https://doi.org/10.1016/j.buildenv.2004.05.013>.
- [68] Venkataraman M, Mishra R, Wiener J, Štěpánková M, Arumugam VK, Militky J. Effect of laser irradiation on kevlar fabric treated with nanoporous aerogel. *NANOCON 2015 - 7th International Conference on Nanomaterials - Research and Application, Conference Proceedings, 2015*.
- [69] Xiong X, Venkataraman M, Jašíková D, Yang T, Mishra R, Militký J, et al. Thermal Behavior of Aerogel-Embedded Nonwovens in Cross Airflow. *Autex Research Journal* 2020. <https://doi.org/10.2478/aut-2019-0082>.
- [70] Chen T, Sun H, Mu P, Zhu Z, An J, Liang W, et al. Fatty amines as a new family of organic phase change materials with exceptionally high energy density. *Solar Energy Materials and Solar Cells* 2020;206. <https://doi.org/10.1016/j.solmat.2019.110340>.
- [71] Karaman S, Karaipekli A, Sar A, Biçer A. Polyethylene glycol (PEG)/diatomite composite as a novel form-stable phase change material for thermal energy storage. *Solar Energy Materials and Solar Cells* 2011;95. <https://doi.org/10.1016/j.solmat.2011.01.022>.
- [72] Gubbins KE, Long Y, Śliwinska-Bartkowiak M. Thermodynamics of confined nano-phases. *J Chem Thermodyn* 2014;74:169–83. <https://doi.org/10.1016/j.jct.2014.01.024>.
- [73] Qian T, Li J, Ma H, Yang J. The preparation of a green shape-stabilized composite phase change material of polyethylene glycol/SiO₂ with enhanced thermal performance based on oil shale ash via temperature-assisted sol-gel method. *Solar Energy Materials and Solar Cells* 2015;132. <https://doi.org/10.1016/j.solmat.2014.08.017>.
- [74] Deng Y, Li J, Qian T, Guan W, Li Y, Yin X. Thermal conductivity enhancement of polyethylene glycol/expanded vermiculite shape-stabilized composite phase change materials with silver nanowire for thermal energy storage. *Chemical Engineering Journal* 2016;295. <https://doi.org/10.1016/j.cej.2016.03.068>.
- [75] Guo J, Xiang HX, Wang QQ, Xu DZ. Preparation and properties of polyacrylonitrile fiber/binary of fatty acids composites as phase change materials. *Energy Sources, Part A: Recovery, Utilization and Environmental Effects* 2013;35. <https://doi.org/10.1080/15567036.2010.518217>.
- [76] Geng X, Li W, Wang Y, Lu J, Wang J, Wang N, et al. Reversible thermochromic microencapsulated phase change materials for thermal energy storage application in thermal protective clothing. *Appl Energy* 2018;217. <https://doi.org/10.1016/j.apenergy.2018.02.150>.
- [77] Venkataraman M, Wiener J, Mishra R, Militky J, Exnar P. A study on penetration of polymers in Aerogel granular particles. *NANOCON 2013 - Conference Proceedings, 5th International Conference, 2013*.

- [78] Shaid A, Wang L, Islam S, Cai JY, Padhye R. Preparation of aerogel-icosane microparticles for thermoregulatory coating on textile. *Appl Therm Eng* 2016;107. <https://doi.org/10.1016/j.applthermaleng.2016.06.187>.
- [79] Xiangfa Z, Hanning X, Jian F, Changrui Z, Yonggang J. Preparation, properties and thermal control applications of silica aerogel infiltrated with solid-liquid phase change materials. *J Exp Nanosci* 2012;7. <https://doi.org/10.1080/17458080.2010.497950>.
- [80] Zhou X, Xiao H, Feng J, Zhang C, Jiang Y. Preparation and thermal properties of paraffin/porous silica ceramic composite. *Compos Sci Technol* 2009;69. <https://doi.org/10.1016/j.compscitech.2009.02.030>.
- [81] Gao H, Wang J, Chen X, Wang G, Huang X, Li A, et al. Nanoconfinement effects on thermal properties of nanoporous shape-stabilized composite PCMs: A review. *Nano Energy* 2018;53. <https://doi.org/10.1016/j.nanoen.2018.09.007>.
- [82] Li G, Huang Y, Lin J, Yu C, Liu Z, Fang Y, et al. Effective capture and reversible storage of iodine using foam-like adsorbents consisting of porous boron nitride microfibers. *Chemical Engineering Journal* 2020;382. <https://doi.org/10.1016/j.cej.2019.122833>.
- [83] Tian F, Zhang S, Zhai M, Sui J, Lan X, Gao J. Thermal properties of nano-sized polyethylene glycol confined in silica gels for latent heat storage. *Thermochim Acta* 2017;655. <https://doi.org/10.1016/j.tca.2017.05.006>.
- [84] Chang CY, Tsai WT, Ing CH, Chang CF. Adsorption of polyethylene glycol (PEG) from aqueous solution onto hydrophobic zeolite. *J Colloid Interface Sci* 2003;260. [https://doi.org/10.1016/S0021-9797\(02\)00174-1](https://doi.org/10.1016/S0021-9797(02)00174-1).
- [85] Yang K, Venkataraman M, Karpiskova J, Suzuki Y, Ullah S, Kim IS, et al. Structural analysis of embedding polyethylene glycol in silica aerogel. *Microporous and Mesoporous Materials* 2021;310. <https://doi.org/10.1016/j.micromeso.2020.110636>.
- [86] Greiner A, Wendorff JH. Electrospinning: A fascinating method for the preparation of ultrathin fibers. *Angewandte Chemie - International Edition* 2007;46. <https://doi.org/10.1002/anie.200604646>.
- [87] Li D, McCann JT, Xia Y, Marquez M. Electrospinning: A simple and versatile technique for producing ceramic nanofibers and nanotubes. *Journal of the American Ceramic Society*, vol. 89, 2006. <https://doi.org/10.1111/j.1551-2916.2006.00989.x>.
- [88] Reneker DH, Yarin AL. Electrospinning jets and polymer nanofibers. *Polymer (Guildf)* 2008;49. <https://doi.org/10.1016/j.polymer.2008.02.002>.
- [89] Wu H, Chen Y, Chen Q, Ding Y, Zhou X, Gao H. Synthesis of Flexible Aerogel Composites Reinforced with Electrospun Nanofibers and Microparticles for Thermal Insulation. *J Nanomater* 2013;2013:1–8. <https://doi.org/10.1155/2013/375093>.
- [90] Venkataraman M, Mishra R, Weiner J, Mazari A, Militky J, Arumugam VK. Novel techniques to analyze thermal performance of aerogel blankets under extreme temperatures. *Textile Bioengineering and Informatics Symposium Proceedings 2014 - 7th Textile Bioengineering and Informatics Symposium, TBIS 2014, in conjunction with the 5th Asian Protective Clothing Conference, APCC 2014, 2014.*

- [91] Venkataraman M, Mishra R, Kotresh TM, Militky J, Jamshaid H. Aerogels for thermal insulation in high-performance textiles. *Textile Progress* 2016;48. <https://doi.org/10.1080/00405167.2016.1179477>.
- [92] Huang D, Shen Y, Yuan Q, Wang C, Shi L. Preparation and characterization of silica aerogel/polytetrafluoroethylene composites. *Mater Res Express* 2019;6. <https://doi.org/10.1088/2053-1591/ab454e>.
- [93] Chen YC, Lin HC, Lee Y Der. The Effects of Filler Content and Size on the Properties of PTFE/SiO₂ Composites. *Journal of Polymer Research* 2003;10. <https://doi.org/10.1023/B:JPOL.0000004620.71900.16>.
- [94] Wei X, Nie Z, Luo Q, Li B, Chen B, Simmons K, et al. Nanoporous Polytetrafluoroethylene/Silica Composite Separator as a High-Performance All-Vanadium Redox Flow Battery Membrane. *Adv Energy Mater* 2013;3:1215–20. <https://doi.org/10.1002/aenm.201201112>.
- [95] Guo X, Bai S, Shan J, Lei W, Ding R, Zhang Y, et al. Fabrication and characterization of MSQ aerogel coating on EPTFE thin films for cable sheaths. *Molecules* 2019;24. <https://doi.org/10.3390/molecules24071246>.
- [96] Huang A, Liu F, Cui Z, Wang H, Song X, Geng L, et al. Novel PTFE/CNT composite nanofiber membranes with enhanced mechanical, crystalline, conductive, and dielectric properties fabricated by emulsion electrospinning and sintering. *Compos Sci Technol* 2021;214. <https://doi.org/10.1016/j.compscitech.2021.108980>.
- [97] Venkataraman M, Yang K, Xiong X, Militky J, Kremenakova D, Zhu G, et al. Preparation of electrosprayed, microporous particle filled layers. *Polymers (Basel)* 2020;12. <https://doi.org/10.3390/polym12061352>.
- [98] Jirsak O, Petrik S. Recent advances in nanofibre technology: needleless electrospinning. *Int J Nanotechnol* 2012;9:836. <https://doi.org/10.1504/IJNT.2012.046756>.
- [99] Brown NA, Zhu Y, German GK, Yong X, Chiarot PR. Electrospray deposit structure of nanoparticle suspensions. *J Electrostat* 2017;90. <https://doi.org/10.1016/j.elstat.2017.09.004>.
- [100] Xiong X, Yang T, Mishra R, Kanai H, Militky J. Thermal and compression characteristics of aerogel-encapsulated textiles. *Journal of Industrial Textiles* 2018;47. <https://doi.org/10.1177/1528083717716167>.
- [101] Xiong X, Venkataraman M, Yang T, Militky J, Wiener J. Preparation and Characterization of Electrosprayed Aerogel/Polytetrafluoroethylene Microporous Materials. *Polymers (Basel)* 2021;14:48. <https://doi.org/10.3390/polym14010048>.
- [102] Castillo JL, Martin S, D. Rodriguez-Perez a, Higuera FJ, Garcia-Ybarra PL. Nanostructured porous coatings via electrospray atomization and deposition of nanoparticle suspensions. *J Aerosol Sci* 2018;125:148–63.
- [103] Pierre AC, Pajonk GM. Chemistry of aerogels and their applications. *Chem Rev* 2002;102. <https://doi.org/10.1021/cr0101306>.

- [104] Rosace G, Guido E, Colleoni C, Barigozzi G. Influence of textile structure and silica based finishing on thermal insulation properties of cotton fabrics. *Int J Polym Sci* 2016;2016. <https://doi.org/10.1155/2016/1726475>.
- [105] Xiong X, Venkataraman M, Yang T, Kucerova K, Militký J, Yang K, et al. Transport properties of electro-sprayed polytetrafluoroethylene fibrous layer filled with aerogels/phase change materials. *Nanomaterials* 2020;10. <https://doi.org/10.3390/nano10102042>.
- [106] Cardoso I, Gomes JR. The application of microcapsules of PCM in flame resistant nonwoven materials. *International Journal of Clothing Science* 2009;21:102–8.
- [107] Shaid A, Wang L, Padhye R. The thermal protection and comfort properties of aerogel and PCM-coated fabric for firefighter garment. *Journal of Industrial Textiles* 2016;45. <https://doi.org/10.1177/1528083715610296>.
- [108] Huang Q, Huang Y, Gao S, Zhang M, Xiao C. Novel ultrafine fibrous poly(tetrafluoroethylene) hollow fiber membrane fabricated by electrospinning. *Polymers (Basel)* 2018;10. <https://doi.org/10.3390/polym10050464>.
- [109] Huang Y, Huang QL, Liu H, Zhang CX, You YW, Li NN, et al. Preparation, characterization, and applications of electrospun ultrafine fibrous PTFE porous membranes. *J Memb Sci* 2017;523. <https://doi.org/10.1016/j.memsci.2016.10.019>.
- [110] Basu BJ, Dinesh Kumar V. Fabrication of Superhydrophobic Nanocomposite Coatings Using Polytetrafluoroethylene and Silica Nanoparticles. *ISRN Nanotechnology* 2011;2011. <https://doi.org/10.5402/2011/803910>.
- [111] Aderikha VN, Shapovalov VA. Tribological Behavior of Polytetrafluoroethylene-Silica Composites. *Journal of Friction and Wear* 2011;32. <https://doi.org/10.3103/S1068366611020024>.
- [112] Burkarter E, Saul CK, Thomazi F, Cruz NC, Roman LS, Schreiner WH. Superhydrophobic electrospayed PTFE. *Surf Coat Technol* 2007;202. <https://doi.org/10.1016/j.surfcoat.2007.05.012>.
- [113] Burkarter E, Saul CK, Thomazi F, Cruz NC, Zanata SM, Roman LS, et al. Electrospayed superhydrophobic PTFE: A non-contaminating surface. *J Phys D Appl Phys* 2007;40. <https://doi.org/10.1088/0022-3727/40/24/027>.
- [114] Venkataraman M, Militký J, Samková A, Karthik D, Křemenáková D, Petru M. Hybrid Prepreg Tapes for Composite Manufacturing: A Case Study. *Materials* 2022;15:619. <https://doi.org/10.3390/ma15020619>.
- [115] Venkataraman M, Mishra R, Wiener J, Militky J, Kotresh TM, Vaclavik M. Novel techniques to analyse thermal performance of aerogel-treated blankets under extreme temperatures. *Journal of the Textile Institute* 2015;106. <https://doi.org/10.1080/00405000.2014.939808>.
- [116] Li Z, Gong L, Cheng X, He S, Li C, Zhang H. Flexible silica aerogel composites strengthened with aramid fibers and their thermal behavior. *Mater Des* 2016;99. <https://doi.org/10.1016/j.matdes.2016.03.063>.

- [117] Li Z, Cheng X, He S, Shi X, Gong L, Zhang H. Aramid fibers reinforced silica aerogel composites with low thermal conductivity and improved mechanical performance. *Compos Part A Appl Sci Manuf* 2016;84:316–25. <https://doi.org/10.1016/j.compositesa.2016.02.014>.
- [118] He S, Sun G, Cheng X, Dai H, Chen X. Nanoporous SiO₂ grafted aramid fibers with low thermal conductivity. *Compos Sci Technol* 2017;146. <https://doi.org/10.1016/j.compscitech.2017.04.021>.
- [119] Venkataraman M, Xiong X, Novotná J, Kašparová M, Mishra R, Militký J. Thermal protective properties of aerogel-coated Kevlar woven fabrics. *Journal of Fiber Bioengineering and Informatics* 2019;12. <https://doi.org/10.3993/JFBIM00321>.
- [120] Lyu J, Liu Z, Wu X, Li G, Fang D, Zhang X. Nanofibrous Kevlar aerogel films and their phase-change composites for highly efficient infrared stealth. *ACS Nano* 2019;13. <https://doi.org/10.1021/acsnano.8b08913>.
- [121] Bhattacharjee D, Kothari VK. Measurement of Thermal Resistance of Woven Fabrics in Natural and Forced Convections. *Research Journal of Textile and Apparel* 2008;12. <https://doi.org/10.1108/RJTA-12-02-2008-B005>.
- [122] China National Standard (GB/T 18319-2001) – Textiles Testing Method for Thermal Retention with Accumulated by Infrared Ray. China National Standard Bureau, Beijing: China Standard Press; 2001.
- [123] Sokolovskaya TS. Measurement of the thermal conductivity coefficient of textile materials by the regular cooling regime method. *Fibre Chemistry* 2005;37. <https://doi.org/10.1007/s10692-005-0054-0>.
- [124] Gustavsson M, Hälldahl L. Thermal conductivity measurements of thin insulating layers deposited on high-conducting sheets. *Int J Thermophys* 2006;27. <https://doi.org/10.1007/s10765-006-0039-0>.
- [125] Hu JY, Li Y, Yeung KW, Wang SX. Characterization of thermal radiation properties of polymeric materials. *Polym Test* 2006;25. <https://doi.org/10.1016/j.polymertesting.2005.11.011>.
- [126] China Textile Industry Council FZ/T 64010-2000 Far Infrared Products. Beijing: China Standard Press; 2000.
- [127] Yuan T, Huang Y, Dong S, Wang T, Xie M. Infrared reflection of conducting polyaniline polymer coating. *Polym Test* 2002;21. [https://doi.org/10.1016/S0142-9418\(01\)00136-2](https://doi.org/10.1016/S0142-9418(01)00136-2).
- [128] Kawabata S, Postle R, Niwa M. Objective Measurement Applications to Product Design and Process Control. Japan: The Textile Machinery Society of Japan; 1985.
- [129] Hes L, Dolezal I. New method and equipment for measuring thermal properties of textiles 1989. https://doi.org/10.4188/transjtmsj.42.8_t124.
- [130] Militký J, Křemenáková D, Venkataraman M, Večerník J, Martínková L, Marek J. Sandwich Structures Reflecting Thermal Radiation Produced by the Human Body. *Polymers (Basel)* 2021;13:3309. <https://doi.org/10.3390/polym13193309>.
- [131] 31092, Determination of physiological properties-Measurement of thermal and water-vapour resistance under steady-state conditions (sweating guarded-hotplate test). 1996.

- [132] Romeli D, Barigozzi G, Esposito S, Rosace G, Salesi G. High sensitivity measurements of thermal properties of textile fabrics. *Polym Test* 2013;32. <https://doi.org/10.1016/j.polymertesting.2013.05.011>.
- [133] Venkataraman M, Mishra R, Militky J, Behera BK. Modelling and simulation of heat transfer by convection in aerogel treated nonwovens. *Journal of the Textile Institute* 2017;108. <https://doi.org/10.1080/00405000.2016.1255124>.
- [134] Venkataraman M, Mishra R, Subramaniam V, Gnanamani A, Kotresh TM, Militky J. Dynamic heat flux measurement for advanced insulation materials. *Fibers and Polymers* 2016;17. <https://doi.org/10.1007/s12221-016-5882-4>.
- [135] Venkataraman M, Militký J, Mishra R, Jandová S. Unconventional measurement methods and simulation of aerogel assisted thermoregulation. *Journal of Mechanical Engineering* 2018;5.
- [136] Venkataraman M, Mishra R, Marek J, Militky J, Arumugam V. Thermal properties of electrospun nanofibers with aerogel. *NANOCON 2016 - Conference Proceedings, 8th International Conference on Nanomaterials - Research and Application, 2016*.
- [137] Yang T, Hu L, Yu D, Xiong X, Chvojka J, Venkataraman M, et al. Simple determination of key structural parameters for fibrous materials enabled by Ergun-Type and Kozeny-type equations. *Polym Test* 2022;108. <https://doi.org/10.1016/j.polymertesting.2022.107514>.
- [138] Wang Y, Yao J, Zhu G, Militky J, Marek J, Venkataraman M, et al. A novel method for producing bi-component thermo-regulating alginate fiber from phase change material microemulsion. *Textile Research Journal* 2020;90. <https://doi.org/10.1177/0040517519886075>.

11 Appendix: Full Texts of Selected Publications

11.1 Author contributions

S. No.	Publication	Author contribution
1	Electrospun nanofibrous membranes embedded with aerogel for advanced thermal and transport properties	<ul style="list-style-type: none"> ● Conceptualization <ul style="list-style-type: none"> ○ Devised the project, the main conceptual ideas and proof outline. ● Methodology <ul style="list-style-type: none"> ○ Material selection and sample design for preparation. ○ Conceived and planned experimental techniques. ● Formal Analysis, Investigation & Data curation <ul style="list-style-type: none"> ○ Characterize the samples and conduct the experiments. ○ Processed the experimental data. ● Software & Validation <ul style="list-style-type: none"> ○ Performed the statistical analysis by using original software tools. ○ Verification of the overall reproducibility of results and other research outputs. ● Writing the manuscript <ul style="list-style-type: none"> ○ Original Draft Preparation, review & editing with input from all authors. ● Visualization <ul style="list-style-type: none"> ○ Preparation, creation and presentation of the published work, specifically visualization/data presentation
2	Preparation of Electrospayed, Microporous Particle Filled Layers	<ul style="list-style-type: none"> ● Conceptualization <ul style="list-style-type: none"> ○ Devised the project, the main conceptual ideas and proof outline. ● Methodology <ul style="list-style-type: none"> ○ Material selection and sample design for preparation ○ Conceived and planned experimental techniques. ● Formal Analysis, Investigation & Data curation <ul style="list-style-type: none"> ○ Characterize the samples and conduct the experiments. ○ Processed the experimental data. ○ Performed the statistical analysis by using QC expert software tools. ● Software & Validation <ul style="list-style-type: none"> ○ Performed the statistical analysis by using software tools. ○ Verification of the overall reproducibility of results and other research outputs. ● Writing the manuscript <ul style="list-style-type: none"> ○ Original Draft Preparation, review & editing with input from all authors. ● Visualization

S. No.	Publication	Author contribution
		<ul style="list-style-type: none"> ○ Preparation, creation and presentation of the published work, specifically visualization/data presentation
3	Modelling and simulation of heat transfer by convection in aerogel treated nonwoven	<ul style="list-style-type: none"> ● Conceptualization <ul style="list-style-type: none"> ○ Devised the project, the main conceptual ideas and proof outline. ● Methodology <ul style="list-style-type: none"> ○ Design for Sample preparation. ○ Conceived, planned and supervised the experiments. ● Formal Analysis, Investigation & Data curation <ul style="list-style-type: none"> ○ Characterized the samples and conducted the experiments. ○ Processed the experimental data. ○ Performed statistical analysis and stochastic modelling by using original software tools. ● Software & Validation <ul style="list-style-type: none"> ○ Designed the model and the computational framework and analysed the data. ○ Planned and carried out the simulations. ○ Verification of the overall reproducibility of results and other research outputs. ● Writing the manuscript <ul style="list-style-type: none"> ○ Original Draft Preparation, review & editing with input from all authors. ● Visualization <ul style="list-style-type: none"> ○ Preparation, creation and presentation of the published work, specifically visualization/data presentation
4	Structural analysis of embedding polyethylene glycol in silica aerogel	<ul style="list-style-type: none"> ● Conceptualization <ul style="list-style-type: none"> ○ Devised the project, the main conceptual ideas and proof outline. ● Methodology <ul style="list-style-type: none"> ○ Conceived, planned and assisted with the experiments ● Validation <ul style="list-style-type: none"> ○ Verification of the overall reproducibility of results and other research outputs. ● Writing – Original Draft Preparation <ul style="list-style-type: none"> ○ Assisted in writing the manuscript, review and editing. ● Others <ul style="list-style-type: none"> ○ Supervision
5	Transport Properties of Electro-Sprayed Polytetrafluoroethylene Fibrous Layer Filled with Aerogels/Phase Change Materials	<ul style="list-style-type: none"> ● Conceptualization <ul style="list-style-type: none"> ○ Devised the project, the main conceptual ideas and proof outline. ● Methodology <ul style="list-style-type: none"> ○ Devised the project, the main conceptual ideas and proof outline.

S. No.	Publication	Author contribution
		<ul style="list-style-type: none"> ● Investigation <ul style="list-style-type: none"> ○ Performing the experiments, and data/evidence collection. ● Writing – Original Draft Preparation <ul style="list-style-type: none"> ○ Assisted in writing the manuscript, review and editing. ● Others <ul style="list-style-type: none"> ○ Supervision
6	Mass transfer and the thermal buffering effect of hydrophobic fabrics with a single-side coating of MPCMs	<ul style="list-style-type: none"> ● Validation <ul style="list-style-type: none"> ○ Verification of the overall reproducibility of results and other research outputs. ● Writing – Original Draft Preparation <ul style="list-style-type: none"> ○ Assisted in writing the manuscript, review and editing. ● Funding Acquisition <ul style="list-style-type: none"> ○ From GAČR as leader of the project ● Others <ul style="list-style-type: none"> ○ Supervision ○ Project Administration
7	Hydrophobicity, water moisture transfer and breathability of PTFE-coated viscose fabrics prepared by electrospraying technology and sintering process	<ul style="list-style-type: none"> ● Conceptualization <ul style="list-style-type: none"> ○ Devised the project, the main conceptual ideas and proof outline. ● Validation <ul style="list-style-type: none"> ○ Verification of the overall reproducibility of results and other research outputs. ● Formal Analysis <ul style="list-style-type: none"> ○ Characterize the samples and conduct the experiments. ○ Processed the experimental data. ○ Performed the statistical analysis by using original software tools. ● Writing – Original Draft Preparation <ul style="list-style-type: none"> ○ Assisted in writing the manuscript, review and editing. ● Funding Acquisition <ul style="list-style-type: none"> ○ From GAČR as leader of the project ● Others <ul style="list-style-type: none"> ○ Supervision ○ Project Administration

11.2 Publication 1: Electrospun nanofibrous membranes embedded with aerogel for advanced thermal and transport properties

Publication

Venkataraman, M., Mishra, R., Militky, J., et al. Electrospun nanofibrous membranes embedded with aerogel for advanced thermal and transport properties. *Polymer Advanced Technologies*. 2018; 29: 2583– 2592. DOI:10.1002/pat.4369.

Author contribution

- Conceptualization
 - Devised the project, the main conceptual ideas and proof outline.
- Methodology
 - Material selection and sample design for preparation.
 - Conceived and planned experimental techniques.
- Formal Analysis, Investigation & Data curation
 - Characterize the samples and conduct the experiments.
 - Processed the experimental data.
- Software & Validation
 - Performed the statistical analysis by using original software tools.
 - Verification of the overall reproducibility of results and other research outputs.
- Writing the manuscript
 - Original Draft Preparation, review & editing with input from all authors.
- Visualization
 - Preparation, creation and presentation of the published work, specifically visualization/data presentation



RESEARCH ARTICLE

Electrospun nanofibrous membranes embedded with aerogel for advanced thermal and transport properties

Mohanapriya Venkataraman¹ | Rajesh Mishra¹ | Jiri Militky¹ | Xiaoman Xiong¹ | Jaromir Marek² | Juming Yao³ | Guocheng Zhu³

¹Technical University of Liberec, Department of Material Engineering, Faculty of Textile Engineering, Liberec, Czech Republic

²Technical University of Liberec, LCS-Cxi, Institute for Nanomaterials, Advanced Technologies and Innovations, Liberec, Czech Republic

³Zhejiang Sci-Tech University, College of Materials and Textiles, Xiasha Education Park, Hangzhou, China

Correspondence

Mohanapriya Venkataraman, Department of Material Engineering, Faculty of Textile Engineering, Technical University of Liberec, Liberec, Czech Republic.
Email: mohanapriya.venkataraman@tul.cz

Funding information

European Union; Ministry of Education, Youth and Sports of the Czech Republic, Grant/Award Number: CZ.02.1.01/0.0/0.0/16_019/0000843

The primary purpose of cold weather clothing is to shield the wearer from the extremities of the external environment. The thermal properties of nanofibers and their potential applications have tremendous scope and application in this area. The objective of this study was to investigate the mechanisms of heat transfer through fibrous insulation where the fiber diameter was less than 1 μm . Electrospinning process was used to produce flexible polyurethane and polyvinylidene fluoride nanofibers embedded with silica aerogel. The thermal and transport behavior of the samples was evaluated, and results were statistically analyzed. Presence of aerogel particles were confirmed through microscopic examination. Thermal behavior was investigated by using thermogravimetric analysis and differential scanning calorimetry. The results showed that the polyvinylidene fluoride nanofibrous membranes embedded with aerogel obtained a good thermal stability with lower weight loss than polyurethane nanofibrous membranes. The glass transition and melting point was not affected by the aerogel content in the layers, validating that polymers are not miscible. The increase in duration of electrospinning led to higher web thickness, which resulted in considerable decrease in air permeability. Considerable improvement of thermal insulation was observed by increasing the number and the weight per unit area of both nanofibrous membranes. The results confirmed increase in thermal insulation by embedding silica aerogel in nanofibrous membranes. With reference to the results, it could be concluded that nanofibers embedded with aerogel are good for thermal insulation in cold weather conditions. Thermal insulation battings incorporating nanofibers could possibly decrease the weight and bulk of current thermal protective clothing.

KEYWORDS

aerogel, heat transfer, Nanofibrous membranes, thermal insulation, transport properties

1 | INTRODUCTION

Textiles may be considered as human's armor against extremities of nature. The fabric performance and efficacy has to withstand the test of extreme climatic conditions. Different fabrics and coating materials have to be evaluated to improve their thermal properties of textiles. Recent advances in the technology of producing nanofibers provide

excellent opportunities to research the heat transfer behavior of low-density nanofibrous membranes. Understanding heat transfer through nanofiber structures will allow us to exploit the unique properties of polymer nanofibers for applications such as improved cold weather clothing, hand wear, sleeping bags, and tent liners.¹ Electrospinning is a simple and low-cost method for making polymer and ceramic fibers with superfine diameters.²⁻⁴ Recently, this

technique has gained in acceptance due to the promising properties of different types of structure and assembled electrospun nanofibers. Silica aerogel is a highly porous material with pore diameters in the range of 2 to 50 nm.^{5,6} The nanoporous structure of the silica aerogel having a high porosity above 90% makes the aerogel a highly thermal insulating materials with a super-low thermal conductivity as low as $0.013 \text{ Wm}^{-1} \text{ K}^{-1}$. It is considered to be an effective thermal insulation material for wide applications in textiles.⁷⁻⁹ The electrospun polyvinylidene fluoride (PVDF) nanofibers could improve the mechanical strength and flexibility of the SiO_2 aerogels while maintaining a lower thermal conductivity.¹⁰ Lightweight and compressible insulation materials maximize insulating value at a minimum weight. Many practical applications focus on fibrous materials that have a low fiber volume fraction (less than 10% fiber for the most part). Heat transfer through porous media is by conduction, convection, and radiation. For these types of materials, heat conduction through the solid portion of the matrix (the fibers) is negligible, so it is not necessary to focus on solid conduction heat transfer. Heat transfer through porous media is by conduction, convection, and radiation. However, conduction through the still-air trapped within the insulation is important, and the thermal conductivity of air, total gas volume fraction, and thickness of air within the material is required to properly analyze both radiation heat transfer and convection heat transfer mechanisms.^{11,12} Literature searches on the subject of submicron fibers in thermal insulation reveal a necessity to conduct further fundamental or applied work by using polymer nanofibers for thermal insulation applications.

In this paper, the mechanisms of heat transfer through fibrous insulation where the fiber diameter less than $1 \mu\text{m}$ was investigated. Flexible electrospun nanofibrous membranes embedded with silica aerogel were produced via electrospinning process by optimizing the solution and spinning parameters. The electrospun polyurethane (PUR) and PVDF nanofibrous microstructures were fabricated and then used to reinforce the SiO_2 aerogel. The effects of thermal and transport properties of the electrospun nanofibrous membranes embedded with SiO_2 aerogel were evaluated to understand their potential for thermal insulation applications.

2 | METHODOLOGY

2.1 | Materials

Commercially available hydrophobic amorphous silica aerogels in powder and granular form were procured from Cabot Aerogel Corporation. The properties of amorphous silica aerogel are given in Table 1. Polyurethane resin (Larithane AL286, Novotex Italiana SpA, molecular weight 2000 g mol^{-1}), PVDF (Solef 1015, molecular weight

TABLE 1 Properties of amorphous silica aerogel

S. No	Properties	Value Range
1	Particle size range	0.1-0.7 mm
2	Pore diameter	~20 nm
3	Density	1.205 kg/m^3
4	Surface chemistry	Fully hydrophobic

TABLE 2 Laboratory equipment setup for production of polyurethane nanofibrous layer embedded with aerogel

Parameters	Specifications
Distance of electrode	175 mm
Wire speed	0.2 mm/s
Substrate speed	15 mm/min
Carriage speed	380-430 mm/s on 500-mm distance
Substrate	Spunbond polypropylene
Voltage	-10/60 kV
Size of the girder	$\varnothing 0.7 \text{ mm}$
Air flow	90/100 m^3h
Humidity	With dry box

$573 \times 103 \text{ g mol}^{-1}$), and dimethylformamide were used as received from the CXI lab (Nanocenter, TUL, Czech Republic; Table 2).

Polyurethane is a polymer composed of organic units joined by carbamate (urethane) links. Polyurethane can be made in a variety of densities and hardnesses by varying the isocyanate, polyol, or additives. Thus, it can be produced with a variety of physical properties by varying its structure, the molecular weight of the segments. It exhibits extremely high insulating effect. The very low thermal conductivity makes it well suited for applications in outdoor wear for extreme conditions.¹³ The chemical structure of the PVDF consists of the repeated monomer. Its complex molecular and crystalline structure exhibits good hydrophobicity, thermal resistance, and mechanical strength and can be easily prepared into membranes with versatile pore structures by electrospinning.¹⁴

2.2 | Solution preparation

The PUR and PVDF were dissolved separately in dimethylformamide at a concentration of 18 wt%. The solutions were stirred in a magnetic stirrer for 2 hours at room temperature. Then, silica aerogels in both powder and granular forms were added to the solution. These mixtures were stirred again for 3 hours at room temperature prior to electrospinning. The solution's viscosity was tuned by adjusting the solution concentration and was then electrospun.

2.3 | Electrospinning using nanospider

Electrospinning was carried out by using nanospider technology as a modified electrospinning technique, nanospider laboratory machine NS LAB 500S from Elmarcos.r.o (Figure S1).¹⁵ Electrospinning is widely accepted as a technique to fabricate submicron polymer fibers. It is a fiber-forming process, where high voltage is used to create an electrically charged jet of polymer solution or melt from the needle. The polymer solidifies as it travels toward the collecting plate, often producing nanometer scale fibers.¹⁶⁻¹⁹ Nanospider is a modified electrospinning method which requires the use of a high-voltage electrostatic field to create an electrically charged stream of polymer solution or melt. The innovative idea of the nanospider is based on the possibility of producing nanofiber in diameters of 50 to 300 nm into nonwoven webs.²⁰

TABLE 3 Sample details of electrospun polyvinylidene fluoride nanofibrous layer embedded with silica aerogel

Type	Samples	Description (Spun PP + NFA)	Areal Density [g/m ²]	Thickness [mm]
Aerogel nanofibrous layer with Spunbond PP back up	SPUR1	Only PUR	34.01 (± 1.71)	0.290 (± 0.014)
	SPUR2	PUR + aerogel (powder)	33.11 (± 1.65)	0.254 (± 0.013)
	SPUR3	PUR + aerogel (granular)	35.28 (± 1.76)	0.300 (± 0.015)
	SPUR4	PUR + aerogel (powder)	35.29 (± 1.65)	0.390 (± 0.020)
	SPUR5	PUR + aerogel (granular)	38.58 (± 1.93)	0.370 (± 0.019)
Aerogel nanofibrous layer	PUR1	Only PUR	6.01 (± 0.31)	0.083 (± 0.004)
	PUR2	PUR + aerogel (powder)	5.11 (± 0.26)	0.089 (± 0.005)
	PUR3	PUR + aerogel (granular)	7.28 (± 0.03)	0.112 (± 0.006)
	PUR4	PUR + aerogel (powder)	7.29 (± 0.07)	0.206 (± 0.010)
	PUR5	PUR + aerogel (granular)	10.58 (± 0.21)	0.248 (± 0.012)

Note: "±" is the upper and lower 95% confidence interval of the mean. PP, polypropylene; PUR, polyurethane.

2.4 | Electrospinning of PUR and PVDF nanofibrous membranes

The prepared solution was placed in a cylinder containing active electrode parallel to collecting electrode. The single wire electrode was selected to spin the nanofibers shown in Figure S2. The solution was delivered under the conditions given in Tables 2, 4, and 6. The details of the PUR and PVDF samples are given in Tables 3 and 5.

The nanofibers were collected on a spunbond polypropylene fabric substrate. The substrate was chosen to provide mechanical properties, while the nanofibrous web dominates thermal performance. The electrospun nanofibrous membranes were then dried for 2 hours before using it for the tests.

2.5 | Characterizations

2.5.1 | Scanning electron microscope

The morphology and microstructure of electrospun PUR and PVDF nanofibrous layer embedded with silica aerogel were studied by using a scanning electron microscopy (VEGA TESCAN Inc. USA) at 30 kV. The densities of the samples were determined by measuring the weight and volume.

2.5.2 | Thermal measurement

Alambeta instrument (developed at the technical university of Liberec, Czech Republic) was used to evaluate the comparative thermal properties of the samples. Alambeta measuring device was used for fast measuring of transient and steady state thermophysical properties (thermal insulation and thermal contact properties). The instrument measures parameters such as thermal conductivity, thermal diffusion (a), thermal absorption (b), thermal resistance (r), the ratio of maximal to stationary heat flow density (q_{max}/q_s), stationary heat flow density at the contact point (q_s), and fabric thickness.²⁰ Netzch STA 409 equipment was used for thermogravimetric analysis (TGA). Analysis was performed within a temperature range of 25 to 450°C at a heating rate of 10°C/min and N₂ atmosphere. Differential scanning calorimetry (DSC) analysis was conducted by using TA Instruments MDSC 2920 equipment within a temperature range of 0 to 400°C at a heating rate of 10°C/min in N₂ atmosphere. ASTM D882-95a specification was followed for strip-cutting samples from a thin sheet. For each sample composition, 5 specimens were tested.

TABLE 4 Air temperature/humidity and size of the girder specifications

Samples	Air Temperature and Humidity	Size of the Girder (mm)
PUR1	22.7%/23°C	ø0.7
PUR2	20.3%/23.6°C	ø0.7
PUR3	20.8%/23.3°C	ø0.7
PUR4	23.1%/24.4°C 23.1%/24.2°C	ø0.7/ø 0.8/ø 1.0
PUR5	23.1%/24.8°C (first layer) 21.5%/26°C (second layer)	ø0.9 ø0.9

2.5.3 | Air permeability

FX 3300 air permeability instrument was used to measure the transport property of the samples (Table 4). The principle of the instrument depends on the measurement of air flow passing through the fabric at a certain pressure gradient Δp . In this instrument, any part of the fabric can be placed between the sensing circular clamps (discs) without the fabric destruction. As the fabric fixes firmly on its circumference (to prevent the air from escaping), the fabric dimensions do not play any role. The enough space between the clamps and the instrument frame allows the measurement for large samples.

3 | RESULTS AND DISCUSSION

3.1 | Microstructures of nanofibrous membranes

Figures 1 and 2 show the morphologies and microstructures of electrospun PUR and PVDF nanofibrous membranes. The different microstructures could be observed with and without aerogel particles present which were electrospun from the solutions with the concentration of 18 wt% (Table 5).²⁰

The electrospun nanofibrous membranes consisted of fibers in the submicrometer range arranged in a 3D network structure with high porosity and fully interconnected pores. Through optimization of concentration of polymer solution, the average fiber diameter was found to decrease gradually. The surface morphology of the electrospun PUR and PVDF fibers largely depends on the polymer solution concentration and composition to maintain the suitable viscosity. These results indicate that the surface morphology and fiber diameter of the electrospun PUR and PVDF layers are significantly influenced by the composition of the polymer solution used for electrospinning. The intact morphology of the nanofibrous membranes embedded with

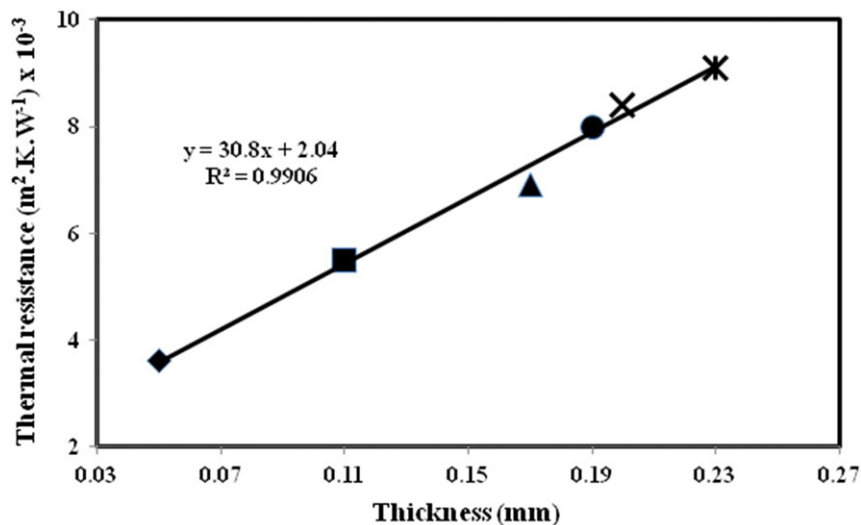


FIGURE 1 Morphology and microstructure of electrospun polyurethane nanofibrous membranes embedded with SiO₂ aerogel from 18 wt% [Colour figure can be viewed at wileyonlinelibrary.com]

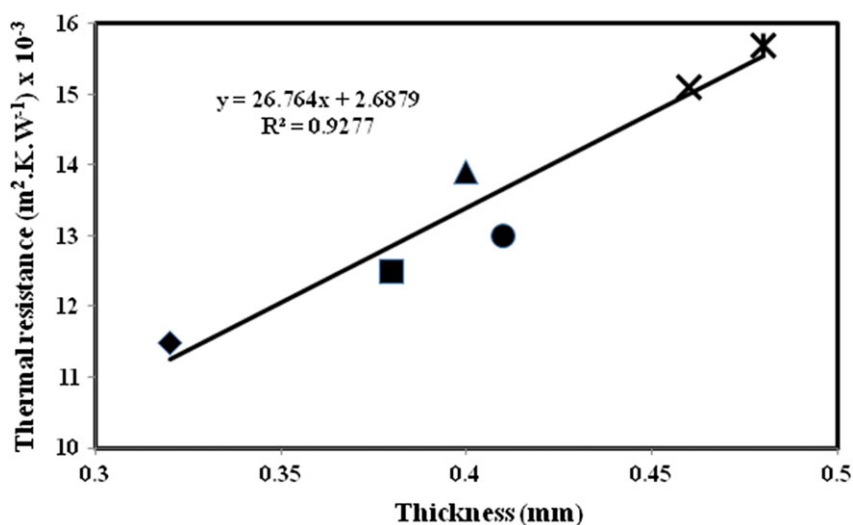


FIGURE 2 Morphology and microstructure of electrospun polyvinylidene fluoride nanofibrous membranes embedded with SiO₂ aerogel from 18 wt% [Colour figure can be viewed at wileyonlinelibrary.com]

TABLE 5 Sample details of electrospun PVDF nanofibrous layer embedded with silica aerogel

Type	Samples	Description (spun PP + NFA)	Areal Density [g/m ²]	Thickness [mm]
Aerogel nanofibrous layer with Spunbond PP backup	SPVDF1	Only PVDF	34.89 (±0.79)	0.48 (±0.045)
	SPVDF2	Only PVDF	38.62 (±0.93)	0.32 (±0.036)
	SPVDF3	PVDF + aerogel (powder)	34.58 (±2.73)	0.46 (±0.048)
	SPVDF4	PVDF + aerogel (powder)	44.00 (±2.38)	0.38 (±0.091)
	SPVDF5	PVDF + aerogel (granular)	37.18 (±1.26)	0.41 (±0.025)
	SPVDF6	PVDF + aerogel (granular)	39.89 (±1.95)	0.40 (±0.102)
Aerogel nanofibrous layer	PVDF1	Only PVDF	6.80 (±0.34)	0.11 (±0.005)
	PVDF2	Only PVDF	10.62 (±0.43)	0.20 (±0.012)
	PVDF3	PVDF + aerogel (powder)	6.58 (±0.13)	0.17 (±0.065)
	PVDF4	PVDF + aerogel (powder)	16.00 (±0.23)	0.05 (±0.025)
	PVDF5	PVDF + aerogel (granular)	9.18 (±0.60)	0.19 (±0.033)
	PVDF6	PVDF + aerogel (granular)	11.89 (±0.55)	0.23 (±0.015)

Note: "±" is the upper and lower 95% confidence interval of the mean. PP, polypropylene; PUR, polyurethane; PVDF, polyvinylidene fluoride.

aerogel implied that the optimized polymer solution concentration effectively could improve the strength and the flexibility of the aerogels (Table 6). It may be due to electrospun nanofibers absorbing the destructive energy and keeping the integration of aerogel composite specimens. The second reason was that the diameters of the nanofibers were around 50 to 250 nm, which is much closer to the size of holes and particles of the aerogels. Moreover, as the

aerogels were electrospun with PUR and PVDF nanofibers, the aerogels were separated into large quantity of small areas as shown in Figures 1 and 2.

3.2 | Influence of aerogel on thermal properties

Thermal conductivity as a function of areal density for PUR and PVDF electrospun nanofibrous layer embedded with silica aerogel is shown

TABLE 6 Laboratory equipment setup for production of polyvinylidene fluoride nanofibrous layer embedded with aerogel

Samples	Substrate Speed (mm/min)	Humidity (%)	Air Temperature (°C)	Size of the Girder (mm)
PVDF1	30	42.3	24.2°C	ø0.7
PVDF2	15	47	24.1°C	ø0.7
PVDF3	30	43.5	24.3°C	ø0.7
PVDF4	15	44.5	24.3°C	ø0.7
PVDF5	30	41.5	24.3°C	ø0.7
PVDF6	15	38.5	24.4°C	ø 1.2

in Figure 3. The results showed that thermal conductivity of the electrospun nanofibrous layer decreased with increase in density. This can be explained by the fact that as the density increases, it makes the fibrous structure more packed. This causes the mean free path (distance travelled by a photon before it collides with another fiber surface²¹⁻²³) for a photon movement to decrease and thus causing a decrease in the heat transfer because of radiative conduction. When the density reaches a critical point, the increase in conduction through solid phase (fibers) and decrease in radiation conductivity result in an increase in total thermal conductivity.^{24,25} In fact, in fibrous structures, the small size of the pores and the complex nature of the air channels present prevent any heat transfer by convection.²⁶ Moreover, due to low fiber volume fraction in fibrous insulation materials, heat conduction through the solid phase (the fibers) is not significant and conduction through air is usually considered to be the conductivity of still air that is poor at room temperature. Thus, radiative conductivity is the prevalent mechanism of conductivity because it has a high porosity percentage of fibrous structures. By adding a nanofiber web, thermal conductivity was enhanced noticeably, which may be attributed to their extremely fine fiber and very high porosity of web. The superfine fibers in the web have better radiation absorption and extinction because their higher surface-area-to-volume ratio leads to decrease in the thermal conductivity. Moreover, smaller pore size between nanofibers decreases the mean free path for photon movement resulting in lower radiative energy transfer. This improvement becomes more significant when bulk density is increased. In high densities, increase in the thermal conductivity of the sample containing web was diminished. This may be attributed to the presence of nanofiber and their natural compact structure that could compensate for increased thermal conductivity. According to thermal conductivity graphs in Figure 3, decrease in the average nanofiber diameter leads to lower limit of conductivity. Higher specific surface of thinner fibers means more surface area for radiative absorption that result in lower thermal conductivity.²⁷

Furthermore, higher porosity of the web with a nanofiber diameter around 250 nm could be the other reason for their lowest thermal conductivity. The thermal insulating efficiency of fiber-based insulation is known to increase as the fiber size is reduced.¹ Another explanation for reduction in conductivity can be smaller pore size in the web containing thinner nanofibers leading to lower radiative conductivity. For better understanding of how reduction in fiber diameter affected porosity of the nanofibers, it is clearly shown in scanning electron microscopy images in Figures 1 and 2. In this context, it could be understood that using thinner nanofibers leads to noticeable

performance and helps in achieving very low limit of thermal conductivity. Of particular interest are the results for the 2 nanofiber insulation materials (electrospun PUR and PVDF nanofibrous layer). Both materials showed excellent reduction in overall heat transfer compared with standard low-density fibrous insulating materials (at areal densities above 40 g/m²).

The PVDF nanofibrous layer showed superior insulation at higher areal density values. Thermal conductivity testing confirmed that lower fiber diameter tends to increase the thermal resistance of fibrous insulation materials. However, the nanofiber/aerogel becomes an effective insulator because the aerogel structure suppresses conduction and convection, and the fibers reduce radiation heat transfer while increasing the strength of the brittle and weak aerogel structure. Although the combination of aerogel and nanofiber has good thermal properties, the volume fraction of fiber is fairly high to support and protect the aerogel matrix. Thus, the aerogel materials cannot achieve the same thermal conductivity at densities as fibrous insulation. However, they do achieve better thermal resistance for an equivalent thickness of material. High porosity of electrospun fibrous mesh is able to trap air which potentially gives it a good thermal insulation property. This is confirmed using thermal conductivity tests which show that lower fiber diameter leads to an increase in thermal resistance.²⁸ Thermal transfer in porous structure of silica aerogel is conducted in multiple pathways like (a) heat transfer through the chain of primary particles forming solid silica network, (b) thermal radiation, and (c) gaseous molecules occupying the gaps in the porous structure.^{29,30} The combination of nanofiber and aerogel has demonstrated superior insulation properties for applications where thickness is of concern. The large pores sizes in the samples often lead to large pore volumes porosity which lowered the thermal conductivity. With respect to high porosity fibrous insulation materials, the combination of aerogel and nanofiber demonstrated excellent insulation per unit thickness properties, as shown in Figure 4. Increase in thermal resistance can be seen to increase with the increase in thickness. The thermal resistance of electrospun PVDF nanofibrous layer embedded with silica aerogel is higher than electrospun PUR nanofibrous layer embedded with silica aerogel. The data were examined by one-way analysis of variance with 95% confidence level. A significant difference ($P < .05$) has been observed between the samples.

3.3 | Thermal stability of nanofibrous membranes

The nanofibrous membranes were analyzed by using DSC as shown in Figure 5. Large differences were observed in the melting

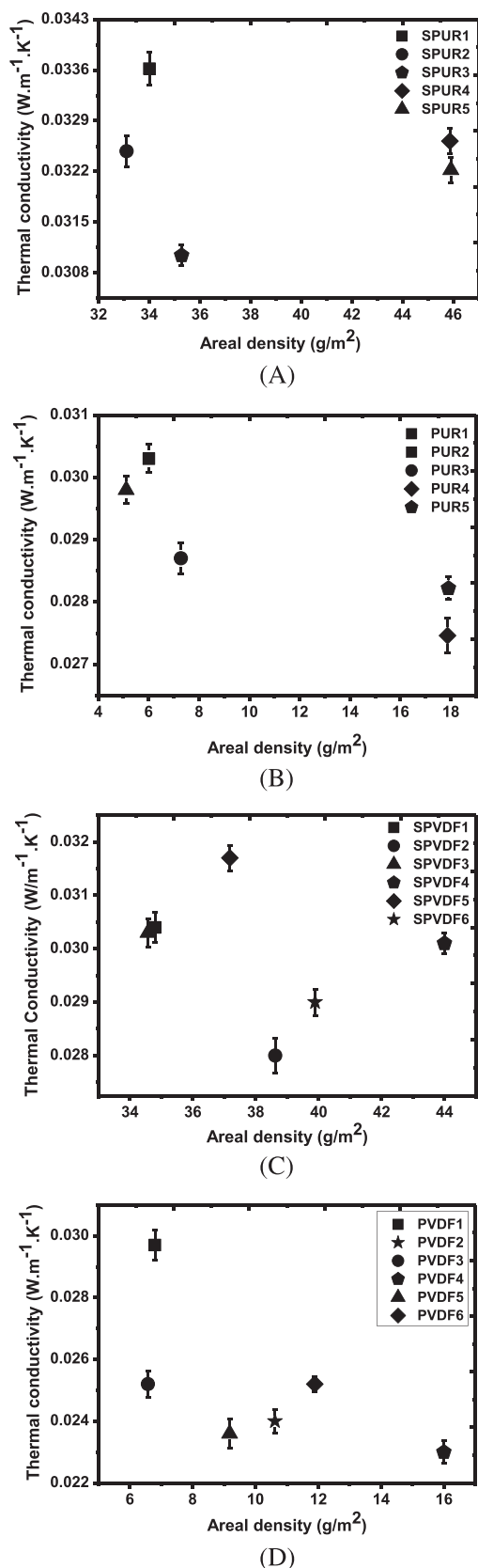


FIGURE 3 Thermal conductivity vs areal density A, polyurethane (PUR) samples with spunbond polypropylene; B, electrospun PUR nanofibrous membranes embedded with silica aerogel; C, electrospun polyvinylidene fluoride (PVDF) nanofibrous membranes embedded with silica aerogel backed up with spun bond polypropylene and D, electrospun PVDF nanofibrous membranes embedded with silica aerogel

endotherm values. A strong endothermic peak was produced at around 240°C and 170°C for PUR and PVDF nanofibrous membranes embedded with and without silica aerogel, which corresponded to oxidation of the surface hydroxyl groups and evaporation of trapped water and alcohol. Polyurethanes are segmented and can demonstrate different degrees of crystallinity according to the processing conditions.³¹ Furthermore, parametric variations in the electrospinning process (eg, applied voltage and infusion rate) can also alter the melting temperatures of fibers prepared from the solution.³² The level of crystallinity is increased when using the electrospinning process, going from film to fiber morphology, resulting in an increase in the T_m values.³³

Figure 6 shows the TGA of the pure SiO₂ aerogel. The weight loss was observed to decrease gradually from around 50 to 800°C. The percentage of weight loss was around for 17.9% for powder form silica aerogel and 21.8% for granular form silica aerogel, respectively. At around 450°C, there was rapid increase in weight loss of pure silica aerogel due to evaporation of trapped H₂O and alcoholic groups, produced from the condensation reactions of Si-OH and Si (OC₂H₅) groups. The TG curve declined slowly after 450°C. Around 600°C, the percentage of weight loss did not reduce because of the structural water evaporating completely. The observed adsorbed water mass losses indicate the ability of the aerogels to retain adsorbed water throughout processing and can result in increased degree of hydrophobicity when alkyl and aryl bridges are incorporated in their microstructures.²⁹

Figure 7 shows the electrospun PUR and PVDF nanofibrous membranes with and without SiO₂ aerogel. Table 7 contains the results of DSC and TGA results. The onset degradation temperature of the polymer chain for PVDF is around 400°C, and PUR is around 290°C. On the other hand, PUR nanofibrous membranes embedded with and without aerogel present considerable weight loss than PVDF nanofibrous membranes. Above 420°C, the weight loss was associated with the degradation of the polymer chain structure, in agreement with previous literature.^{34,35} The analysis shows that the blends in the compositions studied have a stability that is closest to the stability of PVDF, with an intensive weight loss onset at around 400°C.

The PUR and PVDF nanofibrous membranes embedded with aerogel demonstrated higher thermal stability at around 300 and 450°C, respectively. The pure aerogel lost around 10% weight at the temperature range of 350 to 450°C, which may be attributed to the degeneration of Si-O-C₂H₅ group.

Due to degeneration of PVDF, the electrospun PVDF layers showed significant weight loss in the temperature range of 400 to 450°C. The weight loss of the PUR nanofibrous membranes embedded with and without aerogel was between 90% and 95% at around 290°C, and PVDF nanofibrous membranes embedded with and without aerogel were between 5% and 17% at around 430°C, respectively. Therefore, the PVDF nanofibrous membranes showed better stability than PUR nanofibrous membranes. However, it should be noted that the PVDF nanofibrous membranes may melt at 172°C, although no noticeable weight loss exists. Therefore, the PVDF nanofibrous membranes are suitable for the application in thermal insulation below 172°C.

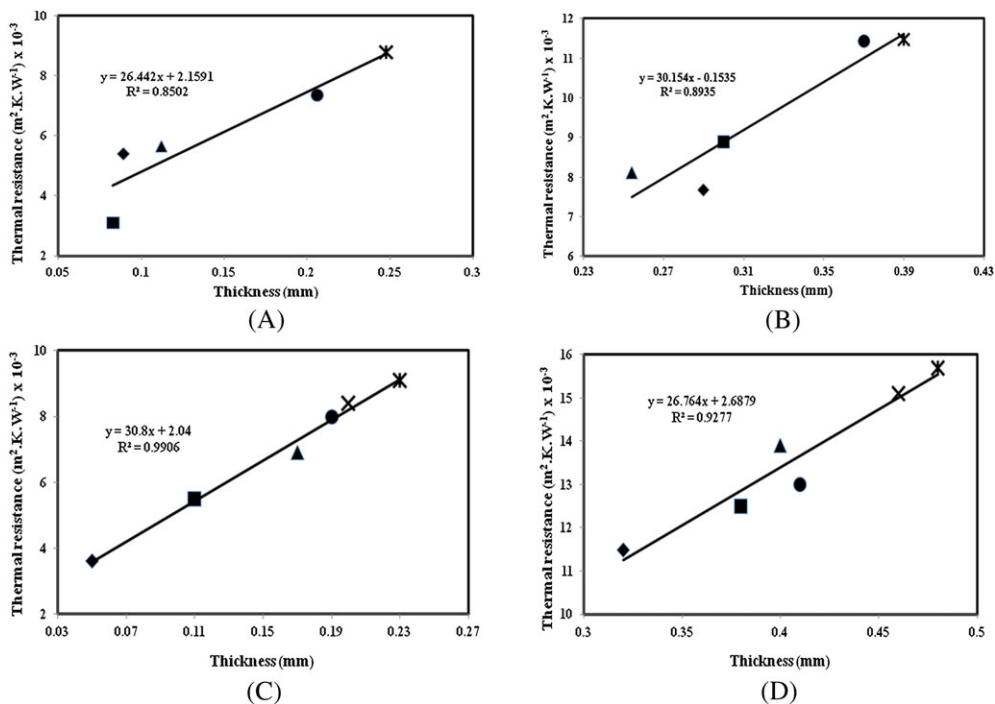


FIGURE 4 Thermal resistance vs thickness linear function A, electrospun polyurethane (PUR) nanofibrous membranes embedded with silica aerogel; B, electrospun PUR nanofibrous membranes embedded with silica aerogel backed up with spun bond polypropylene (PP) linear function; C, electrospun polyvinylidene fluoride (PVDF) nanofibrous membranes embedded with silica aerogel and D, electrospun PVDF nanofibrous membranes embedded with silica aerogel backed up with spun bond PP. [Colour figure can be viewed at wileyonlinelibrary.com]

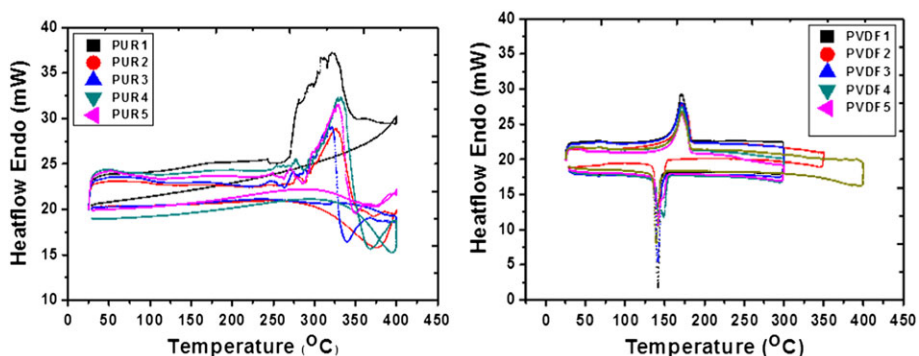


FIGURE 5 Differential scanning calorimetry curves of polyurethane and polyvinylidene fluoride nanofibrous membranes embedded with and without aerogel [Colour figure can be viewed at wileyonlinelibrary.com]

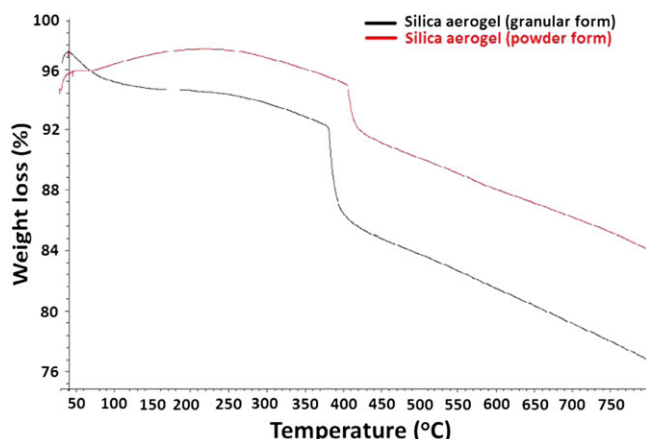


FIGURE 6 Thermogravimetric analysis curve of pure silica aerogel [Colour figure can be viewed at wileyonlinelibrary.com]

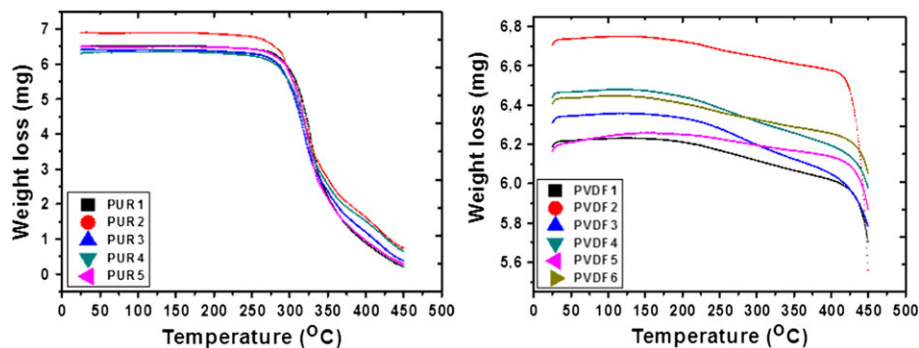


FIGURE 7 Thermogravimetric analysis curves of polyurethane and polyvinylidene fluoride nanofibrous membranes embedded with and without aerogel [Colour figure can be viewed at wileyonlinelibrary.com]

TABLE 7 Differential scanning calorimetry and thermogravimetric analysis results

Sample	Melting Temperature (°C)	Degradation Temperature (°C)	Weight Loss (%)
PUR1	242.6	293.6	96.80
PUR2	252.3	285.7	89.21
PUR3	245.7	287.3	94.04
PUR4	243.4	282.8	89.53
PUR5	247.1	292.9	95.49
PVDF1	170.9	424.9	7.80
PVDF2	172.1	422.1	17.10
PVDF3	171.8	405.7	8.36
PVDF4	171.3	435.3	7.14
PVDF5	171.3	432.7	4.82
PVDF6	172.2	435.7	5.50

3.4 | Transport properties of nanofibrous membranes

The air permeability of nanofibrous membranes is presented in Figure 8.

Air permeability is a very important parameter for thermal insulation of electrospun nanofibrous layer. The influencing factors

are gas, vapor, and liquid transport through the layers.³⁶ The air permeability of electrospun nanofibrous membranes is shown in Figure 6. According to the figures, samples containing PUR nanofiber with double layer (0.16 and 0.24 mm) showed lower air permeability. This behavior may be attributed to the finer diameter of PUR nanofiber compared with PVDF nanofiber. Lower air permeability implies reduced air flow through the layers resulting in better thermal insulation.

As can be seen from the figures, lower air permeability was achieved by increasing the number of nanofibrous membranes. It confirmed the relationship of the important parameter to thermal insulation. Figure 6 shows that sample PUR4, PUR5, and PVDF5 were impermeable at 100 and 200 Pa. The increased weight as well as thickness of electrospun nanofiber web reduced air permeability.³² The PUR samples had low air permeability as compared with PVDF samples. This may be attributed to fiber diameter and web porosity of the samples. Thus, the results of air permeability test show that the relation between thickness and air permeability of nanofibrous membranes is not linear (Figure 8) but equivalent.³⁷ From the results, it was also apparent that increase in duration of electrospinning leads to higher web thickness. This resulted in considerable decrease in air permeability. For other samples, the decrease was lower but statistically significant.

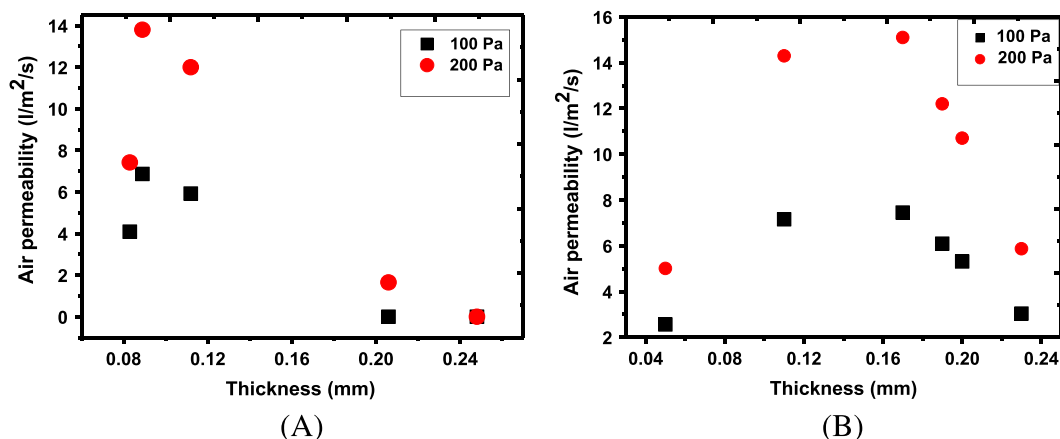


FIGURE 8 Air permeability A, electrospun polyurethane nanofibrous layer embedded with silica aerogel; B, electrospun polyvinylidene fluoride nanofibrous layer embedded with silica aerogel [Colour figure can be viewed at wileyonlinelibrary.com]

4 | CONCLUSION

In this work, the thermal behavior of electrospun PUR and PVDF nanofibrous membranes embedded with silica aerogel was studied. The results show enhancement in thermal insulation by increasing the number and the weight per unit area of nanofibrous membranes. Higher thermal resistance was observed in the case of samples containing PUR and PVDF nanofibrous membranes, which may be attributed to the low air permeability and fiber diameter. Moreover, embedding silica aerogel in nanofibrous membranes enhances thermal insulation confirming superior thermal properties of aerogel. The weight and thickness of thermal wear can be reduced by using nanofiber layers. Thermal behavior investigated by using TGA and DSC showed the PVDF nanofibrous membranes embedded with aerogel exhibits better thermal stability with low weight loss as compared with PUR nanofibrous membranes (Table 7). It was also observed that glass transition and melting point were not affected by the aerogel content in the layers. The results show nanofibers to be useful as components in hybrid battings with high bulk densities. The increase in duration of electrospinning leads to higher web thickness, which results in considerable decrease in air permeability. Performance gains in existing thermal insulation materials may be possible by incorporating a proportion of nanofibers into the structure. The electrospun nanofibrous membranes have been found to strengthen the aerogel, the preparation technique of the electrospun nanofibrous membranes embedded with aerogel with larger size, and lower thermal conductivity has to be further developed. Overall, the elucidation of the relation between transport properties and macrostructures of electrospun nanofibrous membrane will help to design highly comfortable protective garments.

ACKNOWLEDGEMENT

This work was supported by the Ministry of Education, Youth and Sports of the Czech Republic and the European Union, European Structural and Investment Funds in the frames of Operational Programme Research, Development and Education, project Hybrid Materials for Hierarchical Structures (HyHi, Reg. No. CZ.02.1.01/0.0/0.0/16_019/0000843), "Design, optimization and application of smart heat-insulating nano-layers" (LTACH-17014, 18301), and project no. TJ01000292, 14014/136.

ORCID

Mohanapriya Venkataraman  <http://orcid.org/0000-0002-8977-1244>

REFERENCES

- Gibson PW, Lee C, Koi F, Darrell R. Application of nanofiber technology to nonwoven thermal insulation. *J Eng Fib Fabr.* 2007;2(2):32-40.
- Greiner A, Wendorff JH. Electrospinning: a fascinating method for the preparation of ultrathin fibers. *Ang Chem.* 2007;46(30):5670-5703.
- Li D, Mc Cann JT, Xia Y, Marquez M. Electrospinning: a simple and versatile technique for producing ceramic nanofibers and nanotubes. *J Am Ceram Soc.* 2006;89(6):1861-1869.
- Reneker DH, Yarin AL. Electrospinning jets and polymer nanofibers. *Polymer.* 2008;49(10):2387-2425.
- Fricke J, Tillotson T. Aerogels: production, characterization, and applications. *Thin Sol Fil.* 1997;297(1-2):212-223.
- Pierre AC. In: Aegerter MA, ed. *History of Aerogels, Aerogels Handbook.* London, UK: Springer; 2011:3-20.
- Baetens R, Jelle BP, Gustavsen A. Aerogel insulation for building applications: a state-of-the-art review. *Energy Buildings.* 2011;43(4):761-769.
- Schultz JM, Jensen KI, Kristiansen FH. Super insulating aerogel glazing. *Sol Energy Mat Sol C.* 2005;89(2):275-285.
- Smith DM, Maskara A, Boes U. Aerogel-based thermal insulation. *J Non-Cryst Sol.* 1998;225(1-3):254-259.
- Wu H, Chen Y, Chen Q, Ding Y, Zhou X, Gao H. Synthesis of flexible aerogel composites reinforced with electrospun nanofibers and micro-particles for thermal insulation. *J Nanomater.* 2013;8:1-8.
- Venkataraman M, Mishra R, Wiener J, Militky J, Kotresh TM, Vaclavik M. Novel techniques to analyse thermal performance of aerogel-treated blankets under extreme temperatures. *J Text I.* 2014;106(7):736-747.
- Venkataraman M, Mishra R, Venkataraman S, Arumugam G, Kotresh TM, Militky J. Dynamic heat flux measurement for advanced insulation materials. *Fiber Polym.* 2016;17(6):925-931.
- Lee SM, Kimura D, Lee KH, Park JC, Kim IS. The effect of laundering on the thermal and water transfer properties of mass-produced laminated nanofiber web for use in wear. *Textile Res J.* 2010;80:99-105.
- Curcio E, Drioli E. Membrane distillation and related operations: a review. *Separation and Purification Reviews.* 2005;34(1):35-86.
- Kumar A, Ryparovà P, Petrič M, Tywoniak J, Hajek P. Coating of wood by means of electrospun nanofibers based on PVA/SiO₂ and its hydrophobization with octadecyltrichlorosilane (OTS). *Holzforschung.* 2016;71(3):225-231.
- Deitzel JM, Kosik W, McKnight SH, Beck Tan NC, DeSimone JM, Crette S. Electrospinning of polymer nanofibers with specific surface chemistry. *Polymer.* 2001;43(3):1025-1029.
- Nirmala R, Navamathavan R, El-Newehy MH, Kim HY. Preparation and electrical characterization of polyamide-6/chitosan composite nanofibers via electrospinning. *Mater Lett.* 2011;65(3):493-496.
- Pedicini A, Farris RJ. Thermally induced color change in electrospun fiber mats. *J Polym Sci Part B.* 2004;42(5):752-757.
- Zhang S, Shim WS, Kim J. Design of ultra-fine nonwovens via electrospinning of nylon 6: spinning parameters and filtration efficiency. *Mater Design.* 2009;30(9):3659-3666.
- Rozeck Z, Kaczorowski W, Luk D, Louda P, Mitura S. Potential applications of nanofiber textile covered by carbon coatings. *J Archiv Mater Manufact Engg.* 2008;27(1):35-38.
- Venkataraman M, Mishra R, Wiener J, Kotresh TM, Tomonori S, Militky J. Effect of compressibility on heat transport phenomena in aerogel-treated nonwoven fabrics. *J Text I.* 2016;107(9):1150-1158.
- Li Y, Holcombe BV. Mathematical simulation of heat and moisture transfer in a human-clothing-environment system. *Text Res J.* 1998;68(6):389-397.
- Venkataraman M, Mishra R, Militky J, Hes L. Aerogel based nanoporous fibrous materials for thermal insulation. *Fiber Polym.* 2014;15(7):1444-1449.
- Fohr JP, Couton D, Treguiet G. Dynamic heat and water transfer through layered fabrics. *Text Res J.* 2002;72(1):1-12.
- Sukigara S, Yokura H, Fujimoto T. Compression and thermal properties of recycled Fiber assemblies made from industrial waste of sweater products. *Text Res J.* 2003;73(4):310-315.
- Reim M, Korner W, Manara J, et al. Silica aerogel granulate material for thermal insulation and daylighting. *Sol Energy.* 2005;79(2):131-139.
- Venkataraman M, Mishra R, Jasikova D, Kotresh TM, Militky J. Thermodynamics of aerogel-treated nonwoven fabrics at subzero temperature. *J Ind Text.* 2015;45(3):384-404.
- Frydrych I, Dziworska G, Bilka J. Comparative analysis of the thermal insulation properties of fabrics made of natural and man-made cellulose fibers. *Fibres Text East Eur.* 2002;10(4):1-10.

29. Maleki H, Durães L, Portugal A. Synthesis of lightweight polymer-reinforced silica aerogels with improved mechanical and thermal insulation properties for space applications. *Micropor Mesopor Mater.* 2014;197:116-129.
30. Venkataraman M, Mishra R, Militky J, Behera BK. Modelling and simulation of heat transfer by convection in aerogel treated nonwovens. *J Text I.* 2017;108(8):1442-1453.
31. Pompe G, Pohlers A, Potschke P, Pionteck J. Influence of processing conditions on the multiphase structure of segmented polyurethane. *Polymer.* 1998;39(21):5147-5153.
32. Zhuo H, Hu J, Chen S, Yeung L. Preparation of polyurethane nanofibers by electrospinning. *J Appl Polym Sci.* 2008;109(1):406-411.
33. Kaursoin J, Agrawal A. Melt spun thermoresponsive shape memory fibers based on polyurethanes: effect of drawing and heat-setting on fiber morphology and properties. *J Appl Pol Sci.* 2007;103(4):2172-2182.
34. Conklin JA, Huang SC, Huang SM, Wen T, Kaner RB. Thermal properties of polyaniline and poly (aniline-co-o-ethylaniline). *Macromolecules.* 1995;28(19):6522-6527.
35. Li W, Wan M. Stability of polyaniline synthesized by a doping-dedoping-redoping method. *J Appl Polym Sci.* 1999;71(4):615-621.
36. George SC, Thomas S. Transport phenomena through polymeric systems. *Prog Polym Sci.* 2001;26(6):985-1017.
37. Gorji M, Jeddi A, Gharehaghaji AA. Fabrication and characterization of polyurethane electrospun nanofiber membranes for protective clothing applications. *J Appl Polym Sci.* 2012;125(5):4135-4141.

SUPPORTING INFORMATION

Additional supporting information may be found online in the Supporting Information section at the end of the article.

How to cite this article: Venkataraman M, Mishra R, Militky J, et al. Electrospun nanofibrous membranes embedded with aerogel for advanced thermal and transport properties. *Polym Adv Technol.* 2018;1-10. <https://doi.org/10.1002/pat.4369>

11.3 Publication 2: Preparation of Electrospayed, Microporous Particle Filled Layers

Publication

Venkataraman, M., Yang, K., Xiong, X., Militky J. et al. Preparation of Electrospayed, Microporous Particle Filled Layers. *Polymers*. 2020; 12(6):1352. DOI:10.3390/polym12061352#.

Author contribution

- Conceptualization
 - Devised the project, the main conceptual ideas and proof outline.
- Methodology
 - Material selection and sample design for preparation
 - Conceived and planned experimental techniques.
- Formal Analysis, Investigation & Data curation
 - Characterize the samples and conduct the experiments.
 - Processed the experimental data.
 - Performed the statistical analysis by using QC expert software tools.
- Software & Validation
 - Performed the statistical analysis by using software tools.
 - Verification of the overall reproducibility of results and other research outputs.
- Writing the manuscript
 - Original Draft Preparation, review & editing with input from all authors.
- Visualization
 - Preparation, creation and presentation of the published work, specifically visualization/data presentation

Article

Preparation of Electrosprayed, Microporous Particle Filled Layers

Mohanapriya Venkataraman ^{1,*}, Kai Yang ¹, Xiaoman Xiong ¹, Jiri Militky ¹, Dana Kremenakova ¹, Guocheng Zhu ², Juming Yao ², Yan Wang ² and Guoqing Zhang ²

¹ Department of Material Engineering, Faculty of Textile Engineering, Technical University of Liberec, Studentska 2, 46117 Liberec, Czech Republic; kai.yang@tul.cz (K.Y.); Xiaoman.xiong@tul.cz (X.X.); jiri.militky@tul.cz (J.M.); dana.kremenakova@tul.cz (D.K.)

² School of Material Science and Engineering, Zhejiang Sci-Tech University, Xiasha Higher Education Zone, Hangzhou 310018, China; zgc100100@hotmail.com (G.Z.); yaoj@zstu.edu.cn (J.Y.); amywang1021@hotmail.com (Y.W.); zggq@zstu.edu.cn (G.Z.)

* Correspondence: mohanapriya.venkataraman@tul.cz

Received: 1 June 2020; Accepted: 11 June 2020; Published: 15 June 2020

Abstract: Polytetrafluoroethylene (PTFE) is a synthetic fluoropolymer known for its excellent hydrophobic properties. In this work, samples from PTFE dispersions with different combinations of water and carbon microparticles were prepared using an electrospraying method. The morphologies and sizes of carbon particles were investigated and the properties of layers including roughness, hydrophobicity and electrical resistivity were investigated. The non-conductive carbon microparticles were selected as a model particle to check the compatibility and electrospraying ability, and it had no effect on the hydrophobic and electrical properties. Carbon microparticles in polymer solution increased the degree of ionization and was found to be beneficial for the shape control of materials. The results showed that PTFE dispersion with the composition of water and carbon microparticles produced fine sphere particles and the layer fabricated with increased roughness. It was also found that the electrical resistivity and hydrophobicity of all the layers comparatively increased. The fabricated microporous layers can be used in various applications like interlining layer in multilayer textile sandwiches.

Keywords: PTFE; microporous; electrospraying; contact angle; hydrophobic; electrical resistivity

1. Introduction

Polytetrafluoroethylene (PTFE) is a synthetic fluoropolymer with repeated units $[(-CF_2-)_n]$, where the inner strongly bonded fluorine atoms make it a high molecular weight compound characterized with semi-crystalline nature, and a strong C-F bond prevents reaction between other chemicals and PTFE [1]. PTFE is known for its excellent hydrophobic, dielectric, mechanical and thermal properties [2]. It is widely used in films, coating materials and fibers in industry domains such as polymeric gears [3], cables [4], implants [5], textiles [6] and so on. Casting PTFE polymer in sphere or PTFE particles via common methods such as molding, emulsion [7], suspension polymerization [8], etc., is very difficult. This is due to the inhomogeneous particle fabrication and a restricted number of processable polymers that cannot be avoided technically. Precipitation [9], spraying drying [10] and supercritical fluid [11] processes are considered to be better options to produce particles. However, it is hard to generate monodisperse particles.

Electrospraying, otherwise called electro-hydrodynamic spraying or electro-hydrodynamic atomization or steady cone-jet mode, is known as a unique technology to produce novel materials including particles, films or coatings [12]. The fundamental mechanism is similar to electrospinning except for the final output. It is a well-established process based on the application of high electrical

voltage on the polymer solution of suitable surface tension and viscosity. In this process, the polymer liquid flows out from the capillary nozzle in the applied electric field and then forms a fine jet followed by atomization of polymer liquid into the fine droplets. The particles are collected on a grounded conductive substrate. The degree of ionization in polymer solution affects the shapes and diameters of final polymeric particles during electrospray, which is influenced by the components of the polymer solution. The hydrophobic behavior of the electrospray surface can result from the high surface roughness through reduction of the interfacial energy between solid and liquid [13]. However, a relationship between diameters of PTFE particles and components of PTFE solution will have an effect on sizes, shapes and other properties of PTFE particles produced by electrospraying.

Several research groups have proved that the surface energy of materials was closely related to the surface properties, especially surface roughness [14]. This is a novel way to control material surface wettability. Many theoretical research studies on electrospinning process have been conducted [15–17] which showed that distance between nozzle and collector affects morphology, structure, physical and chemical properties of electrospinning fibers and properties based on evaporation rate, deposition time and inconsistency interval. Literature review also revealed that recent research was focused on needle-based electrospraying [18].

The objective of this research was to prepare PTFE microporous layers via electrospraying method [19–21] and study its various properties. It would include a study to improve the particles of PTFE by adjusting its solution components and addition of non-conductive carbon microparticles. The relative properties of the prepared PTFE microporous layers including morphology, roughness, hydrophobicity and electrical resistivity were investigated. Addition of carbon microparticles in polymer solution was meant to study the increase in the degrees of ionization and find out if it is beneficial for the compatibility and shape control of materials during electrospinning. In future, it may be possible to add new functionalities via using of activated carbon, conductive carbon or surface coated carbon. The prepared layers can be used for various applications by optimizing the solution and also the spinning parameters.

2. Experimental

2.1. Materials

For this work, Teflon® PTFE 30 containing 60% wt. PTFE particles and 40% wt. water with surfactant (Chemours, Neu Isenburg, Germany) was used. Tetraethylammonium bromide (TEAB) (Sigma Aldrich, Prague, Czech Republic) was used as salt to increase the conductivity and viscosity of solutions in which the interactions among macromolecules are extensive. A polymer network becomes more solid. It leads to a higher spinning performance of a solution [22,23]. Non-conductive carbon microparticles were milled from pitch-based carbon fiber yarn. The milling process was carried out on a Fritsch pulverisette 7 planetary ball mill. The average size of the carbon microparticle was 1640 nm as shown in Figure 1. The PTFE dispersion was obtained after 24 h-stir of Teflon® PTFE 30 mixed with TEAB at room temperature. Non-conductive carbon microparticles were added in PTFE solution before electrospraying to functionalize the final PTFE layers. The details of the PTFE dispersion preparation are shown in Table 1.

Table 1. Description of PTFE Dispersion (%) Based on different Compositions.

Sample No.	PTFE	Carbon Microparticle	Water & Surfactant
S1	60	-	40
S2	60	0.04	≈40
S3	55	-	45
S4	55	0.04	≈45

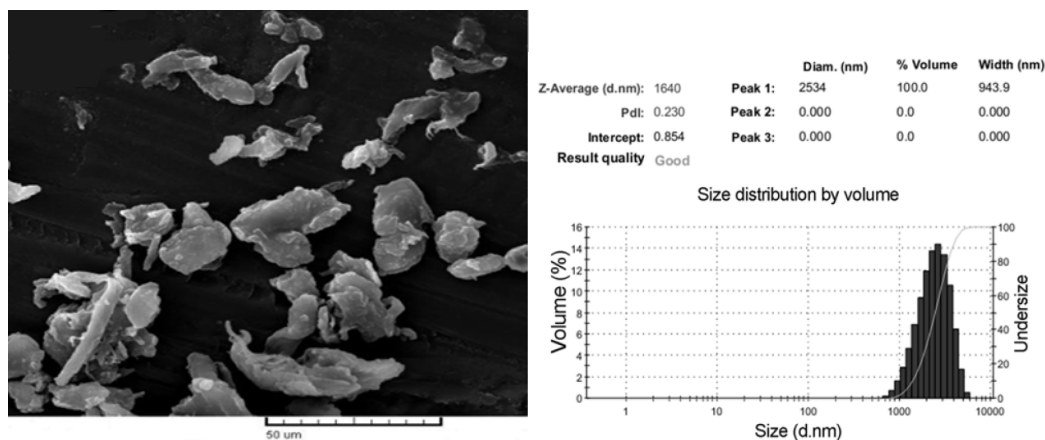


Figure 1. Morphology and size distribution of carbon microparticles.

2.2. Preparation of PTFE Microporous Layers

The Nanospider instrument (Figure 2) is a needleless electrospinning system that was used to prepare the PTFE layers by electrospaying method. Its parts include a high-voltage supplier, solution tank, rotating roller electrode, grounded collector and support material. During the electrospaying process, the electrostatic force produced between the high-voltage supplier and grounded collector draw the charged polymer solution into forms of particles which will be collected on the surface of support material. The electro-rotating cylinder keeps the electrospaying process ongoing to continuously produce the particles and the even layer of particles is obtained with coordination of the movement of support material.

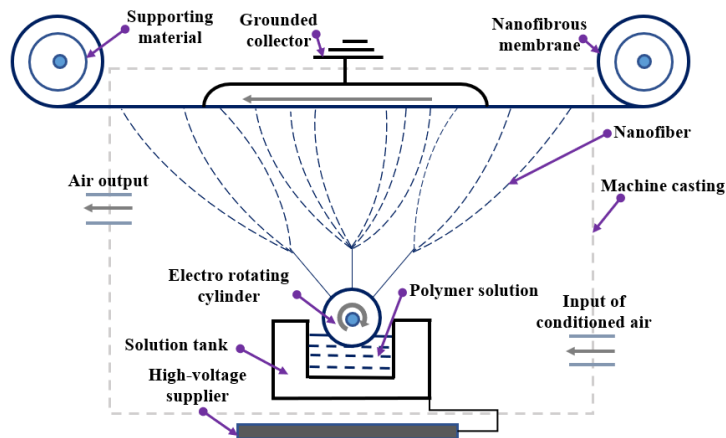


Figure 2. Schematic diagram of the electrospaying method (Nanospider).

The PTFE solution was first prepared to be used for electrospaying. As PTFE was insoluble in water, it was introduced in particle form in the water-based dispersion. During the electrospaying process, the PTFE dispersion was drawn to the form layer being collected on the surface of support materials. The particles and their layers are marked as P1, P2, P3 and P4 corresponding to PTFE dispersion S1, S2, S3 and S4. The spinning parameters, including substrate speed (mm/min), applied voltage of high-voltage supplier and grounded voltage (kV), speed of electrode (rev/min), the temperature of air (°C) and the relative humidity (%). The suitable parameters for producing PTFE layers were optimized and selected shown in Table 2. To achieve the optimized conditions, different combinations of solutions were prepared and trialed on Nanospider to set the spinning parameters. The adjusting of process parameters was necessary for the needleless electrospinning system of Nanospider for preparation of layers with tunable porosity.

Table 2. Spinning parameters.

Substrate Speed(mm/min)	Voltage (kV)	Speed of Electrode (rev/min)	In		Tent		Air	
			RH(%)	T(°C)	RH(%)	T(°C)	RH(%)	T(°C)
Static	10/30	5.0	42	22.3	46.8	22.8	49.9	22.4

2.3. Characterization of PTFE Microporous Layers

2.3.1. Morphologies

To observe the attachment of the PTFE microporous layer to the surface of support materials, scanning electron microscope (SEM), VEGA TESCAN Inc., Lincoln, NE, USA, was used. The HORIBA laser scattering particle size distribution analyzer LA-920 was used to analyze the size distribution of PTFE particles produced by various PTFE solutions as described in Table 1. The refractive index was set as 1.6. Mean size and S.D. size were calculated as well.

2.3.2. Roughness of PTFE Microporous Layers

The roughness of PTFE layers was tested using the OLS5000 LEXT measuring laser microscope. During the test, every ten different lines of the scanned PTFE layers were recorded and then calculated automatically into the main roughness parameters including arithmetic average height (R_a), root mean square roughness (R_q), skewness (R_{sk}) and kurtosis (R_{ku}), as seen in Figure 2. The R_a , known as the central line average (CLA), is the most universal parameter for general roughness control given by Equation (1). R_q is the parameter describing the standard deviation of the distribution of surface heights and is given by Equation (2). R_q , R_{sk} and R_{ku} are separately obtained by Equations (3) and (4). R_{sk} is used to measure the symmetry of profile about the mean line and is very sensitive to peak or valley height. The point is that R_{sk} will be positive if the profile has more high peaks or flat valleys and, oppositely, the profile with few peaks gives negative R_{sk} values, contributing to distinguishing the different profiles with the same R_a and R_q . R_{ku} describes the sharpness of the probability density of the profile. If $R_{ku} < 3$, the profile will have relatively few high peaks and low valleys and, oppositely, the profile will have relatively more high peaks and low valleys with $R_{ku} > 3$.

$$R_a = \frac{1}{l_r} \int_0^{l_r} |Z(x)| dx \quad (1)$$

$$R_q = \sqrt{\frac{1}{l_r} \int_0^{l_r} Z^2(x) dx} \quad (2)$$

$$R_{sk} = \frac{1}{R_q^3} \left(\frac{1}{l_r} \int_0^{l_r} Z^3(x) dx \right) \quad (3)$$

$$R_{ku} = \frac{1}{R_q^4} \left(\frac{1}{l_r} \int_0^{l_r} Z^4(x) dx \right) \quad (4)$$

where x is the direction of calculation, l_r is the reference length along x direction and $Z(x)$ is the height at x position.

2.3.3. Contact Angle Analysis

A See System E instrument is a portable computer-based instrument to measure the contact angle with a special purpose software following ISO 27448:2009 test method. Before measuring, the samples were washed for 6 mins in distilled water to remove the salts and were dried at room temperature. Deionized water was dropped onto each PTFE layer from a needle on a microsyringe (5 μ L) and a picture of the drop was taken. The contact angles could be calculated by analyzing the shape of the drop, which is displayed in the PC. In total, 10 drops were measured for each sample. Two minutes were allowed from the time of water drop until the measurement of the contact angle.

2.4.4. Electrical Resistance

Electrical resistance measurement was done on a 4339B High resistance meter (Hewlett Packard ohmmeter) measuring device shown in Figure 3. Calibration of the instrument (high resistance meter) is done using a standard plate of known electrical resistivity. The electrical surface and volume resistivity of the samples produced were measured according to the standard ASTM D257-07(2007) at the voltage of 100 V, at a temperature of 22.3 °C, and at a relative humidity (RH) of 40.7%. The measurement results were recorded 60 s after the electrodes were placed on the textile samples. The volume resistivity was measured by applying a voltage potential across opposite sides of the sample and measuring the resultant current through the sample. Volume resistivity was calculated from the following Equation (5):

$$\rho_v = R_v \frac{S}{t} \quad (5)$$

where $R_v(\Omega)$ is volume resistivity reading, t is thickness of the fabric (mm), and S is the surface area of the electrodes (mm^2).

Surface resistivity is measured by applying a voltage potential between two electrodes of specified configuration that are in contact with the same side of a material under test (Figure 4). Surface resistivity $\rho_s(\Omega)$ was calculated from Equation (6):

$$\rho_s = R_s \frac{2\pi}{\ln \frac{R_2}{R_1}} \quad (6)$$

where $R_s(\Omega)$ is the surface resistance reading, R_1 is the outer radius of the center electrode (mm), and R_2 is the inner radius of the outer ring electrode (mm), where $R_1 = 58 \text{ mm}$ and $R_2 = 51 \text{ mm}$.

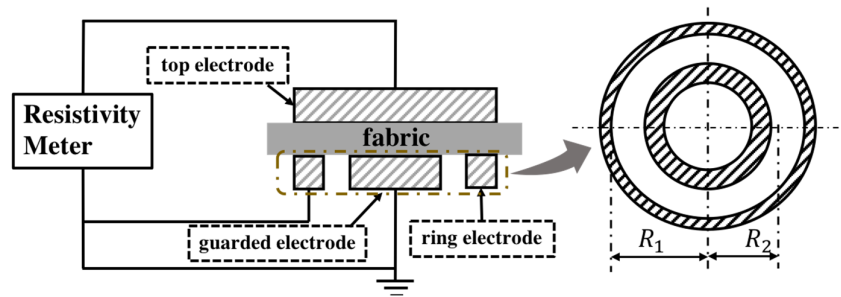


Figure 3. Schematic diagram of an experimental setup to measure electrical resistance.

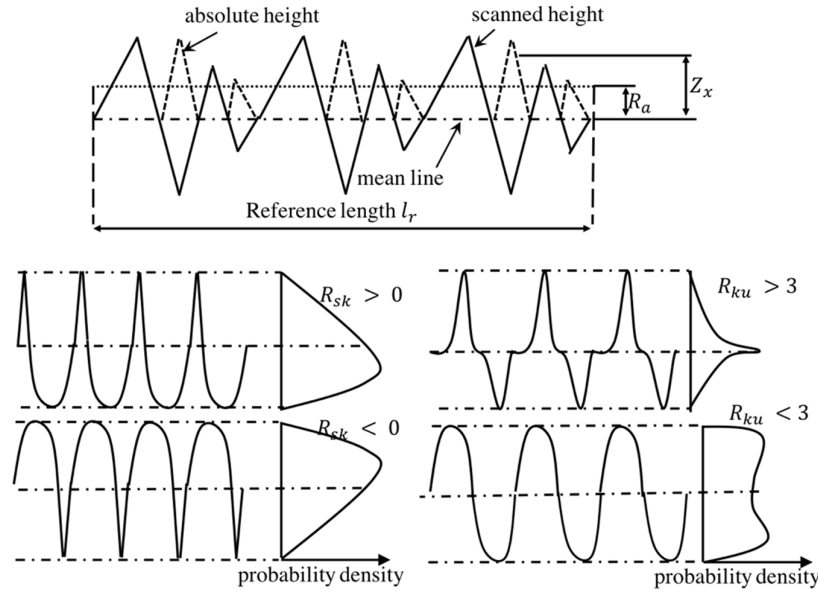
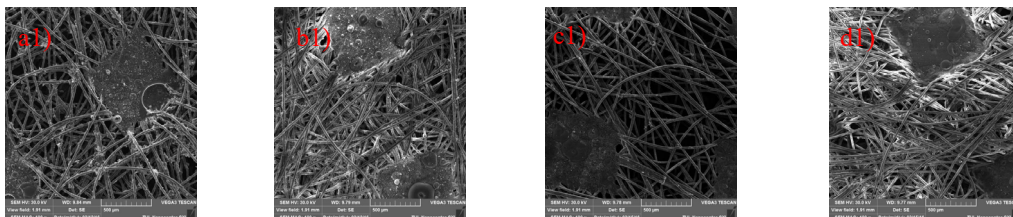


Figure 4. Description of roughness parameters.

3. Results and Discussions

3.1. Morphology of Microporous Layers

The particles on the surface of the substrate were observed in Figure 5 and their size distribution is shown in Figure 6. The layers produced from all combinations of PTFE solution ranges from 0.1–10 μm which proves that the particles are in the range of microns. Figures 5a2, c2 and 6 a, c show the PTFE microporous layers, where the final PTFE product appears in the form of a sphere and has larger sizes when there is more H_2O in PTFE aqueous solution. In Figure 5b2, all the layers appear in the form of a sphere as well, which possibly resulted from the carbon microparticles in PTFE polymers. In Figure 5d2, the particles are almost spherical, but the diameters tend to decrease when compared with Figure 5b2, which can also be proved by comparing Figure 6b or Figure 6d, suggesting that PTFE dispersion with carbon microparticles and higher water content has the ability to produce fine layers via electrospinning method, which is due to the change of viscosity and surface tension of the solution [24–27]. Also, the presence of surfactant in the PTFE emulsion attributes to the change in fiber diameter. The formation of finer fibers is facilitated by the presence of surfactant in the solution which increased the conductivity of the solution and decreased the surface tension [28]. The morphology of the microporous membrane depends, on the temperature, solvent, voltage, physical properties of liquid phase, distance of collector, doping agents and the time of solvent evaporation. The fibers tend to form beadlike structures when the concentration of the polymer solution is lower [29,30].



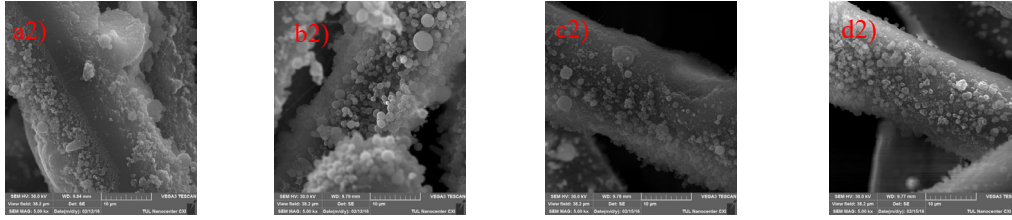


Figure 5. Scanning electron microscope images of PTFE layers (P1: a1,a2; P2: b1,b2; P3: c1,c2; and P4: d1,d2).

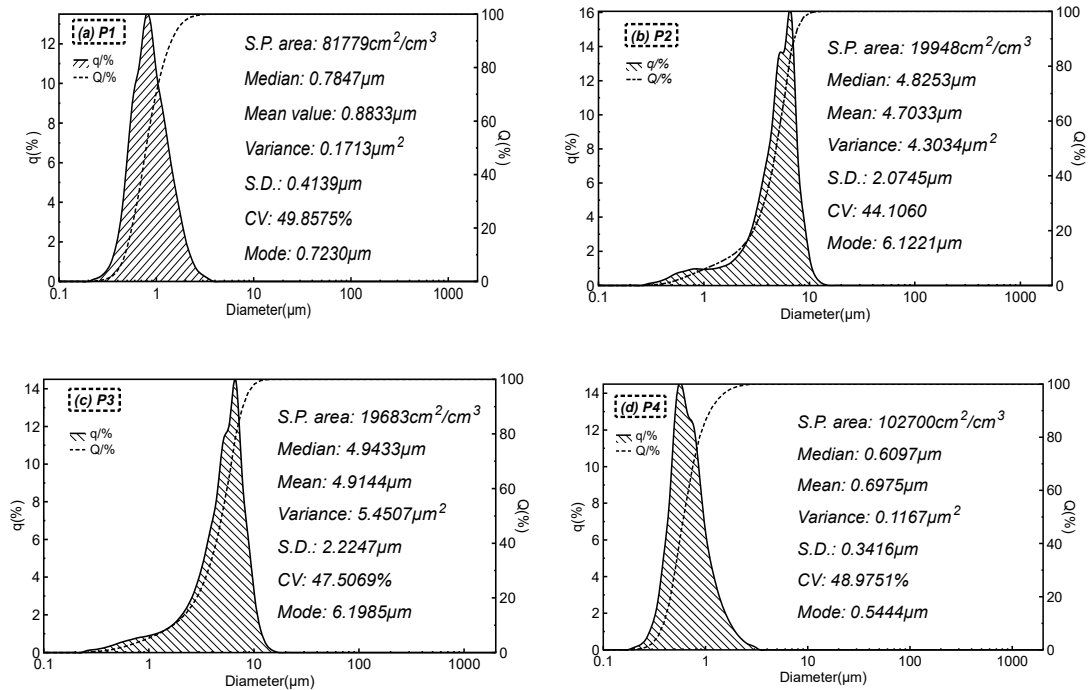


Figure 6. Size distribution of particles (q: density distribution of the particle size; Q: cumulative distribution of the particle size). (a) P1; (b) P2; (c) P3; and (d) P4

3.2. Roughness of PTFE Microporous Layers

Exact distribution of the PTFE layer on the surface of support materials is explained by roughness. Table 3 shows the key parameters of roughness of the PTFE layer, and the 3D morphology of the PTFE microporous layer is shown in Figure 6. PTFE layers P1 and P3, which were separately produced by the S1 and S3 solutions, have the similar surface roughness parameters, shown in Table 3, and the 3D morphologies of the P1 and P3 layers are almost the same as those seen in Figure 7a,c. The R_a mean values are much smaller than others, suggesting that the PTFE layer does not have a rough surface compared with the P2 and P4 layers, which may possibly result in a smoother particle shape. However, the P3 layers have R_{ku} values which are smaller than 3, and partial P3 layers have R_{ku} values which are bigger than 3, suggesting that its surface roughness has two kinds of characters. For P2 layers, the R_a mean value increases when compared with P1 and P3 layers, which is caused by carbon microparticles in the PTFE polymer, and Figure 7b proves it well. However, all the surface roughness parameters of the P2 layers have no essential difference from the P1 and P3 PTFE layers, and the R_{sk} is negative and all the R_{ku} values are bigger than 3. The R_a mean value of the P4 layers increases a lot and reaches $14.617 \mu\text{m}$, meaning that it has the largest surface roughness. The P4 layers have a positive R_{sk} mean value and an R_{ku} mean value which is smaller than 3, suggesting that the

P4 layer surface is totally different from that of the other three particle layers. Figure 7d shows that the P4 layer tends to be sunken and its surface is even. As described in Section 3.1, with PTFE dispersed in water and with the addition of the right amount of water, the viscosity and the surface tension were adjusted, which in turn led to more evenness of the layers.

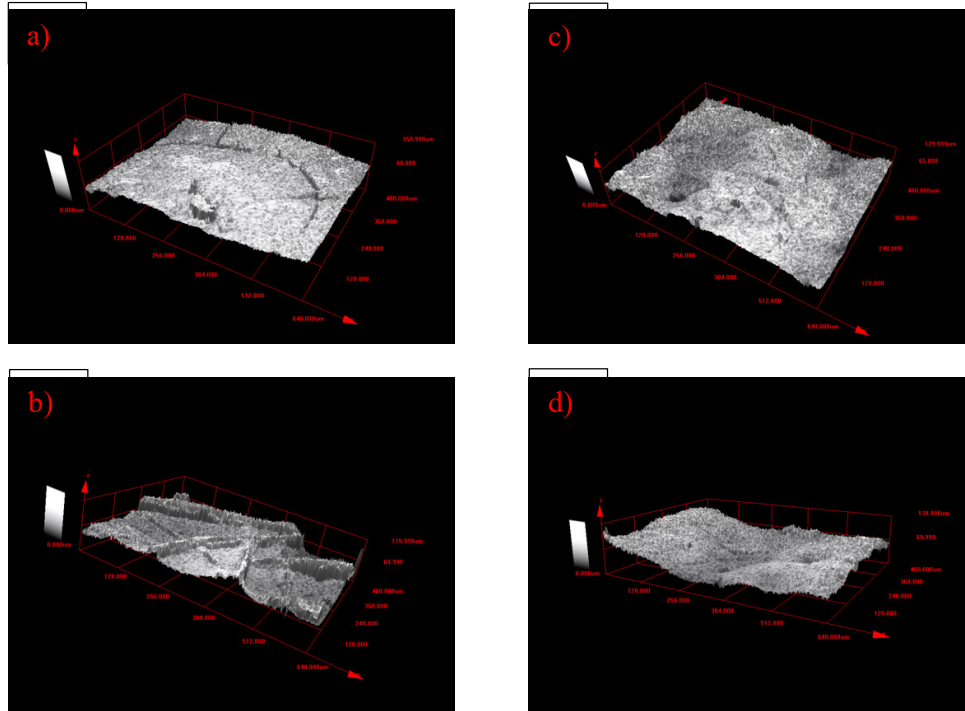


Figure 7. 3D morphology of the PTFE microporous layer (a) P1; (b) P2; (c) P3; and (d) P4).

Table 3. Roughness of PTFE microporous layers.

No.	$R_a(\mu\text{m})$	$R_q(\mu\text{m})$	$R_{sk}(\mu\text{m})$	$R_{ku}(\mu\text{m})$
P1	6.817 ± 2.700	8.679 ± 3.071	-0.213 ± 0.898	4.038 ± 0.995
P2	7.715 ± 1.212	9.820 ± 1.240	-0.9218 ± 0.233	4.108 ± 0.973
P3	6.690 ± 2.122	8.207 ± 2.479	-0.577 ± 0.285	3.154 ± 1.021
P4	14.617 ± 2.453	17.032 ± 2.495	0.074 ± 0.282	1.989 ± 0.289

3.3. Influence on Hydrophobicity

The results of the static contact angle measurements are shown in Figure 8 and the digital images of contact angle measurement is shown in Figure 9. The contact angles are over 90° , which proves that all of the particle layers are hydrophobic. The P1 and P2 layers have a close mean value of contact angles, which may be caused by the similarly low R_a and R_{ku} values. The P3 and P4 layers have a close higher contact angle. The P4 layer has a contact angle of about 140° . This is because of its high R_a , given its high contact angle, and R_{ku} values smaller than 3 improve the uniformity of its surface roughness. The surface roughness of the P3 layer explained in Section 3.2 is complex because the P3 layer has R_{ku} values which are bigger than 3 and other parts have R_{ku} values that are smaller than 3. This complex surface roughness of P3 may lead to higher contact angles than those of P4, but the difference is small. As explained in Section 3.2, the adjusted surface tension, evenness and surface roughness of the electrosprayed layer attributes to the hydrophobicity. As seen in Figure 8, samples P3 and P4 showed improved hydrophobicity. Changes in contact angle after 6 minutes of washing (see Figure 8) is probably due to time-dependent partial removal of a water-soluble component other than PTFE which was part of the original PTFE dispersion.

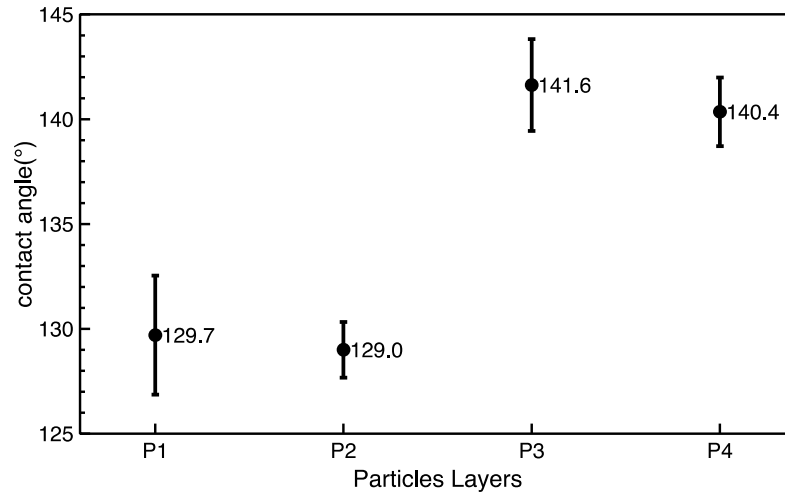


Figure 8. Contact angles after 6 minutes of washing of as-prepared PTFE layers.

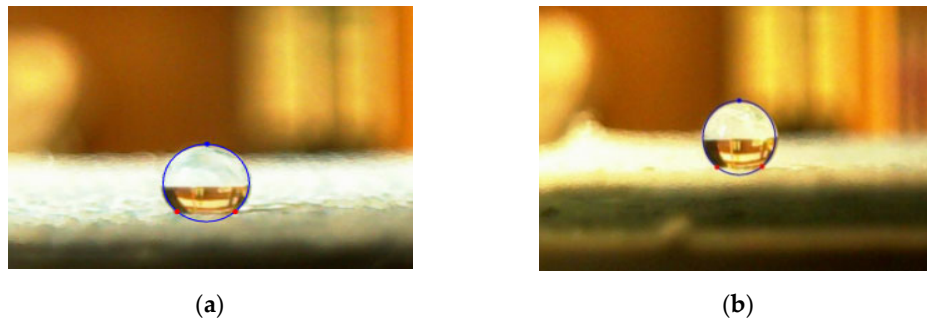


Figure 9. Images of the contact angle measurement: (a) 135.3°; (b) 142.3°.

Stability test under washing in standard conditions was conducted for the PTFE layers. It was found that the morphology of layers was the same.

3.4. Influence of Electrical Property on Microporous Layers

The thickness and final electrical resistivity values of microporous layers are shown in Table 4. The surface resistivity and volume resistivity of all the layers range in $10^9 \Omega$, which means that all of the layers belong to the antistatic body. From the definition of R_{sk} , the R_{sk} is the key parameter suggesting the distribution of the continuous layers of materials. The relationship between R_{sk} and resistivity is shown in Figure 10. Surface resistivity slightly decreases with increasing R_{sk} , which means that the uniform layers of PTFE increase slightly to improve the movement of electric charges during the resistivity tests. Similarly, the uniform layers of materials also account for volume resistivity, and the volume resistivity values tend to decrease with increasing R_{sk} values. Besides, no clear relationships between contents of carbon microparticles and electrical properties can be found due to the non-conductive property of the carbon microparticles.

Table 4. Resistivity values of PTFE layers.

No.	Surface Resistivity(Ω) $\times 10^9$	Volume Resistivity(Ωcm) $\times 10^9$	t(mm)
P1	2.6924 ± 0.3692	4.2960 ± 0.3901	0.34
P2	3.7044 ± 0.8918	8.3430 ± 0.9417	0.28
P3	3.4196 ± 0.5939	7.6942 ± 0.5509	0.26
P4	2.1392 ± 0.0642	4.8132 ± 0.2878	0.31

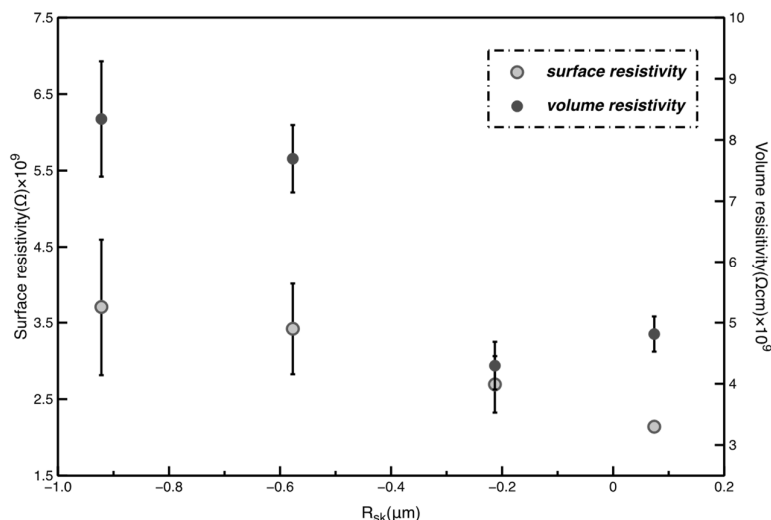


Figure 10. Relationship between resistivity and R_{sk} .

4. Conclusions

Electrosprayed layers were fabricated from optimized concentration of the solution via electro spraying using the Nanospider instrument. PTFE particles containing carbon microparticles appear in the form of spheres and tend to be smaller with dilution of the PTFE solution. Compared to carbon microparticles added in the PTFE solution, the water content had a greater effect on the surface roughness. An increase of the contact angles of the layers was observed. Surface resistivity and volume resistivity values ranging in $10^9 \Omega$ were obtained, suggesting that the particle layers were antistatic. Non-conductive carbon microparticles have no significant influence on electrical properties of the layers. However, adding carbon microparticles in polymer solution increased the degrees of ionization and was found to be beneficial for the shape control of materials during electro spraying. By optimizing conditions, more hydrophobic layers can also be achieved.

Author Contributions: Conceptualization, M.V.; methodology, M.V.; validation, M.V., K.Y. and X.X.; formal analysis, M.V.; investigation, M.V.; resources, M.V.; data curation, M.V.; writing—original draft preparation, M.V.; writing—review and editing, M.V., J.M. and G.Z. (Guocheng Zhu); visualization, J.Y., Y.W. and G.Z. (Guoqing Zhang); supervision, J.M.; project administration, D.K. and J.M.; funding acquisition, D.K. All authors have read and agreed to the published version of the manuscript.

Funding: This research received no external funding.

Acknowledgments: This work was supported by the Ministry of Education, Youth and Sports of the Czech Republic and the European Union-European Structural and Investment Funds in the Frames of Operational Programme Research, Development and Education-project Hybrid Materials for Hierarchical Structures (HyHi, Reg. No. CZ.02.1.01/0.0/0.0/16_019/0000843), the project “Intelligent thermoregulatory fibers and functional textile coatings based on temperature resistant encapsulated PCM” SMARTTHERM (Project No. TF06000048) and the projects “Ministry of Education, Youth and Sports in the frames of support for researcher mobility” (VES19China-mobility, Czech-Chinese cooperation) and “Design of multi-layer micro/nano fibrous structures for air filters applications”, reg. no. 8JCH1064.

Conflicts of Interest: The authors declare no conflict of interest.

References

1. Bodnár, E.; Grifoll, J.; Rosell-Llompart, J. Polymer solution electro spraying: A tool for engineering particles and films with controlled morphology. *J. Aerosol Sci.* **2018**, *125*, 93–118.
2. Butt, H.J.; Graf, K.; Kappl, M. Thin films on surfaces of liquids. In *Physics and Chemistry of Interfaces*; Wiley: Hoboken, NJ, USA, 2003; pp. 280–298.

3. Yuan, X.D.; Yang, X.J. A study on friction and wear properties of PTFE coatings under vacuum conditions. *Wear* **2010**, *269*, 291–297.
4. Light, D.N.; Wilcox, J.R. Process Considerations in the Fabrication of Fluoropolymer Printed Circuit Boards. *IEEE Trans. Compon. Packag. Manuf. Technol. Part A* **1995**, *1*, 118–126.
5. Zhao-Zhu, Z.; Wei-Min, L. Study on the friction and wear properties of glass fabric composites filled with nano- and micro-particles under different conditions. *Mater. Sci. Eng.: A* **2005**, *392*, 359–365.
6. Huang, F.; Wei, Q.; Liu, Y.; Gao, W.; Huang, Y. Surface functionalization of silk fabric by PTFE sputter coating. *J. Mater. Sci.* **2007**, *42*, 8025–8028.
7. Nomura, M.; Tobita, H.; Suzuki, K. Emulsion polymerization: Kinetic and mechanistic aspects. *Adv. Polym. Sci.* **2005**, *175*, 1–128.
8. Manziek, L.; Langenmayr, E.; Lamola, A.; Gallagher, M.; Brese, N.; Annan, N. Functionalized Emulsion and Suspension Polymer Particles: Nanoreactors for the Synthesis of Inorganic Materials. *Chem. Mater.* **1998**, *10*, 3101–3108.
9. Kasai, H.; Nalwa, H.S.; Oikawa, H.; Okada, S.; Matsuda, H.; Minami, N.; Kakuta, A.; Ono, K.; Mukoh, A.; Nakanishi, H. A novel preparation method of organic microcrystals. *Jpn. J. Appl. Phys.* **1992**, *31*, L1132–L1134.
10. Mu, L.; Feng, S.S. Fabrication, characterization and in vitro release of paclitaxel (Taxol®) loaded poly (lactico-glycolic acid) microspheres prepared by spray drying technique with lipid/cholesterol emulsifiers. *J. Control. Release* **2001**, *76*, 239–254.
11. Yeo, S.D.; Kiran, E. Formation of polymer particles with supercritical fluids: A review. *J. Supercrit. Fluid.* **2005**, *34*, 287–308.
12. Dhanumalayan, E.; Joshi, G.M. Performance properties and applications of polytetrafluoroethylene (PTFE)—A review. *Adv. Compos. Hybrid. Mater.* **2018**, *1*, 247–268.
13. Isik, T.; Demir, M.M.; Aydogan, C.; Ciftci, M.; Yagci, Y. Hydrophobic coatings from photochemically prepared hydrophilic polymethacrylates via electrospraying. *J. Polym. Sci. Part A: Polym. Chem.* **2017**, *55*, 1338–1344.
14. Meiron, T.S.; Marmur, A.; Saguy, I.S. Contact angle measurement on rough surfaces. *J. Colloid.* **2004**, *274*, 637–644.
15. Shin, Y.M.; Hohman, M.M.; Brenner, M.P.; Rutledge, G.C. Experimental characterization of electrospinning: The electrically forced jet and instabilities. *Polymer* **2001**, *42*, 09955–09967.
16. Yarin, A.L.; Koombhongse, S.; Reneker, D.H. Bending instability in electrospinning of nanofibers. *J. Appl. Phys.* **2001**, *89*, 3018–3026.
17. Long, Q.; Cai, M.; Li, J.; Rong, H.; Jiang, L. Improving the electrical catalytic activity of Pt/TiO₂ nanocomposites by a combination of electrospinning and microwave irradiation. *J. Nanopart. Res.* **2010**, *13*, 1655–1662.
18. Venkataraman, M.; Mishra, R.; Marek, J.; Kucerova, K.; Militky, J. Aerogel embedded electrospun nanofiber layers for thermal insulation. In Proceedings of the Textile Bioengineering and Informatics Symposium Proceedings, 10th Textile Bioengineering and Informatics Symposium, (TBIS 2017), Pages 745–750, Wuhan Textile University, Wuhan, China, 16–19 May 2017.
19. Burkarter, E.; Saul, C.K.; Thomazi, F.; Cruz, N.C.; Zanata, S.M.; Roman, L.S.; Schreiner, W.H. Electrosprayed superhydrophobic PTFE: A non-contaminating surface. *J. Phys. D: Appl. Phys.* **2007**, *40*, 7778–7781.
20. Venkataraman, M.; Mishra, R.; Subramaniam, V.; Gnanamani, A.; Kotresh, T.M.; Militky, J. Dynamic heat flux measurement for advanced insulation materials. *Fibers Polym.* **2016**, *17*, 925–931.
21. Burkarter, E.; Saul, C.K.; Thomazi, F.; Cruz, N.C.; Roman, L.S.; Schreiner, W.H. Superhydrophobic electrosprayed PTFE. *Surf. Coat. Technol.* **2007**, *202*, 194–198.
22. Venkataraman, M.; Mishra, R.; Yang, K.; Militky, J.; Kremenakova, D.; Zhu, G.; Yao, J. Preparation of electrosprayed microporous membranes. In Proceedings of the IOP Conference Series: Materials Science and Engineering, Volume 460, 18th World Textile Conference (AUTEX 2018), Istanbul, Turkey, 20–22 June 2018.
23. Venkataraman, M.; Mishra, R.; Militky, J.; Xiong, X.; Marek, J.; Yao, J.; Zhu, G. Electrospun nanofibrous membranes embedded with aerogel for advanced thermal and transport properties. *Polym. Adv. Technol.* **2018**, *29*, 2583–2592.

24. Sukigara, S.; Gandhi, M.; Ayutsede, J.; Micklus, M.; Ko, F. Regeneration of Bombyxmori silk by electrospinning—Part 1: Processing parameters and geometric properties. *Polymer*, **2003**, *44*, 5721.
25. Ahn, Y.C.; Park, S.K.; Kim, G.T.; Hwang, Y.J.; Lee, C.G.; Shin, H.S.; Lee, J.K. Development of high efficiency nanofilters made of nanofibers. *Curr. Appl. Phys.* **2006**, *6*, 1030.
26. Fong, H.; Chun, I.; Reneker, D.H. Beaded nanofibers formed during electrospinning. *Polymer*. **1999**, *40*, 4585.
27. Lee, K.H.; Kim, H.Y.; Bang, H.J.; Jung, Y.H.; Lee, S.G. The change of bead morphology formed on electrospun polystyrene fibers. *Polymer*. **2003**, *44*, 4029.
28. Lin, K.; Chua, K.N.; Christopherson, G.T.; Lim, S.; Mao, H.Q. Reducing electrospun nanofiber diameter and variability using cationic amphiphiles. *Polymer*. **2007**, *48*, 6384.
29. Jaworek, A. Electro spray droplet sources for thin film deposition. *J. Mater. Sci.* **2007**, 266–297.
30. Venkataraman, M.; Mishra, R.; Militky, J.; Wiener, J.; Kucerova, K.; Marek, J.; Arumugam, V. Optimization of microporous hydrophobic membranes by electro spraying. In Proceedings of the International Conference on Nanomaterials - Research and Application, Volume 2017, Pages 877–8859, 9th International Conference on Nanomaterials - Research and Application, (NANOCON 2017), Hotel Voronez Brno, Czech Republic, 18 – 20 October 2017.



© 2020 by the authors. Licensee MDPI, Basel, Switzerland. This article is an open access article distributed under the terms and conditions of the Creative Commons Attribution (CC BY) license (<http://creativecommons.org/licenses/by/4.0/>).

11.4 Publication 3: Modelling and simulation of heat transfer by convection in aerogel-treated nonwovens

Publication

Venkataraman, M., Mishra, R., Militky, J., Behera, B.K. Modelling and simulation of heat transfer by convection in aerogel treated nonwovens, *The Journal of The Textile Institute*. 108(8). (2017) 1442-1453. DOI: 10.1080/00405000.2016.1255124.

Author Contribution

- Conceptualization
 - Devised the project, the main conceptual ideas, and the proof outline.
- Methodology
 - Design for Sample preparation.
 - Conceived, planned, and supervised the experiments.
- Formal Analysis, Investigation & Data curation
 - Characterized the samples and conducted the experiments.
 - Processed the experimental data.
 - Performed statistical analysis and stochastic modeling by using original software tools.
- Software & Validation
 - Designed the model and the computational framework and analyzed the data.
 - Planned and carried out the simulations.
 - Verification of the overall reproducibility of results and other research outputs.
- Writing the manuscript
 - Original Draft Preparation, review & editing with input from all authors.
- Visualization
 - Preparation, creation, and presentation of the published work, specifically visualization/data presentation

Modelling and simulation of heat transfer by convection in aerogel treated nonwovens

Mohanapriya Venkataraman^a , Rajesh Mishra^a, Jiri Militky^a and B. K. Behera^b

^aFaculty of Textile Engineering, Department of Material Engineering, Technical University of Liberec, Liberec, Czech Republic; ^bDepartment of Textile Technology, Indian Institute of Technology, Delhi, India

ABSTRACT

Simulation and numerical modeling are becoming increasingly popular due to the ability to seek solutions for a problem without undertaking real-life experiments. For the problems of heat transfer, these techniques to generate relevant data by incorporating different changes to the input parameters. Heat transfer property of textile materials is a major concern since it influences comfort properties of clothing. In this paper, numerical simulation was applied to evaluate the heat flux, temperature distributions, and convective heat transfer coefficients of the fibrous insulating materials treated with aerogel. The computational model simulated the insulation behavior of nonwoven fabrics without and with aerogel. Ansys and Comsol were used to model and simulate heat transfer. The simulation was performed assuming laminar flow and since the Mach number was < 0.3 , the compressible flow model with Mach number < 0.3 was used. The results of simulation were correlated to experimental measurements for validation. Furthermore, aerogel-treated fabric samples showed better thermal performance. Using this model, the heat transfer properties of the nonwoven fabrics treated with aerogel can be optimized further.

ARTICLE HISTORY

Received 10 August 2016
Accepted 26 October 2016

KEYWORDS

Aerogel; thermal insulation; convection; heat transfer; modeling

Introduction

To protect human body from extreme environmental conditions, clothing needs to generate a reasonable thermal microenvironment around the body. Thermal behavior of textile is a function of the interaction between air, fabric, and moisture. The exchange of heat follows distinct phenomena of simultaneous conduction, convection, and radiation. Thermal measurement techniques need to be improved to ensure effective evaluation of thermal performance of textiles. Nonwovens are used extensively as thermal insulating materials. With the nonwovens, different fibrous materials can be used as middle thermal insulating layers to enhance thermal insulation in clothing. Thermal insulation properties of nanoporous aerogel make it a good material to be used to enhance thermal insulation properties of textiles (Venkataraman et al., 2015). At the contact points between the fabric and human body, a large exchange of heat takes place (Darvishzadeh, Semnani, & Shirani, 2012; Etemoglu, Ulcay, & Can, 2009; Lee & Cunningham, 2000; Mohammadi, Banks-Lee, & Ghadimi, 2003; Raeisian, Mansoori, & Hosseini-Abardeh, 2013). Studies (Hatch, Woo, & Barker, 1990) show that the structural features rather than the component fibers have a bigger role in dissipation of heat.

Numerical methods are used due to its reliable accuracy and flexibility in different simulated conditions. For modeling, series of governing equations based on the energy conservation of law is normally used to depict heat transfer process in fabrics (Fan & Wen, 2002; Min, Son, Kim, Lee, & Hong, 2007; Ran, Zhu, & Li, 2011; Zhu, Xie, Yang, & Li, 2011). These equations are based

on some assumptions and solved by supplying the initial and boundary conditions. However, the complex practical problems make it extremely difficult to obtain a numerical solution using conventional calculation methods. Due to its simplicity, finite element analysis (FEA) was considered as an effective tool. It was used for analyzing the factors influencing heat transfer of the fabrics (Sun, Feng, & Liu, 2006). It was also used for predicting the effective thermal conductivity and thermal resistance of the woven fabric (Siddiqui & Sun, 2013). Geometric models have been developed using computational fluid dynamics which was used to predict the thermal resistance of fabrics and simulate the convective heat transfer of the fabric (Kothari & Bhattacharjee, 2008). Studies on thermal behavior of fabric using the fractal derivative method based on the multi-scale profile of textile fabrics have also been conducted (Fan & He, 2012). Ansys software has been used for establishing a one-dimensional heat transfer model to simulate and predict the thermal protection property of textile fabrics (Gong, Zhang, & Mao, 2010). Earlier research on convective heat transfer coefficient of fabric was done on flat plate without pores. The simulated data were in good agreement with experimental values in this work (Bhattacharjee & Kothari, 2008). More research work has been carried out for heat transfer through conduction and radiation as compared to convection due to the challenges in modeling the porous material under heat convection. (Zhu, Kremenakova, & Wang, 2014). The study of permutations and combinations of coatings and treatments to achieve the best thermal performance is an ongoing research activity. Modeling and simulation of woven fabrics for heat

transfer are widely available. However, there are challenges in modeling convective heat transfer through the nonwoven fabric treated with aerogel and limited research has been conducted in this area. In this study, numerical simulation was used to evaluate the heat flux, temperature distributions, and convective heat transfer coefficients of fibrous insulating materials treated with and without aerogel.

Methodology

Materials

For ANSYS, a unit cell was considered due to the highly random structure of nonwoven fabrics (fibers made of a 1:1 combination of polyester and polyethylene with and without aerogel). Individual fibers having circular cross-section and a random shape were modeled. For COMSOL, modeling was done for nonwoven fabrics made of 69.3% aerogel, 0.7% air (approximated as 70% aerogel) and 30% fibers (made of a 1:1 combination of polyester and polyethylene). The samples considered for this study were nonwoven fabrics comprising combinations of fibers with air or aerogel. The represented percentages are by volumes.

Aerogel is mesoporous and has nearly 98% of air and 2% solid. It is also referred to as 'Solid air.' The difference between the presence of just air and aerogel is that aerogel can hold air within its complex structure and does not allow free flow of air. The results were compared with those of the fabric made of 70% air and 30% fibers to establish the advantages of using aerogel in the fabric. The samples used for this study are given in Table 1.

Hydrophobic amorphous silica aerogel was used for this study which is most suitable for application in textile material which provides the superinsulating properties as shown in Table 2, of silica aerogel in a flexible form. It is excellent for ambient and

sub-ambient insulating applications. The aerogel particles were added during thermal bonding of the nonwoven web.

Scanning electron microscopy (SEM), which uses electrons rather than light to form an image, was used for examining structural and surface characteristics of the samples. A typical high resolution images for the aerogel-treated nonwoven fabrics are shown in Figure 1 which shows and confirms aerogel dispersion in between the fibers in the structure.

Methods

Simulating convective heat transfer through aerogel-treated nonwovens using ANSYS

Thermal analysis is used to determine the temperature distribution and related thermal quantities in the model. The outputs from a thermal analysis are (1) temperature distribution; (2) amount of heat loss or gain; (3) thermal gradients and (4) thermal fluxes. In ANSYS workbench, two types of thermal analysis are carried out, namely steady-state and transient Thermal Analysis. The steady-state thermal analysis may be either linear or non-linear, with respect to material properties that depend on temperature. The thermal properties of most of the materials do vary with temperature and hence analysis usually is non-linear. Including radiation effects or temperature-dependent convection in a model also makes the analysis nonlinear. The steps to solve a problem relate to the thermal analysis are the same as that of the structural analysis, except a few steps such as selecting the element-type, applying the load, and post processing results. In the transient thermal analysis, the system is studied under varying thermal loads with respect to time. The temperatures can be derived varying with time, thermal gradients and thermal fluxes in a transient thermal analysis. The transient thermal analysis takes more time compared to other analysis types. It is necessary to understand the basic mechanism of the problem to reduce the time involved in getting the solution. For example, if the problem contains nonlinearity, then it is first need to understand how they affect the response of structures by doing the steady-state thermal analysis.

Finite element model

The FEA is important for design validation. A typical computer-aided engineering process comprises pre-processing, solving, and post-processing steps. FEA simulates the loading conditions of a model and determines its response under those conditions. In space, a rigid body has six degrees of freedom (DOFs). A linear element has a maximum of two nodes. Thermal conduction/convection problems are formulated using the finite element approach, with temperature as the single DOF variable at each node in the mesh and with the material conduction properties used to form the thermal matrix to be solved.

Unit cell

Owing to the highly random structure of nonwovens, a unit cell was considered. Individual fibers were modeled, each having a circular cross-section and a random shape. For this, a spline (a curve) was made, and the profile of a circle was swept over the spline to create the fiber. The modeled fibers were assembled together to create a nonwoven

Table 1. Description of samples.

Samples	Description	Thickness (mm)	Weight (g/m ²)	Density (kg/m ³)
S1	Aerogel-treated nonwoven fabrics	3.424	272.56	79.66
S2	Aerogel-treated nonwoven fabrics	6.212	499.46	80.42
S3	Aerogel-treated nonwoven fabrics	6.608	440.70	66.73
S4	Aerogel-treated nonwoven fabrics	8.060	535.10	66.39
S5	Aerogel-treated nonwoven fabrics	11.120	733.70	65.99
S6	Aerogel-treated nonwoven fabrics	13.800	942.70	68.33
H1	Needle-punched struto nonwoven structure	9.336	402.00	43.06
H2	Needle-punched struto nonwoven structure	8.048	407.50	50.64

Table 2. Properties of amorphous silica aerogel.

S. No.	Properties	Value range
1	Particle size range	0.1–0.7 mm
2	Pore diameter	~20 nm
3	Density	1.205 kg/m ³
4	Surface chemistry	Fully hydrophobic

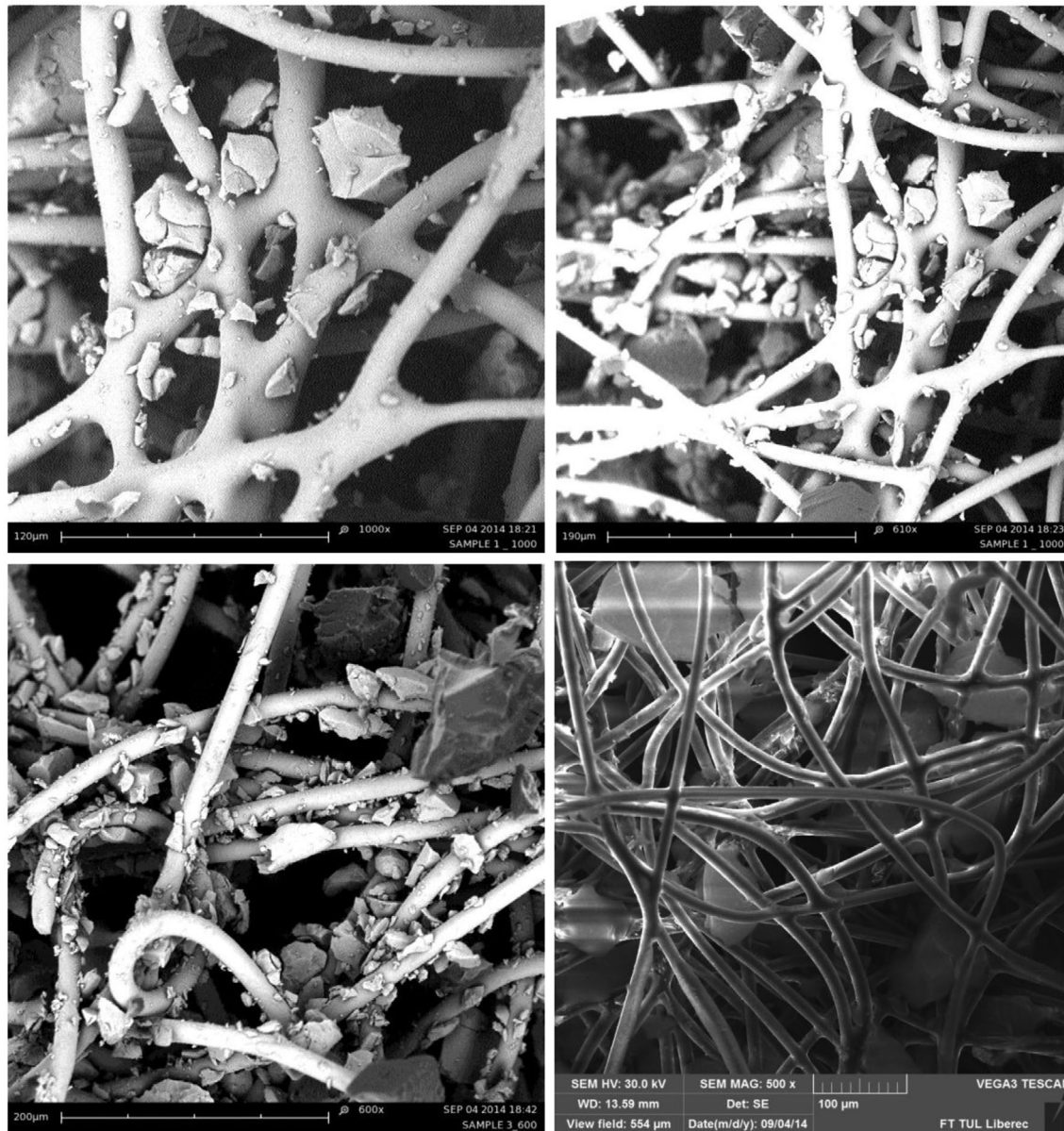


Figure 1. SEM images of aerogel-treated nonwoven fabrics.

structure, such that the fibers occupy 26.27% space inside the unit cell, so as to give 73.73% porosity to the fabric as shown in Figure 1. The unit cell had dimensions measuring $0.58 \text{ mm} \times 0.647 \text{ mm} \times 0.72 \text{ mm}$ (The machine direction and the cross direction in the nonwoven fabric's unit cell can be identified clearly). This assembly of fibers was saved as a PART file so that it could be used as a component in the further complex assembly (Figures 2–4).

Meshing parameters

Steady state thermal analysis was studied with the materials as fabric composed of polyester and polyethylene fibers, air, and aerogel. The value of isotropic thermal conductivity and the corresponding temperature for each of the materials was specified. The step file of the model was created in solidworks and was then imported to generate the 'Geometry'. The materials were assigned to all components to generate a 'Mesh' of

the model. The number of nodes was 5,375,975 and number of elements was 1,035,224.

Boundary conditions

The surface temperatures were setup at temperature gradient 47°C for fabric thicknesses with the convection requirements. The total heat flux, directional heat flux (y -axis), and temperature was set. Then, the model was 'solved' to obtain heat loss. The simulation was repeated twice. In the first case, the simulation was done with stagnant air and in the second case, simulation was done with aerogel occupying the volume of stagnant air. (The underlying fact is that aerogel by itself is composed of 99% air in micro and nanoporous network).

A chain of unit cells was assembled using the 'mate' function to give a more realistic view of the fabric. This was simulated in ANSYS Workbench 14. A model view of the structure of the nonwoven fabric developed is shown in Figure 5.

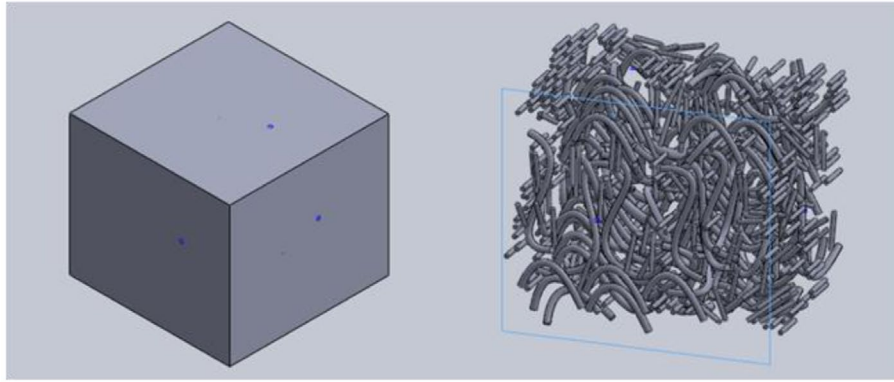


Figure 2. Unit cell model of nonwoven.

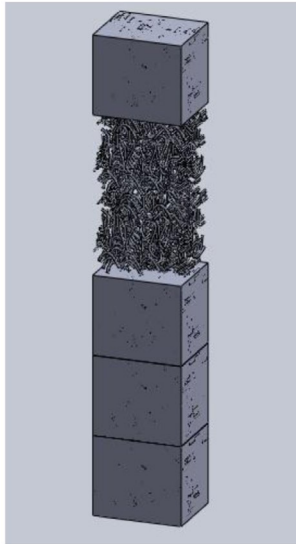


Figure 3. Whole width of the fabric.

Simulating convective heat transfer through aerogel treated nonwovens using COMSOL

Finite element method

The simulation of heat transfer through the fabric unit cell was done in COMSOL, which uses finite element method to carry out simulations. The input given to carry out simulation was heat capacity; density, thermal conductivity (both fiber and the surrounding fluid), viscosity and the ratio of heat capacity at

constant pressure, and constant volume (γ). The viscosity, density, and γ values were the same for both simulations since the fluid responsible for the convection was air. The thermal conductivity and the heat capacity for both fluids were different. In the model used, most of the heat transfer was because of the convection by the fluid. The conduction between air and fiber was relatively small. Moreover, the amount of heat transfer through the contact points between the fibers was negligible. The thermal conductivity and the heat capacity of both the fluids were different. The values are provided in the Table 3.

Unit cell

Solidworks was used to model a unit cell to represent the fabric samples. The unit cell dimensions were $0.565 \text{ mm} \times 0.335 \text{ mm} \times 0.1 \text{ mm}$. The fiber percentage in the unit cell was approximately 26.5%. Most of the fiber parts were aligned in the machine direction and very few in other directions as shown in Figure 6. The width of the unit cell was only about 0.5 mm (only a part of fiber was considered) and had a radius of 0.01 mm.

The conjugate heat transfer module, which combines the heat transfer through solids module and heat transfer through fluids module, was used. The heat transfer in solids module considers the fact that conduction is more prominent and the heat transfer in fluids module considers convection more prominent. This module couples the heat transfer module with the fluid flow module. The simulation was done assuming laminar and compressible flow and results obtained were for the steady state. Simulation was conducted for four cases: (1) Fabric with aerogel

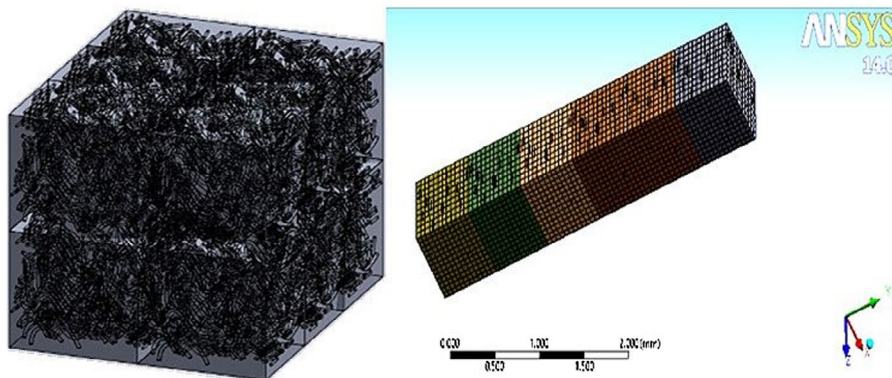


Figure 4. A model view of the structure of the nonwoven fabric.

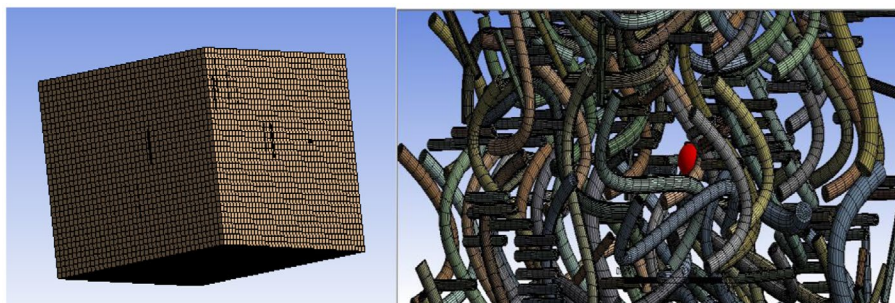


Figure 5. Meshing of elements in the unit cell.

Table 3. Thermal conductivity and the heat capacity of air, fibers, and aerogel.

Properties	Air	Polyester/Polyethylene	Aerogel
Thermal conductivity (W/m K)	0.0257	0.334	0.012
Dynamic viscosity (Pa s)	1.82E-5	–	1.82E-5
Specific heat capacity at constant pressure (J/kg K)	1005	1000	1090
Ratio of specific heats	1.4	–	1.4
Density (kg/m ³)	1.205	1380	1.205

with forced convection (2.5 m/s wind at the outer surface); (2) Fabric with aerogel without forced convection. (3) Fabric without aerogel with forced convection (2.5 m/s wind at the outer surface) and (4) Fabric without aerogel without forced convection.

Meshing parameters and boundary conditions

The model meshed is shown in Figure 7 and various boundary conditions are given as shown in Figure 6. For both with and without forced convection cases, one side was given a temperature of 329.19 K and initial temperature of the whole fabric was

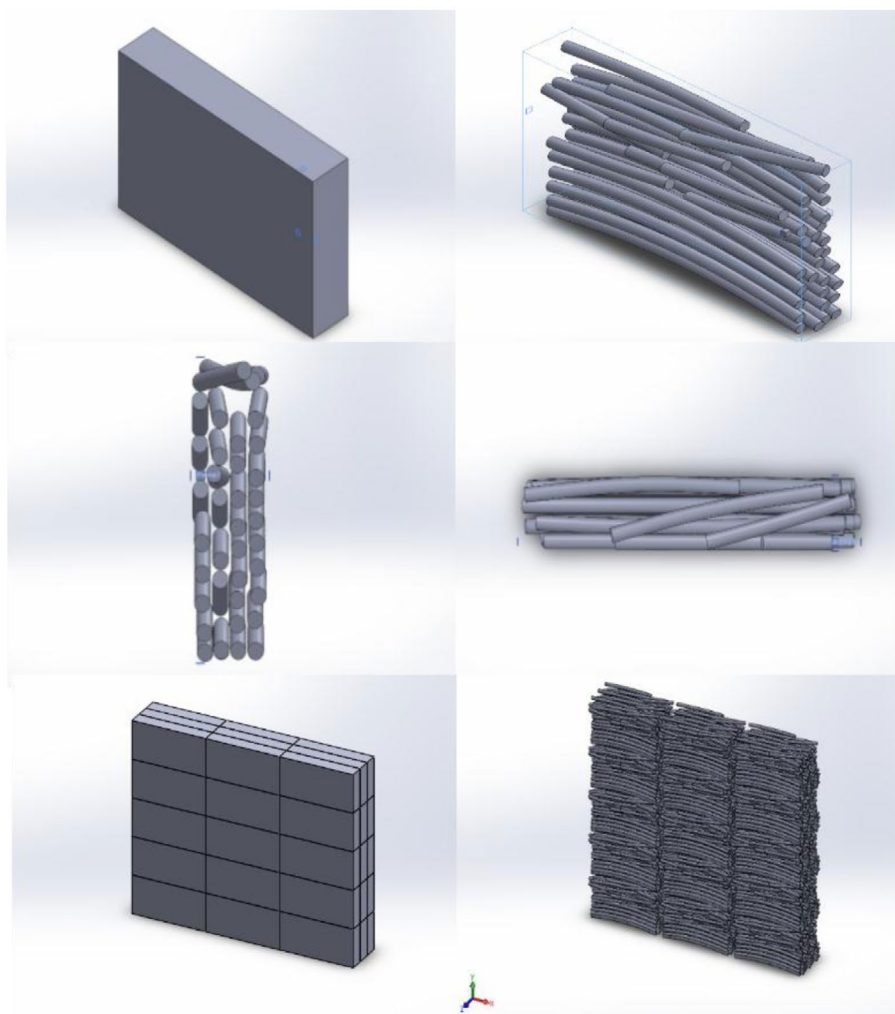


Figure 6. Fiber alignment in the unit cell.

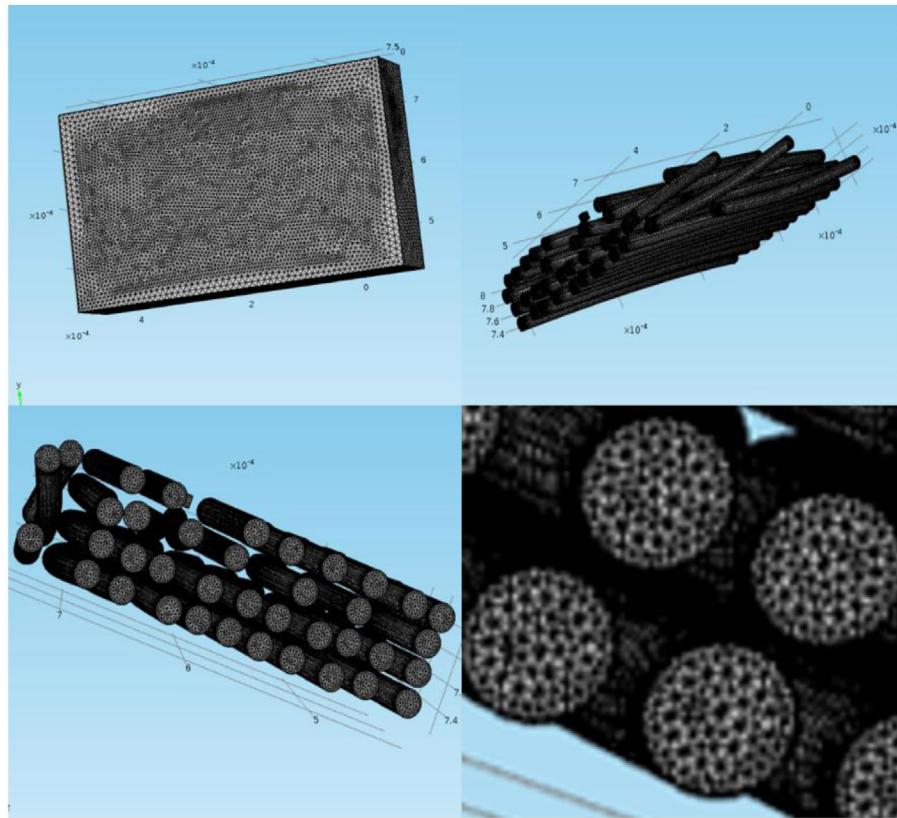


Figure 7. Meshing of the unit cell.

Table 4. Meshing parameters.

Parameter	Value
Maximum size given	5.7 E-5 m
Minimum size given	1.03 E-5 m
Boundary layer thickness	5.7 E-6 m
Total number of mesh elements	1,816,188

given as 263.15 K. For the forced convection case, the opposite side of the fabric was given a convective flux with convection factor 23.76 [W/(m² K)] (2.5 m/s wind) and 263.15 K outside temperature. For the case without forced convection, the opposite side of the fabric was given an open boundary condition with outside temperature of 263.15 K. The meshing parameters are as given in Table 4.

Results and discussion

ANSYS simulation

For ANSYS simulation, a constant ambient temperature of -10 °C was considered. Simulation was done to allow heat to flow along the thickness of the fabric (perpendicular to both the machine and the cross direction). As the heat flows under the temperature gradient provided, various levels of the fabric thickness settle down to different equilibrium temperatures. The equilibrium temperatures are shown in Figures 10 and 13. The variations in the 'Total Heat Flux' and the 'Directional Heat Flux' (along the y -axis which is the major direction for heat transfer) have been shown in Figures 8, 9, 11 and 12. Aerogel has a very

complex network structure which retains air within its micro-porous structure. It interrupts the flow of heat through its tortuous path. This results in higher heat retention. It was observed that the heat retention in nonwoven fabric with aerogel was 67% higher than the nonwoven fabric without aerogel, implying that aerogel hinders heat transfer. In Figure 10, the different colors specify the levels of temperature with respect to thickness. The red color part in the figure describes maximum heat is retained in the fabric. The color change is very quick (red to blue) thus showing higher heat loss in fabric without aerogel. In Figure 13, the red color part which is much thicker than Figure 10 describes that the heat has been retained well in higher portion of the fabric thickness. The heat loss in the fabric with aerogel is less compared to the fabric without aerogel which is shown in Figures 10 and 13. It is visible that more the red color part (higher heat retention), lesser is the heat loss.

Table 5 shows the summarized results of total heat flux, directional heat flux, and temperature of air and aerogel as an insulator for stagnant air conditions.

The percentage reduction in the heat flux can be calculated from the following where the percentage reduction in the heat flux is given in Equation (1):

$$\text{Percentage reduction in the heat flux} = \frac{\text{Total heat flux without aerogel} - \text{Total heat flux with aerogel}}{\text{Total heat flux without aerogel}} \times 100. \quad (1)$$

$$\text{Percentage reduction in the heat flux} = \frac{410.76 - 268.76}{410.76} \times 100 = 34.57\%.$$

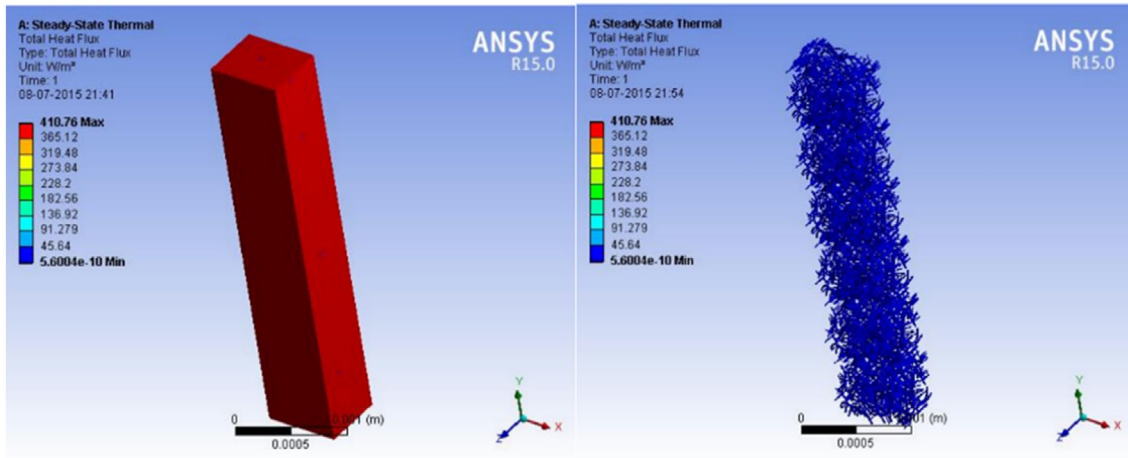


Figure 8. Total heat flux for standard nonwoven without aerogel (Air as insulator – Stagnant air conditions).

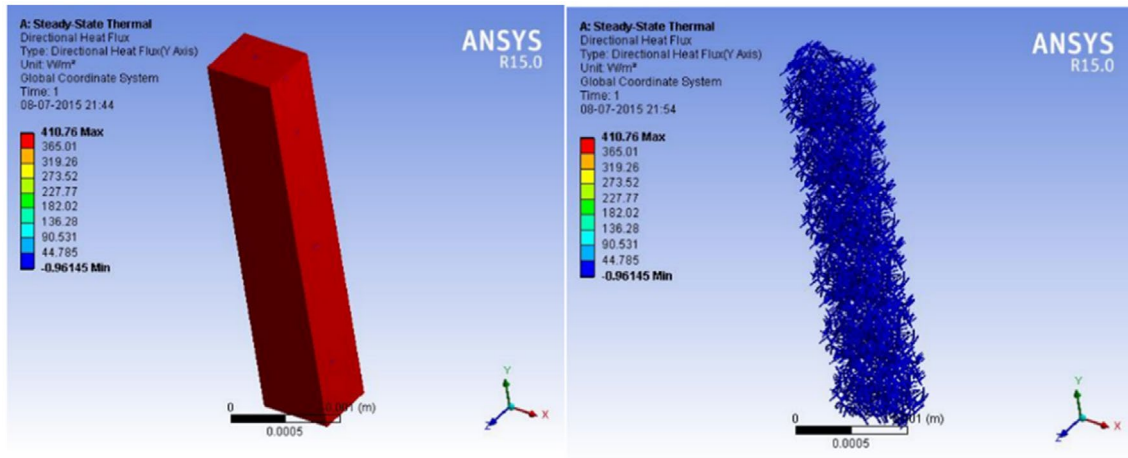


Figure 9. Directional heat flux for standard nonwoven without aerogel (Air as insulator – Stagnant air conditions).

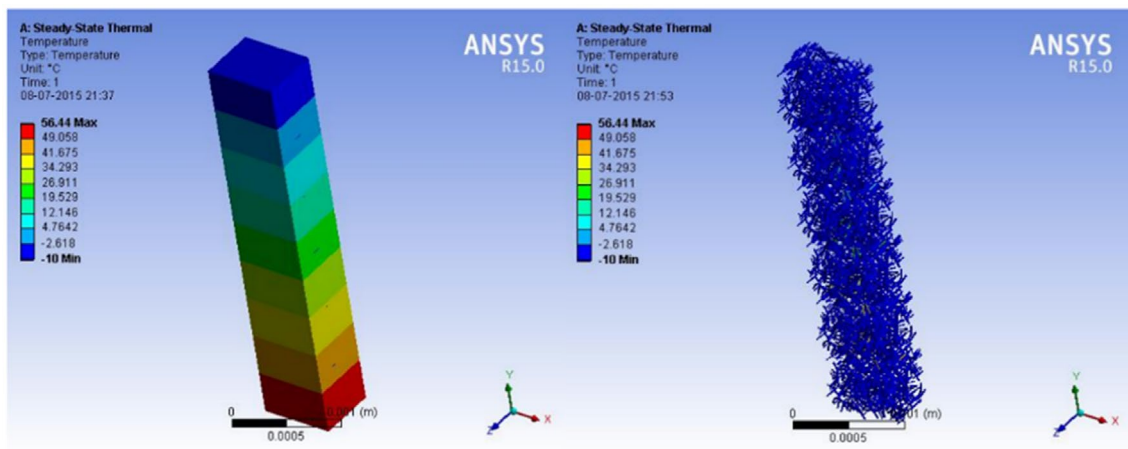


Figure 10. Temperature gradient (level of temperature) for standard nonwoven without aerogel (Air as insulator – Stagnant air conditions).

Model validation

To validate the results, aerogel-treated nonwoven fabric of different thicknesses, kept at an ambient temperature of $-10\text{ }^{\circ}\text{C}$ showed a temperature difference of $59.1\text{ }^{\circ}\text{C}$ ($T_1 = 56.44\text{ }^{\circ}\text{C}$ and

$T_2 = -2.66\text{ }^{\circ}\text{C}$, where T_1 is the hot plate temperature and T_2 is the equilibrium temperature of the fabric surface exposed to the environment) and a heat flux of 260.81 W/m^2 . From the results, it is concluded that the experimental and theoretical readings

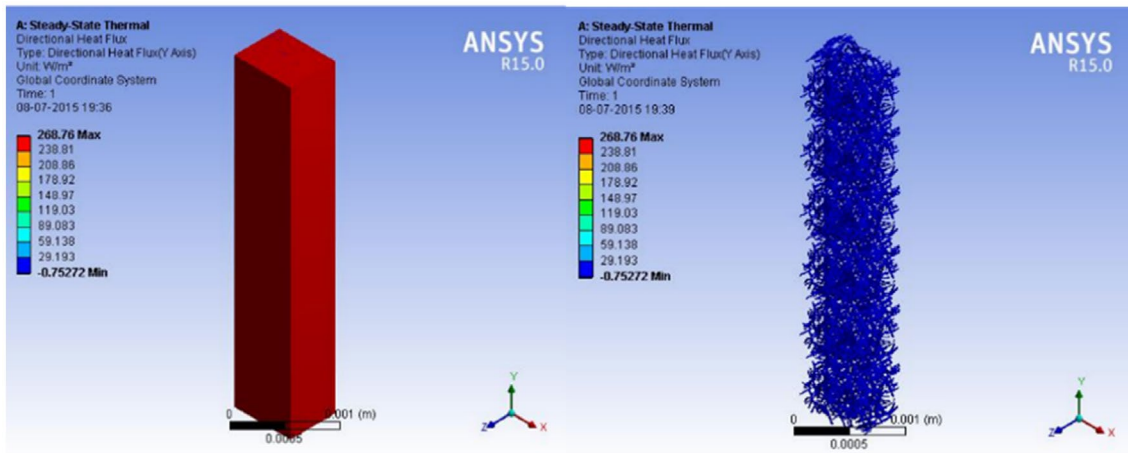


Figure 11. Directional heat flux for aerogel-treated nonwoven (Aerogel as insulator – Stagnant air conditions).

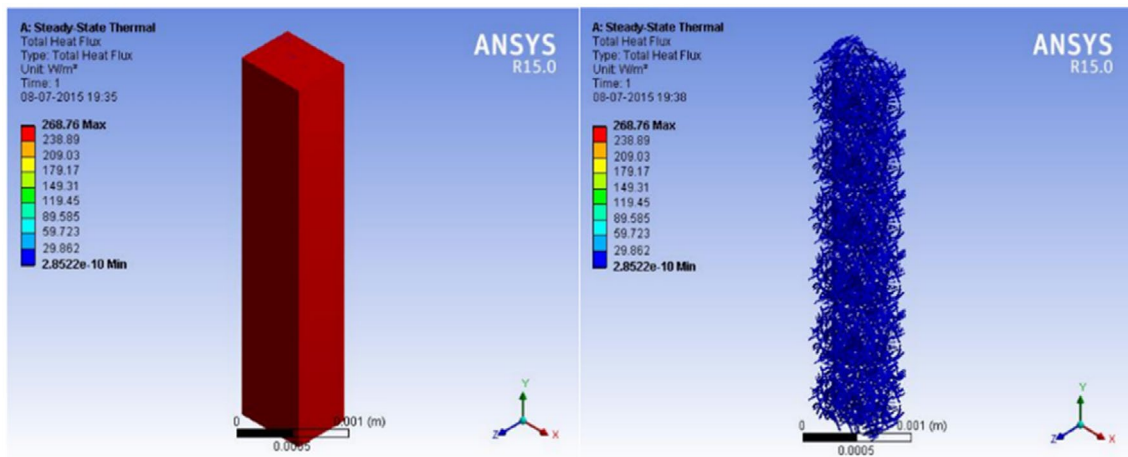


Figure 12. Total heat flux for aerogel-treated nonwoven (Aerogel as insulator – Stagnant air conditions).

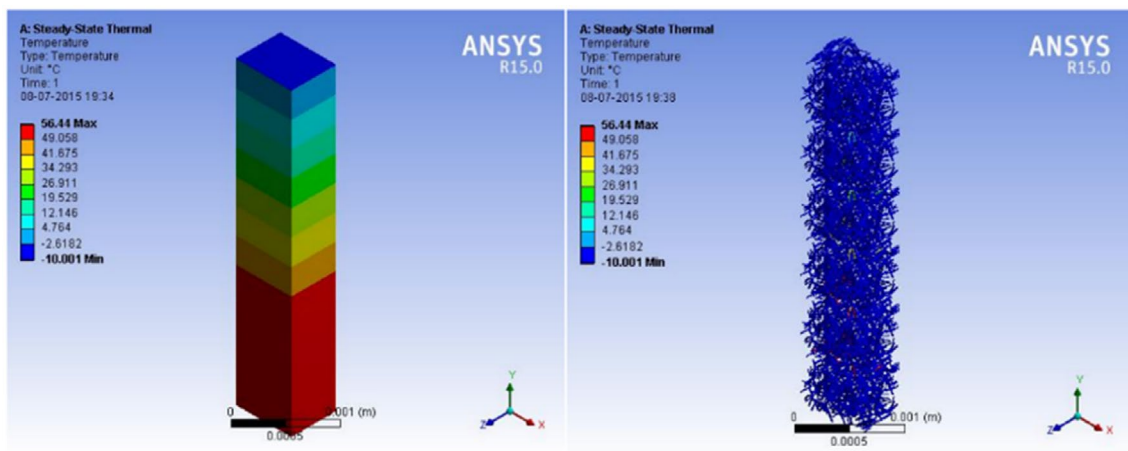


Figure 13. Temperature gradient (level of temperature) for aerogel-treated nonwoven (Aerogel as insulator – Stagnant air conditions).

are in close approximation with each other. The predicted value agrees well with the experimental value, suggesting that the finite element model can successfully predict the thermal conductivity of the fabric (Table 6).

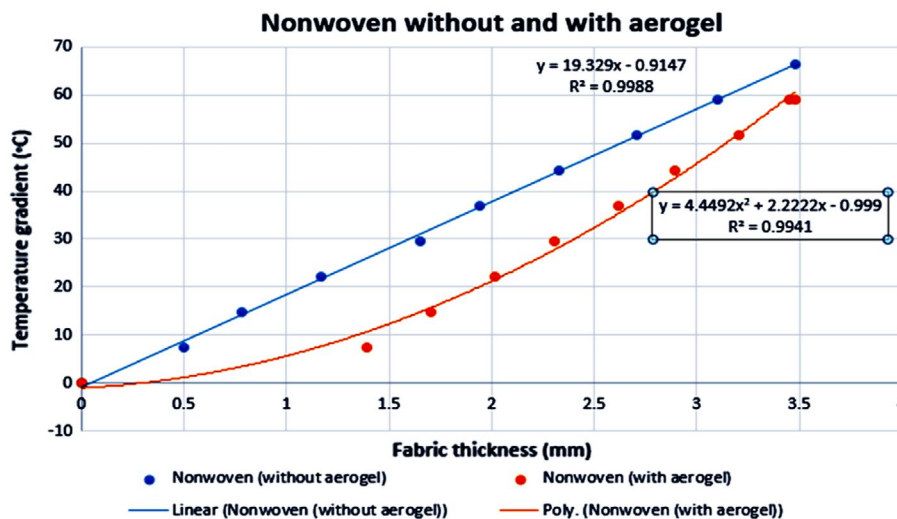
The comparison of temperature gradient shown in the Figure 14 in the nonwoven fabric with aerogel is lesser than in the nonwoven fabric without aerogel implying that aerogel hinders heat transfer. This may be attributed to the nanoporous structure

Table 5. Summarized results of air and aerogel for stagnant air conditions.

Measured property	Air as insulator (Stagnant air conditions)		Aerogel as insulator (Stagnant air conditions)	
	Film coefficient 26.3E-6 W/mm ² °C		Film coefficient 40.2E-6 W/mm ² °C	
	Maximum value	Minimum value	Maximum value	Minimum value
Total heat flux (W/m ²)	410.76	5.604 E-10	268.76	2.852 E-10
Directional heat flux – Y axis (W/m ²)	410.76	–0.962	268.76	–0.752
Temperature (°C)	54.66	–10	54.66	–2.66

Table 6. Comparison for the temperature gradient in nonwoven fibrous structure, without and with aerogel.

Nonwoven fabric without aerogel		Nonwoven fabric with aerogel	
Temperature gradient (K/mm)	Distance from the warmer surface (mm)	Temperature gradient (K/mm)	Distance from the warmer surface (mm)
0	0	0	0
7.38	0.5	7.38	1.39
14.76	0.78	14.76	1.70
22.15	1.17	22.15	2.02
29.53	1.65	29.53	2.31
36.91	1.94	36.91	2.62
44.29	2.33	44.29	2.89
51.68	2.71	51.68	3.21
59.06	3.1	59.06	3.45
66.44	3.48	59.1	3.48

**Figure 14.** Comparison of temperature gradients for with and without aerogel-treated nonwovens.

of the aerogel, which is able to retain heat within the fabric structure that is responsible for reduction in heat flux (Venkataraman, Mishra, & Jasikova, 2014; Venkataraman, Mishra, Militky, & Hes, 2014).

COMSOL simulation

Simulation was done assuming laminar flow and since the Mach number was < 0.3 (for the model, even if air is considered to be an ideal gas and speed is taken into consideration, Mach number < 0.3), the compressible flow model with Mach number < 0.3 was used. For standard nonwoven without forced convection shown in Figure 15, the temperature at the surface exposed to outside air was 329.19 K and the rate at which the heat flows through the fabric was 2.185 E-8 W.

In the case of standard nonwoven with forced convection showed in Figure 16, the temperature at the surface exposed to

outside air was 318.04 K and the heat rate through the fabric was 1.024 E-8 W. In the case of nonwoven with aerogel and without forced convection shown in Figure 17, the temperature at the surface exposed to outside air was 329.19 K and the heat rate through the fabric was 1.267 E-8 W. For the nonwoven with aerogel and with forced convection shown in Figure 18, the temperature at the surface exposed to outside air was 310.17 K and the heat rate through the fabric was 9.801 E-9 W.

In the case of forced convection, the difference between the surface temperatures of air and aerogel is almost 8 K even for a small unit cell. When forced convection was not taken into account, the temperature difference was very less (6 E-5 K). However, in both cases, the heat flow through air is higher than the aerogel. In forced convection, the heat loss through fabric with stagnant air was 5% higher than the fabric with aerogel. Without forced convection, the heat loss through fabric with stagnant air was 72% higher than the fabric with

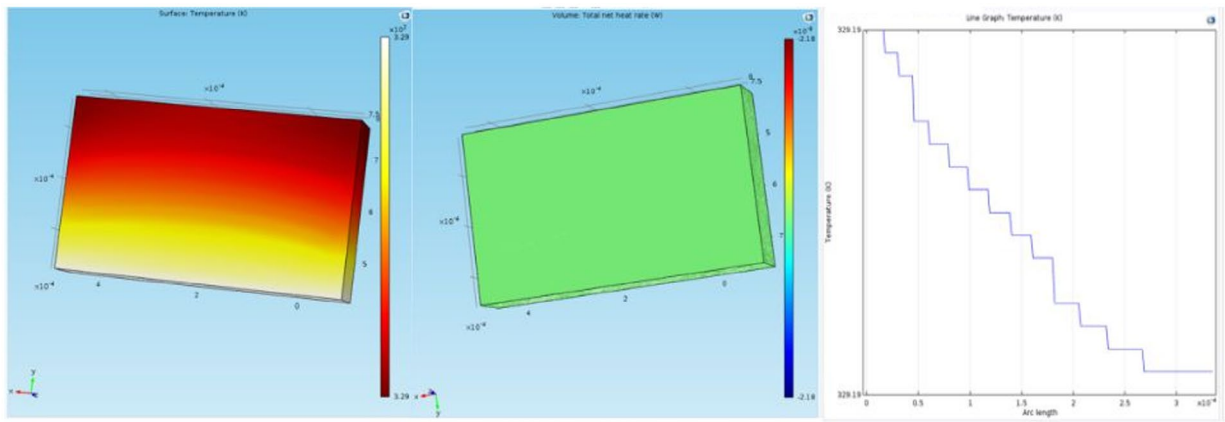


Figure 15. Heat transfer through standard nonwoven without forced convection.

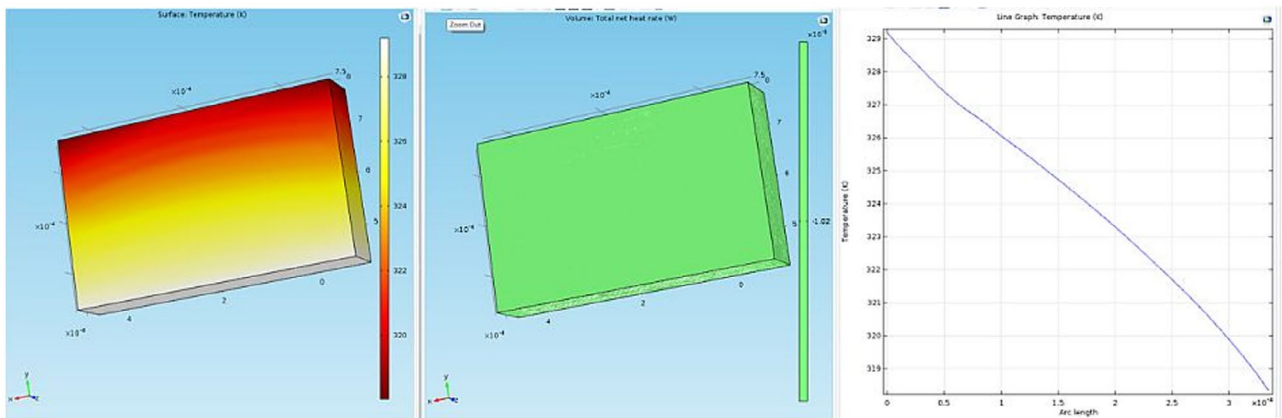


Figure 16. Heat transfer through standard nonwoven with forced convection.

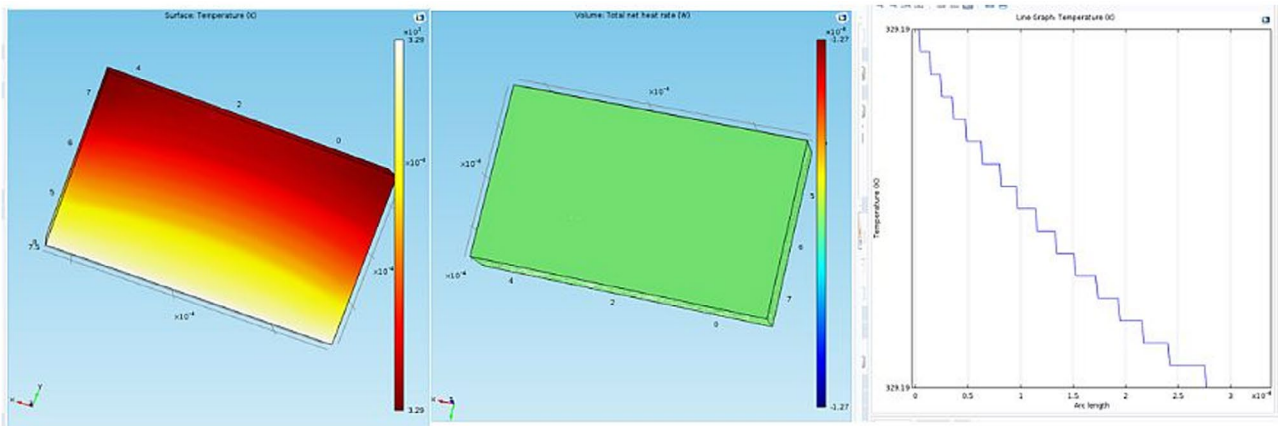


Figure 17. Heat transfer through aerogel-treated nonwoven without forced convection.

aerogel. That is, without any forced convection, the heat loss through the air was 1.7 times higher than the heat loss through aerogel. The total net heat rate is defined as the net incoming and outgoing heat fluxes through all the surfaces of the body. This value for forced convection case is seen to be less in both aerogel and air because the outgoing flux is much more when there is a forced convection. The temperature vs. length plot was also made. The graph was smoother for cases of forced

convections than the cases without forced convections. This may be due to very less variation in temperature in those regions.

Sources of error

Since the memory requirement for simulating bigger structures was high, the simulation was done for a small unit cell.

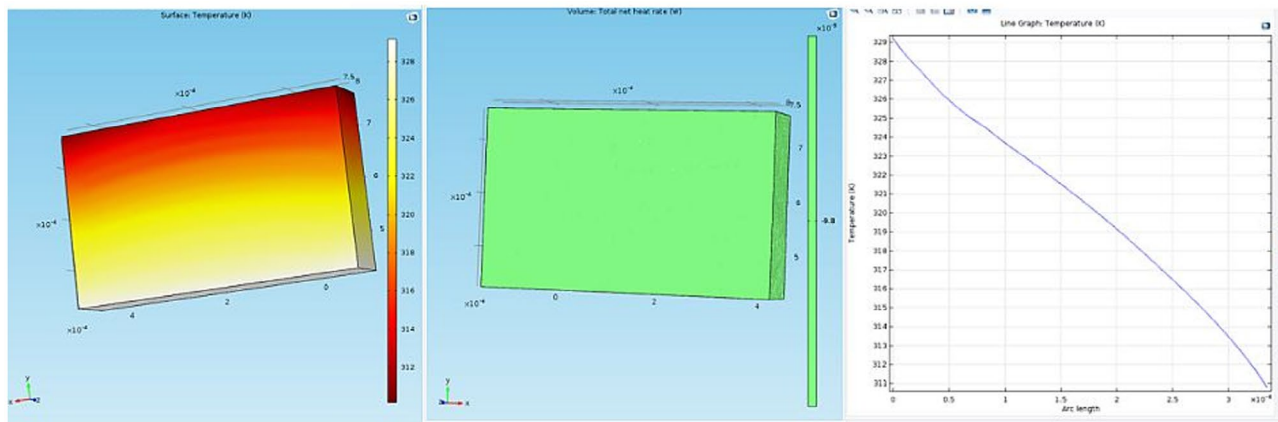


Figure 18. Heat transfer through aerogel-treated nonwoven with forced convection.

Due to this, the fluid motion may be different from what happens in bigger samples and therefore, heat flow in the bigger samples may be different. None of the fiber parts touches each other and therefore conduction between fibers is not considered in the heat flow simulation. Thermal conductivity for the fibers and the surrounding fluid is assumed a constant. The flow was assumed to be laminar instead of turbulent flow since simulation using turbulent model required more time. Mach number is taken to be < 0.3 , and therefore, density and viscosity changes due to the fluid motion are also considered to be negligible.

Conclusion

The modeling and simulation of heat transfer for aerogel-treated nonwoven fabric was carried out by ANSYS and COMSOL. The simulation results showed that thermal behavior of the fabric improved when treated with aerogel. This may be attributed to the nanoporous structure of the aerogel that hinders transfer of heat through its structure. The simulated data agreed well with experimental data. The numerical simulation of convective heat flow fabric can be considered a reliable method since there is a good agreement between simulation and experimental data. Aerogel may be considered a good insulator for improving thermal insulation of textiles. Further research has to be done to investigate convective heat transfer and the effect of aerogel's pore size and distribution on the thermal properties of fabric. The heat transfer properties of the fabric can be further optimized with assistance of this model.

Disclosure statement

No potential conflict of interest was reported by the authors.

Funding

This work was supported by Czech-India project [grant number DEBEL-19027], [project number L1213] of program NPU in Czech Republic.

ORCID

Mohanapriya Venkataraman  <http://orcid.org/0000-0002-8977-1244>

References

- Bhattacharjee, D., & Kothari, V. K. (2008). Measurement of thermal resistance of woven fabrics in natural and forced convections. *Research Journal of Textile and Apparel*, 12, 39–49.
- Darvishzadeh, M., Semnani, D., & Shirani, E. (2012). Improvement modelling of heat transfer by using complex neural net in fibrous structures. *Fibers and Polymers*, 13, 542–548.
- Etemoglu, A. B., Ulcay, Y., & Can, M. (2009). Mathematical modelling of combined diffusion of heat and mass transfer through fabrics. *Fibers and Polymers*, 10, 252–259.
- Fan, J., & He, J. H. (2012). Biomimic design of multi-scale fabric with efficient heat transfer property. *Thermal Science*, 16, 1349–1352.
- Fan, J., & Wen, X. (2002). Modeling heat and moisture transfer through fibrous insulation with phase change and mobile condensates. *International Journal of Heat and Mass Transfer*, 45, 4045–4055.
- Gong, Y. R., Zhang, X., & Mao, Z. P. (2010). Numerical simulation on thermal protection properties of textile materials. *Journal of Donghua University*, 36, 115–117.
- Hatch, K. L., Woo, S. S., & Barker, R. L. (1990). *In vivo* cutaneous and perceived comfort response to fabric. Part 1: Thermophysiological comfort determinations for three experimental knit fabrics. *Textile Research Journal*, 60, 405–412.
- Kothari, V. K., & Bhattacharjee, D. (2008). Prediction of thermal resistance of woven fabrics. Part I: Mathematical model. *The Journal of The Textile Institute*, 99, 421–432.
- Lee, S. C., & Cunningham, G. R. (2000). Conduction and radiation heat transfer in high-porosity fiber thermal insulation. *Journal of Thermophysics and Heat Transfer*, 14, 121–136.
- Min, K., Son, Y., Kim, C., Lee, Y., & Hong, K. (2007). Heat and moisture transfer from skin to environment through fabrics: A mathematical model. *International Journal of Heat and Mass Transfer*, 50, 5292–5304.
- Mohammadi, M., Banks-Lee, P., & Ghadimi, P. (2003). Determining effective thermal conductivity of multilayered nonwoven fabrics. *Textile Research Journal*, 73, 802–808.
- Raeisian, L., Mansoori, Z., & Hosseini-Abardeh, R. (2013). An investigation in structural parameters of needle-punched nonwoven fabrics on their thermal insulation property. *Fibers and Polymers*, 14, 1748–1753.
- Ran, X. J., Zhu, Q. Y., & Li, Y. (2011). Investigation on heat and mass transfer in 3D woven fibrous material. *International Journal of Heat and Mass Transfer*, 54, 3575–3586.
- Siddiqui, M. O. R., & Sun, D. (2013). Finite element analysis of thermal conductivity and thermal resistance behaviour of woven fabric. *Computational Materials Science*, 75, 45–51.
- Sun, Y. C., Feng, X. W., & Liu, C. Y. (2006). Application of finite element method in analysis of heat transfer through textile fabrics. *Journal of Donghua University*, 32, 50–53.
- Venkataraman, M., Mishra, R., Jasikova, D., Kotresh, T. M., & Militky, J. (2014). Thermodynamics of aerogel-treated nonwoven fabrics at subzero temperatures. *Journal of Industrial Textiles*, 45, 387–404.

- Venkataraman, M., Mishra, R., Militky, J., & Hes, L. (2014). Aerogel based nanoporous fibrous materials for thermal insulation. *Fibers and Polymers*, 15, 1444–1449.
- Venkataraman, M., Mishra, R., Wiener, J., Militky, J., Kotresh, T. M., & Vaclavik, M. (2015). Novel techniques to analyse thermal performance of aerogel-treated blankets under extreme temperatures. *The Journal of The Textile Institute*, 106, 736–747.
- Zhu, G., Kremenakova, D., & Wang, Y. (2014). An analysis of effective thermal conductivity of heterogeneous materials. *AUTEX Research Journal*, 14, 14–21.
- Zhu, Q. Y., Xie, M. H., Yang, J., & Li, Y. (2011). A fractal model for the coupled heat and mass transfer in porous fibrous media. *International Journal of Heat and Mass Transfer*, 54, 1400–1409.

11.5 Publication 4: Structural analysis of embedding polyethylene glycol in silica aerogel

Publication

Yang, K., Venkataraman, M., Karpiskova, J., et al. Structural analysis of embedding polyethylene glycol in silica aerogel, *Microporous and Mesoporous Materials*. 2021; 310. DOI: 10.1016/j.micromeso.2020.110636.

Author Contribution

- Conceptualization
 - Devised the project, the main conceptual ideas and proof outline.
- Methodology
 - Conceived, planned and assisted with the experiments
- Validation
 - Verification of the overall reproducibility of results and other research outputs.
- Writing – Original Draft Preparation
 - Assisted in writing the manuscript, review and editing.
- Others
 - Supervision



Structural analysis of embedding polyethylene glycol in silica aerogel

Kai Yang^{a,*}, Mohanapriya Venkataraman^a, Jana Karpiskova^b, Yuji Suzuki^c, Sana Ullah^c, Ick-Soo Kim^c, Jiri Militky^a, Yuanfeng Wang^a, Tao Yang^a, Jakub Wiener^a, Guocheng Zhu^d, Juming Yao^d

^a Department of Material Engineering, Faculty of Textile Engineering, Technical University of Liberec, Liberec, Czech Republic

^b Department of Nanochemistry, Institute for Nanomaterials, Advanced Technologies and Innovation, Technical University of Liberec, Liberec, Czech Republic

^c Nano Fusion Technology Research Group, Division of Frontier Fibers, Institute for Fiber Engineering (IFES), Interdisciplinary Cluster for Cutting Edge Research (ICCER), Shinshu University, Tokida 3-15-1, Ueda, Nagano, 386-8567, Japan

^d College of Materials and Textiles, Zhejiang Sci-tech University, Xiasha Education Park, PR China

ARTICLE INFO

Keywords:

PEG
Aerogel
Crystallinity
Pore volume
Thermal behavior

ABSTRACT

Embedding of the functional materials into aerogel powders was realized via the filtration method. In this work, the effect of aerogel on the molecule structure of the embedded polyethylene glycol (PEG) was investigated by dispersing aerogel powders in 20 wt% PEG aqueous solution with subsequent filtration method. The encapsulation of the PEG in the aerogel was characterized by isothermal nitrogen (N₂) adsorption/desorption. The structure of the embedded PEG in the aerogel powders was investigated via SEM-EDS, FE-SEM, FT-IR, XRD, TG-DTA, DSC, and leakage test. It was found that the only physical capillary force worked to adsorb PEG molecules from its solution by the aerogel powders. The BET surface area and the DFT pore volume of the PEG/aerogel powders were reduced obviously when compared with pure aerogel powders. The ability of the pores in the aerogel powders ranging from 14 nm to 16 nm to adsorbing the PEG molecules from the water system was weak. The crystallinity of the PEG was significantly reduced because of the limited space for crystal growth, and the decomposed temperature and thermal capacity decreased correspondingly.

1. Introduction

Polyethylene glycol (PEG) is a familiar organic polymer characterized by high latent heat with small suitable phase change temperature, high thermal stability, good chemical compatibility, little chemical vaporability, non-toxicity, and non-flammability [1]. The application of PEG has been extended into thermal energy storage [2], drug delivery [3], supporting in dyeing [4], and so on. However, there was a limitation of the direct usage of PEG in practice [5]. For example, the intrinsic solid-liquid phase change of the PEG resulted in the leakage when PEG served as phase change materials [6]. The hydroxyl group (-OH) of the PEG enhanced the adsorption of the water vapor from the various humid environment. Therefore, the incorporation of PEG with other material was taken into consideration [7].

Recently, the incorporation of PEG with porous materials [8] has been attracted more and more attention and provided an alternative way to solve the aforementioned problems [9]. The encapsulation of the PEG by the porous materials was affected by the internal factors and external

factors. The internal factors were determined by the pores, including the pore topology (pore type and pore connection) and pore morphology (pore shape and pore size) [10]. The external factors were from the PH, temperature, and pressure during the encapsulation process [11]. By controlling the factors, various methods to incorporate the PEG into porous materials have been reported, including physical blending [12], sol-gel method [11], soaking [13], encapsulation [12], in-situ synthesis [14], and so on.

The filtration method for the encapsulation of the PEG in the porous materials was realized by the capillary force and suitable for the large-scale production [15]. Besides, little effect on the pores was assumed when the filtration method was used, because no chemical reaction happened. From this point, the encapsulation of the PEG could be well studied by using the filtration method. In most studies, molten PEG was used to be embedded into various porous materials with narrow or specific pore sizes (silicon dioxide [16], silica gel [11] ...). The common results revealed that the embedded PEG in the micropores and mesopores was assumed as nanofluid leading to the conclusion that the

* Corresponding author.

E-mail address: kai.yang@tul.cz (K. Yang).

<https://doi.org/10.1016/j.micromeso.2020.110636>

Received 14 February 2020; Received in revised form 25 August 2020; Accepted 14 September 2020

Available online 19 September 2020

1387-1811/© 2020 Elsevier Inc. All rights reserved.

Table 1
Properties of silica aerogel powders.

Property	Value Range
Particle Size	0.1–0.7 mm
Pore Diameter	~20 nm
Density	1.205 kg/m ³
Surface Chemistry	Fully hydrophobic

thermal dynamics of embedded PEG nanophase change were different from the one of bulk PEG due to reduced dimensionality in the micropores and mesopores [17]. The analysis of pore morphology (diameter and shape) and pore topology (molecular order) supports the in-depth study on phase transition of PEG nanophase change in the pores. Fang Tian et al. [11] revealed that the PEG molecules embedded in the smaller pores of the silica gel had lower enthalpy along with longer phase transition temperature range due to the incomplete crystallization.

Aerogel is an amorphous material with a small size (<1 mm) and characterized with extremely high porosity (>95%) and low density (~1.2 kg/m³) [18]. By comparing with the aforementioned various porous materials, the aerogel had various pores ranging from 2 to 200 nm [19]. The use of silica aerogel in conjunction with materials via filtration method has been explored. Various organic PCMs including eicosane [20], erythritol [21], and paraffin [22] have been embedded in silica aerogel powders. The encapsulation amount of the polymer in the aerogel (50%–90%) was considered large according to the high specific area and pore volume [23,24]. However, there is limited literature available for the structural analysis of the embedded PEG in the aerogel. It was noticeable that the longer PEG molecular chains, as well as intrinsic entanglement, were in the melting PEG [25] and the aerogel was the small powder with micro- and meso-pores [21], which may affect the encapsulation of PEG on the surface or trapped inside of silica aerogel by using filtration method. By comparing with melting PEG, the PEG molecular chains in the solvent were extended and soft [26], which provided an alternative way for the investigation on the encapsulation of the PEG in the aerogel.

In this research, the PEG/aerogel powders were first prepared by dispersing the aerogel powders in the PEG aqueous solution with lower PEG concentration. Then, the structural analysis of the embedded PEG in the aerogel was investigated by measuring the distribution of the PEG encapsulation in the aerogel, the crystal structure, the thermal capacity, and thermal stability.

2. Experimental

2.1. Materials

Commercially available hydrophobic amorphous silica aerogels in the powder form were purchased from Cabot Aerogel Corporation and Table 1 shows the properties of silica aerogel powders. Polyethylene glycol (PEG) powders ($M_w = 6000$) were purchased from Sigma Aldrich. All materials were kept at dry condition under room temperature.

2.2. Preparation of PEG/aerogel powders

PEG/aerogel powders were prepared as described in Fig. 1. The process began with the preparation of a 20 wt% PEG solution was firstly prepared by dissolving PEG powders in the water slowly with a high-speed stir in the room temperature till the PEG solution became homogenous. The obtained PEG solution was ready for the next step where aerogel powders were added in the obtained 20 wt% PEG solution slowly and a high-speed stir was applied to disperse aerogel powders. The ratio of the added aerogel powders to PEG content in the PEG solution was set at 1:20. After 24 h stir, the PEG/aerogel mixture was obtained. The PEG/aerogel mixture was then filtered with a glass-filter paper via a filter flask with a conjunction of a suction filtering mechanism. After filtration, the PEG/aerogel mixture in the form of powders was obtained. The obtained PEG/aerogel mixture in the form of powders was placed in an oven with 60 °C for 48 h to evaporate the excess water inside of PEG/aerogel powders. Finally, the PEG/aerogel powders were obtained.

The encapsulation rate (χ_m) of PEG in the aerogel was calculated by equation (1), where $W_{E,PEG}$ was the mass of the embedded PEG in the aerogel and W_0 was the mass of the used aerogel powders for filtration. The $W_{E,PEG}$ was calculated according to equation (2), where W_E was mass of the final PEG/aerogel powders. The encapsulation efficiency (χ_e) was evaluated by equation (3), where W_i was the initial mass of the PEG powders for the filtration.

$$\chi_m = W_{E,PEG}/W_0. \quad (1)$$

$$W_{E,PEG} = W_E - W_0 \quad (2)$$

$$\chi_e = (W_E - W_0 - W_i)/W_i. \quad (3)$$

2.3. Tests and methods

Scanning electronic microscopy-energy dispersive spectrometry (SEM-EDS) (JSM-5300, JEOL Ltd, Japan) was used to characterize the morphology and element dispersion of aerogel powders and the prepared PEG/aerogel powders, which was performed under 15 kV. The micropores in the aerogel powders and PEG/aerogel powders were observed via field emission scanning electron microscopy (FE-SEM) (JSM6335FS, JEOL, Japan).

The encapsulation of the PEG in the aerogel was also evaluated by using nitrogen (N_2) adsorption/desorption isotherms (AutoSorb-iQ-MP, Quantachrome, Florida, USA) at the temperature of liquid nitrogen. By using ASIQwin software, the specific surface area was calculated based on the Brunauer-Emmett-Teller (BET) method, and pore size distribution was evaluated according to the density functional theory (DFT). The PEG/aerogel powders and the aerogel powders were pre-dried at 50 °C for 48 h and then outgassed under vacuum at 50 °C for at least 24 h before the measurement.

Fourier transform infrared instrument (FT-IR) (ATR Prestige-21, Shimadzu, Japan) was used to characterize the chemical compatibility between PEG and aerogel in the range of 600–4000 cm^{-1} with a

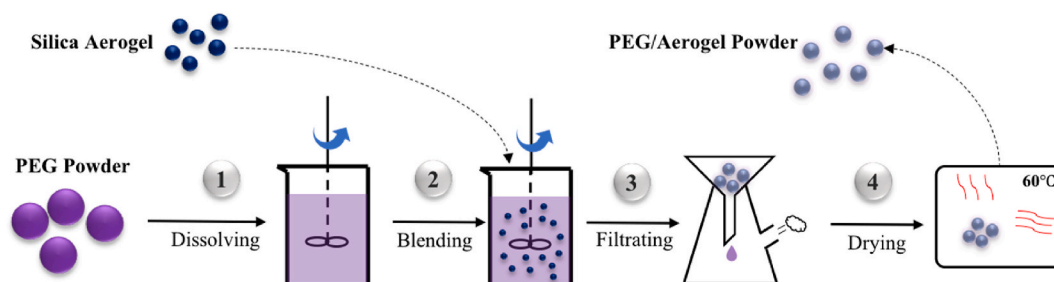


Fig. 1. Preparation of PEG/aerogel powders.

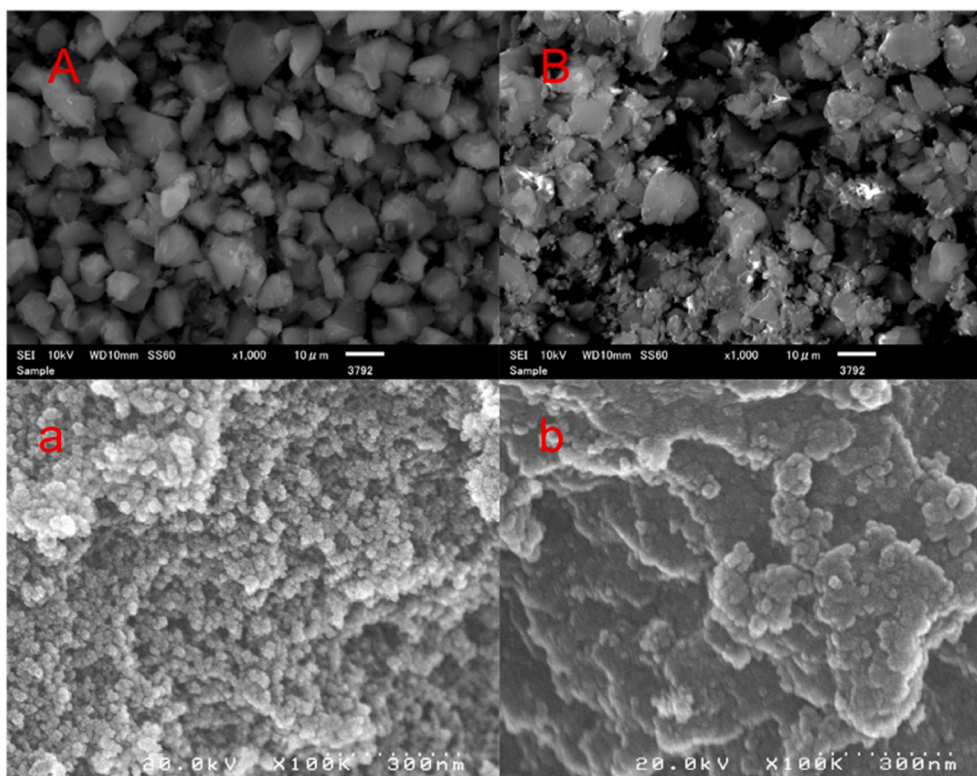


Fig. 2. Morphology of aerogel particles and PEG/aerogel powders (A and B: SEM of aerogel and the prepared PEG/aerogel powders; a and b: FE-SEM of aerogel and the prepared PEG/aerogel powders).

resolution of 4 cm^{-1} .

The crystalline structure of the PEG and the PEG embedded in the aerogel was revealed via XRD (X-ray powder diffraction) (Rotaflex RT300mA, Rigakum Osaka, Japan) at room temperature by using Cu K α radiation (1.54 \AA) source and operating at a power of 40 mA/40 kV in the angle range of $5^\circ \leq 2\theta \leq 45^\circ$ and a step of $2\theta = 0.02^\circ$ under 25°C .

The thermal stability of the PEG and the PEG/aerogel powders as well as the adsorption of PEG in the PEG/aerogel powders was recorded via thermogravimetry-differential thermal analysis (TG-DTA) analysis produced by Thermo plus (TG 8210). All samples were weighted ranging from 0.2 to 0.6 mg for the measurement separately. During the test, the applied temperature increased from 16°C to 500°C with a fixed heating rate of 10 K/min . The thermal stability of the PEG and the prepared PEG/aerogel powders were revealed from the results of TG-DTA curves including the initial decomposition temperature ($T_{d,i}$), the temperature corresponding to the highest weight loss rate ($T_{d,w}$), the final

decomposition temperature ($T_{d,f}$) and the weight loss (χ_w).

The thermal capacity of the PEG and the PEG/aerogel powders was revealed via differential scanning calorimetry (DSC) (METTLER TOLEDO). The PEG/aerogel powders experienced the heating/cooling process ranging from 25°C to 70°C with a 2°C/min heating/cooling rate, which was the 1st heating/cooling round. Then the PEG/aerogel powders experienced a 10 repeated heating/cooling process ranging from 25°C to 70°C with a 20°C/min heating/cooling rate. After the repeated cycles, the PEG/aerogel powders experienced the same heating/cooling process as the 1st round, which was labeled as 11th. The results from 1st and 11th DSC curves included the phase change range as well as melting and solidification enthalpy ($\Delta H_{m/c}$). Besides, theoretical melting and solidification enthalpy of different PEG embedded in aerogel powders ($\Delta H_{m/c}^T$) was also calculated according to equation (4) [27]:

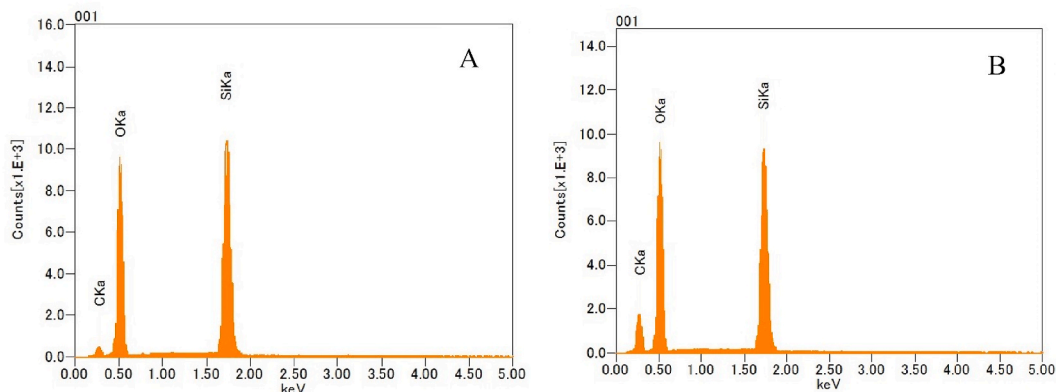


Fig. 3. EDS analysis of aerogel particles (A) and PEG/aerogel powders (B).

Table 2
EDS analysis.

Sample code	Element content		
	C (wt%)	O (wt%)	Si (wt%)
Aerogel particle	14.26	54.77	30.70
PEG/aerogel powders	33.85	45.71	20.44

$$\Delta H_{m/c}^T = \Delta H_{m/c} \times \chi_w \quad (4)$$

where the χ_w was the corresponding weight loss of PEG in the different PEG/aerogel powders measured by TGA-DTA.

Besides, the encapsulation of the PEG in the aerogel was also evaluated by using the FTIR camera to record the leakage result when the prepared PEG/aerogel powders were heated on the hot plate with 120 °C for 30min.

3. Results and discussion

3.1. Analysis of PEG encapsulation in aerogel powders

Fig. 2 shows that the morphology of the prepared PEG/aerogel powders. The aerogel powders were found as micro powders and the significant mesopores were observed. For PEG/aerogel powders, a little amount of adhesion was caused by the remaining water molecules in the PEG/aerogel powders. After filtration of the PEG/aerogel mixture and during the drying process, the water molecules trapped in PEG molecules were not visible. Hence, the adsorption of PEG on the surface of aerogel that has been fixed and covered as agglomeration. Besides, mesopores were found to be covered by PEG were observed from Fig. 2.

Also, SEM-EDS revealed the change of the surface of PEG/aerogel powders (Fig. 3). It was obvious that the content of silica (Si) element reduced while the content of oxygen (O) and carbon (C) increased in PEG/aerogel powders when compared with aerogel powders (Table 2), which suggested that the embedded PEG molecular filled with certain amounts of pores.

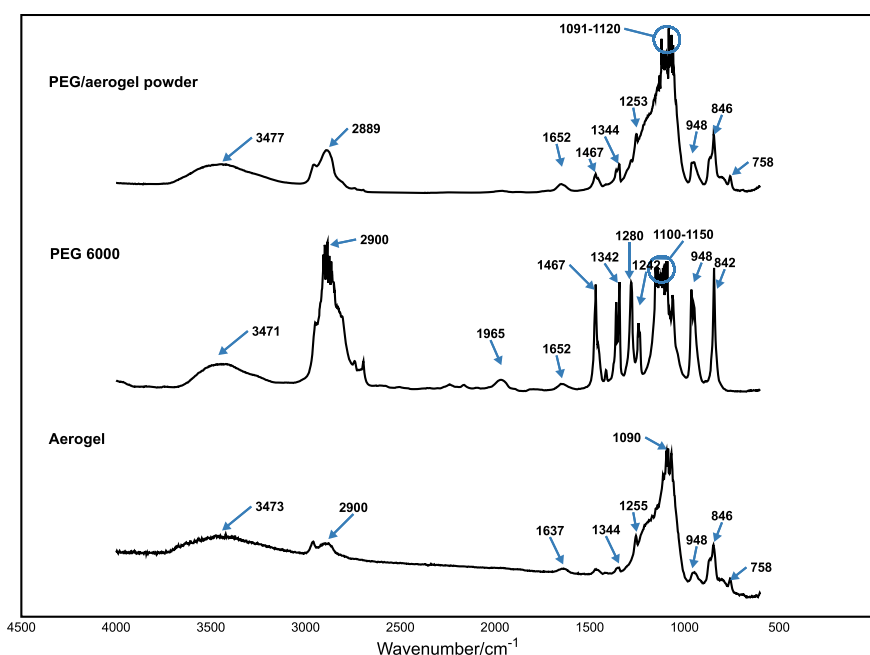
The chemical compatibility between PEG and aerogels was given by FT-IR (Fig. 4). The peaks of all PEG/aerogel powders are shown in Table 3. Especially, the vibration of Si-C at 758 cm⁻¹, the stretching

vibration of C-H at 2900 cm⁻¹, the bending vibration of -CH₂ at 1467 cm⁻¹ were found in the PEG/aerogel powders. Meanwhile, the bending vibration of C-H at 843 cm⁻¹ was not seen in the PEG/aerogel powders. Besides, there was no new peak to be observed, suggesting that only physical change happened during the preparation of PEG/aerogel powders. So, capillary action was the only force to determine the encapsulation.

Isothermal N₂ adsorption/desorption of the aerogel and the PEG/aerogel powders were shown in Fig. 5 (A). During the analysis, all samples should experience three stages: monolayer stage, transition stage, and multilayer stage [28,29]. For aerogel powders, nitrogen gas was absorbed sharply at the lower relative pressure ($P/P_0 < 0.1$), indicating the monolayer formed on the surface of aerogel. The adsorption and desorption curves were almost overlapped. Then the adsorption curve rose slowly in almost a linear way at the medium-high pressure stage ($0.1 < P/P_0 < 0.8$), indicating the transition from monolayer adsorption of nitrogen to multilayer adsorption. During this stage, the hysteresis loop formed gradually with different amplitudes over the relative pressure. At the high-pressure stage ($0.8 < P/P_0 < 1$), the adsorption curve rose sharply and was in a downward concave shape, indicating the capillary condensation. When the relative pressure was close to 1, capillary condensation occurred in micropores, leading to a sharp increase in nitrogen adsorption and sudden rise of isotherm. There was no trend for the decrease of the N₂ adsorption rate at the end of isothermal adsorption. According to the IUPAC scheme shown in Fig. 6, the isothermal adsorption and desorption curve of the aerogel powders were similar to the H3 type [30]. Therefore, the pores in the aerogel powders were proved as slit-shaped. For PEG/aerogel powders, the

Table 3
Main wavelength peaks and their corresponding vibrational assignment.

Wavenumber (cm ⁻¹)	Vibrational assignment
758	Si-C
846,1090	Bending vibration of Si-O
843	Bending vibration of C-H
948	Stretching vibration of Si-OH
1100, 1150, 1200	Stretching vibration of C-OH
1467	Bending vibration of -CH ₂
2900	Stretching vibration of C-H

**Fig. 4.** The FT-IR spectra of aerogel particles and PEG/aerogel powders.

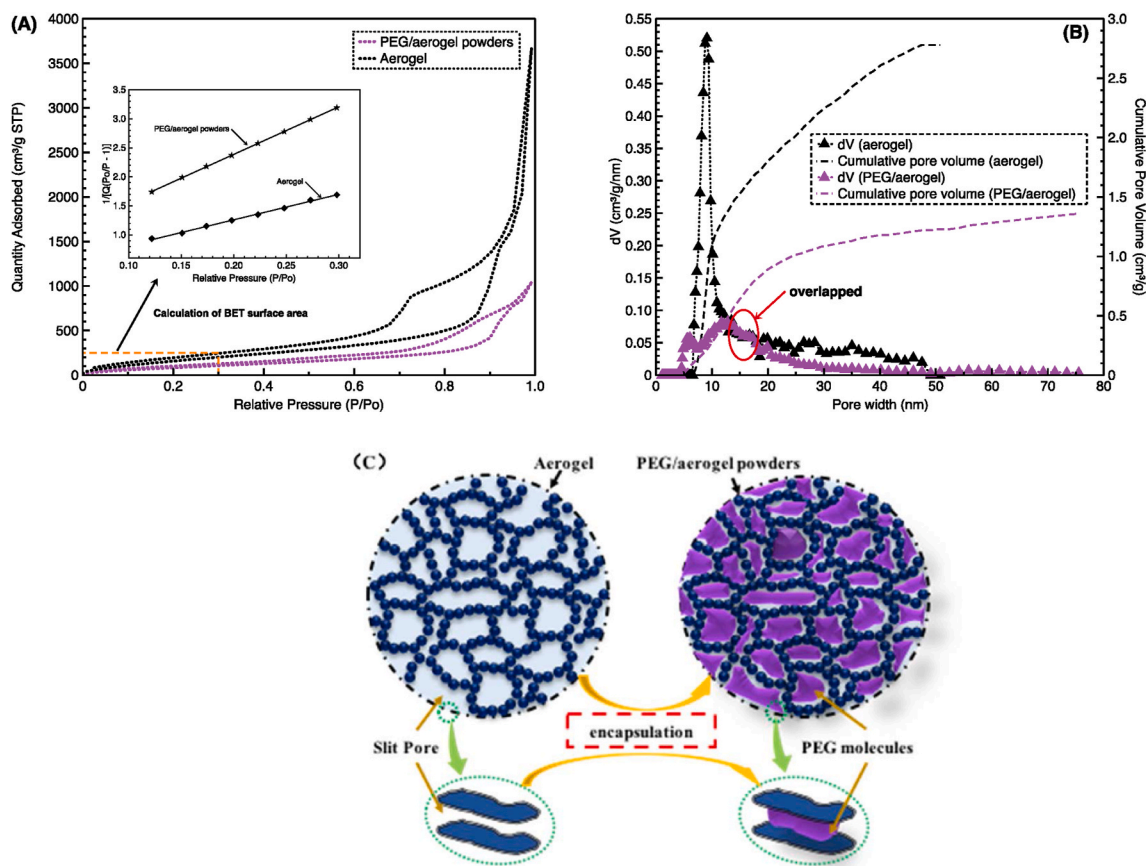


Fig. 5. N₂ adsorption/desorption measurement of the aerogel powders and PEG/aerogel powders (A: Isothermal N₂ adsorption/desorption curves with a calculation of the BET surface area of the aerogel and the prepared PEG/aerogel powders, B: DFT curve of aerogel and the prepared PEG/aerogel powders, C: Scheme of encapsulation of PEG in aerogel).

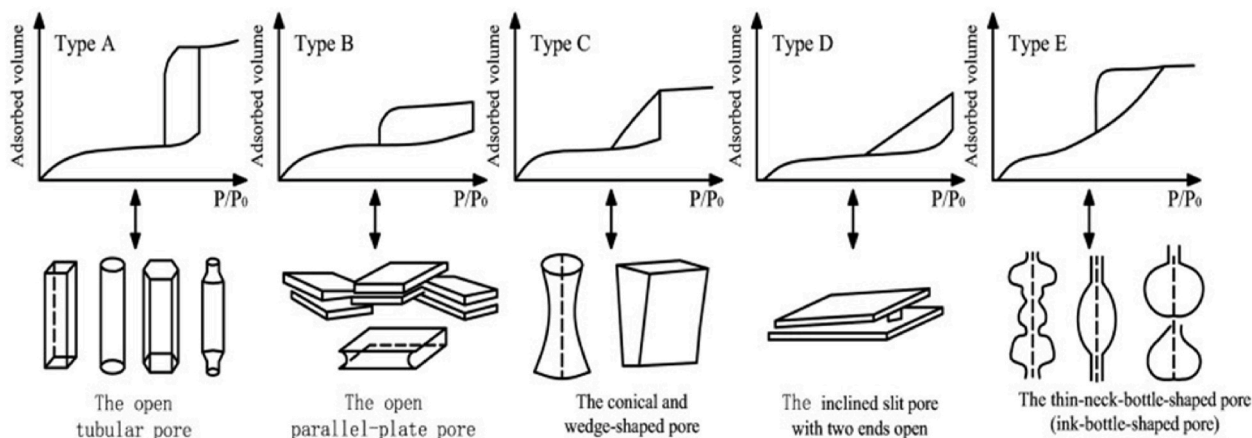


Fig. 6. Classification of adsorption loop curves and pore structure types [26].

Table 4
Porosity characterization of aerogel particles and PEG/aerogel powders.

Sample code	BET surface area (m ² /g)	DFT cumulative pore volume (cm ³ /g)
Aerogel	732	2.78
PEG/aerogel powders	390	1.36

shape of the isotherm curve was similar to those of the aerogel powders, while the amount of the adsorbed N₂ over the relative pressure was reduced. In detail, the BET surface area of aerogel powders and PEG/aerogel powders were separately calculated as 732 m²/g and 390 m²/g, respectively (Table 4). The decrease of the BET surface area proved that the PEG molecules were trapped in the aerogel. It was noticeable that the BET surface area of the PEG/aerogel powders was still large, which suggested that the PEG molecules did not fully fill in the aerogel.

The encapsulation of PEG in the pores of aerogel was also evaluated

Table 5
Mass loaded Rate of PEG inside Aerogel Particles After Preparation.

W_0 (g)	W_i (g)	W_E (g)	$W_{E,PEG}$ (g)	χ_m (wt%)	χ_e (wt%)
2.00	10.00	2.945	0.945	47.25	9.45

W_0 : the mass of the used aerogel powders for filtration, W_i : the initial mass of the PEG powders for the filtration, W_E : the mass of the final PEG/aerogel powders, $W_{E,PEG}$: the mass of the encapsulated PEG in the aerogel, χ_m : encapsulation rate and χ_e : encapsulation efficiency.

by using DFT model and the results (pore volume vs pore size ($\frac{cm^3}{g}$ / Å)) were shown in Fig. 5 (B). It was found that the pore size in the aerogel powders ranged from 6.70 nm to 50.0 nm (67–500 Å) and there was only one highest peak around 9.09 nm, which supported the mesoporous structure of the aerogel powders and that mesopores were in the majority. For the PEG/aerogel powders, the pore volume value reduced obviously over the pore size when compared with pure aerogel powders and the highest peak shifted rightly to the pore size of 11.68 nm. Smaller mesopores of pore sizes between 5 nm and 7 nm appeared in PEG/aerogel, as larger pores had been filled with PEG. The DFT cumulative pore volume decreased from 2.78 to 1.36 cm^3/g when the aerogel was embedded with PEG (Table 4).

According to the static and dynamic properties of the polymer molecules at the adsorbing surface, the polymer molecules had a phase transition from a desorbed state to an adsorbed state, which supported the PEG molecules to move closer to the aerogel surface and became helix-shaped to form a monolayer [31,32]. The PEG monolayer is also stacked together possibly. The difference between the PEG monolayer and the stacked PEG molecular chains was the molecular chain scale. Besides, the adsorption of PEG molecules by the aerogel was only realized by the capillary force, which meant that the pore with various sizes had the selection for the PEG molecules with different molecular scales. In this case, the pores smaller than 14 nm as well as the pores larger than 16 nm were assumed to adsorb the PEG monolayer as well as the stacked PEG chains. Especially, the pore volume values of the PEG/aerogel powders ranging from 14 nm to 16 nm were almost the same as the pure aerogel as seen in the overlapped area in Fig. 5 (B), which meant that the adsorbing ability of the pores ranging from 14 nm to 16 nm for the PEG

molecules from the water system was weak. This may be caused by comprehensive factors including number of pores, pore size and PEG molecular chain scales during the filtration method.

Besides, the encapsulation efficiency (χ_e) (wt%) and the encapsulation rate (χ_m) (wt%) of the PEG in the aerogel was shown in Table 5. It was found that both χ_e and χ_m were much smaller, especially when compared with other work [15]. The main reason was caused by the lower PEG concentration, which was not so significant in this work.

As a result, the PEG was well embedded in various pores of the aerogel powders, which has been schemed in Fig. 5 (C).

3.2. Crystal structure of embedded PEG in aerogel powders

The crystal structure of PEG embedded in the aerogel powders was analyzed in Fig. 7, and the details were given in Table 6. The pure PEG had two main peaks at 18.98° and 23.14°, respectively correspond to the crystal plane of (120) and (112). Therefore, the PEG crystals belonged to the hexagonal crystal system. It was well known that the crystal structure of the pure PEG was spherulite which was composed of the long and fine lamellae with a specific direction [33]. Therefore, (120) and (112) represented the two fine lamellae in the PEG separately [34]. The crystal plane distance (d) of the PEG was 4.67 Å and 3.84 Å. For PEG/aerogel powders, the crystallization ability of the embedded PEG in the aerogel was reduced significantly by observing the large decrease of two main peaks at 19.02° and 23.22° while the crystal plane of the embedded PEG was the same as the pure PEG. Furthermore, the intensity of the (120) crystal plane was reduced more significantly than the (112) crystal plane. The crystal plane distance of the embedded PEG was evaluated as 4.66 Å and 3.82 Å. The small right shift of the two main peaks proved

Table 6
XRD data of PEG and PEG/aerogel powders.

Sample	2θ	d_I (Å)	hkl	$FWHM$ (°)	Crystal size (nm)
PEG 6000	18.98	4.67	120	0.198	503
	23.14	3.84	112	0.50	166
PEG/aerogel powders	19.02	4.66	120	0.351	239
	23.22	3.82	112	0.61	135

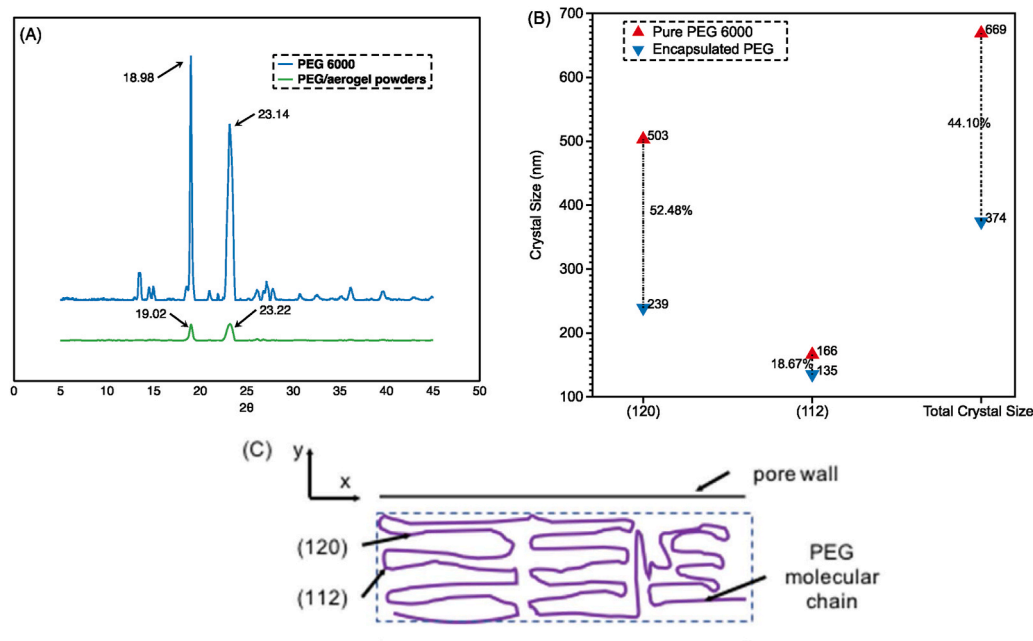


Fig. 7. XRD analysis of the PEG and the prepared PG/aerogel powders (A: XRD curves, B: Crystal size of PEG with and without encapsulation in the aerogel powders and C: scheme of the encapsulated PEG crystals in the aerogel).

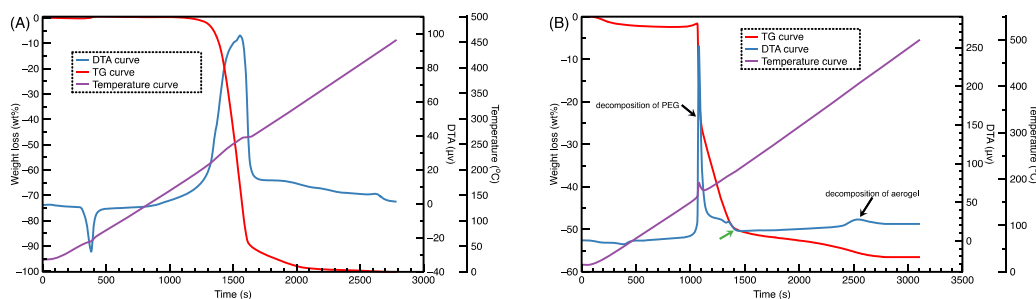


Fig. 8. TG-DTA curves of the PEG (A) and the prepared PEG/aerogel (B).

Table 7

Thermal stability from TG-DTA curves.

Sample code	$T_{d,i}$ (°C)	$T_{d,w}$ (°C)	$T_{d,f}$ (°C)	Weight loss (χ_w) (%)
PEG 6000	218.00	259.26	421.75	100
PEG/aerogel powders	161.76	192.15	220.81	50.25

that there was an adhesion between PEG molecules and aerogel but the effect on the crystal plane was not significant.

The full width at half maximum (FWHM) of the embedded PEG in the aerogel at two peaks increased when compared with pure PEG (Table 6). The crystal size of the two crystal planes of the embedded PEG in the aerogel powders correspondingly decreased (Table 6). Therefore, the limitation of the PEG molecular conformation by the aerogel was found. Furthermore, the different limitations were observed for the different PEG crystal systems by comparing the decreasing rate shown in Fig. 7 (B). In detail, the crystal size of (120) in the embedded PEG in the aerogel decreased 52.48% and the crystal size of (112) decreased 18.67% when compared with pure PEG. Besides, the total crystal size of the embedded PEG in the aerogel was found 44.10% less than the pure PEG.

According to ref. [25], there may be two reasons for the crystal structure of PEG embedded in the aerogel.

- 1) The first factor associated with the size-effect is common to the nano-scale powders. During the adsorption of PEG molecules at a surface form the water solvent, the PEG molecular chains tended to be packed together normally to the pore walls (y-direction). The packed PEG molecular chains formed (120) and (112). However, the small slit-shaped pore size limited such growth along y-direction and the PEG molecular chains were forced to move and fill the pore along x-direction, which was assumed as amorphous. Therefore, the crystallinity of the embedded PEG in the aerogel was reduced and the PEG crystals tended to be 2-D.
- 2) As the pore surface of the aerogel is rough and the pores are irregularly connected, the polymer chains (at least a part of them) may be

adsorbed onto the pore wall randomly during crystallization, which resulted in disordering in the packing of the chains.

As a result, an incomplete PEG crystalline lattice at the surface with a large ratio to the volume of the nano-sized systems was found. Correspondingly, a reduced crystallinity of the PEG in the various mesopores of the aerogel was found.

3.3. Thermal analysis of the embedded PEG in aerogel powders

The thermal stability of the PEG and the embedded PEG in aerogel powders were evaluated via the TG-DTA method (Fig. 8). In details, the initial decomposition temperature ($T_{d,i}$), the temperature corresponding to the highest weight loss rate ($T_{d,w}$) and the final decomposition temperature ($T_{d,f}$) and the weight loss (χ_w) at $T_{d,f}$ of the PEG and the embedded PEG in the aerogel, powders were shown in Table 7. Especially, the $T_{d,f}$ here was evaluated by observing the stable DTA curves.

The overall thermal stability of the embedded PEG in the aerogel powders was reduced significantly. The $T_{d,i}$ and $T_{d,w}$ of PEG/aerogel powders decreased from 218 °C and 248.88 °C to 163.06 °C and 192.15 °C respectively. The $T_{d,f}$ of the pure PEG was investigated around 421.75 °C, after which the DTA curve was stable. While the $T_{d,f}$ of the embedded PEG of the aerogel, powders were considered as 220.81 °C, after which the DTA curve had a slight increase. According to our previous work, the sintering of the aerogel happened when the temperature was higher than 220.81 °C. Besides, there was a slight peak around 400 °C, which was the decomposition of the aerogel powders. As a result, the decomposition process of the embedded PEG in the aerogel powders was much shorter than the PEG. The weight loss of the PEG in the aerogel powders was around 50.25 wt% at the 220.81 °C, which was a little higher than the measured χ_m (47.25 wt%) shown in 'section 3.1' while the difference was not significant. Besides, there was a small rise in the TG-DTA cures of PEG/aerogel powders which suggested that there were little water molecules inside.

There were two reasons for the reduced thermal stability and lower encapsulation efficiency:

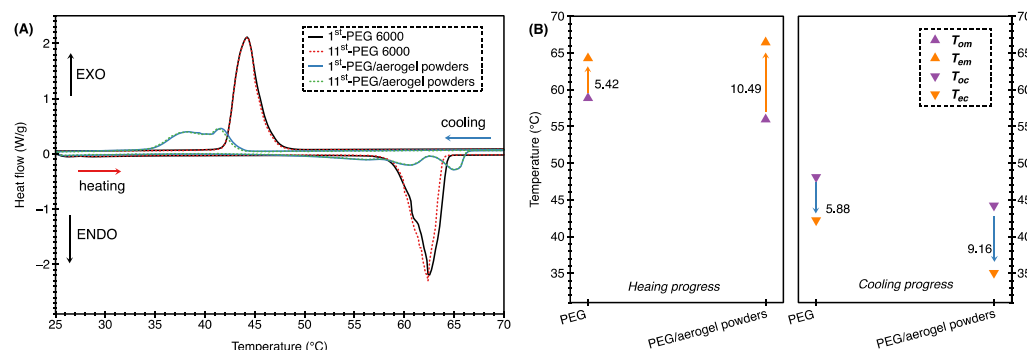


Fig. 9. DSC curves of the PEG and the prepared PEG/aerogel powders (A: 1st and 11th DSC curves and B: phase transition range from the 1st DSC curve).

Table 8

Thermal performance calculated from DSC curves.

Sample code		T_{om} (°C)	T_{pm} (°C)	T_{em} (°C)	ΔH_m (J/g)	T_{oc} (°C)	T_{pc} (°C)	T_{ec} (°C)	ΔH_c (J/g)
PEG 6000	1st	58.85	62.44	64.27	157.45	48.10	44.23	42.22	143.31
	11th	59.59	62.38	63.85	153.72	47.89	44.39	42.01	142.76
PEG/aerogel powders	1st	55.95	64.97	66.44	34.10	44.21	41.61	35.05	59.04
	11th	60.12	65.00	66.92	34.04	43.97	41.57	34.89	58.77

Table 9

Theoretical Enthalpy of the PEG and the encapsulated PEG in aerogel.

Sample Type		ΔH_{mPEG}^T (J/g)	ΔH_{cPEG}^T (J/g)
PEG 6000	1st	74.40	67.71
	11th	72.63	67.45
PEG/aerogel powders	1st	34.10	59.04
	11th	34.04	58.77

- 1) It was obvious that the trapped water molecules accounted for the lower crystallization of embedded PEG and the lower thermal stability of PEG/aerogel powders. For the 20 wt% PEG aqueous solution, a water molecule bridged between PEG oxygens separated by two ethylene oxide (EO) units and the extensive hydrogen-bond network was formed, which promoted the helix conformation of the PEG molecular chains in the water from the random coil chains. Such a structure also enhanced the hydrophilicity of PEG molecules in the water system, which caused limited adsorption by the aerogel correspondingly and a certain trapped water molecule trapped in the PEG/aerogel powders during evaporation.
- 2) Various PEG crystals characterized with different sizes were assumed to be in the various mesopores according to BET analysis. Such a complex crystal structure resulted in the lower thermal stability of PEG/aerogel powders.

The thermal capacity of the PEG and the embedded PEG in aerogel powders was measured by DSC and shown in Fig. 9, and the key parameters including onset melting temperature (T_{om}), peak melting temperature (T_{pm}), endset melting temperature (T_{em}), onset cooling temperature (T_{oc}), peak cooling temperature (T_{pc}), endset cooling temperature (T_{ec}), melting enthalpy change (ΔH_m) and solidification enthalpy change (ΔH_c) was also calculated and shown in Table 8.

Better stability in the thermal capacity of the PEG/aerogel powders was found than the pure PEG by observing the overlapped 1st and 11th DSC curves, which suggested the excellent encapsulation of the PEG in the aerogel. However, the thermal capacity of the PEG/aerogel reduced significantly when compared with the PEG. In detail, the main peak area of PEG/aerogel powders during the heating/cooling process became much smaller. By observing the 1st DSC curves, the enthalpy ($\Delta H_{m/c}$) significantly reduced from 157.45 J/g and 143.31 J/g to 34.1 J/g and 59.04 J/g respectively after the encapsulation of PEG in the aerogel. The theoretical enthalpy of PEG embedded in aerogel was also calculated

and shown in Table 9, which was much smaller than the theoretical enthalpy of the PEG. By combining with BET and XRD analysis, the decreased crystal sizes of the embedded PEG in the aerogel and the limitation of the growth of the (120) crystal system resulted in the reduced overall thermal capacity. Besides, the broader phase transition of the embedded PEG was also found, which was caused by the various PEG crystals embedded in the diverse mesopores.

Besides, Fig. 10 gave the observational information about the leakage of the prepared PEG/aerogel powders under 120 °C for 30min. The prepared PEG/aerogel powders were kept in the form of solid (here is the powder), and there was no trace on the paper. The result proved that melted PEG was well confined in the aerogel during phase change due to the physical capillary force.

4. Conclusion

In this work, PEG/aerogel powders were successfully prepared via the physical blending and filtration method, although the good compatibility between the water and PEG reduced the encapsulation efficiency. It was found that the different slit-shaped mesopores in the aerogel had different adsorption for the PEG molecules. A suitable pore size range for the adsorption of the PEG molecules was considered. Both (120) and (112) crystal plane system in the PEG was limited in the aerogel, which accounted for decreasing crystallinity. The PEG crystals in the aerogel were limited as an uncompleted when compared with pure PEG and tended to be 2-D. No leakage and stable thermal capacity of the PEG/aerogel powders suggested that the good encapsulation of the PEG molecules in the aerogel. The melted PEG molecules in the PEG/aerogel powders could be assumed as such a nanofluid to behold well in various mesopores of the aerogel powders due to the capillary force.

We proposed that this work may initiate similar researches relative with the reasonable choice for porous materials with various pores for the storage of the macromolecules, like dyeing of the porous materials, drug delivery, thermal energy storage, and so on.

CRedit authorship contribution statement

Kai Yang: Conceptualization, Methodology, Software, Validation, Formal analysis, Investigation, Data curation, Writing - review & editing, Writing - original draft, Project administration, Funding acquisition, Supervision. **Mohanapriya Venkataraman:** Conceptualization, Methodology, Validation, Writing - review & editing, Supervision. **Jana**

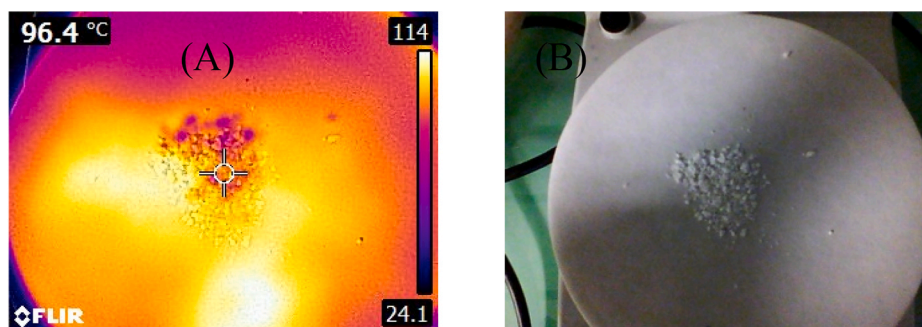


Fig. 10. Leakage test of the prepared PEG/aerogel powders (A: IR image and B: real photo).

Karpiskova: Software, Validation, Formal analysis, Writing - review & editing. **Yuji Suzuki:** Software. **Sana Ullah:** Software, Formal analysis. **Ick-Soo Kim:** Resources. **Jiri Militky:** Writing - review & editing, Project administration, Funding acquisition. **Yuanfeng Wang:** Validation, Data curation. **Tao Yang:** Data curation. **Jakub Wiener:** Resources. **Guocheng Zhu:** Project administration, Funding acquisition. **Juming Yao:** Project administration, Funding acquisition.

Declaration of competing interest

The authors declare that they have no known competing financial interests or personal relationships that could have appeared to influence the work reported in this paper.

Acknowledgment

This work was supported by the research project (No. 21307/2019) of the Student Grant Competition of Technical University of Liberec granted by the Ministry of Education Youth and Sports of Czech Republic, the project 'Hybrid Materials for Hierarchical Structures' (HyHi, Reg. No. CZ.02.1.01/0.0/0.0/16_019/0000843) granted by the Ministry of Education, Youth and Sports of the Czech Republic and the European Union – European Structural and Investment Funds in the Frames of Operational Programme Research, Development, and Education, the project 'design of multi-layer micro/nanofibrous structures for air filters applications' (Reg. No. 8JCH1064) granted by the Ministry of Education, Youth and Sports in the frames of support for researcher mobility (VES19China-mobility, Czech-Chinese cooperation) and the project 'Research Infrastructure NanoEnviCZ' (No. LM2018124) granted by the Ministry of Education, Youth and Sports of the Czech Republic. The work was also supported by the project SMARTTHERM 'Intelligent thermoregulatory fibers and functional textile coatings based on temperature resistant embedded PCM' (Project No. TF06000048) granted by the Technology Agency of the Czech Republic (DELTA Programme).

References

- Y. Kou, S. Wang, J. Luo, K. Sun, J. Zhang, Z. Tan, Q. Shi, Thermal analysis and heat capacity study of polyethylene glycol (PEG) phase change materials for thermal energy storage applications, *J. Chem. Thermodyn.* 128 (2019) 259–274, <https://doi.org/10.1016/j.jct.2018.08.031>.
- A. Kuru, S.A. Aksoy, Cellulose-PEG grafts from cotton waste in thermo-regulating textiles, *Textil. Res. J.* 84 (2014) 337–346, <https://doi.org/10.1177/0040517513494251>.
- K. Knop, R. Hoogenboom, D. Fischer, U.S. Schubert, Poly(ethylene glycol) in drug delivery: pros and cons as well as potential alternatives, *Angew. Chem. Int. Ed.* 49 (2010) 6288–6308, <https://doi.org/10.1002/anie.200902672>.
- A.Y.L. Tang, C.H. Lee, Y.M. Wang, C.W. Kan, A study of PEG-based reverse micellar dyeing of cotton fabric: reactive dyes with different reactive groups, *Cellulose* 26 (2019) 4159–4173, <https://doi.org/10.1007/s10570-019-02340-0>.
- S. Sundararajan, A.B. Samui, P.S. Kulkarni, Versatility of polyethylene glycol (PEG) in designing solid-solid phase change materials (PCMs) for thermal management and their application to innovative technologies, *J. Mater. Chem. A* 5 (2017) 18379–18396, <https://doi.org/10.1039/c7ta04968d>.
- D.G. Prajapati, B. Kandasubramanian, A review on polymeric-based phase change material for thermo-regulating fabric application, *Polym. Rev.* (2019) 1–31, <https://doi.org/10.1080/15583724.2019.1677709>, 0.
- R. Majumdar, K.S. Alexander, A.T. Riga, Physical characterization of polyethylene glycols by thermal analytical technique and the effect of humidity and molecular weight, *Pharmazie* 65 (2010) 342–346, <https://doi.org/10.1691/ph.2010.9280>.
- T. Chen, H. Sun, P. Mu, Z. Zhu, J. An, W. Liang, A. Li, Fatty amines as a new family of organic phase change materials with exceptionally high energy density, *Sol. Energy Mater. Sol. Cells* 206 (2020) 110340, <https://doi.org/10.1016/j.solmat.2019.110340>.
- S. Karaman, A. Karaipekli, A. Sar, A. Biçer, Polyethylene glycol (PEG)/diatomite composite as a novel form-stable phase change material for thermal energy storage, *Sol. Energy Mater. Sol. Cells* 95 (2011) 1647–1653, <https://doi.org/10.1016/j.solmat.2011.01.022>.
- K.E. Gubbins, Y. Long, M. Śliwina-Bartkowiak, Thermodynamics of confined nano-phases, *J. Chem. Thermodyn.* 74 (2014) 169–183, <https://doi.org/10.1016/j.jct.2014.01.024>.
- T. Qian, J. Li, H. Ma, J. Yang, The preparation of a green shape-stabilized composite phase change material of polyethylene glycol/SiO₂ with enhanced thermal performance based on oil shale ash via temperature-assisted sol-gel method, *Sol. Energy Mater. Sol. Cells* 132 (2015) 29–39, <https://doi.org/10.1016/j.solmat.2014.08.017>.
- Y. Deng, J. Li, T. Qian, W. Guan, Y. Li, X. Yin, Thermal conductivity enhancement of polyethylene glycol/expanded vermiculite shape-stabilized composite phase change materials with silver nanowire for thermal energy storage, *Chem. Eng. J.* 295 (2016) 427–435, <https://doi.org/10.1016/j.cej.2016.03.068>.
- J. Guo, H.X. Xiang, Q.Q. Wang, D.Z. Xu, Preparation and properties of polyacrylonitrile fiber/binary of fatty acids composites as phase change materials, *Energy Sources, Part A Recovery, Util. Environ. Eff.* 35 (2013) 1064–1072, <https://doi.org/10.1080/15567036.2010.518217>.
- X. Geng, W. Li, Y. Wang, J. Lu, J. Wang, N. Wang, J. Li, X. Zhang, Reversible thermochromic microembedded phase change materials for thermal energy storage application in thermal protective clothing, *Appl. Energy* 217 (2018) 281–294, <https://doi.org/10.1016/j.apenergy.2018.02.150>.
- W. Aftab, X. Huang, W. Wu, Z. Liang, A. Mahmood, R. Zou, Nanoconfined phase change materials for thermal energy applications, *Energy Environ. Sci.* 11 (2018) 1392–1424, <https://doi.org/10.1039/c7ee03587j>.
- W. Wang, X. Yang, Y. Fang, J. Ding, Preparation and performance of form-stable polyethylene glycol/silicon dioxide composites as solid-liquid phase change materials, *Appl. Energy* 86 (2009) 170–174, <https://doi.org/10.1016/j.apenergy.2007.12.003>.
- B. Coasne, A. Galarnau, R.J.M. Pellenq, F. Di Renzo, Adsorption, intrusion and freezing in porous silica: the view from the nanoscale, *Chem. Soc. Rev.* 42 (2013) 4141–4171, <https://doi.org/10.1039/c2cs35384a>.
- M. Venkataraman, R. Mishra, J. Militky, X. Xiong, J. Marek, J. Yao, G. Zhu, Electrospun nanofibrous membranes embedded with aerogel for advanced thermal and transport properties, *Polym. Adv. Technol.* 29 (2018) 2583–2592, <https://doi.org/10.1002/pat.4369>.
- M. Venkataraman, J. Wiener, R. Mishra, J. Militky, P. Exnar, A STUDY ON PENETRATION OF POLYMERS IN AEROGEL GRANULAR PARTICLES, 2013.
- A. Shaid, L. Wang, S. Islam, J.Y. Cai, R. Padhye, Preparation of aerogel-eicosane microparticles for thermoregulatory coating on textile, *Appl. Therm. Eng.* 107 (2016) 602–611, <https://doi.org/10.1016/j.applthermaleng.2016.06.187>.
- Z. Xiangfa, X. Hanning, F. Jian, Z. Changrui, J. Yonggang, Preparation, properties and thermal control applications of silica aerogel infiltrated with solid-liquid phase change materials, *J. Exp. Nanosci.* 7 (2012) 17–26, <https://doi.org/10.1080/17458080.2010.497950>.
- X. Zhou, H. Xiao, J. Feng, C. Zhang, Y. Jiang, Preparation and thermal properties of paraffin/porous silica ceramic composite, *Compos. Sci. Technol.* 69 (2009) 1246–1249, <https://doi.org/10.1016/j.compscitech.2009.02.030>.
- H. Gao, J. Wang, X. Chen, G. Wang, X. Huang, A. Li, W. Dong, Nanoconfinement effects on thermal properties of nanoporous shape-stabilized composite PCMs: a review, *Nano Energy* 53 (2018) 769–797, <https://doi.org/10.1016/j.nanoen.2018.09.007>.
- G. Li, Y. Huang, J. Lin, C. Yu, Z. Liu, Y. Fang, Y. Xue, C. Tang, Effective capture and reversible storage of iodine using foam-like adsorbents consisting of porous boron nitride microfibers, *Chem. Eng. J.* 382 (2020) 122833, <https://doi.org/10.1016/j.cej.2019.122833>.
- F. Tian, S. Zhang, M. Zhai, J. Sui, X. Lan, J. Gao, Thermal properties of nano-sized polyethylene glycol confined in silica gels for latent heat storage, *Thermochim. Acta* 655 (2017) 211–218, <https://doi.org/10.1016/j.tca.2017.05.006>.
- C.Y. Chang, W.T. Tsai, C.H. Ing, C.F. Chang, Adsorption of polyethylene glycol (PEG) from aqueous solution onto hydrophobic zeolite, *J. Colloid Interface Sci.* 260 (2003) 273–279, [https://doi.org/10.1016/S0021-9797\(02\)00174-1](https://doi.org/10.1016/S0021-9797(02)00174-1).
- N. Shukla, A. Fallahi, J. Kosny, Performance characterization of PCM impregnated gypsum board for building applications, *Energy Procedia* 30 (2012) 370–379, <https://doi.org/10.1016/j.egypro.2012.11.044>.
- R. Wang, S. Sang, D. Zhu, S. Liu, K. Yu, Pore characteristics and controlling factors of the lower cambrian hetang formation shale in northeast Jiangxi, China, *Energy Explor. Exploit* 36 (2018) 43–65, <https://doi.org/10.1177/0144598717723814>.
- M. Hashmi, S. Ullah, I.S. Kim, Copper oxide (CuO) loaded polyacrylonitrile (PAN) nanofiber membranes for antimicrobial breath mask applications, *Curr. Res. Biotechnol.* 1 (2019) 1–10, <https://doi.org/10.1016/j.crbt.2019.07.001>.
- Z. ALOthman, A review: fundamental aspects of silicate mesoporous materials, *Materials* 5 (2012) 2874–2902, <https://doi.org/10.3390/ma5122874>.
- W. Chien, Y.L. Chen, Confinement, curvature, and attractive interaction effects on polymer surface adsorption, *J. Chem. Phys.* 147 (2017), 064901, <https://doi.org/10.1063/1.4996738>.
- N. Derkaoui, S. Said, Y. Grohens, R. Olier, M. Privat, Polyethylene glycol adsorption on silica: from bulk phase behavior to surface phase diagram, *Langmuir* 23 (2007) 6631–6637, <https://doi.org/10.1021/la070199u>.
- W.D. Li, E.Y. Ding, Preparation and characterization of cross-linking PEG/MDI/PE copolymer as solid-solid phase change heat storage material, *Sol. Energy Mater. Sol. Cells* 91 (2007) 764–768, <https://doi.org/10.1016/j.solmat.2007.01.011>.
- X. Fu, Y. Xiao, K. Hu, J. Wang, J. Lei, C. Zhou, Thermosetting solid-solid phase change materials composed of poly(ethylene glycol)-based two components: flexible application for thermal energy storage, *Chem. Eng. J.* 291 (2016) 138–148, <https://doi.org/10.1016/j.cej.2016.01.096>.

11.6 Publication 5: Transport Properties of Electro-Sprayed Polytetrafluoroethylene Fibrous Layer Filled with Aerogels/Phase Change Materials

Publication

Xiong, X., Venkataraman, M., Yang, T., Kucerova, K., Militký, J., Yang, K., Zhu, G., Yao, J. Transport Properties of Electro-Sprayed Polytetrafluoroethylene Fibrous Layer Filled with Aerogels/Phase Change Materials. *Nanomaterials*. 10, (2020). DOI: 10.3390/nano10102042.

Author Contribution

- Conceptualization
 - Devised the project, the main conceptual ideas and proof outline.
- Methodology
 - Devised the project, the main conceptual ideas and proof outline.
- Investigation
 - Performing the experiments, and data/evidence collection.
- Writing – Original Draft Preparation
 - Assisted in writing the manuscript, review and editing.
- Others
 - Supervision



Article

Transport Properties of Electro-Sprayed Polytetrafluoroethylene Fibrous Layer Filled with Aerogels/Phase Change Materials

Xiaoman Xiong ^{1,*}, Mohanapriya Venkataraman ¹, Tao Yang ², Klara Kucerova ², Jiří Militký ¹, Kai Yang ¹, Guocheng Zhu ³ and Juming Yao ³

¹ Department of Material Engineering, Faculty of Textile Engineering, Technical University of Liberec, 46117 Liberec, Czech Republic; mohanapriya.venkataraman@tul.cz (M.V.); Jiri.Militky@tul.cz (J.M.); kai.yang@tul.cz (K.Y.)

² Institute for Nanomaterials, Advanced Technologies and Innovation, Technical University of Liberec, 46117 Liberec, Czech Republic; tao.yang@tul.cz (T.Y.); klara.kucerova2@tul.cz (K.K.)

³ School of Material Science and Engineering, Zhejiang Sci-Tech University, Xiasha Higher Education Zone, Hangzhou 310018, China; guocheng-zhu@hotmail.com (G.Z.); yaoj@zstu.edu.cn (J.Y.)

* Correspondence: xiaoman.xiong@tul.cz

Received: 7 September 2020; Accepted: 14 October 2020; Published: 16 October 2020



Abstract: This work is the first attempt to prepare microporous polytetrafluoroethylene (PTFE) fibrous layers embedded with aerogels/phase change materials. For preparation of this layer, the needle-less electro-spray technology of water dispersion of individual components is used. Microstructure characteristics, including surface morphology and particle size distribution, and various properties of the prepared materials were investigated and explained. Transport performance of the fibrous layers embedded with aerogels/phase change materials, such as the transmission of heat, air, and water vapor was evaluated and discussed in details. It was found that the electro-sprayed materials composed by spherical particles with rough surface had compact disordered stacking structure. Aerogels and phase change materials (PCMs) play different roles in determining structural parameters and transport properties of the materials. Those parameters and properties could be flexibly adjusted by optimizing the spinning parameters, changing the content or proportion of the fillers to meet specific requirements.

Keywords: polytetrafluoroethylene; silica aerogel; phase change material; electro-spray; thermal properties; water vapor permeability

1. Introduction

Polytetrafluoroethylene (PTFE) has many unique characteristics such as outstanding chemical stability, non-stick property, corrosion resistance, low thermal conductivity, good thermal stability under high temperature, strong hydrophobicity and high fracture toughness, as a result of the strong C–C bonds in the carbon backbone and side-F groups responsible for the uniform helical sheath formed by the electron cloud of the fluorine atoms [1]. These properties make PTFE attractive for various engineering applications. However, due to its low solubility to most of the solvents and high melt viscosity, it is impossible to fabricate PTFE porous materials by using of some conventional methods, such as phase inversion process and melting-stretching technique.

Electrospray is a promising and attractive approach to develop PTFE porous materials with the advantage of easy management and good flexibility of obtaining a variety of materials to meet different requirements. Electrospray produces small monodisperse particles, in the form of a thin film of fine particles, from a colloidal suspension of solid nanoparticles or a solution of a material. An electro-spray

uses large electric fields to generate a spray of highly charged droplets, the emitter from which the spray originates is a small diameter capillary outlet connected to a high voltage source relative to a ground electrode positioned in front of the emitter [2]. As the electric field becomes stronger, fluid at the edge of the capillary outlet deforms into a Taylor cone jet. If the spinning fluid has sufficiently high surface tension and lower viscosity the jet disintegrates downstream and subsequently breaks up into charged droplets, forming a spray. These droplets are sub-micrometer or micro-meter in diameter and they rapidly evaporate due to their large surface-to-volume ratio, forming an electro-sprayed particle layer deposited on a substrate. Electrospray enables the use of various fillers for performance modification, offering more possibility for the development of PTFE-based porous materials. Properties of these composites strongly depend on the intrinsic properties and interface performance of the polymer and the fillers used [3], the content, size, and mass fraction of fillers [4,5].

Silica aerogel and phase change material (PCM) are two types of particularly interesting materials widely used as fillers in fibrous materials or composites to improve thermal properties. Silica aerogel, as a gel composed of a porous solid where the dispersed phase is air, exhibits lower thermal conductivity than air under the same condition [6] and thus has the potential for low-weight composites presenting extraordinary thermal and multifunctional properties [7]. The lightweight silica aerogel particles have been coated on cotton woven fabric [8] and wool-Aramid blended fabric [9], incorporated with polyester nonwovens by thermal bonding [10], encapsulated in a multi-layered composites [11], embedded in nanofibrous structure by electrospinning [12], successfully achieving significantly lower thermal conductivity of the overall structures. PCMs, functioning by absorbing external incoming heat flux due to phase change and acting as thermal buffering of sudden heat changes, were used for several years mainly for thermal regulating purposes. Organic PCMs with wide range phase transition from 18 till 65 °C are suitable for thermal applications as they show consistency in repeated phase changes [13] and offer a small temporary heating or cooling effect. The temporary enhancement of thermal protection by using PCMs in firefighter's garment was extensively proved by many researchers [14–16]. The simultaneous use of aerogels and PCMs coated on a multilayer fabric structure in firefighter's protective garment provided superior thermal protection and comfort while the final performance of the proposed combination depends on the amount of PCM and its melting enthalpy [13].

A considerable amount of literature has been published on PTFE porous materials, such as the ultrafine fibrous PTFE porous material [17] and PTFE hollow fiber membrane [18] fabricated by electrospinning, focusing on investigation of surface properties. Publications that concentrate on PTFE/aerogel composites more frequently adopt dry mixing of PTFE particles with aerogels [19], wet mixing using aqueous PTFE dispersion [5] or PTFE powder [7,20] for engineering applications. Applying electrospray technique to fabricate PTFE porous materials has been carried out to investigate superhydrophobic behavior of the materials [21,22]. Previous research on electro-sprayed PTFE layers filled with carbon microparticles emphasized the surface properties including roughness, electrical property, and hydrophobicity [23]. So far, however, there has been no attempts to fabricate aerogel or PCM embedded PTFE microporous materials by using electro-spray technique. Transport performance of electro-sprayed PTFE porous materials, such as the transmission of heat, air, and water vapor, still remains unclear. The objective of this study is to fabricate PTFE porous materials embedded with aerogels/PCMs via needle-less electrospray technology and investigate the microstructure characteristics as well as various transport properties. This work could be an important contribution to the field of development and performance modification of PTFE porous materials. It could help further understand the structural characteristic of electro-sprayed PTFE materials and the effect of aerogels, PCMs, as well as the coupled aerogels and PCMs, on transport properties of the overall structure. The prepared materials have the potential to be used for various applications including protective clothing and barrier sheets, by optimizing the spinning liquid composition and also the spinning parameters.

2. Methodology

2.1. Materials

The basic ingredient for electrospray is a commercially available aqueous dispersion of the polymer named Teflon™ PTFE DISP 30 (Chemours, Wilmington, NC, USA). This product is a fluoropolymer suspension containing 60% by weight of polytetrafluoroethylene with typical particle size 220 nm, suspended in distilled water, together with a 6% by weight surfactant. Density of the dispersion is 1510 kg/m³, the viscosity at 25 °C is 25 MPa s. High-purity (99.999%) silica aerogels in the form of powders and granules were both purchased from Cabot Corporation (Boston, MA, USA) to composite with the PTFE via electro-spraying. Specifications of the aerogel powders are listed in Table 1. These silica aerogels are selected because they are commercially available and widely used for insulative coating applications with various functional advantages such as ultra-low thermal conductivity, fully hydrophobicity, safe touch performance and smooth finish. Since the particle size of aerogels may influence the composition and final performance of the electro-sprayed materials, aerogel granules with majority particle size ranging from 0.1 to 0.7 mm were used for comparison. Besides, PCMs in the form of microcapsules synthesized by Zhejiang Sci-tech University (Hangzhou, China) were selected as filler as well. The PCMs were prepared via mixing the oil-phase solution consisted by n-octadecane, methyl methacrylate, butyl acrylate, 2,2'-azobisisobutyronitrile and 2-hydroxyethyl methacrylate with sodium a-olefinsulfonate aqueous solution, shearing and emulsifying the two-phase system, heating and stirring, followed by polymerization [24]. The microcapsules core PCM material is n-octadecane with a general formula C_nH_{2n+2} and shell material is polymethyl methacrylate known as (C₅O₂H₈)_n [24]. Particle size of the PCMs microcapsules ranged from 91.28 to 1484 nm, with a mean value 826 nm. Density of the PCM microcapsules was about 780 kg/m³. These PCM microcapsules were spherical with a smooth surface, offering larger surface tension and better dispersity for further processing and application. The melting temperature range of microcapsules PCM core was 24.62–28.71 °C [24]. All the mentioned materials were used as received.

Table 1. Specifications of aerogel particles used in the study.

Properties	Aerogel Powder
Majority particle size range	2~40 μm
Pore diameter	~20 nm
Porosity	90~95%
Surface area	600~800 m ² /g
Particle density	120~150 kg/m ³
Thermal conductivity	0.012 W m ⁻¹ K ⁻¹ at 25 °C

2.2. Fabrication of Electro-Sprayed PTFE Embedded with Aerogel/PCM

A certain quantity of fillers (aerogels or PCMs) was weighted and mixed with PTFE dispersion to prepare spinning liquid with a specific filler concentration. The liquid was stirred 2 h at room temperature to achieve homogeneous dispersions. Any visible deposition was avoided. The liquid was subsequently transferred to the solution tank in Nanospider device NS 1WS500U (Elmarco Inc., Morrisville, NC, USA) for electro-spraying. The electrode distance was 125 mm, the electrode rotation speed was set at 8 rpm, the applied voltage was −10/45 kV, and the airflow supply was 90/100 m³/h. A polypropylene (PP) spun-bond nonwoven fabric was used as supporting material, the delivery speed was 15 mm/min. The temperature and relative humidity were respectively kept at (22 ± 1) °C and (40 ± 2)% during the entire electrospray process. These spinning parameters were determined based on previous trials, which could ensure continuous spinning to prepare even materials. Schematic diagram of the needle-less electrospinning system of Nanospider used for electrospray is illustrated in Figure 1. The electrostatic force produced between the high voltage supplier and the grounded collector draws the liquid from the surface of electro rotating cylinder, the charged jet then breaks down

into small droplets that solidify during the course and are collected on the surface of support material due to the sufficiently low liquid viscosity [25]. Since the liquid jets are not continuous, the formed film consists of small particles. The electro rotating cylinder keeps the ongoing electrospray process to produce the particles and the even layer of particles is obtained with coordination of the movement of support material.

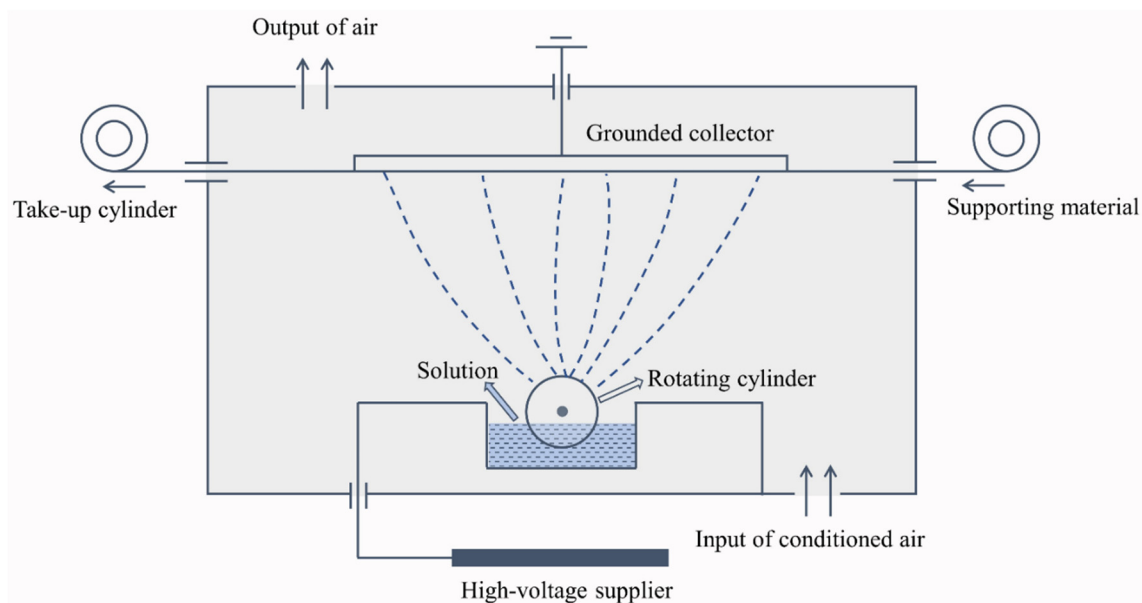


Figure 1. Schematic diagram of needle-less electrospray.

After electro-spraying, the PP nonwoven fabric sheet with electro-sprayed particle surface was dried at 105 °C for 20 min. Besides applying a single type of filler, aerogel particles and PCMs were simultaneously used to prepare electro-sprayed PTFE filled with both aerogels and PCMs, following the same procedure as described. A sample without any fillers was prepared as well. The spinning liquids composition for individual samples is shown in Table 2.

Table 2. Description of the electro-sprayed materials and spinning liquids used for electro-spraying.

Sample Code	Component	Spinning Liquids Used for Electro-Spraying	
		Basic Solution	Fillers
T	PTFE		None
T/C	PTFE + PCM		PCM (3 g/L)
T/AG	PTFE + aerogel granule	Teflon™ PTFE 30	Aerogel granule (3 g/L)
T/AP	PTFE + aerogel powder	aqueous dispersion	Aerogel powder (3 g/L)
T/C/AG	PTFE + PCM + aerogel granule		PCM (3 g/L) + Aerogel granule (3 g/L)
T/C/AP	PTFE + PCM + aerogel powder		PCM (3 g/L) + Aerogel powder (3 g/L)

Note: T—Teflon, C—PCM, AG—Aerogel granule, AP—Aerogel powder.

3. Characterization

3.1. SEM-EDX

Scanning electron microscope (SEM) images were obtained after coating the samples with a gold film, using a VEGA (TESCAN Inc., Warrendale, PA, USA) operating at 30 kV, which provides detailed high-resolution images of the electro-sprayed particles by a focused electron beam across the surface and detecting secondary or backscattered electron signal. The SEM spectrometer was equipped with Energy Dispersive X-Ray (EDX) attachment with Oxford Instruments X-Max^N Silicon Drift Detector (SDD), enabling performing elemental chemical analysis of the electro-sprayed materials. The EDX

measurements were acquired from the characteristic peaks of elements present in the materials via Aztec software (Oxford Instruments, Concord, MA, USA).

3.2. Particle Size Distribution

Based on the SEM images, size distribution of the filler particles was determined via image analysis with Image Tool software. This micro level image analysis is a convenient and effective approach to detect the fillers size and size distribution, dealing with morphological studies in various fields.

3.3. Thickness and Areal Density of the Materials

Thickness of the prepared materials was determined according to the standard ASTM D1777-15 using a fabric thickness tester. Weight per unit length (GSM) of the materials was measured following ASTM D3776-96 standard.

3.4. Air Permeability

Fx-3300 air permeability tester (TESTEST AG, Schwerzenbach, Switzerland) was used to measure air permeability of the electro-sprayed materials following ISO 9237 standard, Determination of the Permeability of Fabrics to Air. Air permeability is described as the ability of a material to transmit air when a certain air pressure drop is applied on both surfaces of the material. Pressure drop 200 Pa was used for the measurements. Each sample was measured 10 times and the values were averaged.

3.5. Thermal Properties from Alambeta

Thermal conductivity and thermal resistance of the electro-sprayed materials were evaluated by using Alambeta Instrument (SENSORIA, Liberec, Czech Republic) according to EN 31092 Standard. The measuring head of the Alambeta moves down to contact with the specimen which is placed on the flat measuring plate, the copper block present in the measuring head is maintained at 32 °C by a thermometer connected to the regulator, the thermal drop between the two surfaces of the specimen is recorded with direct heat flow sensor [26]. According to the Fourier's law of heat conduction, values of thermal conductivity and thermal resistance are automatically calculated and showed on the display screen.

3.6. Water Vapor Permeability

Permetest Instrument (SENSORIA, Liberec, Czech Republic) was employed for the determination of relative water vapor permeability (%) and evaporation resistance R_{et} ($\text{m}^2 \text{ Pa/W}$). The most important component of this device is the measuring head which is covered by semi-permeable foil to keep the sample dry. The heat flow value without a sample is evaluated, and then the fabric was inserted between the measuring head and the orifice in the bottom of the channel to test the heat losses of measuring head covered by a sample. As defined in ISO 11092, water vapor resistance R_{et} is expressed as

$$R_{et} = \frac{P_m - P_a}{q_s^{-1} - q_0^{-1}} \quad (1)$$

where P_m is partial pressure [Pa] of the saturated water vapor of the ambient temperature, P_a is water vapor partial pressure [Pa] of the room, q_s is the heat loss [W/m^2] of measuring head covered by a sample, q_0 is the heat loss [W/m^2] of measuring head without a sample.

4. Results and Discussion

4.1. SEM Analysis of the Electro-Sprayed Materials

As seen in Figure 2, the electro-sprayed particles successfully deposited on the nonwoven substrate, forming a multi-layered cross section structure. The surface morphology of each material is illustrated

in Figure 3. According to the images, the Nanospider technique for this dispersion produced droplets which form spherical solid particles uniformly distributed on the substrate surface. Apparently, the electro-sprayed particles were mostly in spherical shape with rough surface. These particles with different dimensions, mainly in microscale, gathered and partly overlapped with each other, forming a microporous overall structure. The visible single particle is actually a gathering of several small particles, where smaller particles attached on larger ones, exhibiting a compact disordered stacking structure. Aerogels, PCMs, and their combination had insignificant effect on the shape and arrangement of these electro-sprayed particles. However, as the filler used in each material varies, these materials showed slightly different overall surface morphology. Sample T/C/AG and T/C/AP demonstrated more compact structures with smaller particle size variations.

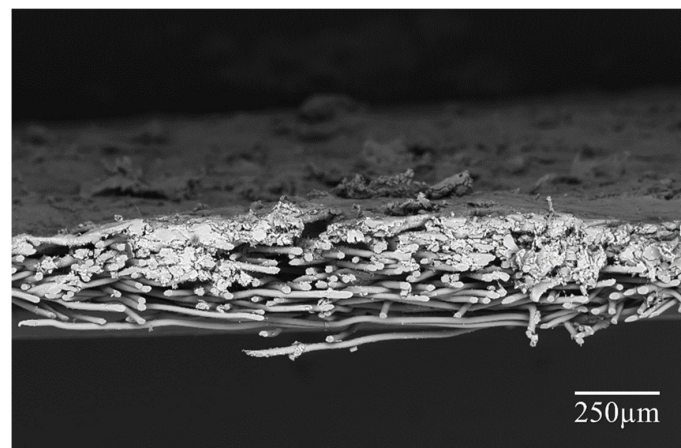


Figure 2. Typical cross section image of the electro-sprayed material.

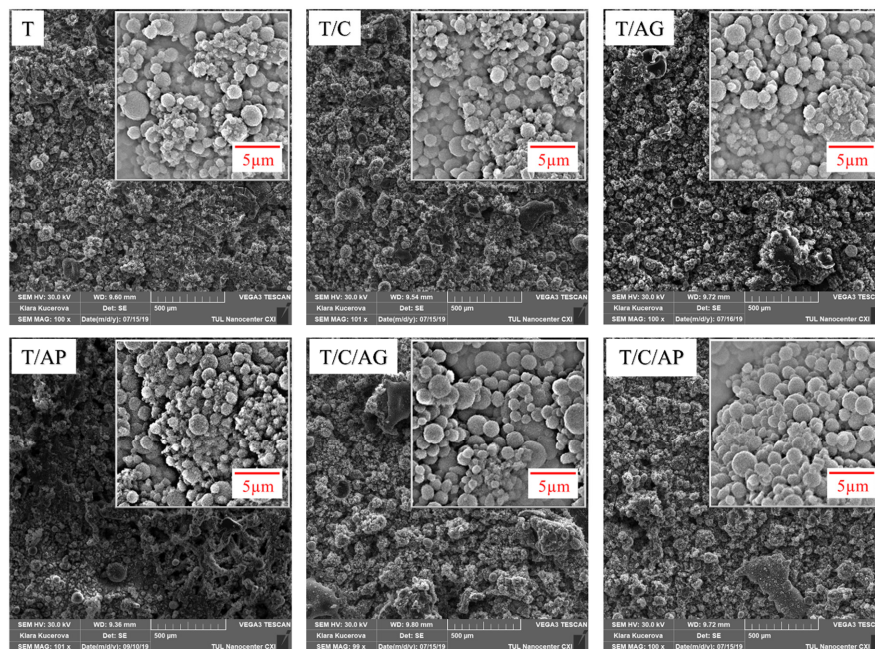


Figure 3. SEMs of the electro-sprayed materials with low magnification (100×) and high magnification (10,000×).

4.2. EDX Analysis of the Electro-Sprayed Materials

The multiple elements in the electro-sprayed materials and element maps obtained from EDX measurement are illustrated in Figure 4. The Au element is attributed to the gold coating necessary for the measurement, while the F element is originated from PTFE and the Si element is the key

characteristics of silica aerogels. Typical element features of the materials without any aerogels are shown as sample T/C. According to the characteristic peaks, the elements F, C and O can be considered to be major elements. The highest peaks observed from F indicates an overwhelmingly dominance of PTFE. The element maps reveal an even distribution of each composition over the entire measuring area. The small amount of silica element appeared on sample T/AG proves the presence of aerogels in the electro-sprayed layer. The uniformly distributed F, C, O and Si element also confirm the homogeneity of the composite. Sample T/C/AP is observed to have similar element characteristic with sample T/AG. However, the O and Si element are found to have higher concentration in this material, indicating more aerogels loaded on the surface. The Cu element is probably resulted from the surfactant presented in PTFE dispersion.

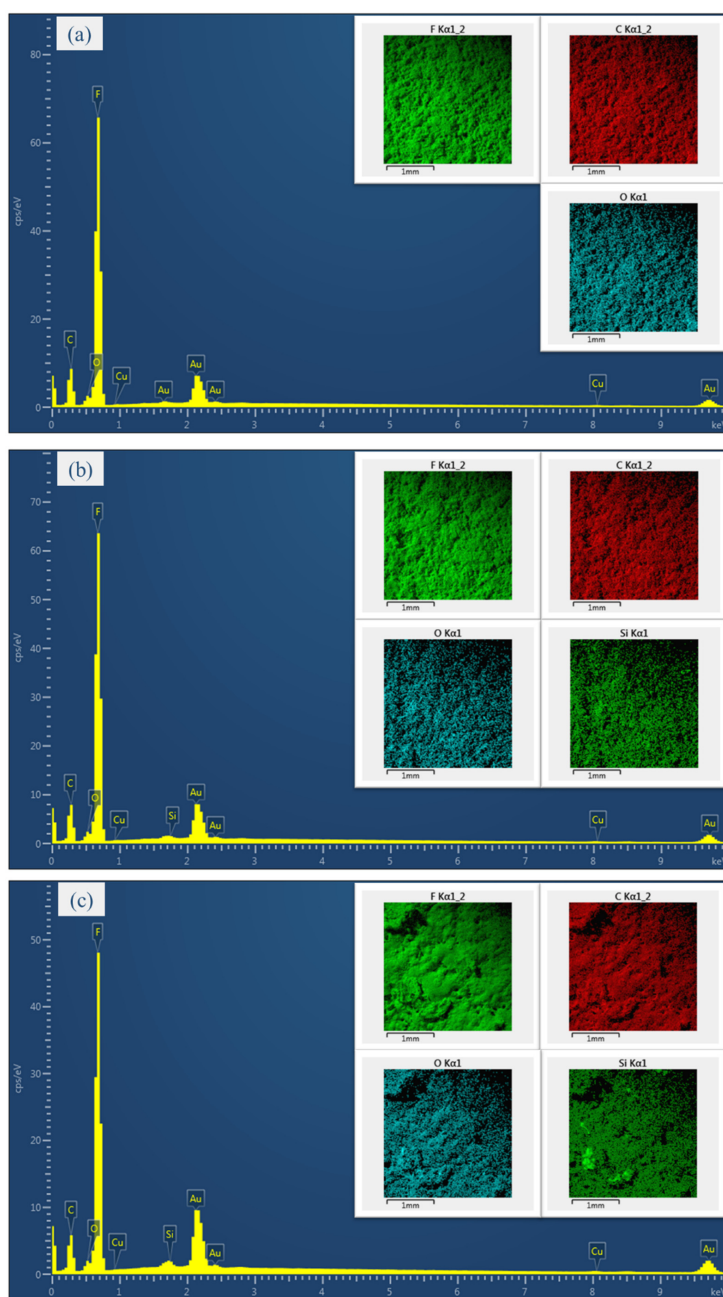


Figure 4. Typical X-ray spectrum and element maps of the electro-sprayed materials (a) sample T/C; (b) sample T/AG; (c) sample T/C/AP.

4.3. Particle Size Distribution of Electro-Sprayed Materials

As seen in Figure 5, the particle diameters of pure PTFE microporous materials are mostly in the range of 0.4–1.8 μm , with a mean value 1.084 μm , which is the smallest among all the samples. It should be noticed that the particle size of PTFE solid present in the suspension is only around 220 nm, but the mean value of the electro-sprayed particles is several times larger. This further indicated that the observed PTFE particles in the microporous materials are coagulations of droplets capturing several single particles. In electro-spray process, the PTFE particles travel with the liquid and get encapsulated inside the droplets after the jet breakup. The emitted droplets undergo solvent evaporation, these droplets disrupt to generate smaller droplets containing fewer or even one single particle in one drop if the electrostatic force is sufficiently strong to overcome surface tension [27,28]. Therefore, the surface charge density of the droplet plays an important role in size distribution of the electro-sprayed particles. The slightly larger average particle dimension in sample T/C is probably attributed to the change of conductivity of the liquid, which influences surface charge density of the droplets as well as the content and distribution of PCMs in the material. Applying aerogels in the spinning liquid could significantly increase the proportion of particles over 2 μm and remarkably decreases small particles under 0.6 μm since the fully hydrophobic surface of aerogels affects the charge density of the droplets and the distribution of different particles. Considering the simultaneous use of aerogels and PCMs, the particle size distributions of these materials are quite close to the samples with only aerogels.

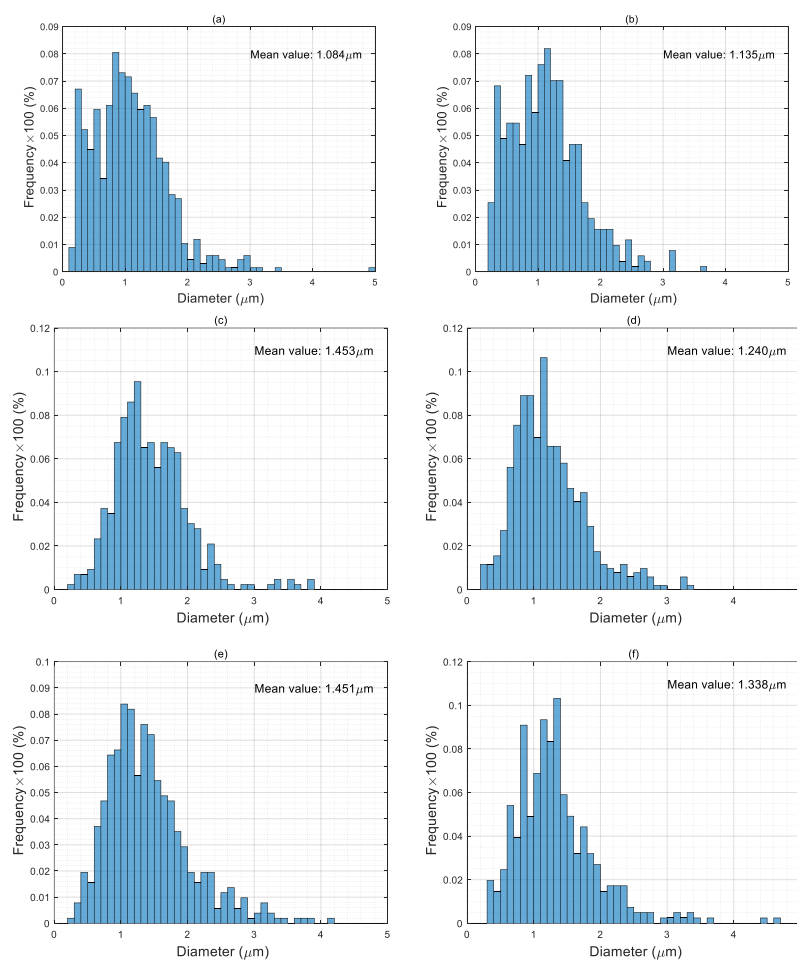


Figure 5. Particle size distributions of the electro-sprayed materials (a) sample T; (b) sample T/C; (c) sample T/AG; (d) sample T/AP; (e) sample T/C/AG; and (f) sample T/C/AP.

4.4. Effect of Aerogels and PCMs on Thickness and Areal Density of the Materials

Thickness and weight of the multi-layered materials are presented in Figure 6. The specimen containing PTFE microparticles has a thickness of 0.424 mm, while the materials consisting aerogels (sample T/AG and T/AP) were only slightly thicker despite the considerably bigger size of aerogels in comparison with PTFE particles. This is probably due to the change of viscosity and electrical conductivity of the solution after adding aerogels, which causes less supply of the particles during electrospray. The significant increase of thickness for those materials containing PCMs is resulted from the hydrophilic surface of PCMs, which improves the ejection of the liquid and therefore create more microparticles. In the case of material weight, PCMs applied in the spinning liquid cause considerable weight increase for the final materials. Besides, both the aerogel granules and aerogel powders decrease the material weight as expected. These materials can be used in applications where less weight burden is necessary.

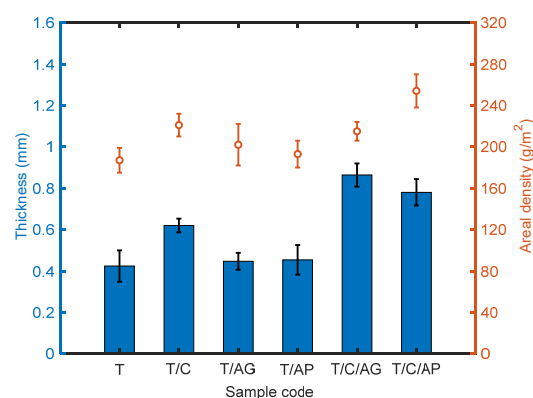


Figure 6. Thickness and areal density of the electro-sprayed materials.

4.5. Effect of Aerogels and PCMs on Air Permeability

Air permeability directly depends on pore size and porosity. All the materials are air permeable as seen in Figure 7, which is mainly attributed to the microporous characteristic of the materials. The highest air permeability value of sample T and relatively lower values of other samples revealed that aerogels and PCMs affect air permeable properties of the electro-sprayed materials. Aerogels could be approximately considered to be air-proof material, therefore, materials containing aerogels showed lower air permeability in comparison with sample T. In particular, aerogel powder has smaller particle size with less pores, which is able to be well incorporated with PTFE microparticles and thus dramatically increases the resistance to airflow. Since the PCM particle inherently has a solid body without any pores, its present in the overall structure leads to lower air permeability as well.

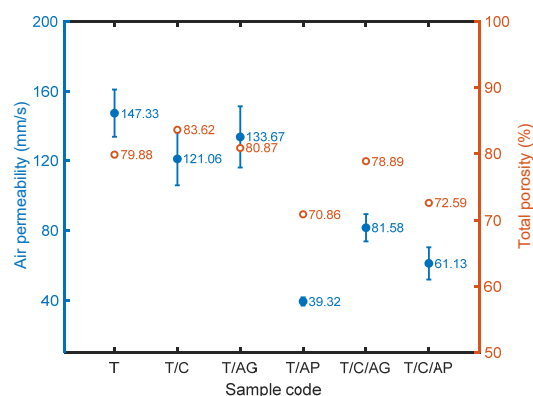


Figure 7. Air permeability and total porosity of the electro-sprayed materials.

The total volume porosity P_0 [-] of layers assembly is defined as

$$P_0 = 1 - \frac{w_T}{h \cdot \rho_F} \quad (2)$$

where w_T [kg/m^2] is planar mass (usually in $\text{gsm}/1000$, where gsm is grams of layer per surface area in square meter), h [m] is layer thickness and ρ_F [kg/m^3] is layer solid phase density. This density is calculated from expression

$$\rho_F = \left(\frac{w_A}{\rho_A} + \frac{w_{PCM}}{\rho_{PCM}} + \frac{w_{PTFE}}{\rho_{PTFE}} + \frac{w_{PP}}{\rho_{PP}} \right)^{-1} \quad (3)$$

where w_A , w_{PCM} , w_{PTFE} , w_{PP} are mass fractions of aerogel, PCM, PTFE, PP and $\rho_A = 120\text{--}150 \text{ kg}/\text{m}^3$, $\rho_{PCM} = 780 \text{ kg}/\text{m}^3$, $\rho_{PTFE} = 2200 \text{ kg}/\text{m}^3$, $\rho_{PP} = 920 \text{ kg}/\text{m}^3$ are corresponding densities. Calculated values of P_0 are shown in Figure 6. As the total porosity decreases, air permeability of the multilayered materials tends to decrease as well.

4.6. Effect of Aerogels and PCMs on Thermal Comfort Properties

Thermal conductivity, measuring the rate at which heat is transferred through unit area of the material across unit thickness under a specified temperature gradient, is an inherent property of a material. As shown in Figure 8, the PCMs present in the electro-sprayed PTFE materials contribute to a lower thermal conductivity probably by means of lower thermal conductivity of PCM shell (polymethylmetacrylate thermal conductivity is $0.19 \text{ W m}^{-1} \text{ K}^{-1}$) in comparison with Teflon ($0.25 \text{ W m}^{-1} \text{ K}^{-1}$). Very low thermal conductivity was achieved by applying aerogels as seen for sample T/AG and T/AP. In particular, sample T/AP has a thermal conductivity as low as $0.029 \text{ W m}^{-1} \text{ K}^{-1}$, behaving better than most of the existing porous insulation materials. Generally, conventional porous or fibrous insulation materials such as polyurethane foam, fiber assembly or fabrics made by various natural or man-made fibers rely on the component of stagnant air in the structure to resist heat transfer through because stagnant air has several times lower thermal conductivity value ($0.024 \text{ W m}^{-1} \text{ K}^{-1}$) than most of the solid and liquid matters. By adjusting the structure characteristics especially overall porosity, conventional porous materials could achieve a thermal conductivity comparable to $0.030 \text{ W m}^{-1} \text{ K}^{-1}$, which could be classified as good insulators since their thermal conductivity is less than $0.033 \text{ W m}^{-1} \text{ K}^{-1}$. However, these materials are several milli-meters or centi-meters thick, which are applicable for engineering use. The electro-sprayed materials have the advantage of low thermal conductivity as well as very small thickness, showing the potential to be used in protective clothing and barrier sheets where the material thickness is greatly restricted. It is also noted that aerogel powder is superior to aerogel granule for decreasing heat transfer rate in this work. This is probably benefited from the smaller particle size which enables the formation of more even material with higher content of aerogels, resulting in lower heat transfer rate. The simultaneous use of aerogels and PCMs leads to slightly lower thermal conductivity than sample T/C, but there is no significant advantage when compared to sample T/AP and T/AG.

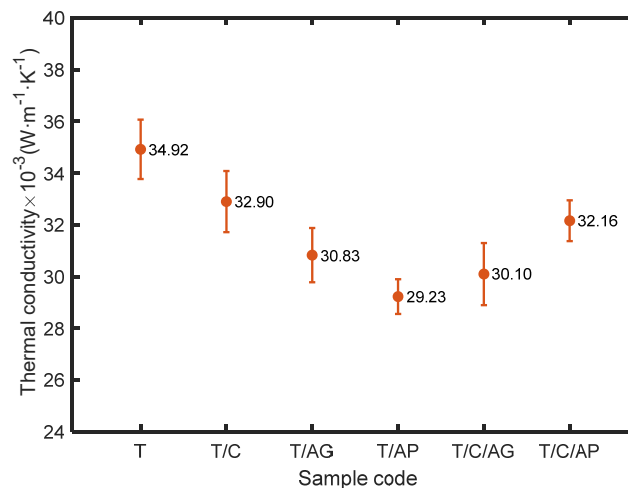


Figure 8. Thermal conductivity of the electro-sprayed materials.

Thermal resistance is determined by thermal conductivity and thickness of the material, expressing the ability of a material to prevent heat flow through the thickness over unit surface area. Figure 9 shows thermal resistance of the prepared materials. Aerogels in the form of powder and granule were both able to achieve slightly thicker materials with higher thermal resistance when compared to sample T. Incorporation of PTFE with PCMs and aerogels (powder or granules) could create much thicker materials with significantly enhanced thermal insulation ability. However, since the electro-sprayed materials are very thin, they could be used as liner in garment or glove to provide better insulation behavior.

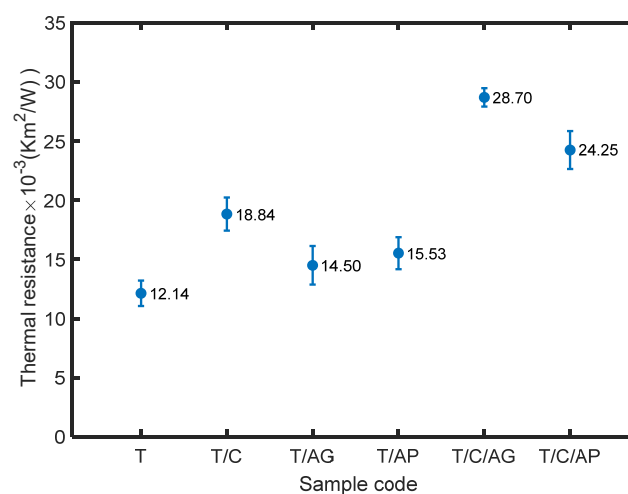


Figure 9. Thermal resistance of the electro-sprayed materials.

4.7. Effect of Aerogels and PCMs on Water Vapor Transmission

As a measure of the passage of water vapor through the material, water vapor permeability depends on the water vapor resistance which indicates the amount of resistance against the transport of moisture through the structure. All the materials are extremely water vapor permeable with water vapor resistance less than $6 \text{ m}^2 \text{ Pa/W}$ as seen in Figure 10. The electro-sprayed PTFE materials, consisting of numerous tiny interconnected pores, are hydrophobic to prevent liquid water from wetting the surface and entering the pores [29]. Since the sorption of water vapor does not occur to any appreciable extent, its water vapor transmission depends on the pathway of moisture vapor diffusion through the air spaces in the materials. Aerogels, present in the electro-sprayed materials, could alter the pore characteristic of the overall structure, thus improve the moisture transmission and decrease the water vapor resistance. Materials that incorporate hydrophilic particles (PCMs) behave

quite differently than materials that depend only on transport through air spaces. The permeability coefficient for hydrophilic particles increases with material thickness, the affinity of the water molecules leads to significant water vapor sorption as well, resulting in significant increase in water vapor permeability [30]. For materials containing PCMs, the resistance to water vapor transmission is independent of the water vapor concentration in the material, but strongly influenced by the relative humidity on both sides of the sample. Therefore, smaller values of water vapor resistance are observed for these materials.

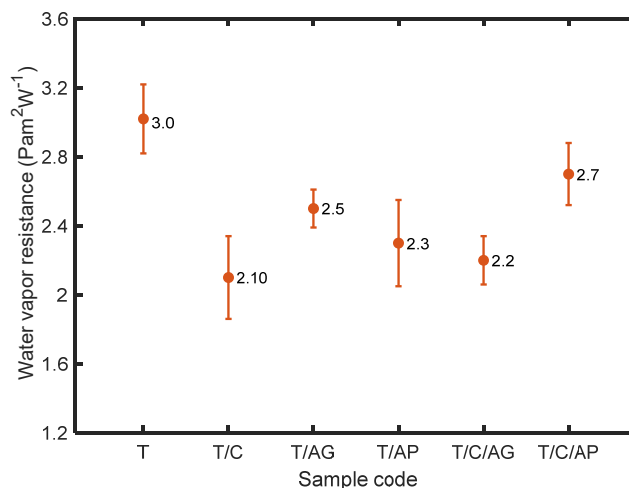


Figure 10. Water vapor resistance of the electro-sprayed materials.

5. Conclusions

Microporous PTFE materials embedded with aerogels/PCMs were prepared via Nanospider technology to investigate various transport properties. It was found that the created materials composed by spherical solid particles had a compact disordered stacking structure. The fillers had insignificant effect on the particle shape and surface morphology of the overall structure, but affected size distribution of the electro-sprayed particles. Results also showed that aerogels could dramatically decrease heat transfer rate of the electro-sprayed materials and slightly increase water vapor transmission by means of influencing the pore characteristic of the overall structure while the PCMs contributed to thicker electro-sprayed materials with better thermal insulation ability and significantly improved water vapor permeability. Therefore, aerogels and PCMs fillers are beneficial for preparing electro-sprayed materials for protective clothing and barrier sheets use where air and moisture permeable properties are essential as well as thermal insulation. By optimizing the component of different fillers, properties of the microporous materials could be adjusted to meet specific requirements.

Author Contributions: Conceptualization, M.V. and X.X.; Methodology, X.X., M.V., K.K. and J.M.; Software, X.X. and T.Y.; Validation, X.X. and T.Y.; Formal analysis, X.X. and J.M.; Investigation, X.X., K.K., M.V. and K.Y.; Resources, K.Y., G.Z. and J.Y.; Data curation, X.X.; Writing—original draft preparation, X.X.; Writing—review and editing, J.M., M.V. and T.Y.; Visualization, X.X. and T.Y.; Supervision, J.M. and M.V. All authors have read and agreed to the published version of the manuscript.

Funding: The result was obtained through the financial support of the Ministry of Education, Youth and Sports of the Czech Republic and the European Union (European Structural and Investment Funds—Operational Programme Research, Development and Education) in the frames of the project “Hybrid Materials for Hierarchical Structures (HyHi)”, Reg. No. CZ.02.1.01/0.0/0.0/16_019/0000843.

Acknowledgments: This work was supported by the Ministry of Education, Youth and Sports of the Czech Republic and the European Union-European Structural and Investment Funds in the frames of Operational Programme, Research, Development and Education-project Hybrid Materials for Hierarchical Structures (HyHi, Reg. No. CZ.02.1.01/0.0/0.0/16_019/0000843), project “Intelligent thermoregulatory fibers and functional textile coatings based on temperature resistant encapsulated PCM” [SMARTTHERM, Project No. TF06000048] and the project “Ministry of Education, Youth and Sports in the frames of support for researcher mobility”

(VES19China-mobility, Czech-Chinese cooperation) and “Design of multi-layer micro/nano fibrous structures for air filters applications”, reg. no. 8JCH1064.

Conflicts of Interest: The authors declare no conflict of interest.

References

1. Feng, S.; Zhong, Z.; Wang, Y.; Xing, W.; Drioli, E. Progress and perspectives in PTFE membrane: Preparation, modification, and applications. *J. Membr. Sci.* **2018**, *549*, 332–349. [[CrossRef](#)]
2. Brown, N.A.; Zhu, Y.; German, G.K.; Yong, X.; Chiarot, P.R. Electro spray deposit structure of nanoparticle suspensions. *J. Electrostat.* **2017**, *90*, 67–73. [[CrossRef](#)]
3. Vail, J.R.; Krick, B.A.; Marchman, K.R.; Sawyer, W.G. Polytetrafluoroethylene (PTFE) fiber reinforced polyetheretherketone composites. *Wear* **2011**, *270*, 737–741. [[CrossRef](#)]
4. Huang, S.; Chen, T.; Chen, H. Study on the composites of two sized silica filled in PTFE. *J. Reinf. Plast. Compos.* **2006**, *25*, 1053–1058. [[CrossRef](#)]
5. Chen, Y.C.; Lin, H.C.; Lee, Y.D. The effects of filler content and size on the properties of PTFE/SiO₂ composites. *J. Polym. Res.* **2003**, *10*, 247–258. [[CrossRef](#)]
6. Pierre, A.C.; Pajonk, G.M. Chemistry of aerogels and their applications. *Chem. Rev.* **2002**, *102*, 243–4265. [[CrossRef](#)] [[PubMed](#)]
7. Huang, D.; Shen, Y.; Yuan, Q.; Wang, C.; Shi, L. Preparation and characterization of silica aerogel/polytetrafluoroethylene composites. *Mater. Res. Express* **2019**, *6*, 115021. [[CrossRef](#)]
8. Rosace, G.; Guido, E.; Colleoni, C.; Barigozzi, G. Influence of textile structure and silica-based finishing on thermal insulation properties of cotton fabrics. *Int. J. Polym. Sci.* **2016**, *2016*. [[CrossRef](#)]
9. Shaid, A.; Fergusson, M.; Wang, L. Thermo-physiological comfort analysis of aerogel nanoparticle incorporated fabric for fire fighter’s protective clothing. *Chem. Mater. Eng.* **2014**, *2*, 37–43.
10. Xiong, X.; Venkataraman, M.; Jašíková, D.; Yang, T.; Mishra, R.; Militký, J.; Petru, M. An experimental evaluation of convective heat transfer in multi-layered fibrous materials composed by different middle layer structures. *J. Ind. Text.* **2019**. [[CrossRef](#)]
11. Xiong, X.; Yang, T.; Mishra, R.; Kanai, H.; Militky, J. Thermal and compression characteristics of aerogel-encapsulated textiles. *J. Ind. Text.* **2017**, *7*, 1998–2013. [[CrossRef](#)]
12. Venkataraman, M.; Mishra, R.; Militky, J.; Xiong, X.; Marek, J.; Yao, J.; Zhu, G. Electrospun nanofibrous membranes embedded with aerogel for advanced thermal and transport properties. *Polym. Adv. Technol.* **2018**, *29*, 2583–2592. [[CrossRef](#)]
13. Shaid, A.; Wang, L.; Padhye, R. The thermal protection and comfort properties of aerogel and PCM-coated fabric for firefighter garment. *J. Ind. Text.* **2016**, *45*, 611–625. [[CrossRef](#)]
14. Cardoso, I.; Gomes, J.R. The application of microcapsules of PCM in flame resistant nonwoven materials. *Int. J. Cloth. Sci. Technol.* **2009**, *21*, 102–108. [[CrossRef](#)]
15. Zhu, F.; Feng, Q.; Liu, R.; Yu, B.; Zhou, Y. Enhancing the thermal protective performance of firefighters’ protective fabrics by incorporating phase change materials. *Fibres Text. East. Eur.* **2015**, *23*, 68–73.
16. Hu, Y.; Huang, D.; Qi, Z.; He, S.; Yang, H.; Zhang, H. Modeling thermal insulation of firefighting protective clothing embedded with phase change material. *Heat Mass Transf.* **2013**, *49*, 567–573. [[CrossRef](#)]
17. Huang, Y.; Huang, Q.; Liu, H.; Zhang, C.; You, Y.; Li, N.; Xiao, C. Preparation, characterization, and applications of electrospun ultrafine fibrous PTFE porous membranes. *J. Membr. Sci.* **2017**, *523*, 317–326. [[CrossRef](#)]
18. Huang, Q.; Huang, Y.; Gao, S.; Zhang, M.; Xiao, C. Novel Ultrafine Fibrous Poly(tetrafluoroethylene)Hollow Fiber Membrane Fabricated by Electrospinning. *Polymers* **2018**, *10*, 464. [[CrossRef](#)]
19. Aderikha, V.N.; Shapovalov, V.A. Tribological behavior of polytetrafluoroethylene-silica composites. *J. Frict. Wear* **2011**, *32*, 124–132. [[CrossRef](#)]
20. Basu, B.J.; Kumar, V.D. Fabrication of superhydrophobic nanocomposite coatings using polytetrafluoroethylene and silica nanoparticles. *Int. Sch. Res. Not.* **2011**. [[CrossRef](#)]
21. Burkarter, E.; Saul, C.K.; Thomazi, F.; Cruz, N.C.; Zanata, S.M.; Roman, L.S.; Schreiner, W.H. Superhydrophobic electrospayed PTFE: A non-contaminating surface. *J. Phys. D Appl. Phys.* **2007**, *40*, 7778–7781. [[CrossRef](#)]
22. Burkarter, E.; Saul, C.K.; Thomazi, F.; Cruz, N.C.; Roman, L.S.; Schreiner, W.H. Superhydrophobic electrospayed PTFE. *Surf. Coat. Technol.* **2007**, *202*, 194–198. [[CrossRef](#)]

23. Venkataraman, M.; Yang, K.; Xiong, X.; Militky, J.; Kremenakova, D.; Zhu, G.; Yao, J.; Wang, Y.; Zhang, G. Preparation of electrospayed, microporous particle filled Layers. *Polymers* **2020**, *12*, 1352. [[CrossRef](#)] [[PubMed](#)]
24. Zhang, G.; Cai, C.; Wang, Y.; Liu, G.; Zhou, L.; Yao, J.; Militky, J.; Marek, J.; Venkataraman, M.; Zhu, G. Preparation and evaluation of thermo-regulating bamboo fabric treated by microencapsulated phase change materials. *Text. Res. J.* **2019**, *89*, 3387–3393. [[CrossRef](#)]
25. Costa, L.M.M.; Bretas, R.E.S.; Gregorio, R. Effect of solution concentration on the electrospay/electrospinning transition and on the crystalline phase of PVDF. *Mater. Sci. Appl.* **2010**, *1*, 247–252. [[CrossRef](#)]
26. Dolezal, I.; Hes, L.; Bal, K. A non-destructive single plate method for measurement of thermal resistance of polymer sheets and fabrics. *Int. J. Occup. Saf. Ergon.* **2019**, *25*, 562–567. [[CrossRef](#)]
27. Lenggoro, I.W.; Xia, B.; Okuyama, K. Sizing of colloidal nanoparticles by electrospay and differential mobility analyzer methods. *Langmuir* **2002**, *18*, 4584–4591. [[CrossRef](#)]
28. Gomez, A.; Tang, K. Charge and fission of droplets in electrostatic sprays. *Phys. Fluids* **1994**, *6*, 404–414. [[CrossRef](#)]
29. Gibson, P.W. Factors influencing steady-state heat and water vapor transfer measurements for clothing materials. *Text. Res. J.* **1993**, *63*, 749–764. [[CrossRef](#)]
30. Swarbrick, J.; Amann, A.H.; Lindstrom, R.E. Factors affecting water vapor transmission through free polymer films. *J. Pharm. Sci.* **1972**, *61*, 1645–1647. [[CrossRef](#)]

Publisher’s Note: MDPI stays neutral with regard to jurisdictional claims in published maps and institutional affiliations.



© 2020 by the authors. Licensee MDPI, Basel, Switzerland. This article is an open access article distributed under the terms and conditions of the Creative Commons Attribution (CC BY) license (<http://creativecommons.org/licenses/by/4.0/>).

11.7 Publication 6: Mass transfer and the thermal buffering effect of hydrophobic fabrics with a single-side coating of MPCMs

Publication

Yang, K., Martinkova, L., Ctibor, O., Zhang, X., **Venkataraman, M.**, Wiener, J., Zhu, G., Zhang, G., Yao, J., Militky, J., Mass transfer and the thermal buffering effect of hydrophobic fabrics with a single-side coating of MPCMs, *Progress in Organic Coatings*. 172, (2022). DOI: 10.1016/j.porgcoat.2022.107151.

Author Contribution

- Validation
 - Verification of the overall reproducibility of results and other research outputs.
- Writing – Original Draft Preparation
 - Assisted in writing the manuscript, review and editing.
- Funding Acquisition
 - From GAČR as leader of the project
- Others
 - Supervision
 - Project Administration



Mass transfer and thermal buffering effect of hydrophobic fabrics with single-side coating of MPCMs

Kai Yang^{a,*}, Lenka Martinkova^b, Ondrej Ctibor^b, Xiuling Zhang^a,
Mohanapriya Venkataraman^a, Jakub Wiener^a, Guocheng Zhu^{c,d}, Guoqing Zhang^e,
Juming Yao^{d,e,f}, Jiri Militky^a

^a Department of Material Engineering, Faculty of Textile Engineering, Technical University of Liberec, Liberec, Czech Republic

^b INOTEX spol. s.r.o., Stefanikova 1208, 544 01 Dvur Kralove nad Labem, Czech Republic

^c College of Textiles and Engineering, Zhejiang Sci-tech University, Xiasha Education Park, PR China

^d Zhejiang-Czech Joint Laboratory of Advanced Fiber Materials, Zhejiang Sci-tech University, Xiasha Education Park, PR China

^e School of Materials and Engineering, Zhejiang Sci-tech University, Xiasha Education Park, PR China

^f School of Materials Science and Chemical Engineering, Ningbo University, Ningbo City, PR China

ARTICLE INFO

Keywords:

MPCM
Hydrophobicity
Fabric
Breathability
Water transfer
Thermal buffering effect

ABSTRACT

The incorporation of microencapsulated phase change materials (MPCMs) into textiles have been realized for personal temperature regulation. However, the hydrophobicity and breathability of MPCM-incorporated fabrics remained improvement. In this work, four commercial fabrics were first treated with a hydrophobic coating and the MPCMs were coated on the hydrophobic fabrics via pad-dry-curing coating method. The morphology, hydrophobicity, thermal energy storage, thermal buffering effect, moisture transfer, and breathability of the MPCM-coated fabrics were investigated. As a result, the MPCMs were well coated on one side of the hydrophobic fabrics. The water contact angles of the MPCM-coated side of MPCM-coated fabrics were higher than 100° and the anti-fouling property was found. Besides, the breathability was reduced when an MPCM coating was on the hydrophobic fabric. The one-way moisture transfer behavior was little affected when there was an MPCM coating on the knitted and woven fabrics while significantly reduced when the 3D knitted fabric was the substrate. The thermal energy storage of the MPCM-coated fabrics ranged from 1.89 to 8 J/g, which was related to the used fabric type. Correspondingly, the thermal buffering effect of MPCM-coated fabrics was found, and a better thermal buffering effect was proposed when the MPCM-coated side faced the heating source.

1. Introduction

Personal temperature management has been studied for decades [1,2]. Incorporation of organic phase change materials (PCMs) (e.g., paraffin wax, fatty acid, polyethylene glycol, etc.) into textiles is proposed as an easy method for temperature management [3–7]. During the phase transition of the PCMs over a certain temperature, the thermal resistance of the PCMs is increased and the thermal energy is absorbed or released [6,8,9]. The leakage of the PCMs is the main problem for the practical applications. To avoid leakage, three main methods have been proposed, including form-stable PCMs (FSPCMs), solid-solid PCMs (SSPCMs) and microencapsulated PCMs (MPCMs) [3,10,11]. Especially, the MPCMs as one kind of PCMs consisting of the shell and the core are aimed to support the high thermal stability and avoid the leakage of

PCMs during phase transition [12,13]. Compared with FSPCMs and SSPCMs, the MPCMs have stable thermal behavior under various environments (e.g., humidity, etc.) because of their shell-core structure. The incorporation of the MPCMs into textiles has been studied for decades and includes two ways: 1) the fabrication of PCM fibers by incorporating MPCMs into polymer fiber matrix [14–16] and 2) coating of MPCMs on the fabrics [17–20]. For the former one, it is suggested that the higher encapsulation amount of the MPCMs in the PCM fibers could enhance the final thermal energy storage while reducing the mechanical property of the final PCM fibers. Still, there is a limitation for the maximum encapsulation amount of the MPCMs in the PCM fibers. Compared with PCM fibers, the coating of the MPCMs on the fabrics is more convenient, and the MPCM amount is controlled.

To prepare the MPCM-coated fabrics, the pad-dry-curing method is

* Corresponding author.

E-mail address: kai.yang@tul.cz (K. Yang).

<https://doi.org/10.1016/j.porgcoat.2022.107151>

Received 10 April 2022; Received in revised form 10 August 2022; Accepted 22 August 2022

Available online 7 September 2022

0300-9440/© 2022 Elsevier B.V. All rights reserved.

Table 1
Description of the used commercial fabrics.

Sample code	Component	S (g/m ²)	L (mm)	Structure
S1	100%PET	200	0.57 ± 0.01	Warp knit
S2	65%cotton/35%PET	240	0.44 ± 0.01	3/1 twill
S3	57%cotton/41%PET/2% Carbon	170	0.38 ± 0.01	3/1 twill
S4	100%PET	378	2.71 ± 0.10	3D knitting

Table 2
Technical parameter for pad-dry-curing coating method.

Process	T_{in} (°C)	T_{room} (°C)	T_{out} (°C)	$v_{feeding}$ (m/min)
Coating process	30	120	30	0.5
Curing process	30	150	30	0.5

Table 3
Basic information of coated fabrics.

Sample code	Used fabric substrate	S (g/m ²)	L (mm)	p_1 (%)	p_2 (%)
SH1	S1	212	0.54 ± 0.01	6.00	–
SH2	S2	250	0.53 ± 0.01	4.17	–
SH3	S3	178	0.41 ± 0.01	4.71	–
SH4	S4	390	2.76 ± 0.02	3.17	–
SMH1	SH1	232	0.52 ± 0.01	–	10.00
SMH2	SH2	280	0.46 ± 0.01	–	12.50
SMH3	SH3	202	0.38 ± 0.01	–	14.12
SMH4	SH4	457	2.80 ± 0.06	–	17.72

S , L , p_1 , and p_2 : areal density of the sample, the thickness of the sample, add-on of the hydrophobic coating layer, and add-on of the MPCM layer.

Table 4
Description of reference samples.

Sample code	Used fabric	Coating type	S (g/m ²)	L (mm)
STB1	S1	Thickner + binder	232.81	0.47 ± 0.01
STB2	S2		246.88	0.42 ± 0.01
STB3	S3		192.19	0.36 ± 0.01
STB4	S4		428.13	2.73 ± 0.01
SMTB1	S1	MPCM + thickner + binder	239.06	0.49 ± 0.01
SMTB2	S2		253.13	0.42 ± 0.01
SMTB3	S3		218.75	0.37 ± 0.01
SMTB4	S4		448.44	2.82 ± 0.02

the most popular method, and the binder is necessary for the MPCM coating to enhance thermal stability [21]. For the MPCM-coated fabrics, three main properties were specified, including thermal property, mechanical property, and breathability. Higher MPCMs amount on the fabrics supported higher thermal energy storage and better thermal buffering effect, while reduced the air permeability [22]. Besides, it was

Table 5
Areal density of washed samples.

Sample code	Washed fabric	S (g/m ²)
SWH1	SH1	210.94 ± 2.43
SWH2	SH2	248.44 ± 2.73
SWH3	SH3	176.56 ± 2.43
SWH4	SH4	387.50 ± 2.99
SWTB1	STB1	231.25 ± 2.19
SWTB2	STB2	248.44 ± 2.45
SWTB3	STB3	193.75 ± 2.22
SWTB4	STB4	426.56 ± 2.91
SWMH1	SMH1	184.38 ± 2.00
SWMH2	SMH2	221.88 ± 2.31
SWMH3	SMH3	162.50 ± 2.13
SWMH4	SMH4	359.38 ± 2.13
SWMTB1	SMTB1	237.66 ± 2.89
SWMTB2	SMTB2	249.53 ± 2.44
SWMTB3	SMTB3	210.94 ± 2.23
SWMTB4	SMTB4	442.81 ± 2.43

revealed that the curing temperature more affected the tensile strength and elongation than MPCM content [23]. The air permeability of MPCM-coated fabrics is reduced while it would be complicated for the water vapor permeability [24,25]. On one hand, the polarity of both MPCMs and binders can enhance the water vapor transmission. On another hand, more content of both MPCMs and binders may also reduce the porosity of the fabric and result in decreased water vapor transmission. Still, the surficial chemistry (e.g. hydrophobicity etc.) of the MPCM-coated fabrics is also significant. The hydrophobicity of the MPCM-coated fabrics could support anti-fouling property, anti-icing property etc. [26,27]. For the MPCM-coated fabrics, the hydrophobicity is determined by inherent hydrophobicity of MPCMs or binders. For example, Fabio Alexandre Pereira Scacchetti et al. made a coating of MPCMs, thyme oil, and monochlorotriazine-beta-cyclodextrin (MCT- β -CD) on cotton fabric. Although MPCMs were hydrophobic, the inherent hydrophilic property of MCT- β -CD had a stronger influence on surface chemistry, and the unstable hydrophobic property was found [28]. M. Karthikeyan et al. made a coating of nano MPCMs on different fabrics by using polyurethane binding agents and revealed that the water absorbance was weakened when there was a nano MPCMs coating on the fabric which was caused by a combination of reduced pores and decreased hydrophilic parts [29,30]. Jun Li et al. fabricated an MPCM consisting of CuO-doped polyurea as shell and n-icosane as core and coated the fabric using binders [31]. It was revealed that the microstructure constructed by the distribution of MPCMs on fabrics supported the hydrophobic fabric, while the hydrophobicity decreased after 30 washing cycles. Although there has been great progress in the MPCM-coated fabric via the pad-dry-curing method, the hydrophobicity stability remains to be improved.

To support highly stable hydrophobicity of MPCM-coated fabrics, a hydrophobic coating layer as outer layer totally covering MPCM-incorporated textiles is feasible [32,33], while no breathability would be found if the similar method was applied for fabrics. How to support the hydrophobicity and the breathability of the MPCM-coated fabric remains to be revealed. It is noticed that the wicking property of hydrophobic fabrics could support the penetration of liquid by adjusting the viscosity and amount of the solution, fabric structure and external pressure [34]. From this point of view, to make a coating of the MPCMs on the hydrophobic fabric is an alternative to support thermal buffering effect while the hydrophobicity is little affected.

In this work, four commercial fabrics were selected for MPCM coatings according to industrial application. We first made a hydrophobic coating on the commercial fabrics and then made the MPCM coating on the fabricated hydrophobic fabrics via pad-dry-curing coating method. A systematic investigation of the MPCM-coated hydrophobic fabrics was done, including the breathability, hydrophobicity, anti-fouling property, water transfer behavior, thermal energy

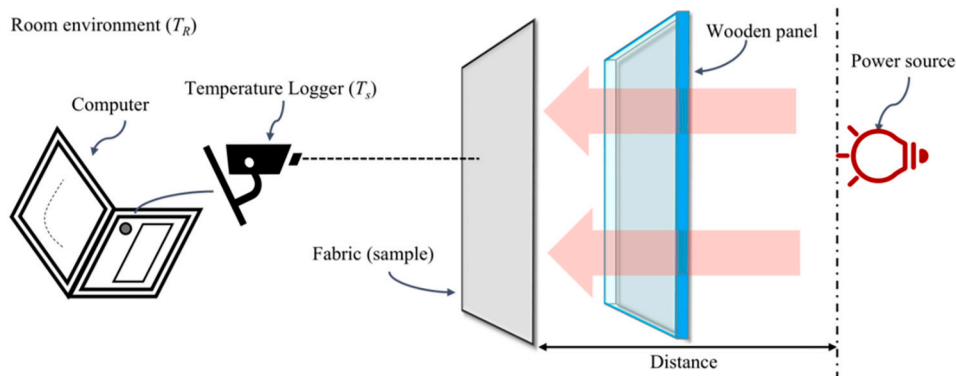


Fig. 1. Schematic diagram of the T-history setup.

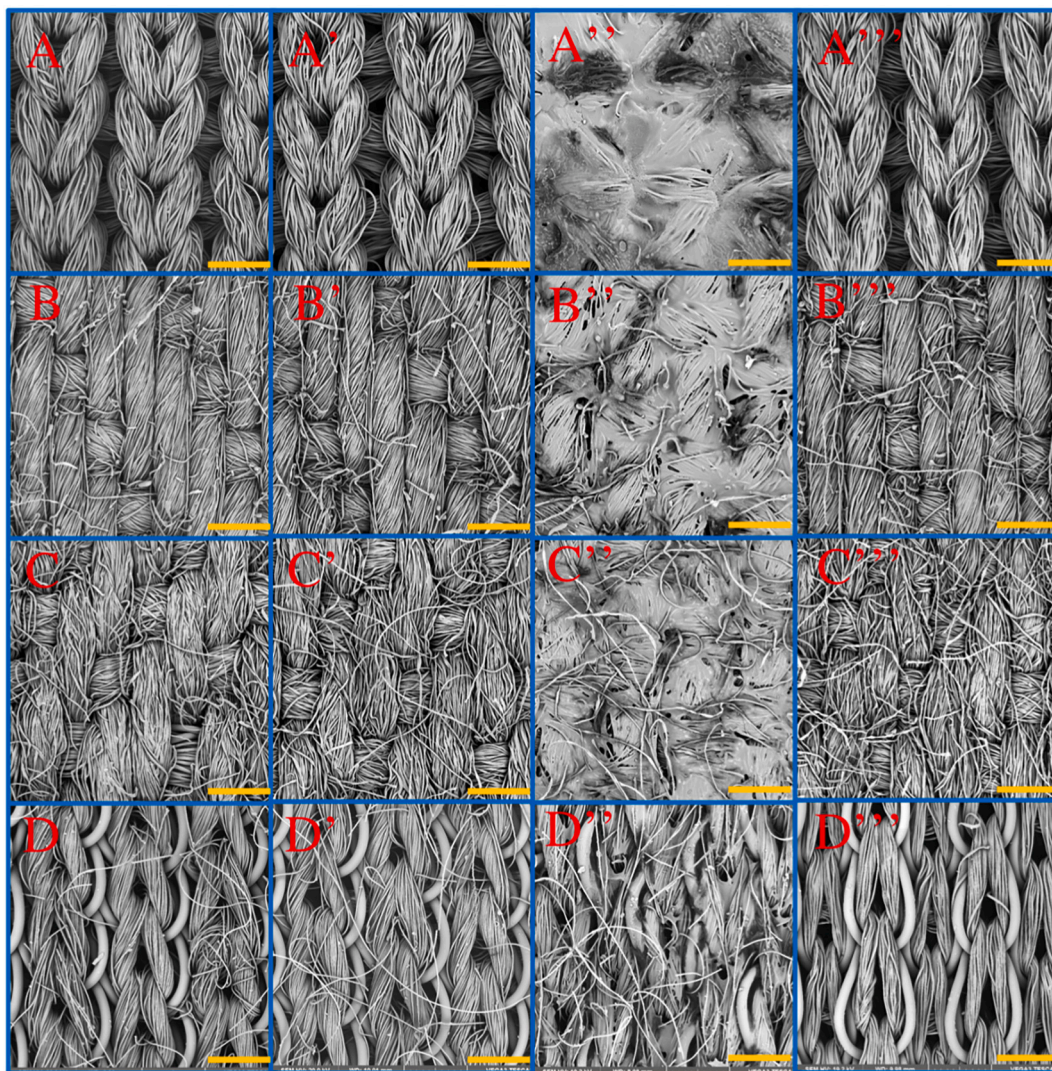


Fig. 2. Morphology of samples (A, B, C, and D: the morphology of pure commercial fabric S1, S2, S3, and S4, respectively; A', B', C' and D': the morphology of hydrophobic fabric HS1, HS2, HS3, and HS4, respectively; A'', B'', C'' and D'': the morphology of MPCM-coated side of hydrophobic MPCM-coated fabric MHS1, MHS2, MHS3, and MHS4, respectively; A''', B''', C''' and D''': the morphology of uncoated side of hydrophobic MPCM-coated fabric MHS1, MHS2, MHS3, and MHS4, respectively) (Length of yellow bar: the scale of 500 μm).

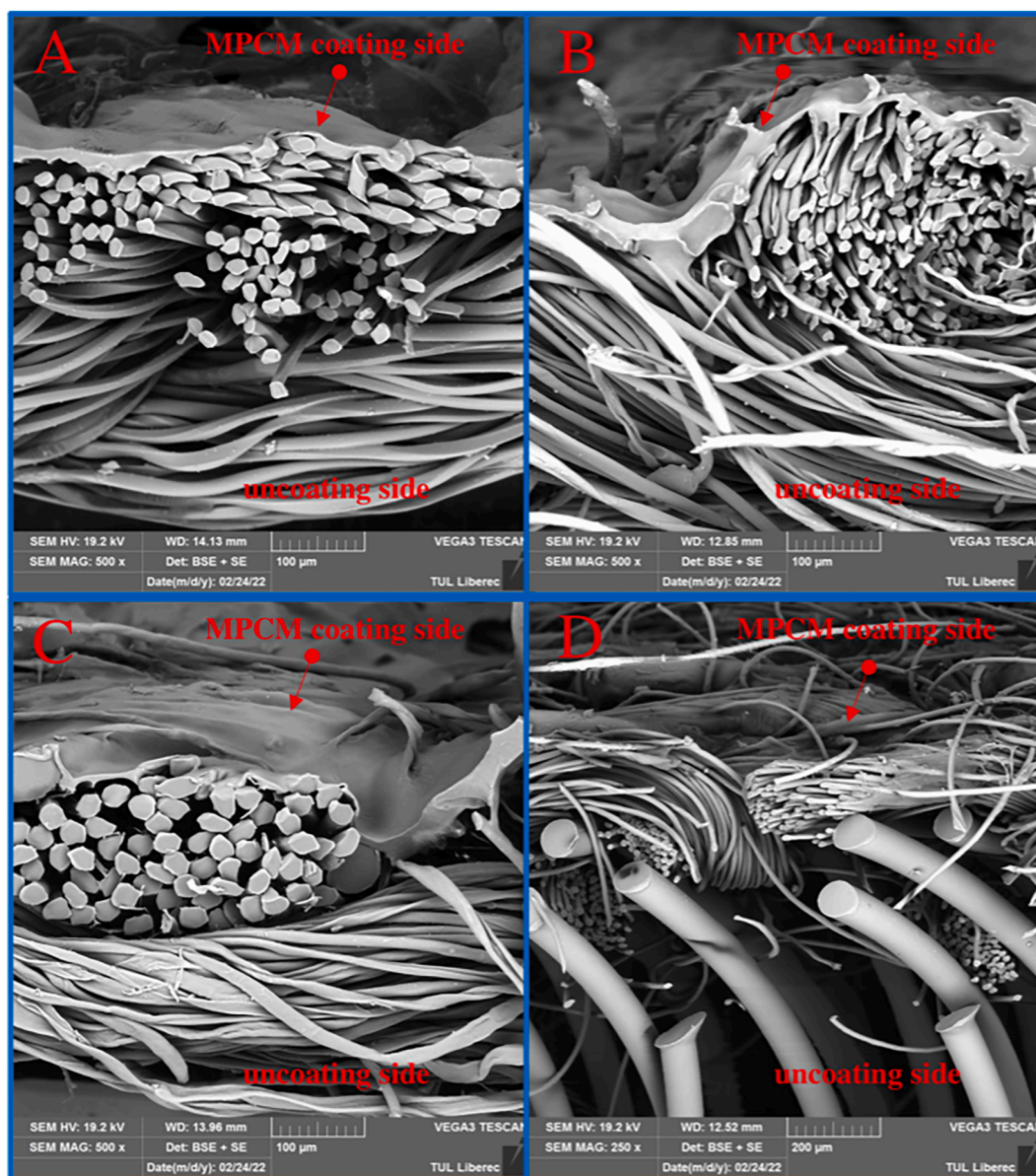


Fig. 3. Cross-section of hydrophobic MPCM-coated fabric (A, B, C, and D: SMH1, SMH2, SMH3, and SMH4, respectively).

storage, and thermal buffering effect.

2. Experimental

2.1. Materials

The details of four commercial fabrics as substrates, including the areal density (S) (g/m^2), the thickness (L) (mm), and the structure, are given in Table 1. The commercial hydrophobic dispersion BCS 01 (C6-based fluorocarbon) was purchased from the BAYGARD company (Einsteinstraat 11, 6716 AC Ede, Netherlands) (<https://tanatexchemical.com/products/baygard-bcs-2/>). The chemical code SW3 (1-(1,5-dimethyl-1H-pyrazol-3-yl)methanamine) was purchased from LAMBERTI S.p.A. The MPCMs slurry was provided by Zhejiang Sci-tech University, which contained 35 wt% MPCMs with dodecanol-laurate as core and modified PMMA as shell and 65 wt% mixture of water and emulsifiers [35].

2.2. Preparation of hydrophobic coating

For the hydrophobic coating process, the hydrophobic solution was prepared firstly by physically blending BCS 01 solution with water (10 g/L) till the homogenous solution was obtained. The stirring speed was 500 rpm. Then, the immersion method was used to prepare the hydrophobic fabrics, including the coating and curing processes (Werner-Mathis continuous R2R pilot finishing line) (Table 2). During the coating process, the fabric was immersed in the hydrophobic solution at room temperature (30 °C) and then experienced the drying temperature of 120 °C for 2 min. Then, the 2 min curing process was subsequently for the hydrophobic fabrics with a higher drying temperature of 150 °C. Finally, the hydrophobic fabrics were successfully prepared and labeled according to the fabrics, given in Table 3 in detail.

2.3. Preparation of MPCM coating

Before the MPCM coating process on the hydrophobic fabrics, the MPCM solution was prepared by physically blending with the acrylic thickener (VERSACOL P, Synthesia, a.s. the Czech Republic), SW3 with

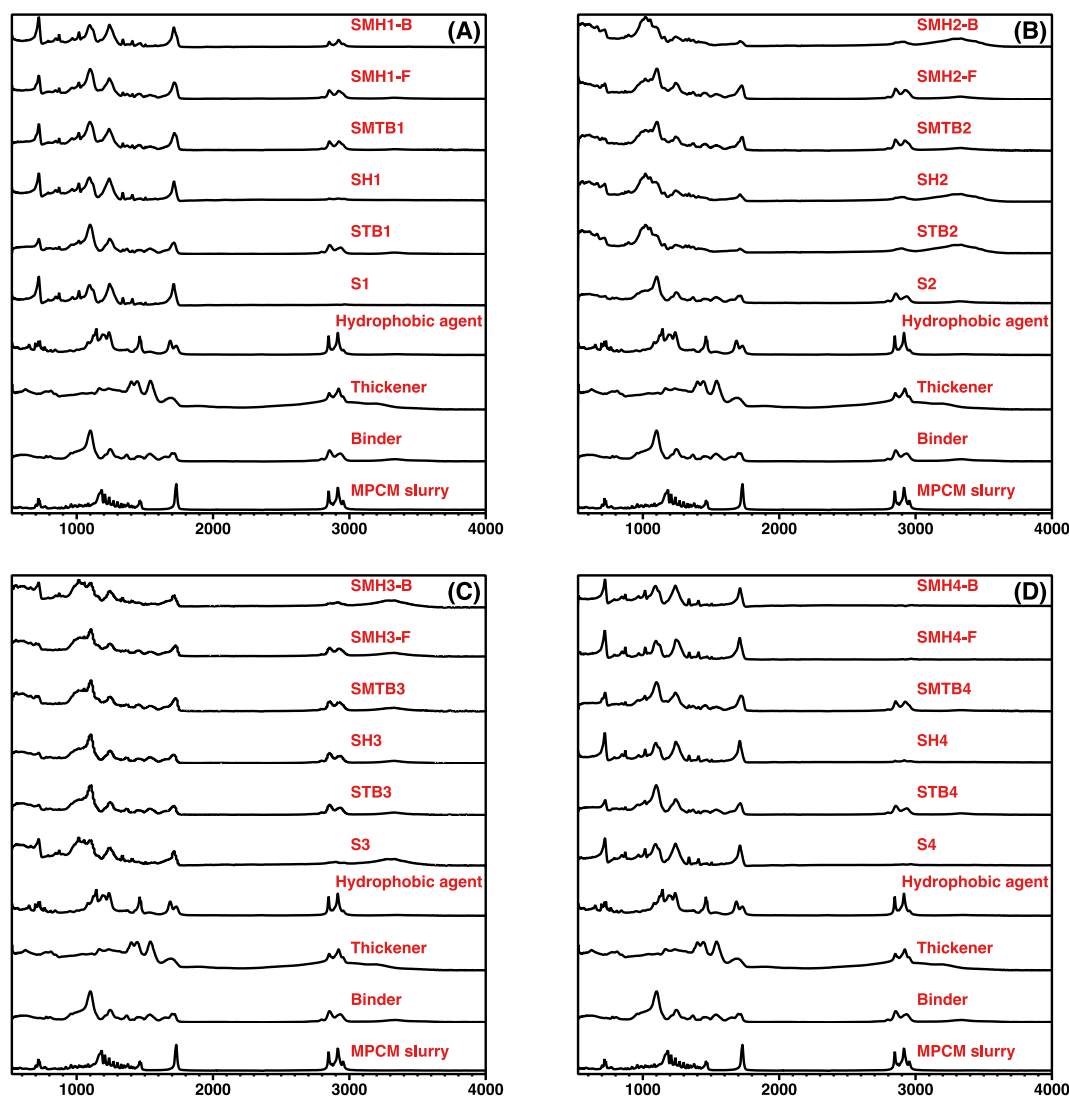


Fig. 4. FTIR curves of MPCM-coated fabrics (A, B, C and D: S1-based samples, S2-bases samples, S3-based samples and S4-based samples).

the MPCM solution. The weight ratio of the SW3 to the MPCM solution was set as 1:1, and a small amount of the thickener (~1 wt% in solution) was added to the SW3/MPCM solution during the physical stirring process with high stirring speed of 500 rpm till the viscosity of the solution reached around 60 dPa s. The prepared MPCM solution was coated on the hydrophobic fabrics via a pad-dry-curing coating process using the coating machine (Werner-Mathis continuous R2R pilot finishing line) and blade coating was used. The parameters of pad-dry-curing process for coating of MPCMs on the hydrophobic fabrics were same as one for the preparation of hydrophobic fabrics, which was given in Table 2. Finally, the MPCM-coated hydrophobic fabrics were successfully prepared and labeled according to the fabrics, which was given in Table 3. Additionally, the add-on of the hydrophobic coating layer (p_1) and add-on of the MPCM layer (p_2) were calculated according to Eqs. (1) and (2), respectively. The subscript S_0 , S_1 and S_2 represented the areal density of the fabric without anything, the hydrophobic fabric, and the MPCM-coated hydrophobic fabric. All details of the samples were given in Table 3.

$$p_1 = \frac{S_1 - S_0}{S_0} \times 100\% \quad (1)$$

$$p_2 = \frac{S_2 - S_1}{S_1} \times 100\% \quad (2)$$

To reveal the effect of thickener, binder or MPCMs slurry on the hydrophobicity, the reference samples coated with thickener and binder or with MPCMs, thickener and binder were also prepared by using blade coating and pad-dry-curing process with same parameters. The details of the reference samples were shown in Table 4.

2.4. Preparation of washed MPCM-coated fabrics

To reveal the lifetime of the prepared MPCM-coated fabrics in practice, a washing treatment was for the MPCM-coated fabrics and carried out by washing MPCM-coated fabrics for 1 h with washing powders. Then, the thermal storage property of the washed MPCM-coated fabrics was investigated. Correspondingly, the samples treated with washing treatment were labeled as SWMH1, SWMH2, SWMH3, and SWMH4, which corresponded to the samples SMH1, SMH2, SMH3, and SMH4, respectively. The areal density values of washed samples were given in Table 5.

2.5. Tests and methods

2.5.1. Characterization of morphology

Scanning electronic microscopy (SEM) (VEGA TESCAN Inc., Lincoln, NE, USA) was used to characterize the morphology and the cross-section of the prepared fabrics. The electronic voltage of 20 kV was applied for

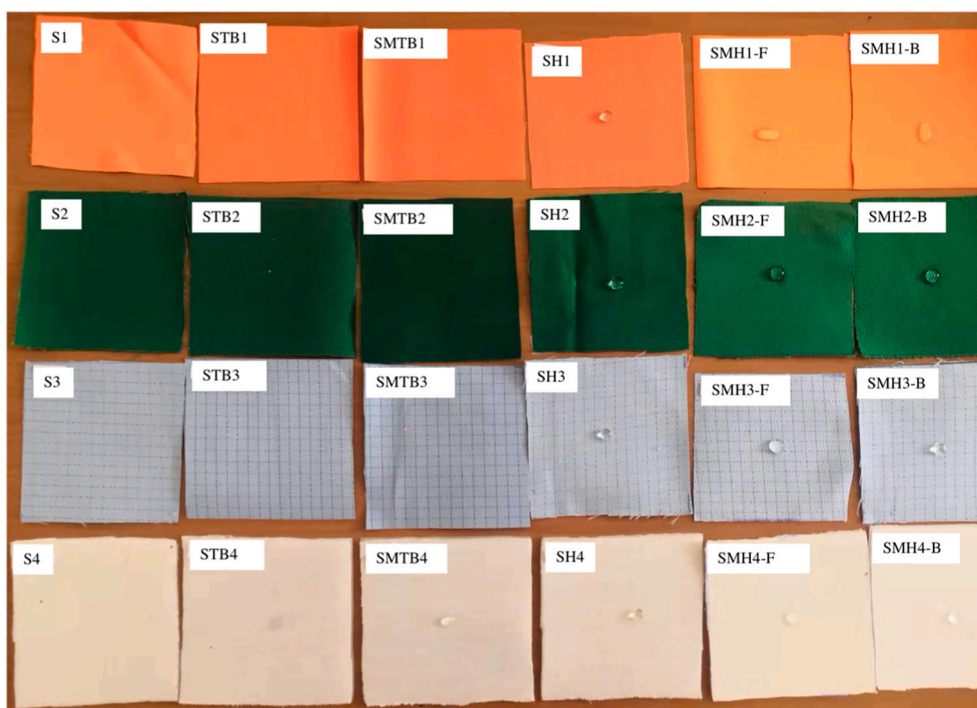


Fig. 5. Wetting behavior of all the samples after 5 min (sample size: 6 cm × 6 cm).

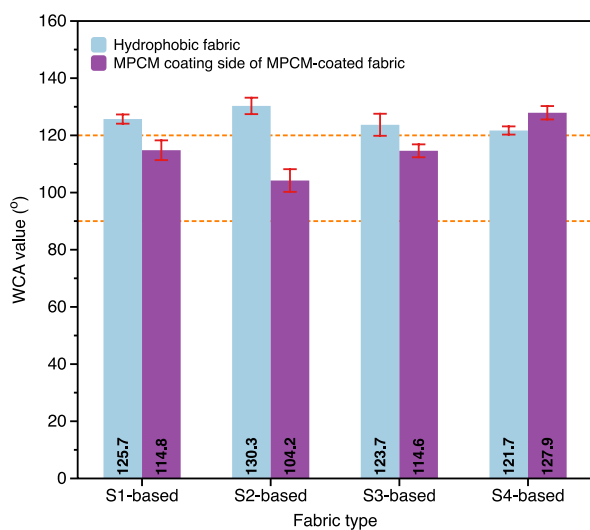


Fig. 6. WCA values of the hydrophobic fabrics and the MPCM-coated side of MPCM-coated fabrics.

SEM measurement. Besides, it was necessary to characterize the morphology of pure MPCMs to compare with the MPCM coating layer on the fabric. In this case, the MPCMs slurry was dropped on the viscose fabric and dried for one week. Then, the MPCM-coated viscose fabric was characterized and only the morphology of MPCMs was focused on.

2.5.2. Characterization of chemical compatibility

The attenuated total reflection-Fourier transforms infrared (ATR-FTIR) spectroscopy was used to characterize the chemical compatibility between various coating layers (including hydrophobic coating and MPCM coating) and fabrics. The machine Thermo Nicolet AVATAR 330 FT-IR was used, and the spectrum was obtained in the spectral region from 4000 cm^{-1} to 525 cm^{-1} with 2 cm^{-1} resolutions.

2.5.3. Characterization of hydrophobicity

The hydrophobic property of the reference fabrics, the hydrophobic fabrics, and the MPCM-coated fabrics was investigated using the droplet method according to standard 27,448:200. $5\text{ }\mu\text{L}$ water droplets were placed on the surface of the reference fabrics, the hydrophobic fabrics and the MPCM-coated side of the MPCM-coated fabrics.

2.5.4. Characterization of anti-fouling property

The anti-fouling property of the samples was evaluated in two steps by using various liquids, including water, coffee, milk, red wine, olive oil, motor oil, mustard, and ketchup: 1) the liquid was dropped on the surface of the sample for 5 min, and 2) the liquid droplet was removed from the surface of the sample. The liquid droplet and wettability on the surface of samples were recorded.

2.5.5. Characterization of breathability

Both the air permeability and the water vapor permeability of the samples were investigated to reveal the effect of the hydrophobic coating and the MPCM coating on the permeability of the fabrics.

The air permeability of the samples was investigated using an FT3300 tester according to ISO 9237. The applied pressure values for measurement were set from 40 Pa to 200 Pa with an interval of 20 Pa. Each measurement was repeated 5 times for each sample, and the statistics were obtained. Furthermore, the *Forchheimer* model was proposed to predict the air permeability of the samples under different pressure, which was expressed in Eq. (3). The Δp was the pressure difference, the L was the fabric thickness, the μ was the dynamic viscosity of the fluid ($1.86 \times 10^{-6}\text{ Pa}\cdot\text{s}$), the q was the velocity of the flow ($1.168\text{ kg}/\text{m}^3$), the ρ was the fluid density, and the k_1 and k_2 were to characterize the permeability related to the porosity properties [36,37]. On the right hand of the equation, the first term ($\frac{\mu}{k_1}q$) represented the viscous energy losses due to friction between the fluid layers. The second term ($\frac{\rho}{k_2}q^2$) represents the kinetic energy losses due to changes in the direction of motion and to acceleration or deceleration of the fluid caused by changes in the flow path (contraction or enlargement of the pore section or pore tortuosity along the flow direction).

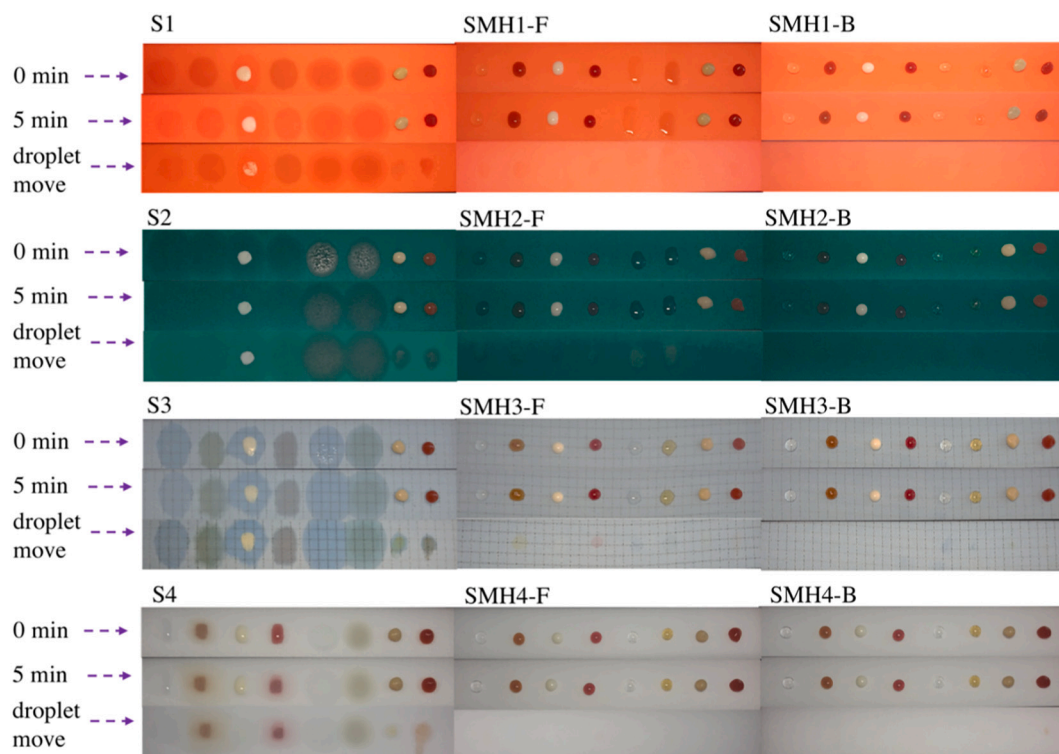


Fig. 7. Antifouling property of samples with or without MPCM coating (used liquid from left to right: water, coffee, milk, red wine, olive oil, motor oil, mustard, and ketchup) (F and B: the MPCM-coated side and uncoated side). (For interpretation of the references to color in this figure legend, the reader is referred to the web version of this article.)

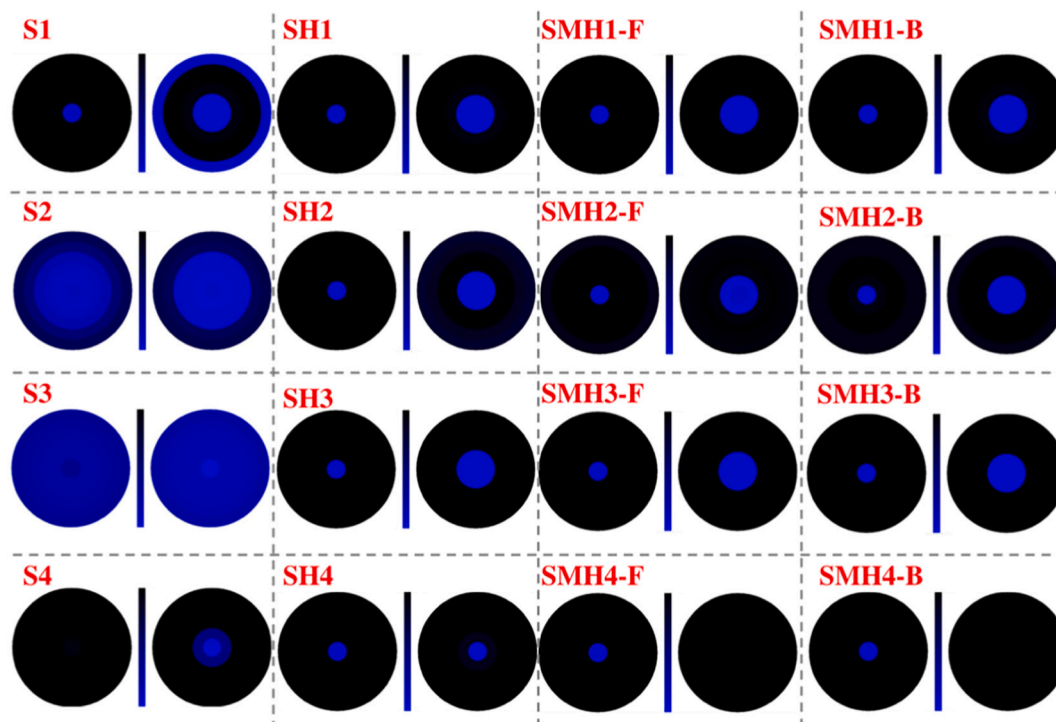


Fig. 8. Wetting areas of the pristine fabric, the hydrophobic fabric, and the MPCM-coated fabric within 2 min after the water penetration with the 30s from MMT measurement (Left image and right image corresponded to the top and bottom water content for each sample; the blue color corresponded to higher water content and the black color corresponded to lower water content; F and B: water transfer from MPCM-coated side to uncoated side and water from uncoated side to MPCM-coated side). (For interpretation of the references to color in this figure legend, the reader is referred to the web version of this article.)

Table 6
Classification of samples from MMT results according to standard ISO 81181.

Sample code	Fabric type
S1	Water penetration fabric
S2	Moisture management fabric
S3	Moisture management fabric
S4	Slow absorbing and slow drying fabric
SH1	Water penetration fabric
SH2	Water penetration fabric
SH3	Water penetration fabric
SH4	Water penetration fabric
SMH1-F	Water penetration fabric
SMH1-B	Water penetration fabric
SMH2-F	Fast absorbing and slow drying fabric
SMH2-B	Water penetration fabric
SMH3-F	Water penetration fabric
SMH3-B	Water penetration fabric
SMH4-F	Water-proof fabric
SMH4-B	Water-proof fabric

$$\frac{\Delta p}{L} = \frac{\mu}{k_1} q + \frac{\rho}{k_2} q^2 \quad (3)$$

The water vapor permeability of the samples was investigated using the PERMETEST instrument (SENSOR, Liberec, Czech Republic) according to ISO 11092. As a result, the water vapor resistance (R_{et}) ($\text{Pa m}^2/\text{W}$) was measured following the Eq. (4), where the P_m value was the water vapor saturate partial pressure and the P_a value was the actual partial water vapor pressure during the measurement under a certain temperature, and both q_s and q_0 were the heat flow value without and with a sample, respectively [38,39]. Each sample was measured 5 times, and the statistics were obtained.

$$R_{et} = (P_m - P_a)(q_s^{-1} - q_0^{-1}) \quad (4)$$

2.5.6. Characterization of moisture transfer behavior

The moisture management tester (MMT) (M290, SDL Atlas) following standard ISO 81181 was used to characterize the moisture transfer [40]. Each sample was measured from both MPCM-coated side and uncoated side. As a result, the classification of the samples was found.

2.5.7. Characterization of thermal energy storage

The differential scanning calorimetry (DSC) (METTLER, Swiss) was used to characterize the thermal energy storage and the phase change temperature range of the MPCM-coated fabrics. All the samples first experienced from 25 °C to 60 °C to erase the thermal history. Then, the sample experienced from 60 °C to 5 °C to have the crystallization process and then was subsequently heated from 5 °C to 60 °C to have the melting process. During the whole DSC process, the heating/cooling rate was set as 10 K/min and nitrogen (N_2) gas rate was set as 50 mL/min. Still, it was

necessary to characterize the phase transition behavior of MPCMs via the DSC method. Especially, it was noticed that MPCM slurry was the solution. Then, the MPCM slurry was dropped on a glass slide and dried under room condition for one week to form MPCM film, which consisted of MPCMs and other additives. Finally, the formed MPCM film experienced the same DSC procedure, and only phase transition behavior was focused under the condition that the mass of MPCMs in the formed film was unclear. As a result, 8 parameters of the samples were obtained, including onset melting temperature (T_{om}), peak melting temperature (T_{pm}), endset melting temperature (T_{em}), onset cooling temperature (T_{oc}), peak cooling temperature (T_{pc}), endset cooling temperature (T_{ec}), melting enthalpy change (ΔH_m) and solidification enthalpy change (ΔH_c). Besides, supercooling degree (ΔT) was calculated and equal to $T_{pm} - T_{pc}$.

2.5.8. Characterization of thermal buffering effect

To characterize the thermal buffering effect of the prepared samples, the custom setup was used (Fig. 1), including the temperature data logger (FLIR E6), the radiator heater, and the computer. The measurement was performed by placing the sample away from the radiator heater at a distance of 40 cm, and the room temperature was recorded. Then, the radiator heater was turned on for 2 min; meanwhile, the temperature data logger recorded the surface temperature of the sample. After that, the radiator heater was turned off. The wooden insulation panel was immediately placed between the sample and the radiator heater to avoid the effect of the remaining heat radiation from the radiator heater on the sample. Meantime, the surface temperature of the sample was also continuously recorded by the temperature data logger after 2 min. It was noticed that the waves from radiator heater could penetrate through the samples because of porous structure of the fabrics. From this point of view, the inaccurate results for T-history during heating process may be suitable for characterization of thermal buffering effect. Therefore, only the cooling process was acceptable since there was no effect of the remaining heat radiation to affect the cooling process of the sample because of the existence of the wooden insulation panel. Besides, the overall thermal conductivity (k) ($\text{W m}^{-1} \text{K}^{-1}$) and thickness (L) (mm) of the samples were measured via ALAMBETA, which was for the further analysis of the thermal buffering effect [41,42].

3. Results and discussion

3.1. Effect of hydrophobic coating and MPCM coating on the morphology of the fabric

Figs. 2 and 3 presented the morphology of all the samples. The hydrophobic coating had little effect on the morphology since the hydrophobic fabrics had similar morphology as the reference fabrics. For MPCM-coated fabrics, the MPCM coating was well kept on one side of

Table 7
The measured air permeability values of all the samples under different pressure difference.

Sample code	Air permeability (mm/s)								
	40 Pa	60 Pa	80 Pa	100 Pa	120 Pa	140 Pa	160 Pa	180 Pa	200 Pa
S1	287 ± 7	400 ± 8	505 ± 8	596 ± 6	681 ± 8	765 ± 7	843 ± 8	920 ± 13	991 ± 10
S2	38 ± 7	56 ± 2	74 ± 2	93 ± 3	110 ± 3	125 ± 3	143 ± 4	158 ± 4	175 ± 5
S3	49 ± 1	75 ± 1	99 ± 1	123 ± 1	144 ± 4	168 ± 2	190 ± 2	212 ± 2	235 ± 3
S4	611 ± 16	853 ± 18	1070 ± 17	1260 ± 26	1443 ± 32	1627 ± 31	1790 ± 36	1937 ± 47	2103 ± 42
SH1	337 ± 1	459 ± 6	567 ± 7	666 ± 6	760 ± 5	848 ± 6	933 ± 8	1013 ± 11	1090 ± 10
SH2	78 ± 4	115 ± 5	151 ± 8	184 ± 10	216 ± 11	248 ± 13	279 ± 14	308 ± 15	337 ± 16
SH3	57 ± 3	86 ± 4	113 ± 5	138 ± 6	164 ± 7	189 ± 8	207 ± 4	238 ± 10	262 ± 12
SH4	590 ± 14	820 ± 18	1037 ± 25	1213 ± 31	1400 ± 36	1570 ± 36	1737 ± 42	1893 ± 38	2037 ± 42
SMH1	22 ± 1	30 ± 1	38 ± 1	46 ± 1	54 ± 1	62 ± 1	69 ± 1	76 ± 1	83 ± 1
SMH2	13 ± 1	18 ± 1	23 ± 1	29 ± 1	34 ± 1	39 ± 2	45 ± 1	50 ± 2	56 ± 2
SMH3	20 ± 1	30 ± 1	39 ± 1	49 ± 1	58 ± 1	68 ± 1	77 ± 1	87 ± 1	96 ± 1
SMH4	227 ± 3	328 ± 4	410 ± 8	489 ± 3	565 ± 6	635 ± 4	704 ± 2	770 ± 1	832 ± 3

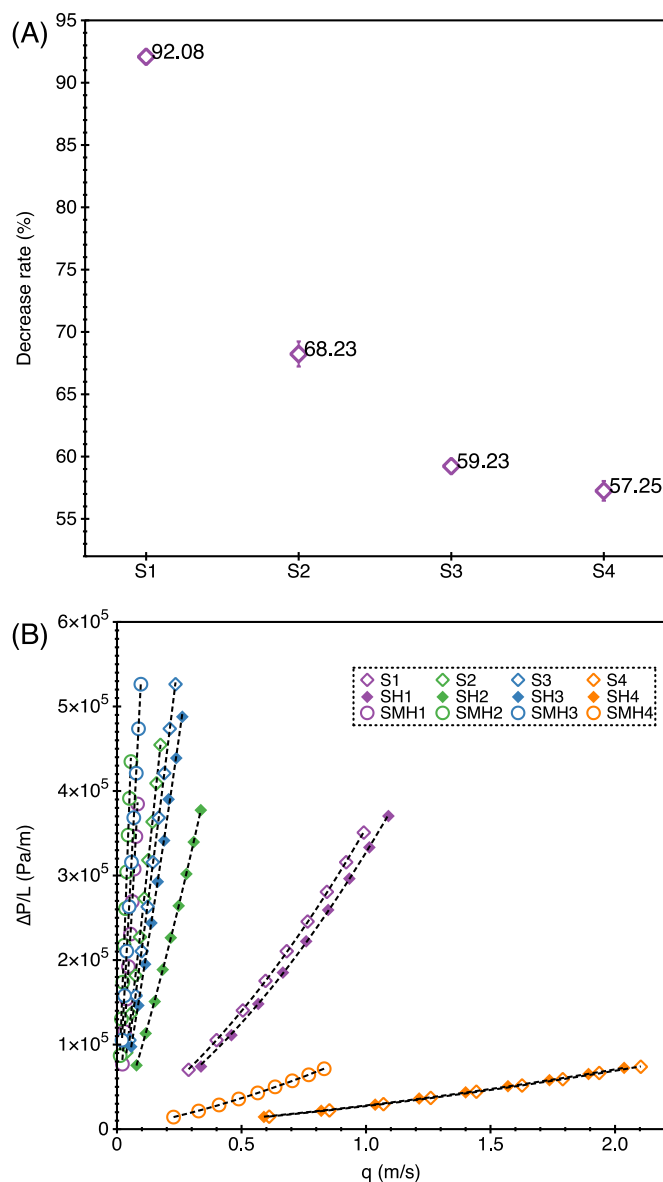


Fig. 9. The decrease rate of the MPCM-coated fabrics when compared with corresponding reference fabrics (A) and the plots of $\Delta P/L$ against q according to Eq. (3) (B) (Error bar: standard values).

Table 8

Estimated k_1 , k_2 and R^2 values according to Eq. (3).

Sample code	$k_1 (\times 10^{-11}) (m^2)$	$k_2 (\times 10^{-5}) (m)$	R^2
S1	9.20	0.76	0.999
S2	0.80	0.07	0.999
S3	0.90	0.14	0.999
S4	93.21	16.02	0.999
SH1	10.65	0.76	0.999
SH2	2.04	0.19	0.999
SH3	1.12	0.14	0.999
SH4	90.16	15.89	0.999
SMH1	0.54	0.01	0.999
SMH2	0.26	0.01	0.999
SMH3	0.35	0.05	0.999
SMH4	34.49	3.03	0.999

the hydrophobic fabrics, and the uncoated side had a similar structure to the hydrophobic fabrics and reference fabrics. The hydrophobic coating activated as a barrier layer to resist the penetration of MPCM solution

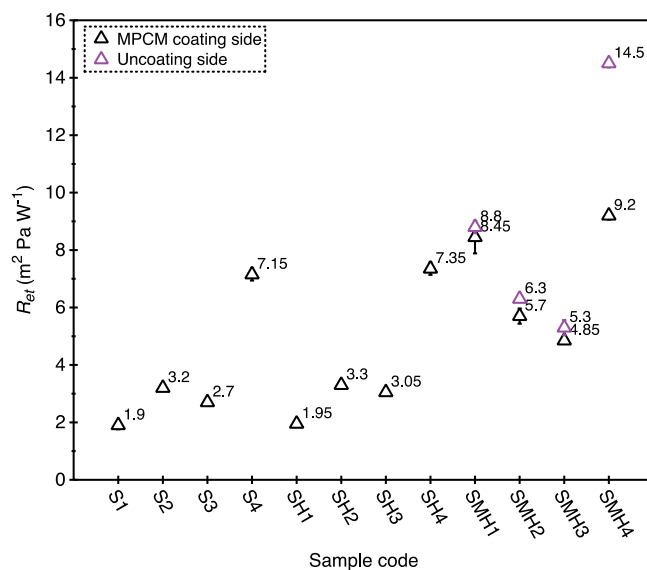


Fig. 10. Water vapor permeability of the fabrics, the hydrophobic fabrics, and the MPCM-coated fabrics.

through the whole hydrophobic fabric during the coating process. Besides, the yarns still can be observed on the MPCM-coated side. Some MPCM solution was adsorbed inside the hydrophobic fabrics because of wicking. Furthermore, no particles corresponding to the MPCMs were observed by referring to the morphology of MPCMs (Appendix 1). On one hand, the MPCMs were embedded in the MPCM coating layer. On another hand, some MPCMs may be destroyed during the preparation of the MPCM solution, although the thickener was added to avoid the destruction of MPCMs [43–45]. Besides, the coverage of the MPCM coating layer on the four hydrophobic fabrics was different from each other, and a much less MPCM coating layer was observed on the surface of SMH4. The 3D knitted fabric had stronger wicking property for MPCM solution than other fabric structures.

ATR-FTIR results provided more details of hydrophobic coatings and MPCM coatings on the fabrics, which was shown in Fig. 4. No new peaks were observed in the hydrophobic fabrics and MPCM-coated hydrophobic fabrics. So, the physical binding between hydrophobic coatings, MPCM coatings and fabrics was proposed. Especially, the unique peaks contributed from MPCMs were almost invisible, which corresponded to morphology analysis and supported that MPCMs were embedded in the coating layer.

3.2. Effect of MPCM coating on the hydrophobicity property and anti-fouling property

Fig. 5 provided wetting behavior of all the samples. By comparing with reference samples fabrics, only the samples with hydrophobic coating had WCA values, the introduction of thickener, binder or MPCM slurry did not support the hydrophobicity. Therefore, the wicking of the MPCM solution into the inner part of hydrophobic fabrics was proposed, where the MPCM coating layer only partially covered the hydrophobic fibers. In details, the hydrophobic fabrics had WCA values higher than 120° , and the MPCM-coated fabrics had WCA values higher than 100° (Fig. 6). By combining with morphology analysis, the hydrophobic 3D fabric had better wicking behavior for MPCM solution than other fabrics. The WCA values of the samples SMH1, SMH2, and SMH3 were smaller than the corresponding samples SH1, SH2, and SH3, respectively. Especially for SMH4, the WCA value was slightly increased when compared with SH4. We proposed that the major MPCM coating layer was adsorbed inside the surface of SH4, where the switch between the Wenzel state and Cassie state possibly happened [46]. Correspondingly,

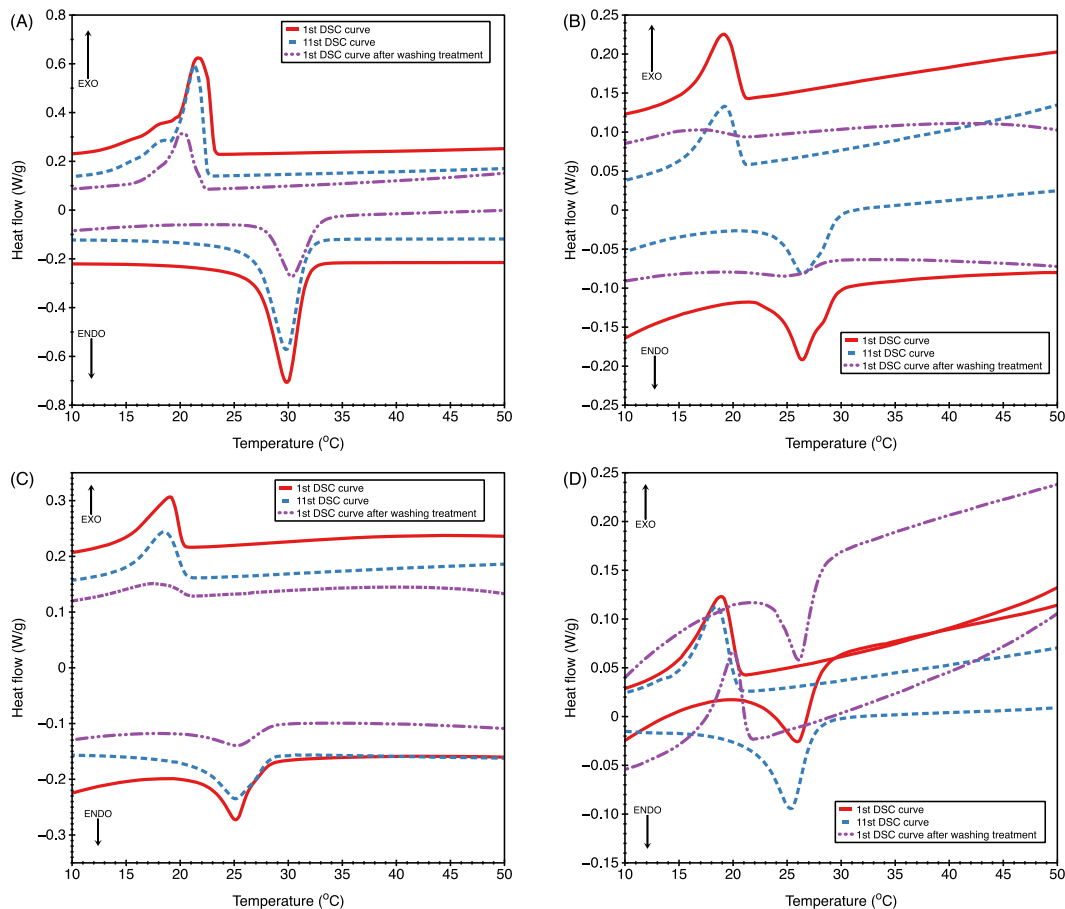


Fig. 11. DSC curves of the prepared samples and the samples after washing (A, B, C and D: SMH1, SMH2, SMH3 and SMH4, respectively).

Table 9

Phase transition range and thermal energy storage of the MPCM slurry and the MPCM-coated fabrics.

Sample code	T_{om} (°C)	T_{pm} (°C)	T_{em} (°C)	ΔH_m (J/g)	T_{oc} (°C)	T_{pc} (°C)	T_{ec} (°C)	ΔH_c (J/g)	ΔT (°C)
SMH1 ^a	27.07	29.92	31.77	8.19	23.35	21.57	19.18	8.89	8.35
SMH1 ^b	27.00	29.77	31.77	8.09	22.64	21.23	18.82	8.84	8.54
SWMH1 ^a	27.97	30.29	32.91	4.03	21.96	20.38	17.88	3.96	9.91
SMH2 ^a	23.93	26.48	29.19	1.74	21.03	19.19	15.73	1.80	7.29
SMH2 ^b	23.81	26.49	29.71	1.57	20.98	19.18	15.12	1.70	7.31
SWMH2 ^a	21.61	26.15	28.72	0.27	20.91	17.68	13.71	0.20	8.47
SMH3 ^a	22.27	25.14	27.19	1.85	20.34	19.03	14.22	2.08	6.11
SMH3 ^b	21.71	25.14	28.34	1.79	20.54	18.53	14.80	1.88	6.61
SWMH3 ^a	21.63	25.48	28.46	0.69	20.81	18.19	14.81	0.37	7.29
SMH4 ^a	21.77	26.10	28.19	1.77	20.62	18.84	14.50	1.85	7.26
SMH4 ^b	22.02	25.33	27.47	1.77	20.31	18.51	15.07	1.67	6.82
SWMH4 ^a	23.55	26.17	27.97	1.33	21.39	20.00	17.05	1.53	6.17

Subscript *a* and *b*: the value corresponded to 1st DSC measurement and 11st DSC measurement, respectively; T_{om} : onset melting temperature; T_{pm} : peak melting temperature; T_{em} : endset melting temperature; T_{oc} : onset cooling temperature; T_{pc} : peak cooling temperature; T_{ec} : endset cooling temperature; ΔH_m : melting enthalpy change; ΔH_c : solidification enthalpy change; ΔT : supercooling degree and equal to $T_{pm} - T_{pc}$.

the anti-fouling property of MPCM-coated fabrics was also found (Fig. 7) and sample SMH4 had best anti-fouling property among all the MPCM-coated hydrophobic fabrics.

3.3. Effect of the MPCM coating on the moisture transfer behavior

Fig. 8 presented the wetting area of all the samples within 2 min after the water penetration with the 30s from MMT measurements, and Table 6 gave the classification of all the samples.

The one-way water moisture transfer behavior was enhanced when there was a hydrophobic coating on the fabrics, which was caused by the capillary force induced by the porous structure in the hydrophobic fabric

and the poor adhesion between water and hydrophobic fibers [47,48]. For MPCM-coated fabrics, no general rules were found for changing the water moisture transfer. The barrier effect for the water moisture transfer from both sides was enhanced when an MPCM coating on sample SH4 while other MPCM-coated hydrophobic fabrics (SMH1, SMH2, and SMH3) had the similar or weaker water transfer property as their corresponding hydrophobic fabrics. We proposed that such a difference in water moisture was caused by the different distributions of MPCM coating inside or on other fabrics.

- For the samples SMH1, SMH2 and SMH3, the water moisture transfer was determined by the interface between the MPCM-coated side and

Table 10
Comparison with melting enthalpy of other MPCM-coated fabrics.

Fabric	MPCM type	ΔH_m (J/g)	Ref.
Woven cotton fabric	Glauber's salt/poly(methyl methacrylate) MPCM	12.2	[49]
Woven cotton fabric	N-Hexadecane/poly(n-butyl acrylate) MPCM	9.85	[53]
Woven cotton/PET fabric		29.88	
Woven Jute fabric	Ethyl myristate/poly(methyl methacrylate) MPCM	10.27	[50]
Woven cotton fabric	Paraffin wax based MPCM	4.7–7.6	[54]
Woven PET fabric	Commercial MPCM	16.7–54.4	[55]
Knitted PET fabric		16.6–50.4	
Woven PET fabric	Graphene-modified n-octadecane/melamine-formaldehyde MPCM	6.1–11	[51]
3D knitted PET fabric	Paraffin-based MPCM	21.78–24.22	[56]
Woven cotton fabric	Poly(diallyldimethylammonium chloride) encapsulated n-octadecane nanocapsules (Cap+)	0.46–1.59	[57]
Knitted PET fabric	Polyurea/dodecanol dodecanoate MPCM	8.89	This work
Woven PET/cotton fabric		1.80	
Woven PET/cotton/carbon fabric		2.08	
3D knitted PET fabric		1.85	

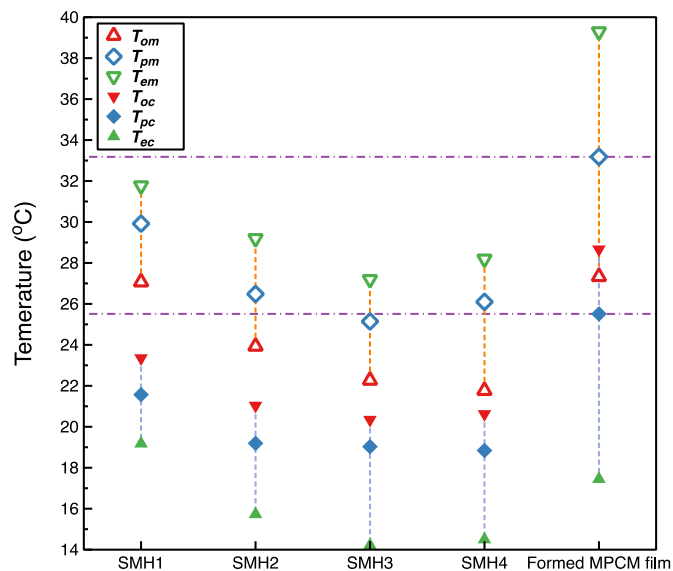


Fig. 12. Comparison of phase transition behavior of MPCM-coated fabrics with formed MPCM film.

the uncoated side. Besides, the samples SMH1, SMH2, and SMH3 were common fabrics with smaller thicknesses. By combining with Section 3.2 analysis, hydrophobic property was considered for the whole MPCM-coated fabric. The capillary force induced the hydrophobic porous fibrous structure supported the one-way water moisture transfer behavior.

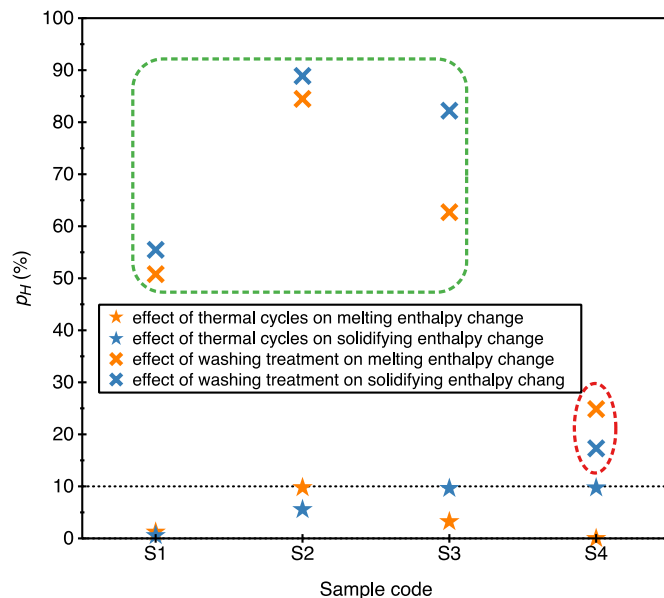


Fig. 13. The effect of the thermal cycles and the washing treatment on the change of the melting/solidifying enthalpy of the MPCM-coated fabrics.

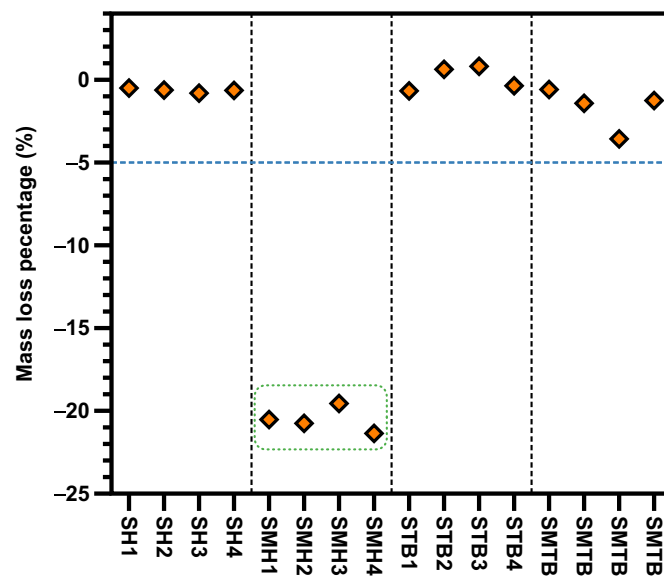


Fig. 14. Add-on percentage change of all the samples after washing treatment.

- For the sample SMH4, a much less MPCM coating layer was observed on the surface, and the MPCMs as well binders filled up the pores of the MPCM-coated side, which significantly reduced the paths of water moisture transfer through both sides

3.4. Effect of the hydrophobic coating and the MPCM coating on the breathability of the fabric

Table 7 provides the measured air permeability values of all the samples. On the one hand, the air permeability values were not generally considered to be decreased after the hydrophobic coating. On the other hand, the air permeability values were significantly reduced when the MPCM coating layer was applied to the hydrophobic fabrics. The fewer paths for the airflow could cause a decrease in the air permeability values by combining with Section 3.1. In detail, the air permeability of

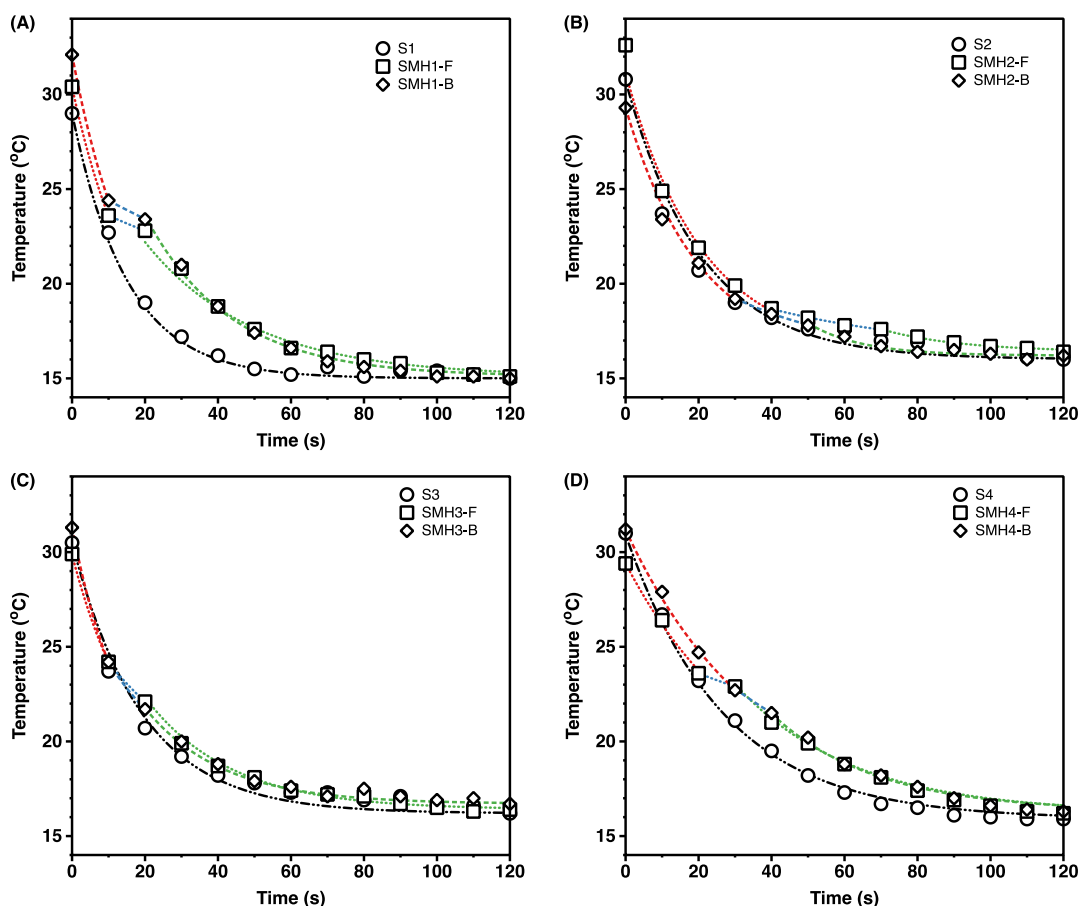


Fig. 15. T-history curves with estimated Newton's cooling law fitting model for the reference fabrics and MPCM-coated fabrics (F and B: the MPCM-coated side and uncoated side towards the radiator; black curve: a fitting model for the reference samples without PCM coating; red curve, blue curve, and green curve: a fitting model for the samples with liquid PCM, the samples with liquid-solid PCM and the samples with solid PCM; large dash and small dash: the F series and B series of samples, respectively). (For interpretation of the references to color in this figure legend, the reader is referred to the web version of this article.)

the sample SMH1, SMH2, SMH3, and SMH4 were decreased by around 92 %, 69 %, 60 % and 61 % compared with corresponding samples S1, S2, S3 and S4, respectively, schemed in Fig. 9 (A). Additionally, the plots of $\Delta P/L$ against q according to Eq. (3) for all the samples were schemed in Fig. 9 (B), and the k_1 , k_2 , and R^2 were provided in Table 8. All the values were around 0.999, which supported that the Forchheimer model could predict air permeability under different pressures. Besides, both k_1 , and k_2 values related to the hydrodynamic permeability were significantly reduced when there was the MPCM coating on the fabrics, which corresponded to the air permeability behavior.

Each sample's evaporation resistance (R_{et}) was schemed in Fig. 10. The hydrophobic coating little affected the R_{et} value, while the R_{et} value was significantly increased when both hydrophobic coating and MPCM coating were on the fabric. The proposed much fewer paths for the water vapor transfer through the MPCM-coated fabrics resulted in the higher R_{et} values. Besides, the R_{et} values measured when the water vapor transferred from the uncoated side to the MPCM-coated side were relatively higher than when the water vapor transferred from the MPCM-coated side to the uncoated side. The reason could be the weaker hydrophobic property of the MPCM-coated side compared with the uncoated side.

3.5. Thermal energy storage of MPCM-coated fabrics

Fig. 11 schemed the DSC curves of all the samples, and Table 9 gave the details of the phase transition and the thermal energy storage. Besides, the DSC curves and details of formed MPCM film were shown in Appendix 1.

3.5.1. Thermal energy storage analysis

The ΔH_m and ΔH_c values of samples without water washing treatment were smaller than 10 J/g, which was much less than the thermal energy storage values in other works (Table 10). The main reason could be that the MPCM coating only covered one side of the fabric, and the MPCM content correspondingly was much less. In detail, the sample S1 had the highest ΔH_m and ΔH_c value among all the samples, which was 8.19 J/g and 8.89 J/g, respectively, while other samples without water washing treatment had the ΔH_m and ΔH_c value less than 2 J/g. The main reason could be that the knitted fabric had a better capacity to adsorb the MPCM solution during the coating process than other fabrics (e.g., woven fabric and 3D knitted fabric in this case).

3.5.2. Phase transition analysis

Since the MPCMs were directly incorporated into fabrics using binders during the coating process, the phase transition, including the melting process (e.g., T_{pm}) and solidifying process (e.g., T_{pc}), should be the same or similar to all the MPCM-coated fabrics. However, it was found that all the MPCM-coated fabrics had earlier phase transition behavior than the MPCMs (Fig. 12). Besides, the different MPCM-coated fabrics had different T_{pm} values and T_{pc} values between each other. Correspondingly, the ΔT values of different samples were different. A similar phenomenon was also observed in other research works [49–51]. Indeed, there was no clear reason for such a change of the phase transition. We proposed that some MPCMs were destroyed during the preparation of the MPCM solution and the coating method, which was caused by the poor mechanical property of MPCMs [52].

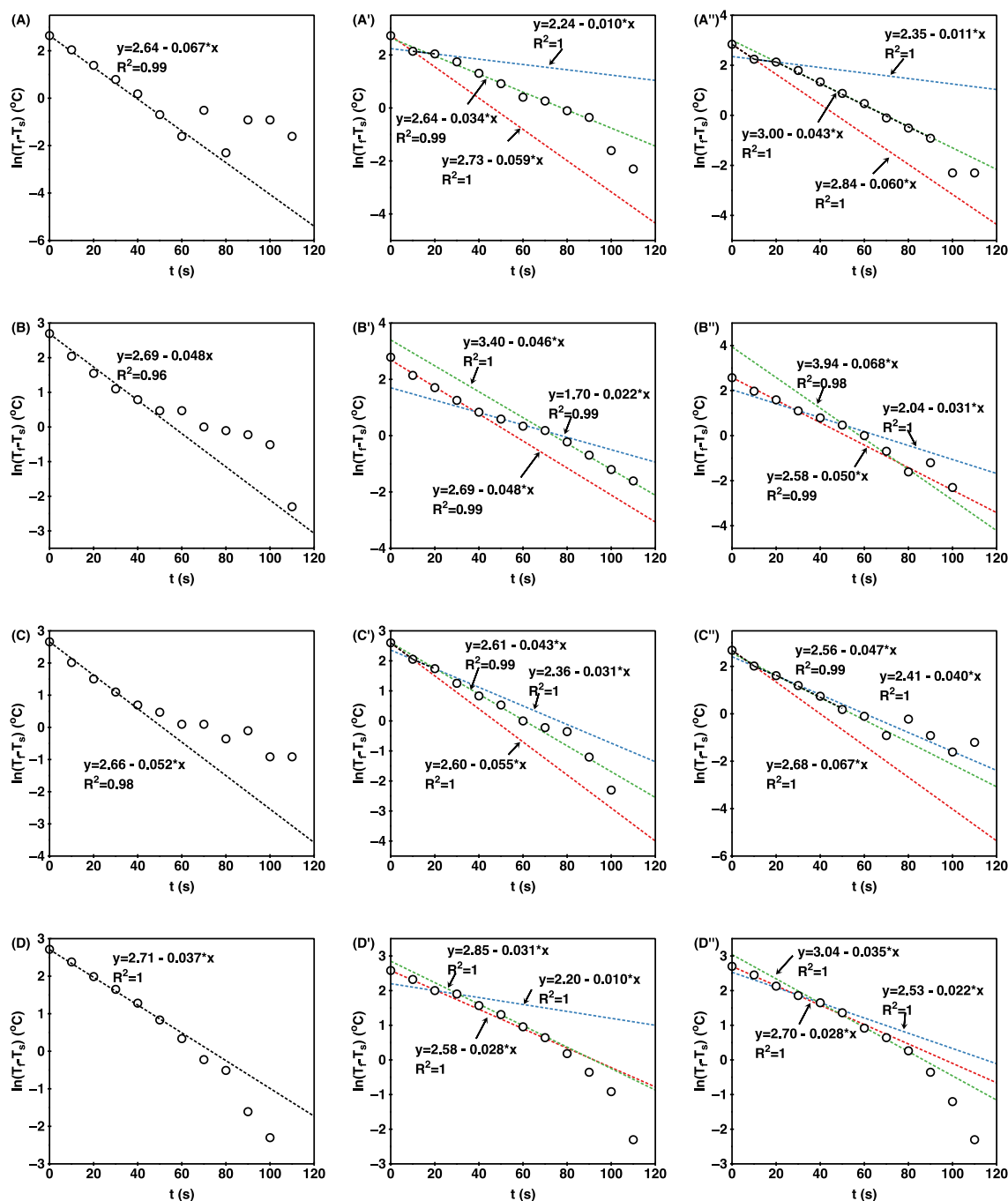


Fig. 16. Plots of $\ln(T_f - T_s)$ against t (A, A' and A'': the sample S1, SMH1-F, and SMH1-B; B, B' and B'': the sample S2, SMH2-F, and SMH2-B; C, C' and C'': the sample S3, SMH3-F, and SMH3-B; D, D' and D'': the sample S4, SMH4-F, and SMH4-B) (Red curve, blue curve, and green curve: the fitting model for the samples with liquid PCM, the samples with liquid-solid PCM and the samples with solid PCM). (For interpretation of the references to color in this figure legend, the reader is referred to the web version of this article.)

3.5.3. Thermal stability analysis after heating/cooling cycles

The results of MPCM-coated fabrics from 1st DSC curves and 11th DSC curve have also been schemed in Fig. 11 and Table 9. The Eq. (5) was used to reveal the effect of treatment (heating/cooling cycles and washing treatment) on the thermal energy storage of the MPCM-coated fabrics, where the $\Delta H_{m/c}^t$ was the enthalpy value of the sample with treatment, $\Delta H_{m/c}$ was the enthalpy value of the sample under 1st heating/cooling cycle and p_H was the enthalpy decrease rate (%). After 10 heating/cooling cycles in the DSC measurement, a slight decrease in both ΔH_m and ΔH_c value was observed for the samples, which was shown in Fig. 13 and p_H value ranged from 0 to 10 %. Besides, the phase

transition process of the samples after 10 heating/cooling processes was similar to the MPCM-coated fabrics during 1st heating/cooling process. From this point of view, the MPCM-coated fabrics had a highly stable thermal energy storage performance after the heating/cooling cycles.

3.5.4. Thermal stability analysis after washing treatment

Unlike the heating/cooling cycles, the washing treatment significantly reduced the thermal energy storage and affected the phase transition process. In detail, the ΔH_m and ΔH_c values of the sample S1 reduced from 8.19 J/g and 8.89 J/g to 4.03 J/g and 3.96 J/g after washing treatment, respectively. Samples S2 and S3 had the ΔH_m and

Table 11
Characterization of T-history of samples.

Sample code	T_i (°C)	t_l (s)	τ_l (s)	T_{l-s} (°C)	t_s (s)	τ_{l-s} (s)	T_s (°C)	t_s (s)	τ_s (s)
S1	–	–	–	–	–	–	[29,15]	[0,120]	1.49
SMH1-F	[30.4,23.6]	[0,10]	16.95	[23.6,22.8]	[10,20]	100.00	[22.8,15.1]	[20,120]	29.41
SMH1-B	[32.1,24.4]	[0,10]	16.67	[24.4,23.4]	[10,20]	90.91	[23.4,15]	[20,120]	23.26
S2	–	–	–	–	–	–	[30.8,16]	[0,120]	20.83
SMH2-F	[32.6,18.7]	[0,40]	20.83	[18.7,17.6]	[40,70]	45.45	[17.6,16.4]	[70,120]	21.74
SMH2-B	[29.3,19.9]	[0,30]	20.00	[19.9,18.2]	[30,50]	32.26	[18.2,16.2]	[50,120]	14.71
S3	–	–	–	–	–	–	[30.5,16.2]	[0,120]	19.23
SMH3-F	[29.9,24.2]	[0,10]	18.18	[24.2,22.1]	[10,20]	32.26	[24.2,16.4]	[20,120]	23.26
SMH3-B	[31.3,24.2]	[0,10]	14.93	[24.2,21.7]	[10,20]	25.00	[21.7,16.7]	[20,120]	21.28
S4	–	–	–	–	–	–	[31,15.9]	[0,120]	27.03
SMH4-F	[29.4,23.6]	[0,20]	35.71	[23.6,22.9]	[20,30]	100.00	[22.9,16.2]	[30,120]	32.26
SMH4-B	[31.2,22.7]	[0,30]	35.71	[22.7,21.5]	[30,40]	45.45	[21.5,16.3]	[40,120]	28.57

Subscript l , $l-s$, and s : the τ value of the samples with liquid PCM, the samples with liquid-solid PCM, and the sample with solid PCM, respectively. (The τ_s was also for the sample without PCMs).

ΔH_c values less than 0.8 J/g after the washing treatment. The sample S4 had the ΔH_m and ΔH_c values of 1.33 J/g and 1.53 J/g after the washing treatment, respectively. The calculated p_H values were shown in Fig. 13. The sample S4 with washing treatment had the lowest p_H value ranging from 10 % to 30 %, while other samples with washing treatment had the p_H values higher than 50 %. The decrease of thermal energy storage of the samples after washing treatment was caused by loss of MPCMs. By comparing weight loss of all the samples (Fig. 14), it was found only the hydrophobic fabrics with MPCMs had more weight loss percentage after washing treatment while other samples had much small weight loss percentage.

It was noticed that there are binders, thickeners, MPCMs and hydrophobic coating in the MPCM-coated hydrophobic fabrics. To reveal which part accounted for the decrease of enthalpy and weight, the mass loss percentage (p_m) of reference samples, hydrophobic fabrics and MPCM-coated hydrophobic fabrics was compared, which was calculated according to Eq. (6). The m_0 was the weight of sample before washing and m_1 was the weight of sample after washing. Fig. 14 provided the p_m values. As a result, the hydrophobic fabrics had smaller weight loss than 2 wt%, the fabrics coated with binders and thickeners almost had same weight, the fabrics coated with MPCMs, binders and thickeners had more weight loss, and MPCM-coated hydrophobic fabrics had highest weight loss. Therefore, weak adhesion between MPCMs and thickeners and binders as well as weak adhesion between MPCMs and hydrophobic coating layers accounted for reduce of thermal energy storage after washing treatment.

$$p_H = \left| \frac{\Delta H_{m/c}^i - \Delta H_{m/c}}{\Delta H_{m/c}} \right| \times 100\% \quad (5)$$

$$p_m = \frac{m_0 - m_1}{m_0} \times 100\% \quad (6)$$

3.6. The thermal buffering effect of MPCM-coated fabrics

Fig. 15 presented the T-history results of the samples with or without MPCMs. It took a long time for the MPCM-coated fabrics to cool down compared with the reference fabrics, which supported the thermal buffering effect. Besides, it was found that the initial surface temperatures were different between both sides of the MPCM-coated fabrics. The main reason was that the heating process of the samples was a result of the thermal radiation, which was affected by the porosity, the thickness, the specific heat capacity, etc. Furthermore, there were three parts in the T-history results of MPCM-coated fabrics, which corresponded to the three states of MPCMs, including liquid state, liquid-solid state (phase transition), and solid-state. To characterize the T-history, Newton's cooling law was applied [58] under the condition of small Biot number (Bi) (Calculation of Bi number was shown in Appendix 2), which was expressed in Eqs. (7) and (8). The T_f was the final stable temperature of

the sample, T_s was the recorded temperature of the sample at different times, T_i was the initial time, t was the time, and τ was the cooling constant (s). High τ value corresponded to the lower cooling rate.

$$T_f - T_s = (T_f - T_i)e^{-t/\tau} \quad (7)$$

$$\ln(T_f - T_s) = \ln(T_f - T_i) - t/\tau \quad (8)$$

Fig. 16 presented the plots of $\ln(T_f - T_s)$ against t for all the samples, and Table 11 gave the τ values. The τ_{l-s} value (τ value of samples with liquid-solid PCM) was higher than both τ_l (τ value of samples with liquid PCM) and τ_s (τ value of samples with solid PCM) values, which supported the thermal buffering effect. Additionally, the τ_{l-s} value of the F-side was higher than τ_{l-s} value of the B-side, which supported that the better thermal buffering effect was found when the MPCM-coated side faced towards the heating source.

4. Conclusion

In this work, four commercial fabrics, including two woven fabrics, one knitted fabric, and one 3D knitted fabric, were used for coating of the MPCMs. The pretreatment of the hydrophobic coating for the fabrics activated as the barrier layer for the penetration of MPCM solution, the MPCMs and binders were well deposited on one side. Besides, the wicking of MPCM solution in the surface of hydrophobic fabrics was proposed, and the hydrophobic fibers were on the surface of MPCM-coated side. As a result, the addition of the MPCM coating layer on the hydrophobic fabrics little affected the hydrophobic property, and the anti-fouling property of MPCM-coated fabrics was found. Besides, the one-way directional water moisture transfer behavior was enhanced for the samples with woven fabric structure or knitted fabric while reduced for the samples with 3D knitted fabric structure, which was caused by the difference in the distribution of MPCMs on the coated fabric surface. In addition, the breathability was reduced when there was an MPCM coating on the fabrics. Besides, the thermal enthalpy of the MPCM-coated fabrics ranged from 1 to 10 J/g. Correspondingly, the thermal buffering effect of the MPCM-coated fabrics was found and was better when MPCM-coated side towards the heating source. The heating/cooling cycles little affected the thermal energy storage and phase transition of the MPCM-coated fabrics, while the washing treatment significantly reduced the thermal energy storage. We propose that the prepared MPCM-coated fabrics be applied for personal use (e.g., underwear, jacket, shoes, etc.). Besides, the work is beneficial for the application of hydrophobic porous materials.

CRedit authorship contribution statement

Conceptualization: Kai Yang, Lenka Martinkova and Ondrej Ctibor.
Methodology: Kai Yang, Lenka Martinkova and Ondrej Ctibor.

Software: Kai Yang.

Validation: Kai Yang, Jakub Wiener, Mohanapriya Venkataraman and Jiri Militky.

Formal analysis: Kai Yang, Xiuling Zhang.

Investigation: Kai Yang, Guocheng Zhu and Juming Yao.

Resources: Jakub Wiener, Guoqing Zhang, Jiri Militky.

Data Curation: Kai Yang and Xiuling Zhang.

Writing-Original Draft: Kai Yang.

Writing-Review&Editing: Kai Yang, Xiuling Zhang, Mohanapriya Venkataraman and Jiri Militky.

Supervision: Kai Yang, Mohanapriya Venkataraman and Jiri Militky.

Project administration: Mohanapriya Venkataraman and Jiri Militky.

Funding acquisition: Mohanapriya Venkataraman and Jiri Militky.

Declaration of competing interest

We declare that we do not have any commercial or associative interest that represents a conflict of interest in connection with the work submitted.

Data availability

Data will be made available on request.

Acknowledgement

This work was supported by the project ‘Advanced structures for thermal insulation in extreme conditions’ (Reg. No. 21-32510M) granted by the Czech Science Foundation (GACR). Additionally, Kai Yang would like to thank Ing. Yuanfeng Wang for his assistance in providing a 3D fabric model, Ing. Jana Grabmullerova for her assistance in measuring SEM images, Ing. Denisa Knizkova for her assistance in the measurement of MMT and breathability, and Dr. Miroslava Pechocikova for her assistance in DSC measurement.

Appendix A. Supplementary data

Supplementary data to this article can be found online at <https://doi.org/10.1016/j.porgcoat.2022.107151>.

References

- [1] S. Zeng, S. Pian, M. Su, Z. Wang, M. Wu, X. Liu, M. Chen, Y. Xiang, J. Wu, M. Zhang, Q. Cen, Y. Tang, X. Zhou, Z. Huang, R. Wang, A. Tunuhe, X. Sun, Z. Xia, M. Tian, M. Chen, X. Ma, L. Yang, J. Zhou, H. Zhou, Q. Yang, X. Li, Y. Ma, G. Tao, Hierarchical-morphology metafabric for scalable passive daytime radiative cooling, *Science* 373 (2021) 692–696, <https://doi.org/10.1126/science.abi5484>.
- [2] R. Hu, Y. Liu, S. Shin, S. Huang, X. Ren, W. Shu, J. Cheng, G. Tao, W. Xu, R. Chen, X. Luo, Emerging materials and strategies for personal thermal management, *Adv. Energy Mater.* 10 (2020), 1903921, <https://doi.org/10.1002/aenm.201903921>.
- [3] S. Sundararajan, A.B. Samui, P.S. Kulkarni, Versatility of polyethylene glycol (PEG) in designing solid–solid phase change materials (PCMs) for thermal management and their application to innovative technologies, *J. Mater. Chem. A* 5 (2017) 18379–18396, <https://doi.org/10.1039/c7ta04968d>.
- [4] L. Xiang, D. Luo, J. Yang, X. Sun, J. Jin, S. Qin, Construction and design of paraffin/PVDF hollow fiber linear-phase change energy storage materials, *Energy Fuel* 33 (2019) 11584–11591, <https://doi.org/10.1021/acs.energyfuels.9b02852>.
- [5] H. Ke, Morphology and thermal performance of quaternary fatty acid eutectics/polyurethane/Ag form-stable phase change composite fibrous membranes, *J. Therm. Anal. Calorim.* 129 (2017) 1533–1545, <https://doi.org/10.1007/s10973-017-6399-9>.
- [6] K. Yang, M. Venkataraman, X. Zhang, J. Wiener, G. Zhu, J. Yao, J. Militky, Review: incorporation of organic PCMs into textiles, *J. Mater. Sci.* (2022) 1–50, <https://doi.org/10.1007/s10853-021-06641-3>.
- [7] K. Yang, M. Venkataraman, J. Wiener, X. Zhang, M. Stuchlik, G. Zhu, J. Yao, J. Militky, Crystallization mechanism of micro flake cu particle-filled Poly(ethylene glycol) composites, *Thermochim. Acta* (2022), 179172, <https://doi.org/10.1016/j.tca.2022.179172>.
- [8] L. Hes, luboshes@vslib.cz, B.I. Lu, Using a thermal simulator to determine the amount of time that humans are thermally protected by fabrics containing phase change materials, *Res. J. Text. Appar.* 8 (2004) 51–56, <https://doi.org/10.1108/rjta-08-02-2004-b007>.
- [9] M. Jaworski, Mathematical model of heat transfer in PCM incorporated fabrics subjected to different thermal loads, *Appl. Therm. Eng.* 150 (2019) 506–511, <https://doi.org/10.1016/j.applthermaleng.2019.01.019>.
- [10] K. Yang, M. Venkataraman, J. Karpiskova, Y. Suzuki, S. Ullah, I.-S. Kim, J. Militky, Y. Wang, T. Yang, J. Wiener, G. Zhu, J. Yao, Structural analysis of embedding polyethylene glycol in silica aerogel, *Microporous Mesoporous Mater.* 310 (2021), 110636, <https://doi.org/10.1016/j.micromeso.2020.110636>.
- [11] L. Pathak, G.V.N. Trivedi, R. Parameshwaran, S.S. Deshmukh, Microencapsulated phase change materials as slurries for thermal energy storage: a review, *Mater. Today Proc.* 44 (2021) 1960–1963, <https://doi.org/10.1016/j.matpr.2020.12.101>.
- [12] J.L. Reyez-Araiza, J. Pineda-Piñón, J.M. López-Romero, J.R. Gasca-Tirado, M. A. Contreras, J.C.J. Correa, L.M. Apátiga-Castro, E.M. Rivera-Muñoz, R. R. Velazquez-Castillo, J.de J.P. Bueno, A. Manzano-Ramirez, Thermal energy storage by the encapsulation of phase change materials in building elements—a review, *Materials* 14 (2021) 1420, <https://doi.org/10.3390/ma14061420>.
- [13] H. Liu, X. Wang, D. Wu, Innovative design of microencapsulated phase change materials for thermal energy storage and versatile applications: a review, *Sustain. Energy Fuels* 3 (2019) 1091–1149, <https://doi.org/10.1039/c9se00019d>.
- [14] Y. Wu, C. Chen, Y. Jia, J. Wu, Y. Huang, L. Wang, Review on electrospun ultrafine phase change fibers (PCFs) for thermal energy storage, *Appl. Energy* 210 (2018) 167–181, <https://doi.org/10.1016/j.apenergy.2017.11.001>.
- [15] Y. Wang, J. Yao, G. Zhu, J. Militky, J. Marek, M. Venkataraman, G. Zhang, A novel method for producing bi-component thermo-regulating alginate fiber from phase change material microemulsion, *Text. Res. J.* 90 (2020) 1038–1044, <https://doi.org/10.1177/0040517519886075>.
- [16] Z. Qin, L. Yi, S. Wang, L. Wang, J. Yao, G. Zhu, J. Militky, M. Venkataraman, M. Zhang, Supercooling suppression and mechanical property improvement of phase change nanofibers by optimizing core distribution, *Polymer* 233 (2021), 124176, <https://doi.org/10.1016/j.polymer.2021.124176>.
- [17] K. Iqbal, A. Khan, D. Sun, M. Ashraf, A. Rehman, F. Safdar, A. Basit, H.S. Maqsood, Phase change materials, their synthesis and application in textiles—a review, *J. Text. Inst.* 110 (2019) 625–638, <https://doi.org/10.1080/00405000.2018.1548088>.
- [18] H. Peng, J. Wang, X. Zhang, J. Ma, T. Shen, S. Li, B. Dong, A review on synthesis, characterization and application of nanoencapsulated phase change materials for thermal energy storage systems, *Appl. Therm. Eng.* 185 (2021), <https://doi.org/10.1016/j.applthermaleng.2020.116326>.
- [19] D.G. Prajapati, B. Kandasubramanian, A review on polymeric-based phase change material for thermo-regulating fabric application, *Polym. Rev.* 60 (2020) 389–419, <https://doi.org/10.1080/15583724.2019.1677709>.
- [20] J. Gu, W. Wang, D. Yu, Temperature control and low infrared emissivity double-shell phase change microcapsules and their application in infrared stealth fabric, *Prog. Org. Coat.* 159 (2021), 106439, <https://doi.org/10.1016/j.porgcoat.2021.106439>.
- [21] Y. Su, W. Zhu, M. Tian, Y. Wang, X. Zhang, J. Li, Intelligent bidirectional thermal regulation of phase change material incorporated in thermal protective clothing, *Appl. Therm. Eng.* 174 (2020), 115340, <https://doi.org/10.1016/j.applthermaleng.2020.115340>.
- [22] F. Salaün, E. Devaux, S. Bourbigot, P. Rumeau, Thermoregulating response of cotton fabric containing microencapsulated phase change materials, *Thermochim. Acta* 506 (2010) 82–93, <https://doi.org/10.1016/j.tca.2010.04.020>.
- [23] I. Kim, K. Lee, G. Cho, Heat storage/release characteristics and mechanical properties of combat uniform fabrics treated with microcapsules containing octadecane as phase change materials, *Fiber Polym.* 17 (2016) 1726–1734, <https://doi.org/10.1007/s12221-016-6796-x>.
- [24] T.R. Kar, A.K. Samanta, H.D. Sinnur, M. Kumar, Studies on effect of application of capric acid and stearic acid based reactive phase change materials (rPCM) with PHAMS binder on thermal comfort of cotton khadi fabric as thermo-tropic smart textiles, *J. Nat. Fibers* (2021), <https://doi.org/10.1080/15440478.2021.1880517>.
- [25] M. Khosrojerdi, S.M. Mortazavi, Impregnation of a porous material with a PCM on a cotton fabric and the effect of vacuum on thermo-regulating textiles, *J. Therm. Anal. Calorim.* 114 (2013) 1111–1119, <https://doi.org/10.1007/s10973-013-3144-x>.
- [26] Y. Yuan, H. Xiang, G. Liu, R. Liao, Fabrication of phase change microcapsules and their applications to anti-icing coating, *Surf. Interfaces* 27 (2021), 101516, <https://doi.org/10.1016/j.surfin.2021.101516>.
- [27] Y. Li, G. Wang, Z. Guo, P. Wang, A. Wang, Preparation of microcapsules coating and the study of their bionic anti-fouling performance, *Materials* 13 (2020) 1669, <https://doi.org/10.3390/ma13071669>.
- [28] F.A.P. Scacchetti, E. Pinto, G.M.B. Soares, Functionalization and characterization of cotton with phase change materials and thyme oil encapsulated in beta-cyclodextrins, *Prog. Org. Coat.* 107 (2017) 64–74, <https://doi.org/10.1016/j.porgcoat.2017.03.015>.
- [29] M. Karthikeyan, T. Ramachandran, O.L. Shanmugasundaram, Synthesis, characterization, and development of thermally enhanced cotton fabric using nanoencapsulated phase change materials containing paraffin wax, *J. Text. Inst.* 105 (2014) 1279–1286, <https://doi.org/10.1080/00405000.2014.886368>.
- [30] M. Karthikeyan, T. Ramachandran, O.L.S. Sundaram, Nanoencapsulated phase change materials based on polyethylene glycol for creating thermoregulating cotton, *J. Ind. Text.* 44 (2014) 130–146, <https://doi.org/10.1177/1528083713480378>.
- [31] J. Li, X. Zhu, H. Wang, P. Lin, L. Jia, L. Li, Y. Chen, Synthesis and properties of multifunctional microencapsulated phase change material for intelligent textiles, *J. Mater. Sci.* 56 (2021) 2176–2191, <https://doi.org/10.1007/s10853-020-05399-4>.

- [32] G. Li, G. Hong, D. Dong, W. Song, X. Zhang, Multiresponsive graphene-aerogel-directed phase-change smart fibers, *Adv. Mater.* 30 (2018), <https://doi.org/10.1002/adma.201801754>.
- [33] K. Zhu, X. Li, J. Su, H. Li, Y. Zhao, X. Yuan, Improvement of anti-icing properties of low surface energy coatings by introducing phase-change microcapsules, *Polym. Eng. Sci.* 58 (2018) 973–979, <https://doi.org/10.1002/pen.24654>.
- [34] H. Wang, W. Wang, H. Wang, X. Jin, J. Li, Z. Zhu, One-way water transport fabrics with hydrophobic rough surface formed in one-step electrospray, *Mater. Lett.* 215 (2018) 110–113, <https://doi.org/10.1016/j.matlet.2017.12.066>.
- [35] C. Cai, X. Ouyang, L. Zhou, G. Liu, Y. Wang, G. Zhu, J. Yao, J. Militky, M. Venkataraman, G. Zhang, Co-solvent free interfacial polycondensation and properties of polyurea PCM microcapsules with dodecanol dodecanoate as core material, *Sol. Energy* 199 (2020) 721–730, <https://doi.org/10.1016/j.solener.2020.02.071>.
- [36] D. Bhattacharjee, V.K. Kothari, Prediction of thermal resistance of woven fabrics. Part II: Heat transfer in natural and forced convective environments, *J. Text. Inst.* 99 (2008) 433–449, <https://doi.org/10.1080/00405000701582596>.
- [37] G. Zhu, Y. Fang, L. Zhao, J. Wang, W. Chen, Prediction of structural parameters and air permeability of cotton woven fabric, *Text. Res. J.* 88 (2018) 1650–1659, <https://doi.org/10.1177/0040517517705632>.
- [38] A. Razaque, P. Tesinova, L. Hes, J. Salacova, H.A. Abid, Investigation on hydrostatic resistance and thermal performance of layered waterproof breathable fabrics, *Fiber Polym.* 18 (2017) 1924–1930, <https://doi.org/10.1007/s12221-017-1154-1>.
- [39] L. Hes, M. Boguslawska-Baczek, M.J. Galdes, Thermal comfort of bedsheets under real conditions of use, *J. Nat. Fibers* 11 (2014) 312–321, <https://doi.org/10.1080/15440478.2013.867826>.
- [40] K. Yang, Q. Peng, M. Venkataraman, J. Novotna, J. Karpiskova, J. Mullerova, J. Wiener, M. Vikova, G. Zhu, J. Yao, J. Militky, Hydrophobicity, water moisture transfer and breathability of PTFE-coated viscose fabrics prepared by electrospraying technology and sintering process, *Prog. Org. Coat.* 165 (2022), 106775, <https://doi.org/10.1016/j.porgcoat.2022.106775>.
- [41] J. Diswat, L. Hes, K. Bal, Thermal resistance of cut pile hand tufted carpet and its prediction, *Text. Res. J.* 86 (2016) 1759–1767, <https://doi.org/10.1177/0040517515612356>.
- [42] L. Hes, K. Bal, I. Dolezal, Principles of clothing comfort and their use in evaluation of sensorial and thermal comfort of Men's casual jacket, *Fiber Polym.* 22 (2021) 2922–2928, <https://doi.org/10.1007/s12221-021-0425-z>.
- [43] K. Ghasemi, S. Tasnim, S. Mahmud, PCM, nano/microencapsulation and slurries: a review of fundamentals, categories, fabrication, numerical models and applications, *Sustainable Energy Technol. Assess.* 52 (2022), 102084, <https://doi.org/10.1016/j.seta.2022.102084>.
- [44] Z. Qiu, X. Ma, P. Li, X. Zhao, A. Wright, Micro-encapsulated phase change material (MPCM) slurries: characterization and building applications, *Renew. Sust. Energy Rev.* 77 (2017) 246–262, <https://doi.org/10.1016/j.rser.2017.04.001>.
- [45] M. Delgado, A. Lázaro, C. Peñalosa, J. Mazo, B. Zalba, Analysis of the physical stability of PCM slurries, *Int. J. Refrig.* 36 (2013) 1648–1656, <https://doi.org/10.1016/j.ijrefrig.2013.04.020>.
- [46] D. Murakami, H. Jinnai, A. Takahara, Wetting transition from the Cassie-Baxter state to the Wenzel state on textured polymer surfaces, *Langmuir* 30 (2014) 2061–2067, <https://doi.org/10.1021/la4049067>.
- [47] N. Mao, J. Ye, Z. Quan, H. Zhang, D. Wu, X. Qin, R. Wang, J. Yu, Tree-like structure driven water transfer in 1D fiber assemblies for functional moisture-wicking fabrics, *Mater. Des.* 186 (2020), 108305, <https://doi.org/10.1016/j.matdes.2019.108305>.
- [48] J. Wu, N. Wang, L. Wang, H. Dong, Y. Zhao, L. Jiang, Unidirectional water-penetration composite fibrous film via electrospinning, *Soft Matter* 8 (2012) 5996–5999, <https://doi.org/10.1039/c2sm25514f>.
- [49] K. Iqbal, D. Sun, Synthesis of nanoencapsulated Glauber's salt using PMMA shell and its application on cotton for thermoregulating effect, *Cellulose* 25 (2018) 2103–2113, <https://doi.org/10.1007/s10570-018-1692-8>.
- [50] A. Shahid, S. Miah, A. Rahim, Thermal and breathability management of microencapsulated phase change material (MPCM) incorporated jute fabric, *J. Eng. Fiber Fabr.* 16 (2021), <https://doi.org/10.1177/15589250211029564>, 1558925021102956.
- [51] A.S. Hicyilmaz, S. Teke, Z.I. Cin, A.C. Bedeloglu, Development of thermo-regulating fabrics with enhanced heat dissipation via graphene-modified n-octadecane microcapsules, *Polym. Eng. Sci.* (2021), <https://doi.org/10.1002/pen.25845>.
- [52] X. Lin, X. Zhang, J. Ji, L. Zheng, Research progress on preparation, characterization, and application of nanoparticle-based microencapsulated phase change materials, *Int. J. Energy Res.* 45 (2021) 9831–9857, <https://doi.org/10.1002/er.6538>.
- [53] S. Alay, F. Göde, C. Alkan, Synthesis and thermal properties of poly(n-butyl acrylate)/n-hexadecane microcapsules using different cross-linkers and their application to textile fabrics, *J. Appl. Polym. Sci.* 120 (2011) 2821–2829, <https://doi.org/10.1002/app.33266>.
- [54] P. Sánchez, M.V. Sánchez-Fernandez, A. Romero, J.F. Rodríguez, L. Sánchez-Silva, Development of thermo-regulating textiles using paraffin wax microcapsules, *Thermochim. Acta* 498 (2010) 16–21, <https://doi.org/10.1016/j.tca.2009.09.005>.
- [55] A. Nejman, E. Gromadzinska, I. Kamínska, M. Ciésłak, Assessment of thermal performance of textile materials modified with PCM microcapsules using combination of DSC and infrared thermography methods, *Molecules* 25 (2020), <https://doi.org/10.3390/molecules25010122>.
- [56] V. Skurkyte-Papieviene, A. Abraitiene, A. Sankauskaite, V. Rubeziene, J. Baltusnikaite-Guzaitiene, Enhancement of the thermal performance of the paraffin-based microcapsules intended for textile applications, *Polymers-Basel* 13 (2021) 1120, <https://doi.org/10.3390/polym13071120>.
- [57] Y. Iamphaojeen, P. Siriphannon, Adjustable thermal barrier of cotton fabric by multilayer immobilization of PCM nanocapsules, *Cellulose* 25 (2018) 3649–3661, <https://doi.org/10.1007/s10570-018-1804-5>.
- [58] K. Yang, J. Wiener, M. Venkataraman, Y. Wang, T. Yang, G. Zhang, G. Zhu, J. Yao, J. Militky, Thermal analysis of PEG/Metal particle-coated viscose fabric, *Polym. Test.* 100 (2021), 107231, <https://doi.org/10.1016/j.polymertesting.2021.107231>.

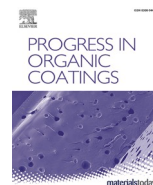
11.8 Publication 7: Hydrophobicity, water moisture transfer and breathability of PTFE-coated viscose fabrics prepared by electrospraying technology and sintering process

Publication

Yang, K., Peng, Q., **Venkataraman, M.**, Novotna, Karpiskova, J., Mullerova, J., Wiener, J., Vikova, M., Zhu, G., Yao, J., Militky, J. Hydrophobicity, water moisture transfer and breathability of PTFE-coated viscose fabrics prepared by electrospraying technology and sintering process, *Progress in Organic Coatings*. 165, (2022). DOI: 10.1016/j.porgcoat.2022.106775.

Author Contribution

- Conceptualization
 - Devised the project, the main conceptual ideas and proof outline.
- Validation
 - Verification of the overall reproducibility of results and other research outputs.
- Formal Analysis
 - Characterize the samples and conduct the experiments.
 - Processed the experimental data.
 - Performed the statistical analysis by using original software tools.
- Writing – Original Draft Preparation
 - Assisted in writing the manuscript, review and editing.
- Funding Acquisition
 - From GAČR as leader of the project
- Others
 - Supervision
 - Project Administration



Hydrophobicity, water moisture transfer and breathability of PTFE-coated viscose fabrics prepared by electro spraying technology and sintering process

Kai Yang^{a,*}, Qingyan Peng^a, Mohanapriya Venkataraman^a, Jana Novotna^a, Jana Karpiskova^b, Jana Mullerova^b, Jakub Wiener^a, Martina Vikova^a, Guocheng Zhu^c, Juming Yao^{d,e}, Jiri Militky^a

^a Department of Material Engineering, Faculty of Textile Engineering, Technical University of Liberec, Liberec, Czech Republic

^b Department of Nanochemistry, Institute for Nanomaterials, Advanced Technologies and Innovation, Technical University of Liberec, Liberec, Czech Republic

^c College of Textile Science and Engineering, Zhejiang Sci-tech University, Xiasha Education Park, People's Republic of China

^d School of Materials Science and Engineering, Zhejiang Sci-tech University, Xiasha Education Park, People's Republic of China

^e School of Materials Science and Chemical Engineering, Ningbo University, Ningbo, People's Republic of China

ARTICLE INFO

Keywords:

PTFE
Viscose fabric
Electrospraying
Sintering
Hydrophobic
Janus fabric

ABSTRACT

Coating of PTFE on the fabrics is one facial method to obtain the hydrophobic/superhydrophobic property. However, the breathability of the PTFE-coated fabrics prepared by traditional methods (e.g., sputtering) is significantly affected. Electro spraying technology was able to create the pure PTFE coating layer on any substrates and the following sintering process is necessary to obtain the hydrophobic/superhydrophobic property. In this work, the PTFE-coated viscose fabrics were firstly prepared via electro spraying technology and then stabilized after 10 min sintering process with different temperatures ranging from 150 °C to 210 °C. The morphology, hydrophobicity, breathability, and water moisture transfer of the PTFE-coated viscose fabrics as well as the chemical compatibility between PTFE microparticles and viscose fabric were investigated. With increased sintering temperature, the PTFE coating layer on the viscose fabric became physically denser, which corresponded to the reduced breathability. Only when sintering temperature was equal to or higher than 190 °C, the stable hydrophobicity of PTFE-coated viscose fabric was found. When sintering temperature was increased from 190 °C to 210 °C, the contact angle hysteresis of the hydrophobic PTFE-coated viscose fabric decreased from 9.2° to 3.4° and the one-way water moisture transfer was enhanced.

1. Introduction

Hydrophobic/superhydrophobic fabrics have been developed for various applications including self-cleaning fabrics [1,2], oil/water separation [3], water repellent fabrics [4], etc. The hydrophobic/superhydrophobic fabrics could be developed via various methods including dip coating [5], sol-gel technology [6,7], sputtering coating [8], electro spinning technology [9], atomic layer deposition (ALD) [10], etc. Generally, the water contact angle (WCA) value of the hydrophobic/superhydrophobic fabrics is focused on when the aforementioned

technologies are used, while there are fewer details related to the permeability of the hydrophobic/superhydrophobic fabrics which is considered to be significantly affected. Besides, the ALD is not proposed for large-scale production although the deposition of the objective atoms or polymers is controlled through the whole process [11]. For the electro spinning technology, the prepared nanofibrous membranes are deposited on the fabrics as a hydrophobic/superhydrophobic coating layer for surface modification [12]. Besides, the nanofibrous membrane-coated fibrous materials alter the ability of water transfer through the coated fibrous materials [13,14]. So, it is proposed that the deposited

Abbreviations: ALD, atomic layer deposition; ATR-FTIR, attenuated total reflection-Fourier transforms infrared; BET, Brunauer, Emmett and Teller; CAH, water contact angle hysteresis; Kr, Krypton; LOSM, laser optical scanning microscopy; MMT, moisture management tester; OMMC, overall moisture management capacity; PTFE, poly(tetrafluoroethylene); RF, radio frequency; SEM, scanning electronic microscopy; WCA, water contact angle; WVP, water vapor permeability.

* Corresponding author.

E-mail address: kai.yang@tul.cz (K. Yang).

<https://doi.org/10.1016/j.porgcoat.2022.106775>

Received 13 December 2021; Received in revised form 3 February 2022; Accepted 4 February 2022

Available online 10 February 2022

0300-9440/© 2022 Elsevier B.V. All rights reserved.

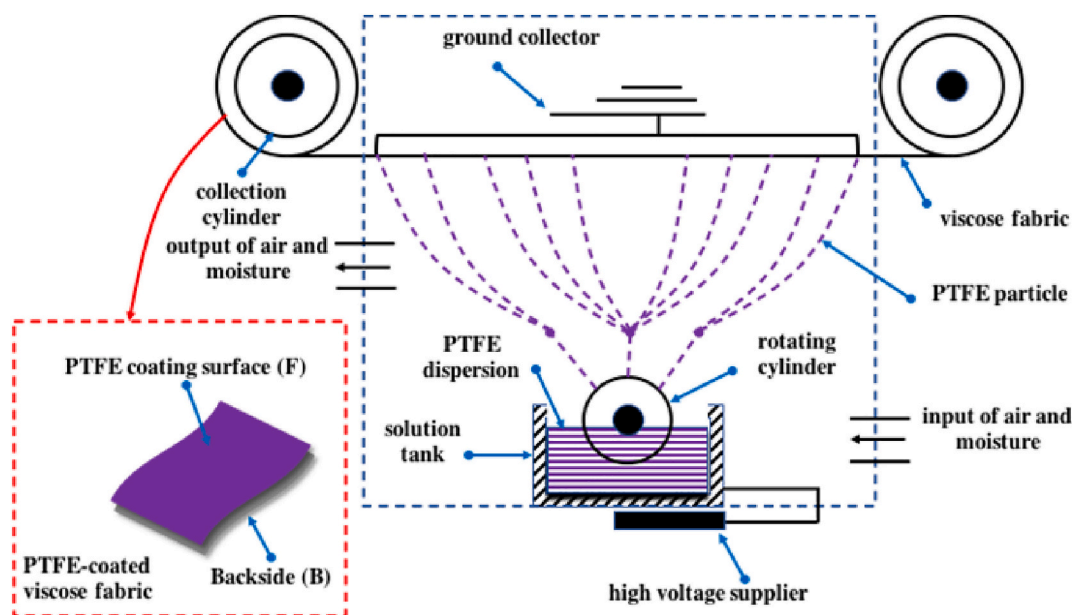


Fig. 1. Electrospaying process for PTFE-coated viscose fabric.

nanofibrous membranes as a hydrophobic/superhydrophobic coating layer have a great potential for surface modification for various topics. However, the nanofibrous membranes are not suitable as the outer layer and the interface compatibility of the nanofibrous membrane with the substrates still needs enhancement [15].

Poly(tetrafluoroethylene) (PTFE) is a synthetic fluoropolymer with repeated unit $[-(CF_2)_n]$ [16]. The strong C–F bonds (485 kJ/mol) supports the highly stable chemical and thermal properties [17]. The unique property of PTFE supports itself for the various applications, including the anti-icing, food processing industry, air purification, water purification, electronic, aerospace, wires, cables, textiles etc. [18–24]. To create the hydrophobic fabric by using PTFE, there are two main methods: 1) to make a coating of PTFE on fabric and 2) to incorporate the pure PTFE fibrous membrane on fabric surface. The first method is the facial one. For example, Fenglin Huang et al. made a coating of the PTFE nanoparticles on the silk fabric [8]. Da-Yeon Wi et al. made a coating of the PTFE on the cotton fabric via radio frequency (RF) sputtering method [25]. The higher pressure and longer sputtering time supported the better hydrophobic, while the breathability of the final PTFE-coated fabrics was possibly affected. For the second method, it is necessary to first fabricate the PTFE fibrous membrane. It is noticed that the inherent molecular structure of the PTFE determines that it is very hard to prepare PTFE fibers by traditional melting spinning and solution spinning [26]. The electrospinning method is available to fabricate the PTFE fibers by blending other supporting materials with PTFE. For example, Jin-Young Park et al. prepared the pure PTFE nanofibrous membrane by firstly blending PEG with PTFE for the electrospinning process and then the removed the PEG content via sintering process [27]. Xiao Li et al. also prepared PTFE fibrous materials for the PM 2.5 filtration by firstly blending PVA with PTFE for the electrospinning process and then the sintering process to distinguish the blended PVA [28]. The higher sintering temperature supported the higher mechanical property of the pure PTFE fibrous membrane. Although the final hydrophobic PTFE fibrous membranes could be incorporated on the fabric surface, the PTFE could be toxic when the sintering temperature was higher than 260 °C [29]. So, it is necessary to control the sintering temperature to obtain the PTFE fibrous membranes.

Apart from the aforementioned methods, the electrospaying technology is able for the fabrication of pure PTFE coating layer [30]. Electrospaying is a novel technology sharing the similar mechanism with electrospinning technology [31,32]. The significant difference

between the electrospaying and electrospinning technology is the jet flow which was classified in the region of Taylor cone-jet [33]. In details, the jet flow is forced to break up into the droplets with the stronger chain interactions after solvent evaporation, and the final products are considered as coating layers or films composed from the micro-/nanopolymers particles [34,35]. Still, the adhesion between electrospayed polymer particles and substrate still needs improvement.

Recently, our group already have applied the PTFE microparticle-filled coating layer on the polypropylene (PP) nonwoven fabric and optimized the electrospaying parameters [36–38]. Especially, the following sintering process with temperature between glass transition temperature and melting temperature of PTFE was applied to treat PTFE-coated fabric and the sintered PTFE-coated fabric had hydrophobicity. However, the final water contact angle value of the PTFE-coated PP fabrics was around 119°, which is possibly caused by the lower applied sintering temperature of 140 °C since the melting temperature of the PP fabric is around 160 °C. Then, the higher sintering temperature for the PTFE-coated fabric is possible to obtain the better hydrophobic property. The cellulosic fabrics are characterized as higher thermal stability (thermal degradation temperature was higher than 250 °C), high chemical stability, and good compatibility with other materials, and have been applied for various topics including fluorescence, self-cleaning, anti-bacterial, anti-UV, flame-resistance, thermal energy storage etc. [39–45], which is suitable to desposit PTFE microparticle-filled coating layer via electrospaying technology and sintering process.

In this work, the viscose fabric was selected as the substrate for PTFE coating by using electrospaying technology and the following 10 min sintering process with temperature ranging from 150 °C to 210 °C was applied. The optimized sintering temperature was found for the hydrophobic PTFE-coated viscose fabric. Furthermore, the effect of the sintering temperature on the PTFE coating layer was investigated by using ATR-FITR and RAMAN spectrum. Besides, the fabricated PTFE-coated viscose fabric was a Janus fabric, which consisted of the PTFE microparticle-coated viscose fibers as the hydrophobic layer and the pure viscose fibers as the hydrophilic layer. So, the water moisture transfer and breathability of the hydrophobic PTFE-coated viscose fabrics were investigated as well.

Table 1
Electrospraying parameters for fabrication of PTFE-coated viscose fabric.

Substrate speed (mm/min)	Voltage (kV)	Speed of electrode (ot/min)	In		Tent		Air	
			RH (%)	T (°C)	RH (%)	RH (%)	T (°C)	RH (%)
static	-10/30	5.0	42	22.3	46.8	22.8	49.9	22.4

2. Experimental

2.1. Materials

The PTFE dispersion (Teflon® PTFE 30) was purchased from DuPont company. According to the technical description, the PTFE dispersion contained 60 wt% of the PTFE particles and 34 wt% of the distilled water, and 6 wt% of a mixture of the nonionic wetting agent and the stabilizer. The PTFE particles in the PTFE dispersion ranged from 0.05 to 0.5 μm . Besides, the viscose nonwoven fabric (47 g/m^2) was used, which was provided by faculty of textile engineering, Technical University of Liberec.

2.2. Electrospraying process

The PTFE-coated viscose fabric was prepared via electrospraying technology. The needleless ‘Nanospider’ instrument NS 1S500U (ELMARCO s.r.o., Liberec, Czech Republic) (<https://www.elmarco.com/production-lines/ns-1s500u>) was used [46]. As seen in Fig. 1, the main parts of the ‘Nanospider’ instrument included the high-voltage power supplier, the solution storage tank, the electro rotating cylinder, the ground collector, and the substrate on the collectors. During the electrospraying process, the polymer solution or the polymer dispersion adhered to the electro rotating cylinder escaped under the applied electrostatic force field between the high-voltage power supplier and the ground collector formed the polymer particles or the polymer fibers and then the formed polymer particles and polymer fibrous fragments on the substrate on the collectors.

In this case, the PTFE dispersion was kept stirring for 24 h before the electrospraying process. The viscose fabric was set as the substrate for the deposition of PTFE particles. The optimized spinning parameters were proposed according to previous work and shown in Table 1 [38]. As a result, the PTFE microparticle-filled porous layer was formed on the viscose fabric during the electrospraying process. The PTFE-coated side was labeled as F-side and the uncoated side was labeled as B-side.

2.3. Sintering process

The sintering process was used for the activation of the hydrophobicity and the stabilization of the PTFE-coated viscose fabric. The sintering process was realized by 10 min treatment in the oven with temperatures of 150 °C, 170 °C, 190 °C, and 210 °C, respectively, where the shape of the PTFE-coated viscose fabric was fixed to avoid the thermal shrinkage in advance. As a result, each sample was labeled as S150, S170, S190, and S210 corresponding to the sintering temperature, respectively. The sample S25 was for the PTFE-coated viscose fabric without any sintering process.

2.4. Tests and methods

2.4.1. Morphology characterization

The surface and the cross-section of the prepared PTFE-coated viscose fabric were characterized by scanning electronic microscopy (SEM) (produced by VEGA TESCAN Inc., Lincoln, NE, USA) at the voltage of 20 kV.

The laser optical scanning microscopy (LOSM) (OLS5000 LEXT) was used to characterize the surface roughness. The surface roughness was measured by using the line model in the system. The profile $Z(x)$ related

to the height at the x position was automatically measured in the system along the length of the measured part of the sample (l_r). Three parameters including the arithmetic average height (R_a), the root mean square roughness (R_q) and the skewness (R_{sk}) were the outputs to characterize the surface roughness. The R_a value is for the surface roughness and expressed in Eq. (1). The R_q value is for the standard deviation of the distribution of surface heights, which was expressed in Eq. (2). The R_{sk} value is measured based on the R_q values and expressed in Eq. (3) respectively. The R_{sk} is for the symmetry of the recorded profile about the mean line, which is used to distinguish the different profiles with the same R_a and R_q . Especially, the negative R_{sk} value supports the lubrication of the hydrophobic surface from the point of symmetry.

$$R_a = \frac{1}{l_r} \int_0^{l_r} |Z(x)| dx \quad (1)$$

$$R_q = \sqrt{\frac{1}{l_r} \int_0^{l_r} Z^2(x) dx} \quad (2)$$

$$R_{sk} = \frac{1}{R_q^3} \left(\frac{1}{l_r} \int_0^{l_r} Z^3(x) dx \right) \quad (3)$$

The BET (Brunaue, Emmett and Teller) specific surface area (S_{BET}) of the prepared PTFE-coated viscose fabrics was determined by using the Krypton (Kr) gas adsorption (AutoSorb-iQ-MP, Quantachrome, Florida, USA) at the temperature of liquid nitrogen. All the samples were pre-dried at 50 °C for 48 h and then outgassed under vacuum at 50 °C for at least 24 h before the measurement. Besides, the thickness and the areal density of the prepared PTFE-coated viscose fabrics were measured by standard techniques.

2.4.2. Water contact angle (WCA)

The WCA of the PTFE-coated viscose fabrics were measured by using a portable computer-based instrument (See System E Advex Instrument) following ISO 27448:200 test method. The deionized water was deposited on the F-side of the PTFE-coated viscose fabric from a needle on a microsyringe (5 μL) and then the WCA value was automatically calculated in the system. To reveal the hydrophobic stability of the F-side of the PTFE-coated viscose fabric, the WCA values with the deposited time of 1 min was continuously recorded. The 5 second interval was proposed in this case.

Additionally, the water contact angle hysteresis (CAH) of the PTFE-coated viscose fabric was performed by using the sessile droplet method. The WCA values after 1 min deposition were obtained by controlling the volume of the water droplet on the F-side of the PTFE-coated viscose fabric. Both advancing WCA model and receding WCA model were recorded. The advancing WCA was modeled by increasing the water droplet volume and the receding WCA was modeled by decreasing the deposited water droplet volume. The addition or reduction of the water droplets was controlled by using a microsyringe (5 μL). In details, the WCA value of one water droplet with 1 min deposition was first recorded. Then one more water droplet was added to the previously deposited water droplet and the corresponding WCA was recorded after 1 min. The same steps were repeated 5 times and the final maximum water droplet was 25 μL . Then five WCA values were recorded, and the advancing model was finished. For the receding model, one water droplet was firstly sucked out from the deposited final maximum water droplet and the WCA was recorded after 1 min. The steps were repeated 4 times till there was only a 5 μL water droplet on the F-side of the PTFE-coated

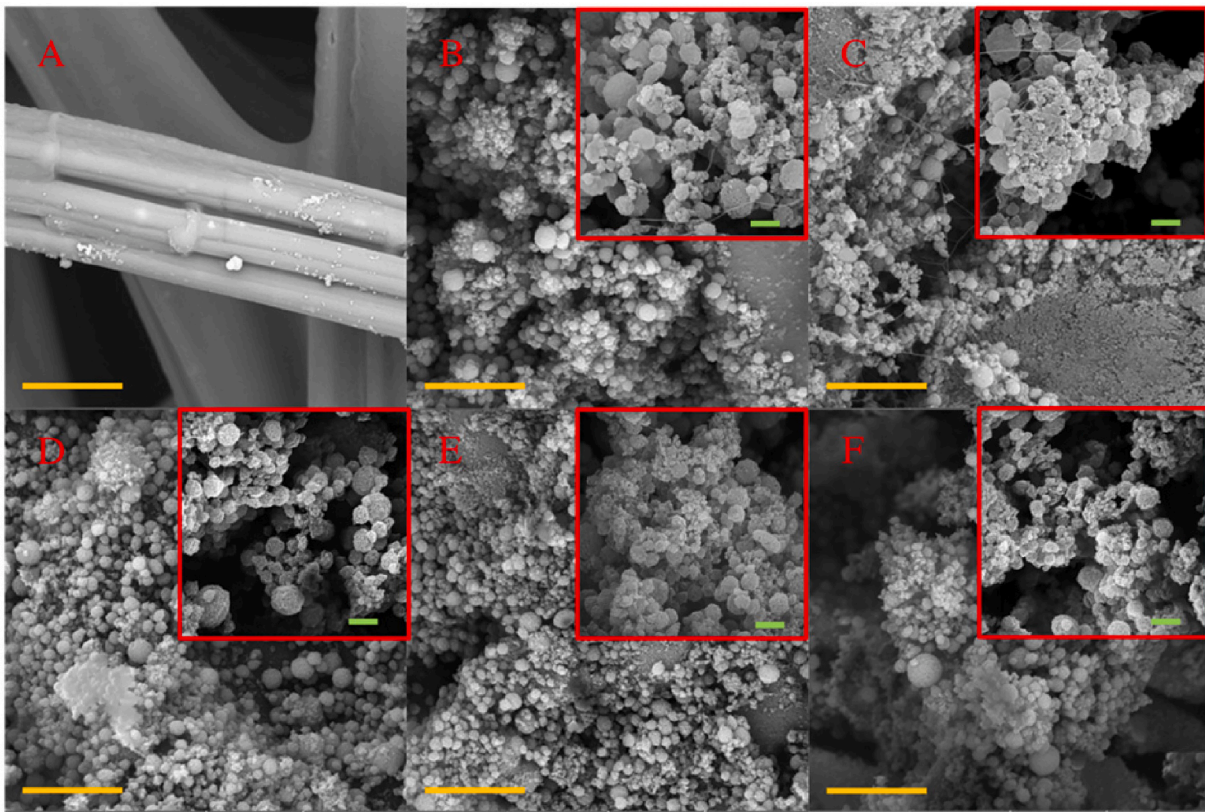


Fig. 2. Surface structure of F-side on PTFE-coated viscose fabric (A, B, C, D, E and F: the viscose fabric, the sample S25, S150, S170, S190 and S210) (length of yellow and green scale: 10 μm and 2 μm). (For interpretation of the references to color in this figure legend, the reader is referred to the web version of this article.)

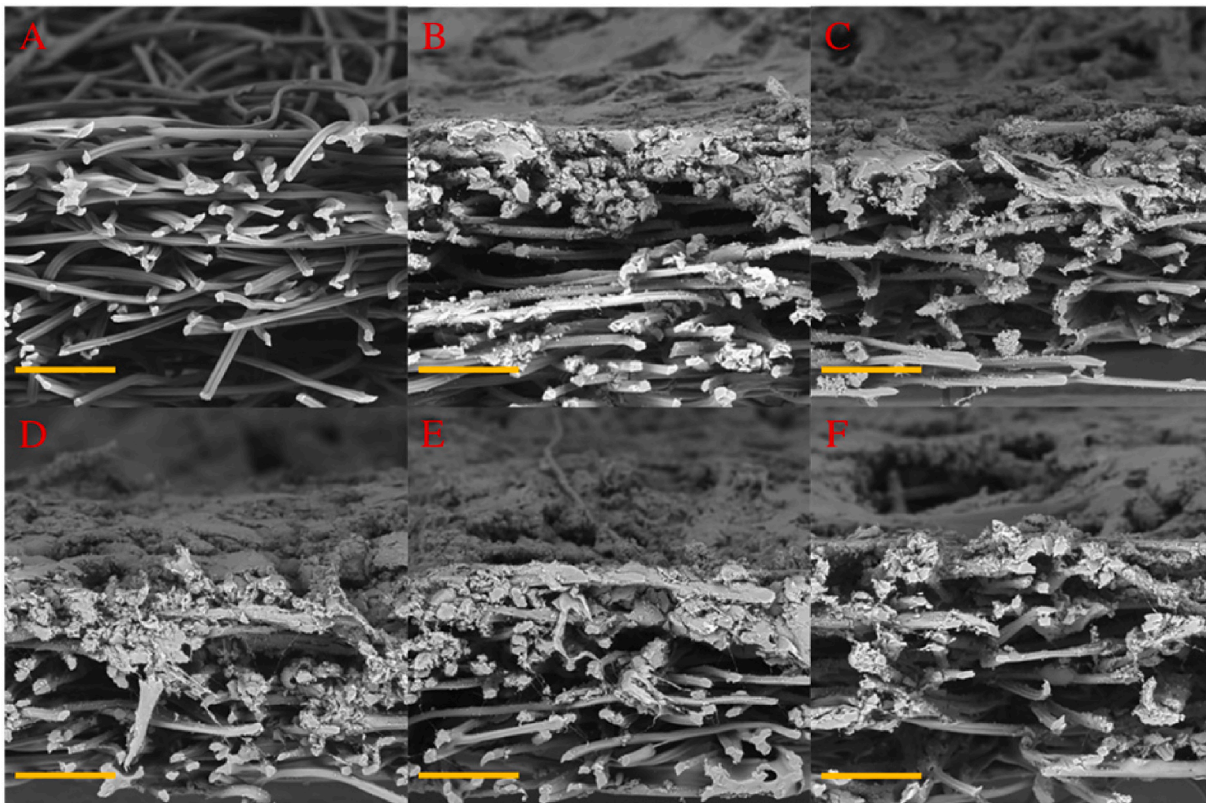


Fig. 3. Cross-section of PTFE-coated viscose fabric (A, B, C, D, E and F: the viscose fabric, the sample S25, S150, S170, S190 and S210) (length of yellow scale: 10 μm). (For interpretation of the references to color in this figure legend, the reader is referred to the web version of this article.)

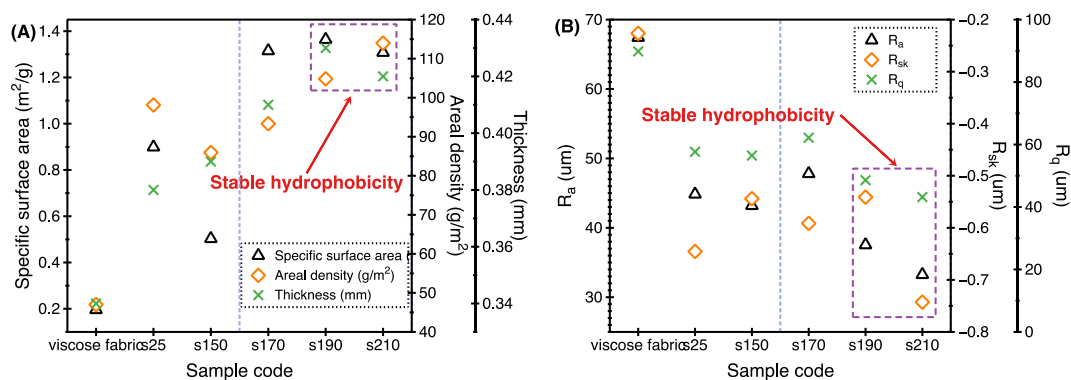


Fig. 4. Characterization for morphology of PTFE-coated viscose fabric (A: the characterization for density of PTFE coating layer and B: the roughness change with sintering temperature).

viscose fabric. Then four WCA values were recorded, and the receding model was finished. The complete one cycle for the measurement of WCH contained the one advancing model and one receding model. The 5 cycles were recorded for the statistics and repeatability.

2.4.3. Chemical compatibility evaluation of PTFE-coated viscose fabric

Both the F-side and B-side of the PTFE-coated viscose fabrics as well as the viscose fabric were characterized via the attenuated total reflection-Fourier transforms infrared (ATR-FTIR) spectroscopy. In details, a FTIR spectrometer iS50 (Thermo Scientific™, USA) with ATR attachment VarigATR (Harrick) was used with an angle of 65°, and a spectrum was obtained in the spectral region between 400 and 4000 cm⁻¹ with 2 cm⁻¹ resolutions. Besides, the DXR™ RAMAN spectrometer (Thermo Scientific™, USA) was used to characterize the macromolecular structure of the fabricated PTFE microparticle-filled coating layer on the viscose fabric.

2.4.4. Moisture transfer evaluation

The moisture management tester (MMT) (M290, SDL Atlas) following standard ISO 81181 was used to characterize the moisture transfer. Each sample was measured from both F-side and B-side. The six parameters including wetting time (t), absorption rate (k), max wetted radius (R), spreading speed (v), one-way transport capacity (I), and overall moisture management capacity (OMMC) were used to characterize the moisture transfer.

2.4.5. Breathability characterization

The breathability characterization of the PTFE-coated viscose fabric was evaluated by measuring the air permeability and the water vapor resistance (R_{et}) [47]. The measurement of the air permeability (mm/s) was performed by using the tester FX3300 according to ISO 9237 under 100 Pa and 200 Pa, respectively. The water vapor permeability (WVP) measurement was performed by using the tester PERMETEST in line with ISO 11092. After measurement, the water vapor resistance (R_{et}) (Pa m² W⁻¹) was measured following Eq. (4), where the P_m value was the water vapor saturate partial pressure and the P_a value was the actual partial water vapor pressure during the measurement under a certain temperature, and both q_0 and q_s were the heat flow value without and with a sample, respectively.

$$R_{et} = (P_m - P_a)(q_s^{-1} - q_0^{-1}) \quad (4)$$

3. Results and discussion

3.1. Influence of sintering temperature on the morphology of the PTFE-coated viscose fabric

Both Figs. 2 and Fig. 3 showed the surface and cross-section of the prepared PTFE-coated viscose fabric, respectively. The PTFE coating

layer was well deposited on one side of the viscose fabric (F-side), which consisted of various sphere PTFE microparticles ranging from 0.1 to 10 μm. The PTFE microparticles were also randomly adhered to each other. Besides, there were still some microfibers apart from the electrospayed PTFE microparticles. By comparing with the electrospayed PTFE microparticles on PP fabric in previous work [36–38], the existence of the microfibers was caused by the change of the substrate. In this case, viscose fabric was set as substrate, which slightly altered the formation process of the electrospayed PTFE microparticles.

Fig. 4(A) schemed S_{BET} , areal density and thickness of all the samples (detailed values were shown in Appendix 1, Table S1-1). It was noticed that the order of S_{BET} for the sintered PTFE-coated viscose fabric was S150 < S170 < S210 < S190. On one hand, a sharp increase in the S_{BET} value when the sintering temperature reached 170 °C, which suggested that the PTFE microparticles became smaller and the sintering temperature of 170 °C was considered as enough to remove wetting agents and the remaining water content. On another hand, the sintering situation of the PTFE coating layer which was accompanied with removal of the wetting agents and remaining water content resulted in the formation of different PTFE coating layers with various sizes of PTFE microparticle and pores in PTFE-coating layer. In addition, the areal density of PTFE-coated viscose fabric was increased when the sintering temperature was increased and correspondingly PTFE coating layer became denser, which was caused by higher compact density of the PTFE microparticle-filled coating layer.

Fig. 4(B) presented the surface roughness of the PTFE-coated viscose fabrics (detailed values were shown in Appendix 1, Table S1-1). Obviously, the surface roughness of PTFE-coated viscose fabric was reduced after sintering process, which was caused by the stronger adhesion between PTFE microparticles each other as well as PTFE microparticles and viscose fabric during sintering process. The decrease trend of R_a and R_q values was found when sintering temperature was higher than 170 °C, which was considered to share the similar reason as change of S_{BET} and areal density. Besides, the mean R_{sk} values of all the samples were negative, which supported the lubrication property of the surface. The physical meaning of roughness values was described with hydrophobic property in the following Section 3.2.

To further understand the sintering situation of PTFE coating layer on the viscose fabric, both ATR-FTIR and RAMAN provided more details (Appendix 2). No new chemical bonds were detected from ATR-FTIR analysis, and only physical interaction between PTFE microparticles and viscose fabric was found [48–50]. Besides, the fabricated PTFE microparticles had the 13₆ configurations as well as the reversal-helix structure [51,52]. Among the PTFE crystalline phases, the 13₆ configurations tended to be transformed into reversal-helix structure when the sintering temperature reached 190 °C. The intensity of the peak at 1020 cm⁻¹ (I_{1020}) which was only supported by viscose fabric was used to characterize the relative amount of the PTFE coating layer on the viscose

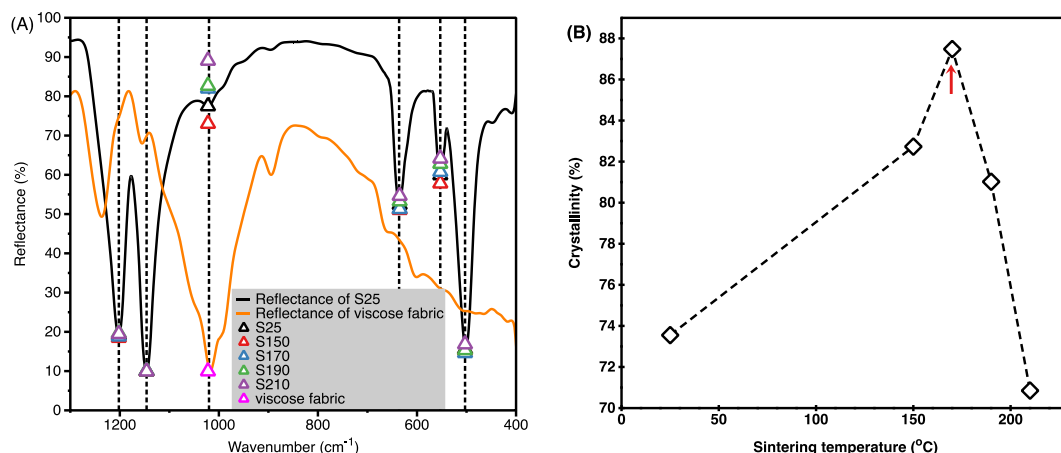


Fig. 5. The reflectance intensity of selected peaks in ATR-FTIR curves with sintering temperature for F-side (A) and estimated crystallinity of PTFE microparticles on F-side via RAMAN analysis (B).

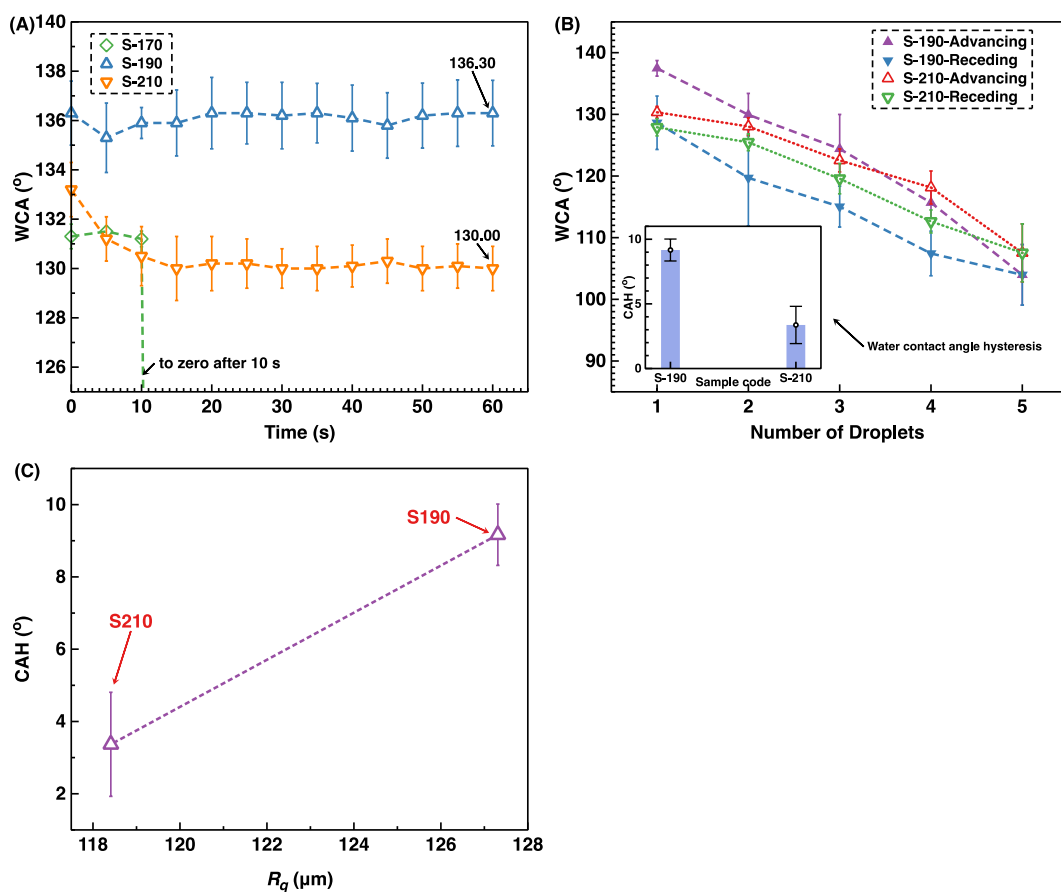


Fig. 6. WCA of the PTFE-coated viscose fabric (A: the WCA value with time, B: CAH curve and C: change of CAH value with R_q value).

fabric, and the I_{1020} values were schemed in Fig. 5(A). The I_{1020} of F-side was much smaller than the pure viscose fabric, which was contributed by the coverage of the PTFE microparticle on the viscose fabric. Besides, the sample S170, S190 and S210 had I_{1020} value of F-side than the sample S25 and S150, which corresponded to the analysis of areal density. As a result, the order for the PTFE microparticles amount on the F-side of the samples was $S170 < S190 < S210$, which supported that the increase in sintering temperature from 170 °C to 210 °C supported the formation of the denser PTFE microparticle-based coating layer. Fig. 5 (B) presented the estimated crystallinity of PTFE coating layer on the F-

side [52]. It was found that the crystallinity was increased and reached the maximum value of 87.42% when the sintering temperature was increased to 170 °C and then was decreased when the sintering temperature was higher. The PTFE crystallinity changes with sintering temperatures suggested that the order of adhesion force between the PTFE microparticles and viscose fabric was $S170 < S190 < S210$.

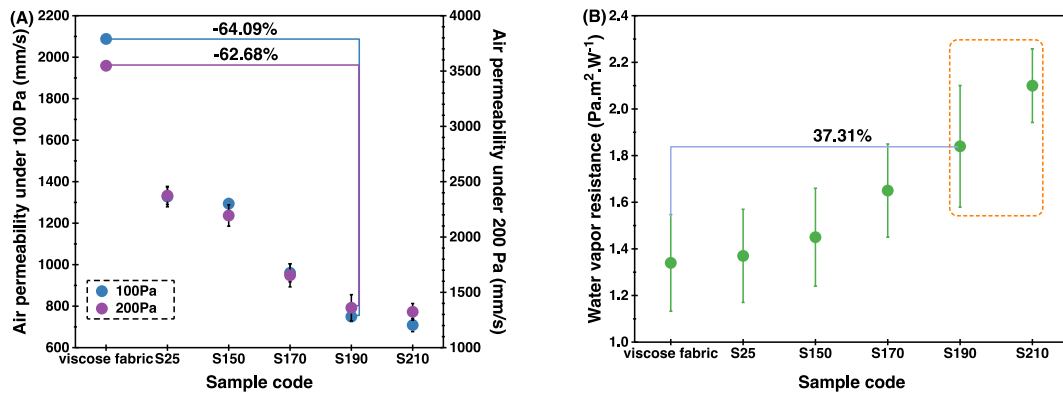


Fig. 7. Breathability of the PTFE-coated viscose fabric (A: air permeability, and B: water vapor resistance).

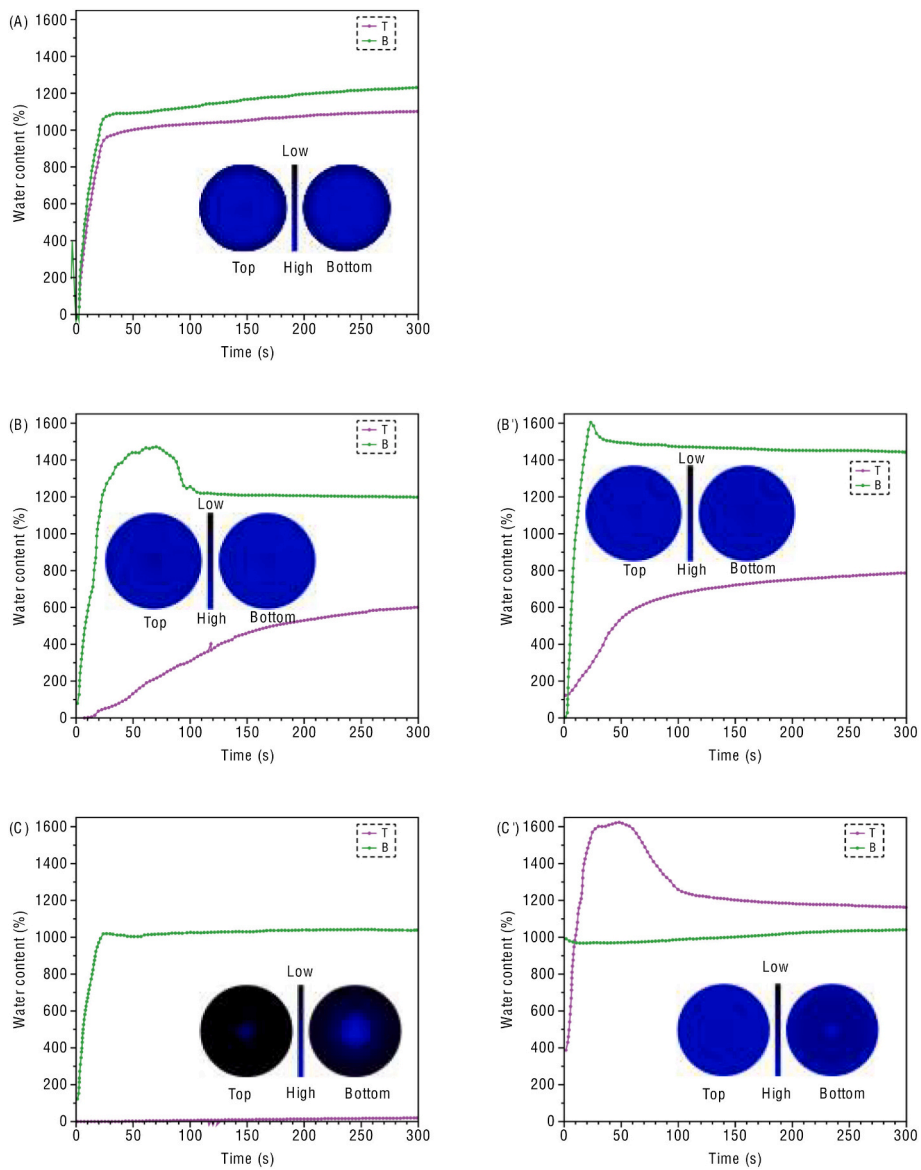


Fig. 8. MMT curves of the prepared PTFE-coated fabrics (T: top and B: bottom; A, B and C: the sample viscose fabric, S190 and S210 with PTFE coating side as the top side during the MMT measurement, respectively; B', and C': the sample S190 and S210 with PTFE coating side as the back side during the MMT measurement, respectively).

3.2. Influence of sintering temperature on the hydrophobicity of PTFE-coated viscose fabric

The WCA results were shown in Fig. 6(A). In details, the S190 had the final stable WCA as 136.3° , the S210 had the final stable WCA as 130.0° , the sample S170 can keep the WCA for 10s and both sample S25 and S150 had no WCA values. In this case, the factors for the WCA values included the morphology structure (dense degree) and roughness of the PTFE-coated viscose fabric. Still, the crystallinity of the electrospayed PTFE microparticles affected the final WCA, while the effect of the crystalline or amorphous part of the PTFE macromolecules on the WCA could be included in the roughness [53]. So, the effect of crystallinity of the electrospayed PTFE microparticles on the WCA was not specified.

For the sample S25 and S150, the remaining water content and the wetting agents in the S25 and S150 accounted for the hydrophilic PTFE coating layer. For the sample S170, we proposed that the loosen PTFE coating layer did not support the stable hydrophobic property. For the sample S190 and the sample S210, the hydrophobic property was supported by the formed dense PTFE coating layer. Besides, the sample S210 had a lower stable WCA than the S190, which could be supported by the higher surface roughness R_a value and the estimated higher crystallinity [54].

Furthermore, the CAH curves of the S190 and S210 were presented in Fig. 6(B) (detailed values were given in Appendix 1, Table S1-2). The WCA of both sample S190 and S210 tended to decrease with the higher volume of the water droplet. For the advancing model, the WCA value of the sample S190 higher than the sample S210 when there was the maximum $15\mu\text{L}$ volume of the water droplet on the F-side, and then the sample S210 became to have a higher WCA value than S190 when the water droplet was continuously increased (here the final maximum volume of a water droplet was $25\mu\text{L}$). For the receding model, the S210 had a visible higher WCA value than the S190 till there was only a $5\mu\text{L}$ volume of the water droplet on the surface. The difference in hydrophobicity comparison for both advancing and reducing model between S190 and S210 may be caused by the different wetting situations with increased water droplet volume. The final CAH value of the sample S210 as 3.4° was smaller than the CAH value of the sample S190 as 9.2° . On one hand, the CAH values were affected by roughness. In this case, R_q value accounted for the CAH values [55], which was presented in Fig. 6(C). The higher R_q value resulted in the higher CAH value. On another hand, the lower CAH values supported other surficial properties (e.g., self-cleaning, anti-fouling etc.) The CAH values of the fabricated PTFE-coated viscose fabric were comparable with other (super)hydrophobic fabrics [2,56], which supported potential applications.

3.3. Effect of sintering temperature on breathability of PTFE-coated viscose fabric

The breathability including the air permeability and the WVP values of the PTFE-coated viscose fabrics were presented in Fig. 7 (detailed values were given in Appendix 1, Table S1-3).

It was found that the air permeability was decreased significantly when there was PTFE coating on the viscose fabric under both 100 Pa and 200 Pa. With the sintering temperature increase, the air permeability was decreased correspondingly. It was noticed that a decrease in the air permeability of the PTFE-coated viscose fabrics became more significant when the sintering temperature was at least higher than 150°C , and then the decrease rate tended to be much lower when the sintering temperature was higher than 190°C . The change of the air permeability with sintering temperature corresponded to the results in Section 3.1 and suggested that sample S190 and S210 had the dense PTFE coating layer. Besides, the lowest decrease rate was evaluated ranging from 62% to 65% to have the hydrophobic PTFE-coated viscose fabric by comparing the sample S190 with the viscose fabric. However, the air permeability values of both samples S190 and S210 were higher than 700 mm/s under 100 Pa and 1300 mm/s under 200 Pa,

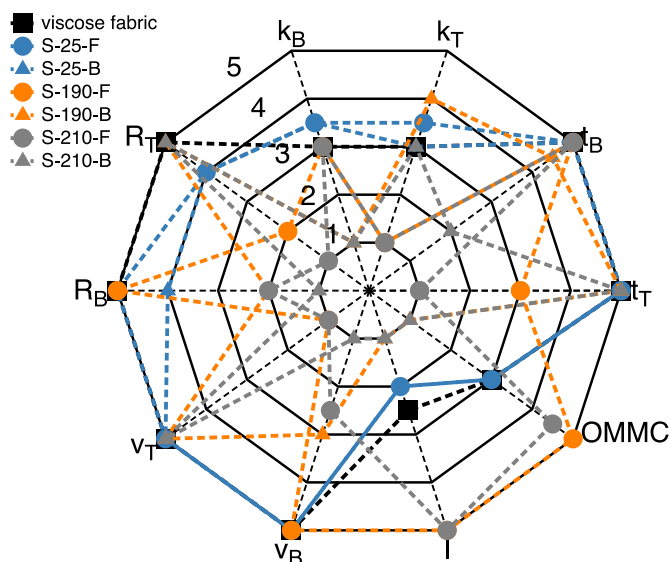


Fig. 9. MMT evaluation according to ISO 81181 (subscript T and B: the top side and bottom side).

respectively. As a result, the excellent air permeability of the hydrophobic PTFE-coated viscose fabric was proposed.

For the WVP measurement, it was noticeable that there was a slight increase in the water vapor resistance when there was a PTFE coating layer on the viscose fabric by comparing the viscose fabric with S25. The main reason was that the original PTFE coating layer was hydrophilic because of the wetting agents and the water. With the sintering temperature increase, the water vapor resistance was increased due to the loss of the wetting agents and the water. Furthermore, the water vapor resistance of the sample S170 was increased when compared with S150, S25, and the viscose fabric. Such a change trend was proposed to correspond to the morphology change as analyzed in Section 3.1. Besides, the lowest increase rate was evaluated to be around 37% to have the hydrophobic PTFE-coated viscose fabric by comparing the sample S190 with the pure viscose fabric. As a result, the samples S190 and S210 had the water vapor resistance of $1.84\text{ Pa m}^2\text{ W}^{-1}$ and $2.10\text{ Pa m}^2\text{ W}^{-1}$, respectively.

3.4. Moisture transfer through the hydrophobic PTFE-coated viscose fabrics

Section 3.3 proved that only sample S190 and S210 were sufficiently hydrophobic. So, here only the sample S190, S210 and pure viscose fabric were focused on. Since the hierarchy structure along the thickness direction of the PTFE-coated viscose fabric was found, both sides of the sample S190, S210 were measured via MMT method. Fig. 8 presented the moisture transfer curves and the details of obtained moisture transfer behaviors were presented in Appendix 1, Fig. S1-1.

The order of the water moisture transfer ability through F-side to B-side was viscose fabric < S190 < S210. It was noticed that the water firstly penetrated through the porous hydrophobic layer consisting of the PTFE-coated viscose fibers because of the capillary force. Then, the water was adsorbed by the hydrophilic layer and finally reached outer layer. By combining with hydrophobicity analysis in Section 3.2, the better hydrophobicity of sample S210 than sample S190 not only supported the difficult to wet the F-side but also resulted in the water moisture transfer from F-side to B-side. For the water moisture transfer ability through B-side to F-side, both sample S190 and S210 had negative I values while viscose fabric had positive I value. Then main reason was that resistance of the water moisture to keep penetrating the whole sample sharply increased when the water moisture reached the porous hydrophobic layer.

Table 2

Comparison of the breathable PTFE-coated viscose fabrics with other works related to PTFE-coated fabrics.

Type of fabrics	Coating method	Highest WCA (°)	CAH ⁱ (°)	Air permeability (100 Pa) (mm/s)	WVP ⁱ (Pa m ² W ⁻¹)	Ref.
PTFE-coated silk fabric	Sputtering	140.0	5.00	N/A	N/A	[8]
PTFE-coated cotton fabric	RF Sputtering	138.0	N/A	N/A	N/A	[25]
PTFE-coated PP fabric	Electrospraying	119.5	N/A	~500	N/A	[37]
PTFE-coated viscose fabric	Electrospraying	137.5	3.4	800	2.1	This work

The subscript *i*: the highest value in references and this work.

As a result, the viscose fabric, the sample S25, the sample S190 and the sample S210 were evaluated according to ISO 81181 and shown in Fig. 9. The S190 and the S210 were classified into moisture management fabric and water penetration fabric when the water moisture transferred from the F-side to B-side.

4. Conclusion

In this work, the hydrophobic PTFE-coated viscose fabrics were successfully prepared via electrospraying technology and sintering process.

In details, the physical formation for the creation of the pure PTFE microparticles occurred during the sintering process and the wetting agents and the remained water content tended to be distinguished when the sintering temperature was 170 °C. The stronger adhesion between the PTFE microparticles and viscose fabric was suggested when the sintering temperature was increased from 170 °C to 210 °C, which was supported by observing the decreased crystallinity of the PTFE microparticles. Correspondingly, PTFE coating layer became denser by observing that the relative amount of the PTFE microparticles on the coated side tended to be more when the sintering temperature was increased from 170 °C to 210 °C. Only when the sintering temperature was equal to or higher than 190 °C, the PTFE-coated viscose fabric had the stable hydrophobicity. It was found that the hydrophobicity became poorer while the water contact angle hysteresis became stable when sintering temperature was increased from 190 °C to 210 °C, which caused by the change of the surface roughness. Still, the lower sintering temperature to obtain the hydrophobicity of the PTFE-coated viscose fabric in this work was safer for the practical application and fabrication [29]. The fabricated PTFE-coated viscose fabric potentially supported self-cleaning property, anti-fouling property etc. Besides, the significant decrease in the air permeability and the water vapor permeability of the PTFE-coated viscose fabrics after sintering process was found, but still the air permeability and the water vapor permeability of the optimized hydrophobic PTFE-coated viscose fabric were 800 mm/s under 100 Pa and 2.1 Pa m² W⁻¹, respectively. By comparing with other PTFE-coated viscose fabric via other methods (Table 2), the hydrophobicity of the prepared breathable PTFE-coated viscose fabrics in this work was similar and the breathability was considered as the advantage. What's more, the water moisture transfer was enhanced when the sintering temperature was increased from 190 °C to 210 °C, which was caused by the difference between the PTFE-coated side and the uncoated side.

We propose that this work extends the application of the electrospraying technology to fabricate the polymer-coated fabrics. Besides, this work could support similar works to fabricate the Janus fabric with the particle-filled coating layer on the surface. Besides, this work deepens the understanding for the effect of the sintering process on electrosprayed PTFE microparticles.

CRedit authorship contribution statement

Conceptualization: Kai Yang, Qingyan Peng, Mohanapriya Venkataraman;
 Methodology: Kai Yang, Qingyan Peng, Jana Novotna;
 Software: Kai Yang, Jana Karpiskova, Jana Mullerova, Martina Vikova;

Validation: Kai Yang, Mohanapriya Venkataraman, Jakub Wiener and Jiri Militky;

Formal analysis: Kai Yang, Qingyan Peng and Mohanapriya Venkataraman;

Investigation: Kai Yang and Qingyan Peng;

Resources: Jakub Wiener and Jiri Militky;

Data Curation: Kai Yang and Qingyan Peng;

Writing-Original draft: Kai Yang;

Writing-Review & editing: Kai Yang, Mohanapriya Venkataraman and Jiri Militky;

Supervision: Kai Yang, Mohanapriya Venkataraman and Jiri Militky;

Visualization: Kai Yang;

Project administration: Kai Yang, Mohanapriya Venkataraman, Jiri Militky, Guocheng Zhu and Juming Yao;

Funding acquisition: Mohanapriya Venkataraman, Jiri Militky, Jana Karpiskova and Jana Mullerova.

Declaration of competing interest

We declare that we do not have any commercial or associative interest that represents a conflict of interest in connection with the work submitted.

Acknowledgement

This work was financially supported by the project 'Advanced structures for thermal insulation in extreme conditions' (Reg. No. 21-32510M) granted by the Czech Science Foundation (GACR) and the project 'Research Infrastructure NanoEnviCz' (No. LM2018124) granted by the Ministry of Education, Youth and Sports of the Czech Republic. Last but not least, the authors are indebted to Ing. Martin Stuchlik for his assistance in ATR-FTIR and RAMAN measurement.

Appendix A. Supplementary data

Supplementary data to this article can be found online at <https://doi.org/10.1016/j.porgcoat.2022.106775>.

References

- [1] K. Sasaki, M. Tenjimbayashi, K. Manabe, S. Shiratori, Asymmetric superhydrophobic/superhydrophilic cotton fabrics designed by spraying polymer and nanoparticles, ACS Appl. Mater. Interfaces 8 (2016) 651–659, <https://doi.org/10.1021/acsami.5b09782>.
- [2] Y. Wang, V. Baheti, M.Z. Khan, M. Vikova, K. Yang, T. Yang, J. Militky, A facile approach to develop multifunctional cotton fabrics with hydrophobic self cleaning and UV protection properties using ZnO particles and.pdf, J. Text. Inst. (2021), <https://doi.org/10.1080/00405000.2021.1975905>.
- [3] J. Wang, F. Han, B. Liang, G. Geng, Hydrothermal fabrication of robustly superhydrophobic cotton fibers for efficient separation of oil/water mixtures and oil-in-water emulsions, J. Ind. Eng. Chem. 54 (2017) 174–183, <https://doi.org/10.1016/j.jiec.2017.05.031>.
- [4] A. Mukhopadhyay, V.K. Midha, A review on designing the waterproof breathable fabrics part I: fundamental principles and designing aspects of breathable fabrics, J. Ind. Text. 37 (2008) 225–262, <https://doi.org/10.1177/1528083707082164>.
- [5] C.-H. Xue, P.-T. Ji, P. Zhang, Y.-R. Li, S.-T. Jia, Fabrication of superhydrophobic and superoleophilic textiles for oil–water separation, Appl. Surf. Sci. 284 (2013) 464–471, <https://doi.org/10.1016/j.apsusc.2013.07.120>.
- [6] M. Espanhol-Soares, L. Costa, M.R.A. Silva, F.S. Silva, L.M.S. Ribeiro, R. Gimenes, Super-hydrophobic coatings on cotton fabrics using sol–gel technique by spray,

- J. Sol-Gel Sci. Technol. 95 (2020) 22–33, <https://doi.org/10.1007/s10971-020-05307-x>.
- [7] M. Yang, W. Liu, C. Jiang, S. He, Y. Xie, Z. Wang, Fabrication of superhydrophobic cotton fabric with fluorinated TiO₂ sol by a green and one-step sol-gel process, *Carbohydr. Polym.* 197 (2018) 75–82, <https://doi.org/10.1016/j.carbpol.2018.05.075>.
- [8] F. Huang, Q. Wei, Y. Liu, W. Gao, Y. Huang, Surface functionalization of silk fabric by PTFE sputter coating, *J. Mater. Sci.* 42 (2007) 8025–8028, <https://doi.org/10.1007/s10853-007-1580-3>.
- [9] H.B. Madalosso, R. Machado, D. Hotza, C. Marangoni, Membrane surface modification by electrospinning, coating, and plasma for membrane distillation applications: a state-of-the-art review, *Adv. Eng. Mater.* 23 (2021) 2001456, <https://doi.org/10.1002/adem.202001456>.
- [10] C. Li, L. Ren, X. Liu, C. Zhang, D. Chen, W. Xu, Y. Qin, Superhydrophilic and underwater superoleophobic poly(propylene) nonwoven coated with TiO₂ by atomic layer deposition, *Adv. Mater. Interfaces* 8 (2021), 2001485, <https://doi.org/10.1002/admi.202001485>.
- [11] R. Li, N. Li, J. Hou, Y. Yu, L. Liang, B. Yan, G. Chen, Aquatic environment remediation by atomic layer deposition-based multi-functional materials: a review, *J. Hazard. Mater.* 402 (2020), 123513, <https://doi.org/10.1016/j.jhazmat.2020.123513>.
- [12] K. Li, D. Hou, C. Fu, K. Wang, J. Wang, Fabrication of PVDF nanofibrous hydrophobic composite membranes reinforced with fabric substrates via electrospinning for membrane distillation desalination, *J. Environ. Sci.* 75 (2019) 277–288, <https://doi.org/10.1016/j.jes.2018.04.002>.
- [13] N. Mao, J. Ye, Z. Quan, H. Zhang, D. Wu, X. Qin, R. Wang, J. Yu, Tree-like structure driven water transfer in 1D fiber assemblies for functional moisture-wicking fabrics, *Mater. Des.* 186 (2020), 108305, <https://doi.org/10.1016/j.matdes.2019.108305>.
- [14] H. Wang, X. Wang, T. Lin, Unidirectional water transfer effect from fabrics having a superhydrophobic-to-hydrophilic gradient, *J. Nanosci. Nanotechnol.* 13 (2013) 839–842, <https://doi.org/10.1166/jnn.2013.6008>.
- [15] K. Yang, M. Venkataraman, Y.F. Wang, X.M. Xiong, T. Yang, J. Wiener, J. Militky, R. Mishra, J. Marek, G.C. Zhu, J.M. Yao, Thermal performance of a multi-layer composite containing peg/laponite as pcms, *J. Fiber Bioeng. Informatics* 13 (2020) 61–68, <https://doi.org/10.3993/jfbim00330>.
- [16] Q. Chao, L. Meng, C. Shuxian, Anti-icing characteristics of PTFE super hydrophobic coating on titanium alloy surface, *J. Alloy Compd.* 860 (2021), 157907, <https://doi.org/10.1016/j.jallcom.2020.157907>.
- [17] G.J. Puts, P. Crouse, B.M. Ameduri, Polytetrafluoroethylene: synthesis and characterization of the original extreme polymer, *Chem. Rev.* 119 (2019) 1763–1805, <https://doi.org/10.1021/acs.chemrev.8b00458>.
- [18] E. Dhanumalayan, G.M. Joshi, Performance properties and applications of polytetrafluoroethylene (PTFE)—a review, *Adv. Compos. Hybrid Mater.* 1 (2018) 247–268, <https://doi.org/10.1007/s42114-018-0023-8>.
- [19] S. Feng, Z. Zhong, F. Zhang, Y. Wang, W. Xing, Amphiphobic polytetrafluoroethylene membranes for efficient organic aerosol removal, *ACS Appl. Mater. Interfaces* 8 (2016) 8773–8781, <https://doi.org/10.1021/acsami.5b11315>.
- [20] R. Jafari, G. Momen, M. Farzaneh, Durability enhancement of icephobic fluoropolymer film, *J. Coat. Technol. Res.* 13 (2016) 405–412, <https://doi.org/10.1007/s11998-015-9759-z>.
- [21] M. Wegener, W. Wirges, B. Tiersch, Porous polytetrafluoroethylene (PTFE) electret films: porosity and time dependent charging behavior of the free surface, *J. Porous. Mater.* 14 (2007) 111–118, <https://doi.org/10.1007/s10934-006-9015-0>.
- [22] J.A. Barish, J.M. Goddard, Anti-fouling surface modified stainless steel for food processing, *Food Bioprod. Process.* 91 (2013) 352–361, <https://doi.org/10.1016/j.fbp.2013.01.003>.
- [23] K.D. Dearn, T.J. Hoskins, D.G. Petrov, S.C. Reynolds, R. Banks, Applications of dry film lubricants for polymer gears, *Wear* 298 (2013) 99–108, <https://doi.org/10.1016/j.wear.2012.11.003>.
- [24] F.-H. Su, Z.-Z. Zhang, W.-M. Liu, Study on the friction and wear properties of glass fabric composites filled with nano- and micro-particles under different conditions, *Mater. Sci. Eng.* 392 (2005) 359–365, <https://doi.org/10.1016/j.msea.2004.09.036>.
- [25] D.-Y. Wi, I.W. Kim, J. Kim, Water repellent cotton fabrics prepared by PTFE RF sputtering, *Fiber Polym.* 10 (2009) 98–101, <https://doi.org/10.1007/s12221-009-0098-5>.
- [26] S.J. Zhu, Y.Y. Zhou, O. Takashi, G. Wu, Preparation of polytetrafluoroethylene ultrafine fiber mats with electrospinning process, *Mater. Sci. Forum* 675–677 (2011) 827–830, <https://doi.org/10.4028/www.scientific.net/msf.675-677.827>.
- [27] J.-Y. Park, J.-H. Lee, C.-H. Kim, Y.-J. Kim, Fabrication of polytetrafluoroethylene nanofibrous membranes for guided bone regeneration, *RSC Adv.* 8 (2018) 34359–34369, <https://doi.org/10.1039/c8ra05637d>.
- [28] X. Li, X.-X. Wang, T.-T. Yue, Y. Xu, M.-L. Zhao, M. Yu, S. Ramakrishna, Y.-Z. Long, Waterproof-breathable PTFE nano- and microfiber membrane as high efficiency PM_{2.5} filter, *Polymers-Basel* 11 (2019) 590, <https://doi.org/10.3390/polym11040590>.
- [29] M. Sajid, M. Ilyas, PTFE-coated non-stick cookware and toxicity concerns: a perspective, *Environ. Sci. Pollut. Res.* 24 (2017) 23436–23440, <https://doi.org/10.1007/s11356-017-0095-y>.
- [30] E. Burkarter, C.K. Saul, F. Thomazi, N.C. Cruz, L.S. Roman, W.H. Schreiner, Superhydrophobic electrospayed PTFE, *Surf. Coat. Technol.* 202 (2007) 194–198, <https://doi.org/10.1016/j.surfcoat.2007.05.012>.
- [31] J. Xie, J. Jiang, P. Davoodi, M.P. Srinivasan, C.-H. Wang, Electrohydrodynamic atomization: a two-decade effort to produce and process micro-/nanoparticulate materials, *Chem. Eng. Sci.* 125 (2015) 32–57, <https://doi.org/10.1016/j.ces.2014.08.061>.
- [32] D.-N. Phan, M.Q. Khan, N.-T. Nguyen, T.-T. Phan, A. Ullah, M. Khatri, N.N. Kien, I.-S. Kim, A review on the fabrication of several carbohydrate polymers into nanofibrous structures using electrospinning for removal of metal ions and dyes, *Carbohydr. Polym.* 252 (2021), 117175, <https://doi.org/10.1016/j.carbpol.2020.117175>.
- [33] J. Rosell-Llompart, J. Grifoll, I.G. Loscertales, Electrospays in the cone-jet mode: from Taylor cone formation to spray development, *J. Aerosol Sci.* 125 (2018) 2–31, <https://doi.org/10.1016/j.jaerosci.2018.04.008>.
- [34] A. Jaworek, A.M. Gañán-Calvo, Z. Machala, Low temperature plasmas and electrospays, *J. Phys. D. Appl. Phys.* 52 (2019), 233001, <https://doi.org/10.1088/1361-6463/ab0fdb>.
- [35] T. He, J.V. Jakerst, Structured micro/nano materials synthesized via electrospay: a review, *Biomater. Sci.-UK* 8 (2020) 5555–5573, <https://doi.org/10.1039/d0bm01313g>.
- [36] M. Venkataraman, R. Mishra, K. Yang, J. Militky, D. Kremenakova, G. Zhu, J. Yao, Preparation of Electrospayed Microporous Membranes, 2018, <https://doi.org/10.1088/1757-899x/460/1/012017>.
- [37] Q. Peng, K. Yang, M. Venkataraman, X. Tan, X. Xiong, J. Novotna, J. Karpiskova, J. Hruza, M. Stuchlík, J. Militky, Preparation of electrospayed composite coated microporous filter for particulate matter capture, *Nano Sel.* (2021), <https://doi.org/10.1002/nano.202100186>.
- [38] M. Venkataraman, K. Yang, X. Xiong, J. Militky, D. Kremenakova, G. Zhu, J. Yao, Y. Wang, G. Zhang, Preparation of electrospayed, microporous particle filled layers, *Polymers-Basel* 12 (2020), <https://doi.org/10.3390/polym12061352>.
- [39] I.S. Marae, W. Sharmoukh, E.A. Bakhite, O.S. Moustafa, M.S. Abbady, H.E. Emam, Durable fluorescent cotton textile by immobilization of unique tetrahydrothienoisoquinoline derivatives, *Cellulose* 28 (2021) 5937–5956, <https://doi.org/10.1007/s10570-021-03871-1>.
- [40] H.E. Emam, Generic strategies for functionalization of cellulosic textiles with metal salts, *Cellulose* 26 (2019) 1431–1447, <https://doi.org/10.1007/s10570-018-2185-5>.
- [41] H.E. Emam, M. El-Shahat, M.S. Hasanin, H.B. Ahmed, Potential military cotton textiles composed of carbon quantum dots clustered from 4-(2,4-dichlorophenyl)-6-oxo-2-thioxohexahydropyrimidine-5-carbonitrile, *Cellulose* 28 (2021) 9991–10011, <https://doi.org/10.1007/s10570-021-04147-4>.
- [42] H.E. Emam, O.M. Darwesh, R.M. Abdelhameed, Protective cotton textiles via amalgamation of cross-linked zeolitic imidazole frameworks, *Ind. Eng. Chem. Res.* 59 (2020) 10931–10944, <https://doi.org/10.1021/acs.iecr.0c01384>.
- [43] H.B. Ahmed, K.M. Abualnaja, R.Y. Ghareeb, A.A. Ibrahim, N.R. Abdelsalam, H. E. Emam, Technical textiles modified with immobilized carbon dots synthesized with infrared assistance, *J. Colloid Interface Sci.* 604 (2021) 15–29, <https://doi.org/10.1016/j.jcis.2021.07.014>.
- [44] K. Yang, J. Wiener, M. Venkataraman, Y. Wang, T. Yang, G. Zhang, G. Zhu, J. Yao, J. Militky, Thermal analysis of PEG/Metal particle-coated viscose fabric, *Polym. Test.* 100 (2021), 107231, <https://doi.org/10.1016/j.polymertesting.2021.107231>.
- [45] S. Faheem, V. Baheti, M. Tunak, J. Wiener, J. Militky, Flame resistance behavior of cotton fabrics coated with bilayer assemblies of ammonium polyphosphate and casein, *Cellulose* 26 (2019) 3557–3574, <https://doi.org/10.1007/s10570-019-02296-1>.
- [46] O. Jirsak, F. Sanetrik, D. Lukas, V. Kotek, L. Martinova, J. Chaloupek, Method of Nanofibres Production From a Polymer Solution Using Electrostatic Spinning and a Device for Carrying Out the Method, 2009. US7585437B2.
- [47] L. Hes, M. Bogusławska-Baczek, M.J. Gerales, Thermal comfort of bedsheets under real conditions of use, *J. Nat. Fibers* 11 (2014) 312–321, <https://doi.org/10.1080/15440478.2013.867826>.
- [48] R. Wang, G. Xu, Y. He, Structure and properties of polytetrafluoroethylene (PTFE) fibers, *E-Polymers* 17 (2017) 215–220, <https://doi.org/10.1515/epoly-2016-0059>.
- [49] C. Chung, M. Lee, E.K. Choe, Characterization of cotton fabric scouring by FT-IR ATR spectroscopy, *Carbohydr. Polym.* 58 (2004) 417–420, <https://doi.org/10.1016/j.carbpol.2004.08.005>.
- [50] A. Kljun, T.A.S. Benians, F. Goubet, F. Meulewaeter, J.P. Knox, R.S. Blackburn, Comparative analysis of crystallinity changes in cellulose I polymers using ATR-FTIR, X-ray diffraction, and carbohydrate-binding module probes, *Biomacromolecules* 12 (2011) 4121–4126, <https://doi.org/10.1021/bm201176m>.
- [51] C. Quarti, A. Milani, C. Castiglioni, Ab initio calculation of the IR Spectrum of PTFE: helical symmetry and defects, *J. Phys. Chem. B* 117 (2013) 706–718, <https://doi.org/10.1021/jp3102145>.
- [52] J.T. Shen, Y.T. Pei, J.Th.M.D. Hosson, Structural changes in polytetrafluoroethylene molecular chains upon sliding against steel, *J. Mater. Sci.* 49 (2014) 1484–1493, <https://doi.org/10.1007/s10853-013-7829-0>.
- [53] Y. Wang, D.K. Sang, Z. Du, C. Zhang, M. Tian, J. Mi, Interfacial structures, surface tensions, and contact angles of diiodomethane on fluorinated polymers, *J. Phys. Chem. C* 118 (2014) 10143–10152, <https://doi.org/10.1021/jp501683d>.
- [54] J. Yang, R. Wang, F. Long, X. Zhang, J. Liu, W. Hu, L. Liu, New perspectives on structural parameters and hydrophobic model inspired by a superhydrophobic cu cone-flower coating, *Mater. Des.* 206 (2021), 109827, <https://doi.org/10.1016/j.matdes.2021.109827>.
- [55] J. Wang, Y. Wu, Y. Cao, G. Li, Y. Liao, Influence of surface roughness on contact angle hysteresis and spreading work, *Colloid Polym. Sci.* 298 (2020) 1107–1112, <https://doi.org/10.1007/s00396-020-04680-x>.
- [56] M.Z. Khan, V. Baheti, J. Militky, A. Ali, M. Vikova, Superhydrophobicity, UV protection and oil/water separation properties of fly ash/trimethoxy(octadecyl)

silane coated cotton fabrics, *Carbohydr. Polym.* 202 (2018) 571–580, <https://doi.org/10.1016/j.carbpol.2018.08.145>.